

Detecting Load Induced Thermal Damage in Concrete

Robert Stein

A thesis submitted for the degree of Doctor of Philosophy

University of Sheffield

Department of Civil and Structural Engineering

September 2014

Copyright

Attention is drawn to the fact that copyright of this thesis rests with the author. A copy of this thesis has been supplied on condition that anyone who consults it is understood to recognize that its copyright rests with the author and they must not copy it or use material from it except as permitted by law or with the consent of the author.

This thesis may be made available for consultation within the University Library and may be photocopied or lent to other libraries for the purposes of consultation.

EXECUTIVE SUMMARY

Ordinary Portland cement based materials that are subjected to mechanical load during heating experience Load Induced Thermal Strain (LITS). LITS is known to have a significant effect on material strength and loading stiffness¹ and may completely suppress thermal expansion in the loaded axes². It has been proposed that LITS occurs as a result of a mechanical damage mechanism known as Load Induced Thermal Damage¹ (LITD) which occurs in the microstructure of the hydrated material.

This investigation has undertaken to characterise the pore structure of LITS affected concrete in order to quantify any microstructural changes and verify the LITD hypothesis. Pore structure was chosen as the principal feature for investigation due to its inherent relationship with mechanical strength and permeability along with the range of quantifiable features through which it can be described.

Mercury Intrusion Porosimetry, Backscattered Electron Image Analysis and X-ray Computed Tomography were employed to characterise LITS affected, heat only and unconditioned control specimens. Specimens were characterised both *ex-situ* and *in-situ* in the case of X-ray Computed Tomography using a purpose built thermo-mechanical loading rig.

Experimental results indicate that in terms of total porosity, LITS affected specimens do not appear to differ from those which experience only heating. However, evidence is presented of other developments in the material pore structure which can uniquely be associated with LITS. These include data from the *ex-situ* characterisation of pore size distribution and interfacial transition zone porosity along with *in-situ* data relating to pore volume during fracture testing following conditioning. These observations provide new insight into macrostructural observations made on material strength and permeability in existing research.

Evidence from this investigation does not provide substantive support for the LITD hypothesis and further research into the calcium-silicate-hydrate structure of OPC based materials is required to develop a better understanding of LITS development.

TABLE OF CONTENTS

Executive Summary	2
Table of Contents	3
Acknowledgements	6
List of Tables	7
List of Figures	8
List of Symbols	12
List of Abbreviations	13
1. General Introduction	15
1.1. Background to the project	15
1.2. Aim and scope of the research	16
1.3. Research strategy	17
1.4. Outline of the thesis	18
Part 1: Theoretical Background	20
2. LITS in mature concrete	21
2.1. Introduction.....	21
2.2. Strain in Concrete.....	22
2.3. Load Induced Thermal Strain	23
2.4. Macroscopic Features of LITS.....	24
2.5. Summary	32
3. Mechanisms for the development of LITS in mature concrete.....	33
3.1. Introduction.....	33
3.2. Concrete microstructure	33
3.3. Mechanisms for Basic and Drying Creep in Concrete.....	42
3.4. Mechanisms for LITS in Concrete	46
3.5. Conclusions.....	48
Part 2: <i>Ex-situ</i> Analysis.....	50
4. <i>Ex-situ</i> specimen conditioning	51

4.1.	Introduction.....	51
4.2.	The mac ^{2T} apparatus.....	51
4.3.	Materials and Experimental Set-up.....	53
4.4.	Experimental Results	57
4.5.	Discussion.....	60
4.6.	Conclusions.....	63
5.	Multi-scale X-ray Computed Tomography.....	64
5.1.	Introduction.....	64
5.2.	Evaluation of experimental techniques for pore structure analysis.....	64
5.3.	X-ray CT Imaging Principals.....	68
5.4.	X-ray CT Methodology.....	69
5.5.	Results.....	73
5.6.	Discussion	80
5.7.	Conclusions.....	82
6.	Scanning Electron Microscopy	84
6.1.	Introduction.....	84
6.2.	SEM Imaging Principals	85
6.3.	Specimen Preparation	87
6.4.	BSE image acquisition	88
6.5.	BSE image analysis.....	88
6.6.	Results.....	92
6.7.	Discussion	98
6.8.	Conclusions.....	99
7.	Mercury Intrusion Porosimetry.....	100
7.1.	Introduction.....	100
7.2.	Mercury Intrusion Principals	100
7.3.	MIP Limitations	103
7.4.	Methodology	105
7.5.	Results.....	106

7.6.	Discussion	109
7.7.	Conclusions.....	111
Part 3: <i>In-situ</i> Analysis.....		112
8.	<i>In-situ</i> specimen conditioning and experimental methodology	113
8.1.	Introduction.....	113
8.2.	Existing Literature.....	113
8.3.	Experimental Design and Methodology.....	115
8.4.	Materials	121
8.5.	Rig Commissioning.....	124
8.6.	Discussion	128
8.7.	Conclusions.....	129
9.	<i>In-situ</i> thermo-mechanical loading	130
9.1.	Introduction.....	130
9.2.	Experimental Set-up.....	130
9.3.	Image Analysis.....	132
9.4.	Results.....	133
9.5.	Discussion	142
9.6.	Conclusions.....	144
Part 4: Summary of Results		145
10.	General Discussion	146
11.	Conclusions.....	152
11.1.	Key Findings	152
11.2.	General Conclusions	153
11.3.	Further Research	153
	References.....	155
Appendix A: BSE-IA Matlab Analysis Script		163
Appendix B: Thermo-mechanical Load Rig Fabrication Drawings		177
Appendix C: <i>In-situ</i> X-ray CT Matlab Analysis Script		190

ACKNOWLEDGEMENTS

The work presented in this thesis would not have been possible without the help and support of a great number of generous people. First, I must thank my supervisors; Dr. Mihail Petkovski and Dr. Dirk Engelberg. Dr. Petkovski has provided a great deal of support with respect to the understanding of Load Induced Thermal Strain and the use of his purpose built mac^{2T} thermo-mechanical load rig at the University of Sheffield which he was kind enough to let me operate.

Dr. Engelberg has guided me on the use of a range of microstructural analysis techniques and particularly in the use of X-ray CT where he facilitated a partnership with the Manchester X-ray Imaging Facility which allowed me to use a range of state of the art equipment.

I am also indebted to the staff based in the structure laboratory at the University of Sheffield and in particular; Paul Blackbourn, Kieran Nash, Chris Todd and Don Jenkins for their help in a number of areas including specimen preparation, *in-situ* rig component manufacture and commissioning. Without their support and guidance large parts of the experimental program would not have been possible.

The help of the staff based in the Manchester X-ray Imaging Facility, University of Manchester has been invaluable in helping me to obtain and quantify the X-ray CT data which has formed a large part of this thesis. Support staff including Tristan Lowe, Rob Bradley and Fabien Leonard have provided both their guidance and their time to enable my work. I must also thank summer placement students Jeremy Deschamps and Alexandre Brunet for their efforts in supporting data quantification.

Support and guidance in the use of SEM equipment was gratefully received from Shirley Zhong in the Department of Materials at the University of Manchester. Likewise, the training and support time provided by Bev Lane in the Department of Engineering Materials at the University of Sheffield to support mercury intrusion work was key in enabling those experiments.

On a personal note, I would also like to thank the teaching staff and my fellow cohort on the Nuclear FiRST doctoral training centre as well as fellow students both in E111a in the Department of Civil and Structural Engineering at the University of Sheffield and at the Manchester X-ray Imaging Facility for their humour and our interesting conversations.

Finally, I would also like to thank my friends and family for their support over the years and also Jennie Garbutt, without whom this definitely would not have been possible!

LIST OF TABLES

Table 3.1: Summary of properties of hydration products in Portland Cement paste (from Mindess and Young ²⁴).....	34
Table 3.2: Size distribution of pores in cementitious materials and accepted nomenclature ³⁰	38
Table 4.1: Concrete mix proportions (OPC = Ordinary Portland cement; PFA = Pulverised fuel ash)53	
Table 4.2: Conditioning regimes of the concrete cubes for microstructural analysis (fcu = uniaxial compressive strength of concrete).....	55
Table 6.1: Treatment effects. (F is the test statistic. P is the significance value).....	94
Table 6.2: Pairwise comparisons.	96
Table 6.3: With-in treatment effects.	96
Table 7.1: Treatment effects.	106
Table 7.2: Pairwise comparisons.	106
Table 8.1: Cement paste mix proportions (OPC = Ordinary Portland cement; PFA = Pulverised fuel ash).....	121
Table 8.2: Cement paste trial compressive strength test results.....	122
Table 8.3: Mortar mix proportions (OPC = Ordinary Portland cement; PFA = Pulverised fuel ash). 122	
Table 8.7: Thermal expansion coefficients, measured and actual expansion in three reference materials.....	127
Table 8.8: Mechanical strength of three specimens tested under uniaxial compression at elevated temperature	128
Table 9.1: Conditioning regimes of the concrete specimens for microstructural analysis (fcu = ultimate compressive strength of concrete)	131

LIST OF FIGURES

Figure 2.1: Typical stress- strain diagram for concrete ²⁴	22
Figure 2.2: Petkovski and crouch – influence of heating rates ¹⁶	29
Figure 3.1: – Schematic model of C-S-H in cement paste after Mindess and Young ²⁴	35
Figure 3.2: Micrograph of ettringite needles from Scrivener ³⁰	37
Figure 3.3: Micrograph of anhydrous cores.....	37
Figure 3.4: Relationship between w/c and permeability in cement paste and concrete (from Mindess and Young ²⁴).....	39
Figure 3.5: Schematic representation of cement microstructure as proposed by the microprestress-solidification model (from Bazant <i>et al.</i> ³²)	41
Figure 3.6: Macro and Microdiffusion (from Bazant and Chern ⁴⁴).....	44
Figure 3.7: Microprestress-solidification model after Bazant <i>et al.</i> ³²	45
Figure 3.8: Transitional thermal creep at variable water content after Bazant <i>et al.</i> ⁵²	47
Figure 4.1: Mac2T experimental apparatus (Left) and load frames including specimen enclosure (Right).....	52
Figure 4.2: Temperature matched curing profile for concrete showing instrument controlled water bath temperature during first ten days following casting.....	54
Figure 4.3: (a) Temperature profile in H250 tests (b) Stress profile in H250 tests, (c) Temperature profile in L06H250 tests, and (d) Stress profile in L06H250 tests.	55
Figure 4.4: Cube with core extracted. Extraction carried out using a water cooled diamond tipped coring drill. Each core specimen was surface dried on extraction and stored at ambient temperature in the laboratory environment.	56
Figure 4.5: Volumetric strain in conditioned specimens. Elastic strains due to hydrostatic compression removed from L06H250 specimen traces for comparison. Compactive strains shown positive.	57
Figure 4.6: (a) shows the change in volumetric strain in conditioned specimens with temperature during heating. Here, the contribution of thermal expansive strains within the specimens has been removed.	59
Figure 4.7: (a) Residual strength in concrete cubes following removal of 28 mm diameter core for microstructural analysis. (b) Mass loss in specimen following removal of cube from mac ^{2T} apparatus	60
Figure 5.1: Pore sizes and techniques for microstructural analysis	67
Figure 5.2: a) Nikon Custom Bay at the HMXIF with a schematic plan of the XCT equipment Grey-scale value histogram showing tri-modal distribution of 16-bit XCT data and approximate phase distribution for a control specimen	68
Figure 5.3: a) ROI showing orthoslices of the reconstructed data from a control specimen and b) Segmented porosity within the same volume	74

Figure 5.4: Porous volume results for the three conditioning regimes.	74
Figure 5.5: Equivalent pore diameter distribution results for three conditioning regimes; H250, L06H250 and the unconditioned control. Error bars show standard error calculated for 4 X-ray CT scans from 2 cubes repeated using the same conditions.	75
Figure 5.6: ROI showing orthoslices of the reconstructed data from an unconditioned control specimen and segmented porosity within the same volume	76
Figure 5.7: Porous volume results from 5 μm image resolution data for the three conditioning regimes.	77
Figure 5.8: Pore size distribution results from the 5 μm image resolution data.	77
Figure 5.9: Median filtered orthoslice from an unconditioned control specimen imaged at a resolution of 0.6 μm	78
Figure 5.10: Total porosity from 0.6 μm datasets.....	78
Figure 5.11: Pore size distribution results from the 0.6 μm image resolution data.	79
Figure 5.12: Median filtered orthoslice from an unconditioned control specimen imaged at a resolution of 0.15 μm	80
Figure 6.1: Schematic of SEM.....	85
Figure 6.2: Signal generation in the Scanning Electron Microscope (SEM) from Scrivener ³⁰	86
Figure 6.3: Phase identification in BSE-SEM image.....	86
Figure 6.4: Aggregate segmentation	89
Figure 6.5: Greyscale histogram for a typical BSE image used in this study. The phases of interest and their greyscale ranges are approximately identified. The challenges associated with a lack of phase peak for porosity can be observed.....	90
Figure 6.6: Cumulative greyscale intensity plot for a typical BSE image.	90
Figure 6.7: Porous segmentation.....	91
Figure 6.8: Typical SEM image and segmented porosity within the ITZ.....	91
Figure 6.9: Typical BSE images from each of the conditioning regimes indicating features of interest.	92
Figure 6.10: Variation of average total porosity with number of frames analysed. After twenty-five frames a relatively stable value of porosity was obtained. (Do average here.).....	93
Figure 6.11: Statistical analysis of results for total porosity and porosity within the ITZ region at increments of 10, 20, 30, 40 and 50 μm away from the surface of the aggregate. Significance is indicated by *.....	95
Figure 7.1: a) Mercury Penetrometer, b) Micromeritics PoreSizer 9320 mercury intrusion porosimeter	100
Figure 7.2: Contact between liquid mercury and a porous solid recreated from Guang ¹⁰⁴	102
Figure 7.3: Pore size distribution	103

Figure 7.4: Classification of pore geometry: a) closed pore, b) connected pore, c) connected pore with “ink bottle” and d) cul-de-sac pore with “ink bottle” .	104
Figure 7.5: Other metrics results	107
Figure 7.6: Pore size distribution	108
Figure 8.1: High temperature tensile rig employed by Terzi <i>et al</i> ¹²³	115
Figure 8.2: 5 kN uniaxial compression rig at the HMXIF	116
Figure 8.3: Optioneering study	118
Figure 8.4: Schematic drawing of key rig components	119
Figure 8.5: Thermo-mechanical load rig	121
Figure 8.6: Temperature matched curing profile for concrete showing instrument controlled water bath temperature during first ten days following casting.	123
Figure 8.7: Force data logging readout in force control during one thermal cycle of heating between ambient temperature and 200 °C	124
Figure 8.8: Variance in heater temperature with respect to the target temperature during one heating cycle from ambient temperature to 200 °C	125
Figure 8.9: a) Specimen temperature variance with respect to target temperature during one thermal heat cycle from ambient temperature to 200 °C, b) Temperature recorded in thermocouples mounted within the body and base of the rig during one thermal heat cycle from ambient to 200 °C	126
Figure 8.10: Thermal expansion of aluminium, copper and mild steel during one thermal cycle between ambient and 180 °C	127
Figure 8.11: Stress - strain data for three 11 mm diameter, 10 mm high specimens loaded in a cyclic profile at 0.25, 0.5 and 0.75 f_{cu} before testing to failure	128
Figure 9.1: <i>In-situ</i> rig installed within Nikon Custom bay at the HMXIF	131
Figure 9.2: a) Stress-strain profiles for Load only, H200L and LH200 (LITS affected) <i>in-situ</i> conditioning regimes, b) Ultimate compressive failure strengths for two specimens tested under each regime.	134
Figure 9.3: a) Average temperature-strain relationships from H200L and LH200 tests: a) LITS and shrinkage, b) LITS. Compactive strains are shown as positive. Instantaneous strain has been removed from LH200 test results.	135
Figure 9.4: Image analysis results from <i>in-situ</i> X-ray CT study of porosity in one specimen tested to failure under load: a) Conditioning regime and approximate scan times, b) percentage change in total porosity and No. of pores during conditioning, c) Equivalent pore size diameter distribution during conditioning.	137
Figure 9.5: Image analysis results from <i>in-situ</i> X-ray CT study of porosity in one specimen tested to failure under load following heating (H200L): a) Conditioning regime and approximate scan times, b) percentage change in total porosity and No. of pores during conditioning, c) Equivalent pore size diameter distribution during conditioning.	139

Figure 9.6: Image analysis results from *in-situ* X-ray CT study of porosity in one specimen tested to failure under load following LITS development (LH200): a) Conditioning regime and approximate scan times, b) percentage change in total porosity and No. of pores during conditioning, c) Equivalent pore size diameter distribution during conditioning. 141

LIST OF SYMBOLS

A	Total pore surface area
D_i	Representative diameter of pore
D_{mean}	Average pore diameter
f_{cu}	Ultimate Compressive Strength
g	gram
H	Global threshold value
I	Intensity
I_0	Incident intensity
J	macro-diffusion
j	micro-diffusion
N	Newton
P	Pressure
P_d	applied macrostress
r	radius
V_i	Representative volume of pore
x	mass thickness
ε_{cr}	basic creep
ε_{cr-d}	drying creep
ε_H	Strain due to heating without load
ε_{LITS}	Load Induced Thermal Strain
ε_{LH}	Strain in Load-Heat test
ε_{sh}	drying shrinkage
ε_{ttc}	Transient thermal creep
$\varepsilon_{cr-t-dep}$	Time dependent creep
ε_{σ}	Instantaneous deformation due to mechanical loading
$\varepsilon_{\Delta el}$	Elastic strain during heating
ρ	Density
μ	Mass attenuation coefficient of material
γ	Surface tension
θ	Contact angle
σ_0	Hydrostatic stress
σ	Applied stress

LIST OF ABBREVIATIONS

AGR	Advanced Gas-cooled Reactor
ANOVA	Analysis of Variance method
BSE	Backscattered Electron
CaO	Lime
CCD	Charge Coupled Device
COR	centre of rotation
C ₂ S	Di-Calcium Silicate
Ca(OH) ₂	Calcium Hydroxide
C-S-H	Calcium-Silicate-Hydrate
C ₃ S	Tri-Calcium Silicate
CO ₂	Carbon Dioxide
DVC	Digital Volume Correlation
EDX	Energy Dispersive X-ray microanalysis
EPSRC	Engineering and Physical Research Council
GDF	Geological Disposal Facility
GSV	Grey-scale Value
HALES	High Activity Liquid Effluent Storage
Hz	Hertz
IA	Image Analysis
ITZ	Interfacial Transition Zone
kN	kilo Newton
kV	kilo Volt
LITD	Load Induced Thermal Damage
LITS	Load Induced Thermal Strain
LH	Load-Heat
LOCA	Loss of Coolant Accident
LVDT	Linear Variable Displacement Transducer
mac ^{2T}	apparatus for testing concrete under multiaxial compression at elevated temperature
mbar	millibar
mL	millilitre
MN	Mega Newton
MPa	Mega Pascal
mm	millimetre
MIP	Mercury Intrusion Porosimetry

MXIF	Manchester X-ray Imaging Facility
nm	nanometre
N/m^2	Newton per metre squared
Nuclear FiRST	Nuclear Fission Research Science and Technology
OPC	Ordinary Portland Cement
PC	Personal Computer
PFA	Pulverised Fuel Ash
PID	Proportional-Integral-Derivative
PMMA	Poly(methyl methacrylate)
PTFE	Poly-Tetra-Fluoro-Ethylene
RH	Relative Humidity
ROI	Region of Interest
rpm	Revolutions per minute
RPV	Reactor Pressure Vessel
SANS	Small Angle Neutron Scattering
SAXS	Small Angle X-ray Scattering
SCM	Supplementary Cementitious Material
SE	Secondary Electron
SEM	Scanning Electron Microscopy
STFC	Science and Technology Facilities Council
TTC	Transient thermal creep
w/c	water/cement ratio
$\text{W/m}\cdot\text{K}$	Watt per metre Kelvin
X-ray CT	X-ray Computed Tomography
μA	microAmp
μm	micrometre
μmHg	micrometres mercury
$\mu\epsilon/^{\circ}\text{C}^{-1}$	microstrain per degree Centigrade
$\mu\epsilon$	microstrain
$^{\circ}\text{C}$	degrees Centigrade
$^{\circ}\text{C}/\text{min}$	degrees Centigrade per minute
2D	Two-dimension
3D	Three-dimension

1. General Introduction

1.1. BACKGROUND TO THE PROJECT

The project reported in this thesis is titled “An investigation into the effects of load induced thermal strain on cementitious microstructure”. The research has been funded by the Engineering and Physical Research Council (EPSRC) through the Nuclear Fission Research Science and Technology (Nuclear FiRST) doctoral training centre run jointly between the University of Sheffield and the University of Manchester. The Nuclear FiRST doctoral training centre was formed in 2009 in order to address a perceived doctoral level skills shortage in the United Kingdom nuclear industry. The project title was jointly developed between the author and Dr. Mihail Petkovski in the Department of Civil and Structural Engineering at the University of Sheffield. It aims to build upon extensive research into the macro-effects of load induced thermal strain (LITS) by Dr. Petkovski in providing quantitative microstructural evidence of a mechanism controlling the process.

The deformation response of concrete structures subjected to thermo-mechanical loading is of particular interest across the nuclear industry. In power generation, existing Advanced Gas-Cooled Reactor (AGR) stations utilize a pre-stressed concrete Reactor Pressure Vessel (RPV). Under service load conditions the temperature in the concrete is between 37.2 °C and 85.4 °C and the coolant pressure in the vessel is 3.96 MPa³. In the case of accident loading, such as that during the interruption of the primary cooling system, the temperature in the concrete may rise to 250 °C. Containment structures for future generation III designs such as the Westinghouse AP1000 are also likely to experience coupled thermo-mechanical loadings during accidental conditions. Here, the primary coolant circuit would be vented into the containment to prevent catastrophic failure of the RPV, thereby subjecting the concrete structure to reactor core conditions.

At the back end of the nuclear fuel cycle, management of heat generating radioactive waste will also present situations where concrete structures used for processing and storage experience elevated temperatures⁴ such as the high activity liquid effluent storage (HALES) facility at Sellafield. Further, in order to guarantee that nuclear waste in a Geological Disposal Facility (GDF) would be retrievable, stabilization may be achieved using concrete liners⁵. The Yucca mountain repository incorporated this design feature, and whilst drifts were to remain at ambient temperature during filling, according to Glasser and Hong⁵, temperatures “could reach a maximum of 160 – 200 °C in the post-closure phase”. A comprehensive knowledge of processes which affect concrete under such conditions is therefore required in order to ensure adequate structural performance over what may be significant timescales.

Concrete which is subjected to mechanical load during its first heating cycle experiences LITS. LITS is the term used to describe the combined effects of several different strain components⁶ in thermally treated materials based on ordinary Portland cement (OPC) or an OPC-PFA (pulverised fuel ash) combination. Under a significant pre-stressing force, LITS is capable of completely suppressing thermal expansion in the loaded axes². LITS can have a significant effect on stress-strain distribution in structures and, in certain conditions, it can have a detrimental effect on the strength and loading stiffness of cementitious materials¹. Therefore, it is of great importance that the effects of LITS are captured accurately when modelling the deformation behaviour of safety critical infrastructure such as nuclear reactor pressure vessels and containment structures.

Significant attention has been paid to identifying the conditions which affect the development of LITS and its components since it was first identified by Hansen and Eriksson⁷ in the 1960's. Research into the effects of these factors on alterations in the mechanical strength and durability of cementitious materials has also been carried out. A number of environmental factors are known to influence LITS including:

- The maximum temperature experienced^{2, 6, 7, 8, 9, 10, 11, 12, 13, 14, 15}
- The magnitude and orientation of applied mechanical load^{2, 6, 8, 10, 13, 16, 17, 18, 19, 20, 21}
- Applied heating rate^{6, 2, 7, 16, 17, 13}
- The moisture content of the concrete during the transient temperature phase^{2, 6, 7, 10, 11, 14, 16, 17, 19, 22, 23}

These parameters determine the rate and magnitude of LITS development along with the magnitude of changes in mechanical strength and durability.

Data on microstructural changes in LITS affected materials e.g. pore volume fraction changes, will aid in the formulation of material models that accurately predict not only stress/strain response but also strength and durability. It can also be used to inform our understanding of the mechanisms which are activated during combined thermal and mechanical loading of concrete. To this end, a study on the effect of LITS on the pore structure and density of mature mortar and concrete is therefore undertaken.

1.2. AIM AND SCOPE OF THE RESEARCH

The aim of this research project was to investigate experimentally the development of microstructure and porosity in mature mortar and concrete subjected to LITS. Through the quantitative analysis of experimental data, the hypothesis that LITS occurs as a result of load induced thermal damage could then be tested. The quality and validity of a number of experimental techniques used to characterise

concrete microstructure was also assessed. The results obtained from this study can be used to inform further research into the origins and development of LITS. They will potentially contribute to improvements in LITS modelling. It would be too complicated to study microstructural changes related to all influencing factors which affect the development of LITS as described above. Therefore the experiments presented here were restricted as follows:

- Only one binder mix design was studied (OPC+PFA)
- Water/cement ratio was kept at 0.55
- Only one heating rate was used ($0.2\text{ }^{\circ}\text{C}/\text{min}^{-1}$).
- The maximum temperature achieved was kept constant ($250\text{ }^{\circ}\text{C}$)

Experimental studies of microstructural development in LITS affected concrete employed extended steady-state periods to ensure the complete development of LITS for the given temperature, stress/strain ratio and environmental conditions.

1.3. RESEARCH STRATEGY

The study of changes in concrete microstructure such as those which may occur with LITS is particularly challenging due to the heterogeneity of OPC materials. Many of the available experimental techniques are limited to *ex-situ* characterisation; i.e. the specimen must be conditioned before analysis. This means that the processes which cause LITS cannot be observed directly. Consequently, a statistically significant sampling regime must be employed to ensure that results may be determined to be quantitative. This is especially important since each of the techniques have specific limitations that may relate to specimen preparation, experimental method and/or interpretation of results.

An alternative method of obtaining quantitative results is to employ *in-situ* characterisation techniques where experimental data is obtained during conditioning. However, only a limited number of experimental techniques are suitable for this kind of analysis and the equipment required to carry out these experiments is not readily available.

The research strategy for this project has employed both methodologies. With respect to *ex-situ* characterisation, concrete specimens were conditioned under multi-axial compression at elevated temperature to induce LITS (load-heat regime) and compared with specimens that were subjected to a heat-load regime (no LITS) and control specimens (no heat/no load). These specimens were then analysed *ex-situ* using three experimental techniques including X-ray computed tomography (CT), backscattered electron microscopy and mercury intrusion porosity. These were used to study features in the pore structure of the material including pore volume and pore size distribution. This

experimental procedure also allowed for a comparison of results from individual techniques and a relative assessment of their validity.

With respect to *in-situ* characterisation, only X-ray CT was used. Due to the novelty of *in-situ* studies using X-ray CT and a complete lack of studies in the area of coupled thermo-mechanical processes such as LITS, a new experimental test rig was developed for this project. The rig was developed from an existing 5 kN tension rig to provide for uniaxial compressive forces up to 5 kN and thermal loading of up to 200 °C. A full set of commissioning tests has been carried out along with an investigation into LITS which has culminated in an investigation at the Diamond light source where sub-micron resolution imaging of LITS affected specimens was carried out to understand its effects on capillary porosity in mortar specimens.

1.4. OUTLINE OF THE THESIS

The results of this research project are described in the four parts of this thesis. The flowchart of the structure is shown in Figure 1.1.

- Part 1: Introduction (Chapters 2 – 3)
- Part 2: *Ex-situ* experimental analysis (Chapters 4 – 7)
- Part 3: *In-situ* experimental analysis (Chapters 8 – 9)
- Part 4: Discussion (Chapter 10) and Conclusions (Chapter 11)

In the first part of this thesis, the theoretical background of this research is outlined. A brief review of the principal microstructural features of concrete is presented. Then the macro-structural features of LITS are described and the limited body of research into proposed microstructural mechanisms is reviewed along with the mechanisms proposed for related phenomena including drying creep.

In the second part, the results of the specimen conditioning and *ex-situ* experimental analyses are presented in detail. Conditioning was carried out using the multi-axial compression of concrete at elevated temperature apparatus at the University of Sheffield (Chapter 4). In chapter 5, chapter 6 and chapter 7 the pore structure of the conditioned concrete was studied using X-ray CT, mercury intrusion porosimetry and scanning electron microscopy.

In part three, an *in-situ* rig was developed and commissioned along with appropriate mortar specimens (Chapter 8). The results of the *in-situ* analysis of mortar specimens under thermo-mechanical loading is then studied first using laboratory X-ray CT apparatus (Chapter 9).

The final part of this thesis presents a comparison of *ex-situ* and *in-situ* characterisations (Chapter 10) along with relevant conclusions based on the experimental findings (Chapter 11).

Part 1: Theoretical background

- Macrostructural effects of LITS (Chapter 2)
- Microstructural characteristics of strain components in OPC (Chapter 3)



Part 2: *Ex-situ* Analyses

- *Ex-situ* specimen conditioning (Chapter 4)
- Multi-scale X-ray computed tomography (Chapter 5)
- Scanning electron microscopy (Chapter 6)
- Mercury intrusion porosimetry (Chapter 7)



Part 3: *In-situ* Analyses

- Specimen preparation, *in-situ* rig design and calibration (Chapter 8)
- *In-situ* 5 micron imaging (Chapter 9)



Part 4: Summary of results

- Discussion (Chapter 10)
- Conclusions (Chapter 11)

PART 1: THEORETICAL BACKGROUND

2. LITS in mature concrete

2.1. INTRODUCTION

Under the stimulus of an applied stress and/or changes to environmental conditions, concrete will experience a combination of reversible, irreversible and time dependent strains. These may be separated into four broad categories²⁴:

1. Instantaneous deformation that occurs on the application of an external mechanical stress
2. Shrinkage that is the result of moisture loss from the concrete microstructure
3. Thermal expansion that results from a change in temperature
4. Creep which is a time dependent deformation that develops during extended application of an external stress

Additionally, in concrete that is heated under mechanical load, a deformation component known as load induced thermal strain (LITS) is recorded. Since the first documentation by Hansen and Eriksson⁷ in 1966 detailed studies into the development of LITS have been carried out by Illston and Sanders⁸ (1973), Anderberg and Thelandersson² (1976), Parrott^{9,25} (1979,1980), Khoury^{22,26} (1985, 2006) and Petkovski^{16,1} (2008,2010) among others. Each of these components can contribute significantly to the total deformation of concrete and must therefore be considered individually in the design of concrete structures²⁴.

During deformation, a number of complex physical and chemical processes take place within the concrete microstructure. Physical processes include cracking and redistribution of microstructural constituents and chemical processes include increased hydration and degradation of existing hydration products. Following material deformation, macroscopic properties such as mechanical strength and durability may be altered significantly from their original state.

In this chapter, the four principal types of deformation in concrete are introduced along with LITS. The macroscopic features of LITS are then presented along with key literature concerning the influence of environmental conditions and concrete mix design on LITS development. Additionally, the effect of LITS on the mechanical strength and durability of cementitious materials is highlighted to provide support for potential microstructural mechanisms which are reviewed in Chapter 3.

2.2. STRAIN IN CONCRETE

2.2.1. Instantaneous deformation

Concrete can be considered as a quasi-brittle material which exhibits a non-linear stress – strain relationship when subjected to mechanical load even over a short duration (Figure 2.1). The non-linearity is a consequence of progressive micro-cracking of the material under deviatoric loading. The modulus of elasticity is often used to compare concretes with differing mix designs. However its calculation is complicated by the non-linear material behaviour. Porosity is one of the principal microstructural properties that govern the modulus of elasticity. As the water/cement (w/c) ratio of the mix is reduced, a significant increase in the modulus of elasticity is observed²⁴.

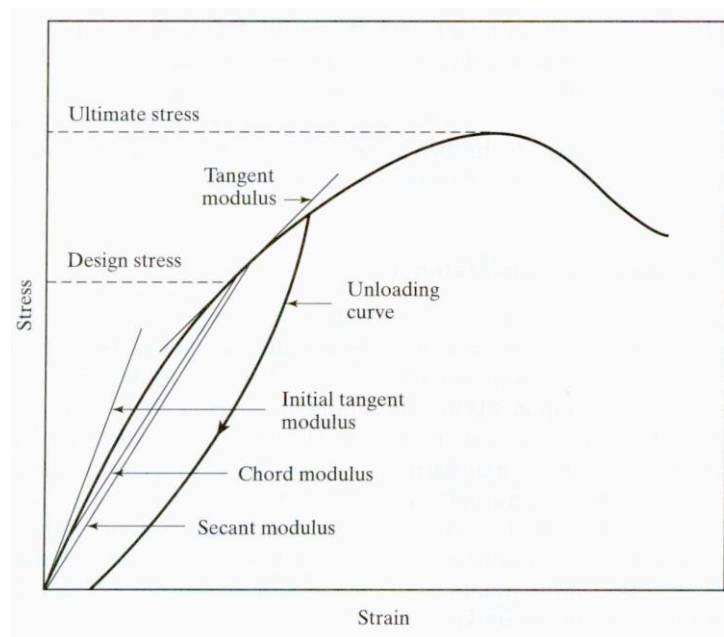


Figure 2.1: Typical stress- strain diagram for concrete²⁴

2.2.2. Shrinkage

Shrinkage is the term used to describe volume changes due to loss of moisture. Shrinkage may be used to describe a number of different phenomena in concrete. In fresh concrete, plastic and autogenous shrinkage refer to volume changes caused by moisture loss to external influences and self-desiccation respectively. These processes can be suppressed by appropriate mix design and environmental control during casting. With respect to mature concrete, plastic and autogenous shrinkage are insignificant compared to drying shrinkage. Drying shrinkage is related to processes which occur in the cement paste. The presence of aggregate will act only to restrain deformation²⁷.

Concrete exhibits both reversible and irreversible drying shrinkage strains. The irreversible component is particularly evident on first drying²⁴. The reversible component of drying shrinkage is thought to occur as a result of either capillary stress or disjoining pressure which will be discussed in Chapter 3. The exact mechanism which causes the irreversible shrinkage is unknown. However, it has been recorded to correspond in magnitude to the total porosity of the concrete where an increase in porosity particularly in the 3-10 nm equivalent diameter range leads to increase drying shrinkage²⁴.

2.2.3. Thermal expansion

Material expansion during increase in temperature is a property inherent of all materials due to an increase in kinetic molecular movement. The thermal expansion coefficients of the major concrete constituents; cement paste and aggregate differ significantly. The coefficient of thermal expansion for cement paste varies depending on the moisture content, w/c ratio and age and lies in the range of 1 – 1.3 W/m·K²⁴. The thermal expansion coefficient of aggregates varies with mineral composition. These tend to be significantly higher than that of the cement paste and as much as 4.3 W/m·K in the case of quartzite. Consequently the behaviour of the aggregate often dominates when considering bulk concrete²⁴. However, with respect to the material microstructure, the different behaviour of the individual constituents can result in an increase in material damage in the form of microcracking particularly located in the paste in close proximity to aggregate inclusions.

2.2.4. Creep

Creep can be subdivided into two components: basic creep (ϵ_{cr}) and drying creep (ϵ_{cr-d}). Specimens that experience mechanical load at constant humidity exhibit only basic creep and no drying shrinkage. Conversely, under mechanical load and drying conditions, both basic creep and drying shrinkage are recorded. However, the total deformation is greater than the sum of these two components. The additional creep that is recorded is known as drying creep. Creep and drying shrinkage in mature concrete are thought by some researchers to be inter-related because they are often of a similar magnitude and occur at similar rate²⁴. As for drying shrinkage, both basic and drying creep are known to occur only in the cement paste component of concrete microstructure²⁷. Their precise microstructural mechanisms are uncertain and existing hypotheses will be discussed in Chapter 3 of this thesis.

2.3. LOAD INDUCED THERMAL STRAIN

Load induced thermal strain (LITS) (ϵ_{LITS}) is an umbrella term that is used to encompass a group of different strain components that occur on first heating of concrete under load. LITS is determined by subtracting the total strain of concrete during first heating under load (ϵ_{LH}) from the total strain of

concrete during first heating without load (ε_H) and the instantaneous deformation due to mechanical loading (ε_σ):

$$\varepsilon_{LITS} = \varepsilon_{LH} - \varepsilon_H - \varepsilon_\sigma$$

According to Khoury²⁸, LITS is comprised of four strain components. The principal contributor to LITS is known as transient creep or transient strain⁶. The difference in nomenclature reflects the observation that in certain conditions, transient creep may occur “quasi-instantaneously”² on heating. This component may be sub-divided into two depending on the boundary conditions of the specimen. In sealed conditions only transitional thermal creep (ε_{ttc}) contributes. This is an irrecoverable component which occurs during and immediately following an increase in temperature beyond that which has previously been experienced by a material under mechanical load¹⁰. Additionally in unsealed conditions, drying creep (ε_{cr-d}) will also occur. However, in this case the relative contribution of each component is difficult to determine.

$$\varepsilon_{LITS} = \varepsilon_{ttc} + \varepsilon_{cr-d} + \varepsilon_{cr-t-dep} + \varepsilon_{\Delta el}$$

The two other components included in LITS according to Khoury²⁸ are time dependent creep ($\varepsilon_{cr-t-dep}$) and a change in elastic strain during heating ($\varepsilon_{\Delta el}$). The former relates to the influence of heating rate on recorded LITS observed by a number of authors^{26,16,6,17}. At slower heating rates this component has been observed to have greater influence.

2.4. MACROSCOPIC FEATURES OF LITS

Significant attention has been paid to identifying the conditions which affect the evolution of LITS and its components since it was first identified in the 1960’s. The findings of what is a large body of work are presented here with respect to the principal environmental and material factors which are known to influence LITS development. These observations will be used to inform the experiment design and interpret results in later chapters.

2.4.1. Temperature

LITS has been shown to develop at temperatures both below and above 100 °C. Hansen and Eriksson⁷ confirmed the presence of TTC in specimens which were heated during submersion in water at up to 80 °C. By studying the behaviour of specimens which had previously been loaded and heated in effectively sealed conditions they were able to confirm that on cooling, TTC did not continue to develop and no recovery took place. In fact, there is no evidence to suggest that any of the LITS components experience recovery on cooling^{8,10,11}. Hansen and Eriksson⁷ also reported that further repeated heating in a cyclic pattern up to 60 °C produced no additional LITS. Research suggests that no significant LITS development occurs when the material experiences an increase in temperature to a

level below the maximum to which it had earlier been exposed^{8,12,13,9}. In fact, if the material is subjected to an increase in temperature before loading, then LITS will be completely suppressed on future heating under load until the earlier temperature is reached^{8,9}.

The existence of LITS has been confirmed at temperatures of up to 800 °C². The limiting value of LITS has been found to exist as an incremental non-linear function of temperature^{8,6,14}. Khoury *et al.*⁶ proposed a series of ‘master’ LITS curves relating LITS evolution to temperature at differing stress levels in Calcium-Silicate-Hydrate (C-S-H) based materials for temperatures up to at least 450 °C. This curve was specified with the understanding that the stress/strength ratio, preheating condition, heating rate and curing regime of specimens utilised in the study were similar. An earlier attempt at modelling the behaviour of concrete under multi-axial mechanical stress at temperatures up to 800 °C by Thelandersson¹⁵ related LITS evolution to mechanical stress and temperature only. However, this author acknowledged that the model was only valid for temperatures well in excess of 100 °C, in unsealed conditions where moisture could dissipate easily.

The thermal stability of aggregates used in the concrete mix have been shown not to affect the magnitude of recorded LITS at temperatures below 450 °C with the exception of concrete composed of gravel aggregate⁶. The thermal instability of gravel at temperatures above 350 °C resulted in an increase in the recorded values of creep over that of other concretes²² that was likely to be caused by microstructural damage.

Further evidence of the minimal impact of aggregate on LITS was seen at 573 °C where the phase inversion of quartz results in volumetric expansion. No difference in the development of LITS was detected at this temperature⁶. This, coupled with the LITS “master” curve⁶, implies that thermal incompatibility between aggregate and cement paste does not play a role. Khoury *et al.*⁶ also reported that the cement blend did not influence LITS development; therefore it must occur in a phase which is common to all OPC based materials such as the C-S-H structure.

Khoury *et al.*⁶ reported a peak in the coefficient of LITS development at 150 °C that was more pronounced in cement paste specimens than in concrete which may be expected if LITS originates in the cement paste only. This corresponded with a peak in the rate of moisture loss²² and prompted the authors to suggest that the drying creep component contributed to the peak in LITS coefficient. Khoury *et al.*⁶ also suggested that a significant drop in the coefficient of LITS development between 500 °C and 600 °C coincided with a decrease in the content of Ca(OH)₂.

Whilst in most cases LITS has been observed to occur only during the transient temperature period for temperatures above 100 °C, it has been observed to develop more slowly at temperatures below this level. This may however be attributed to the sealed boundary conditions employed in most of the tests

below 100 °C as LITS has also been observed to continue beyond the transient heating phase in partially sealed tests at 250 °C by Petkovski and Crouch¹⁶.

In conclusion, the influence of temperature on LITS magnitude is well understood. Microstructural analysis shall be carried out on heat only and LITS affected specimens above 150 °C to ensure the peak LITS in LITS development has occurred, but below 450 °C above which according to Khoury *et al*⁶ the type of aggregate in the concrete mix plays a significant role. Microstructural analysis should also take special account of zones within the cement paste close to aggregate inclusions in order to understand the reduction of LITS in concrete when compared with cement paste.

2.4.2. Mechanical Loading

Hassen and Colina¹³ tested 100MPa mean cold compressive strength concrete under a uniaxial compression of 0.5MPa during thermal treatment. An increase in LITS was observed with increase in temperature which confirmed the occurrence of LITS even in specimens tested under exceptionally low compressive loads. The effect of mechanical load on the rate of LITS development however is less clear.

Based on the experimental investigation of sealed specimens tested under torsional load during heating below 100 °C^{8,10}, Illston and Sanders designed a model of LITS described solely as a function of temperature where mechanical load served only to activate LITS and had no influence on its magnitude or rate of development. The behaviour of unsealed concrete specimens at temperatures below 100 °C has received little attention. However, above 100 °C, in uniaxial stress conditions, investigators^{6,2} have found a mostly linear relationship between the increase in applied stress and LITS development.

Khoury *et al.*⁶ found that the linear relationship was seen to hold for low uniaxial stress between 0.1 f_{cu} and 0.3 f_{cu} . However, below a stress level of 0.1 f_{cu} LITS was observed to develop as a decreasing function of stress where LITS development was seen to be greater between 0-0.1 f_{cu} than for 0.1-0.2 f_{cu} . Conversely, at 0.6 f_{cu} LITS appeared to develop as an increasing function of stress. Higher heating rates and the presence of additional moisture beyond the air dried state also appeared to enhance non-linearity at all stress levels. However, due to the limited number of tests above 0.3 f_{cu} stress level, Khoury *et al.*⁶ suggested that the mechanisms which cause LITS development may not have been linearly related to stress.

The behaviour of specimens heated under multiaxial compression appears to be significantly different from that of those heated under uniaxial compression. Thienel and Rostasy¹⁸ performed unsealed biaxial compression experiments on concrete at temperatures of up to 750 °C. Tests were performed at differing stress levels and σ_1/f_{cu} and σ_1/σ_2 ratios. They found that LITS in uniaxially stressed specimens was smaller than that in biaxially stressed specimens and differences due to the variation in

stress ratio remained stable until 600 °C. This corresponds with observations made by Petkovski and Crouch¹⁶ who reported that the “LITS Poisson's ratio” at 250 °C was 0.34 for uniaxial and 0.37 for equal-biaxial compression tests. Thienel and Rostasy¹⁸ also found that the LITS component reached a maximum in compression at a stress level of $\sigma_{0,T}/f_{cu} = 0.3$ where $\sigma_{0,T}$ is the hydrostatic stress component at a given temperature. These observations support Petkovski and Crouch's¹⁶ explanation of LITS as an anisotropic phenomenon.

The magnitude of stress applied during LITS development was found to affect both the residual and hot strengths of concrete specimens. Results presented by Khoury *et al.*¹⁷, showed that the residual strength of specimens heated to 600 °C was increased by as much as 15% over those which experienced thermal load only. Exact values of strength increase varied depending on the aggregate used in each test primarily because of the variation in damage to the concrete caused by the different aggregates on cooling. The effect was most pronounced between 0-0.1 f_{cu} and reached a maximum at 0.2-0.3 f_{cu} . The increase in strength was proposed¹⁷ to occur as a result of suppression mechanisms which reduced the damage associated with specimens heated without a confining load where the residual strength was found to be less than 50 % of the unheated value.

Schneider¹⁹ also found that an increase in uniaxial stress up to 0.3 f_{cu} at temperatures between 150 °C and 750 °C resulted in an increase in the modulus of elasticity of specimens. No additional increase was observed for higher uniaxial stress states between 0.3 and 0.5 f_{cu} but it was concluded that “stressed strength was higher than unstressed strength”. A large confining load may therefore induce sufficient damage on its own to overcome the beneficial strength increase likely provided by LITS. Research inconsistent with the aforementioned findings was presented by Abrams²⁰ and Malhotra²¹ who found that the level of stress during heating had no effect on specimens tested to peak stress in uniaxial compression. Despite this, an increase in hot strength of between 5-25 % was observed for all specimens heated under the presence of mechanical load.

The assertion that LITS is beneficial to the hot strength of concrete was contradicted in research by Petkovski¹. Specimens that were heated under low levels of uniaxial compression in partially sealed conditions and tested to peak stress in the same orientation appeared to have very similar strength and loading stiffness to those which were heated without load. Further, specimens which experienced the same mechanical and thermal conditioning showed lower strength and loading stiffness with respect to specimens heated without load when tested in compression to peak in the opposite orientation.

Petkovski¹ also found a reduction in the strength of specimens which were heated under equal biaxial compression when tested to peak stress in both the same (extension meridian) and the opposing compression meridional plane. Specimens heated under hydrostatic compression experienced as much as 10% lower strength when tested to peak stress in all three meridional planes (compression, shear

and extension) when compared with concrete that was heated without load. This degradation of mechanical strength was explained as a detrimental effect of a LITS specific damage mechanism¹.

Only limited data is available on the effect of mechanical load on transport properties in LITS affected cementitious materials. Černý et al.²⁹ reported that the moisture diffusivity of specimens heated without mechanical load was found to be twice as great as that of specimens heated under load. This was explained through the assumption that the load applied before heating caused cracks which allowed pore pressures to dissipate. In specimens that experienced heating only, pore pressures were dissipated through explosive pore failure, resulting in the observed increase in diffusivity. These tests were carried out in unsealed conditions at 800 °C, under a uniaxial stress of 0.9 f_{cu} and a relatively high heating rate of 6.7 °C/min⁻¹.

The effect of mechanical stress on the LITS development and the subsequent impact of this on the mechanical strength of test materials have received significant attention. With respect to the design of experiments to perform microstructural investigation on LITS affected specimens it is preferable, particularly in *ex-situ* experiments where only a single observation is made on each specimen that load is applied hydrostatically so as not to induce material damage through deviatoric loading. Hydrostatic loading also appears to have most detrimental effect in terms of strength in the work of Petkovski¹ and therefore would seem to be most appropriate choice in order to observe any LITS specific damage mechanism. Since specimens used in the *ex-situ* experiments presented in this thesis are of the same batch as those used in the Petkovski tests, a higher mechanical stress will be used to investigate the non-linearity of LITS development with increasing mechanical load. This also allows an opportunity to test the observations of Thienel and Rostasy¹⁸ who concluded that the LITS component is at maximum where $\sigma_{0,T}/f_{cu} = 0.3$. Based on the Khoury *et al.*¹⁷ it might be expected that the microstructure of LITS affected specimens would experience a lower degree of damage than heat only specimens. This is also the case when considering the work of Černý et al.²⁹. Finally, microstructural observations should be carried out in both *ex-situ* conditions following cooling and *in-situ* at high temperature in order to determine the discrepancy between the hot strength and residual strength of concretes recorded in the literature.

2.4.3. Heating Rate

The impact of differing heating rates on the development of LITS in cementitious materials is the subject of some disagreement in existing literature. Based on observations from unsealed tests using both solid cylindrical specimens with a diameter of 75-80 mm² and hollow cylindrical specimens with a diameter of 160 mm¹³ at temperatures above 100 °C, heating rates below 5 °C/min⁻¹ were shown to exert little effect on LITS evolution.

A comprehensive study by Khoury *et al.*⁶ on specimens with similar dimensions in unsealed conditions directly contradicted this assertion. Beyond 200 °C, an increase of between 5 % and 20 % was recorded in the magnitude of LITS for specimens heated at 0.2 °C/min⁻¹ over those heated at 1 °C/min⁻¹ before the values converged at a temperature of 570 °C. The coefficient of LITS development also highlights this difference. LITS development at the slow heating rate is generally ahead of the faster heating rate until approximately 500 °C where it experiences a significant decrease which is only replicated for the faster heating rate at approximately 550 °C.

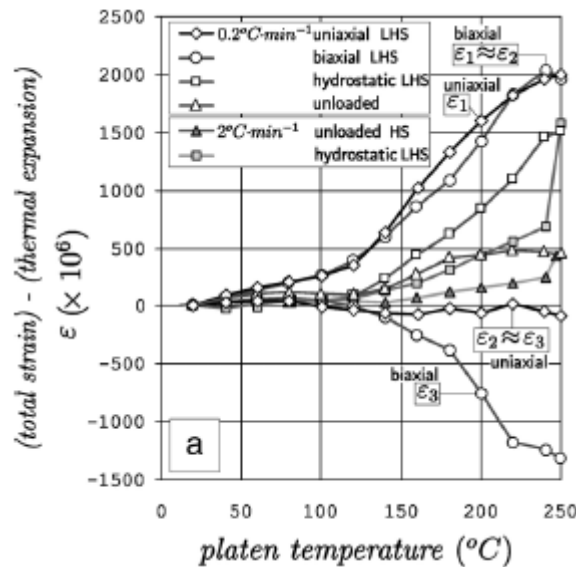


Figure 2.2: Petkovski and crouch – influence of heating rates¹⁶

One explanation for the observed effect of heating rate on LITS was proposed by Petkovski and Crouch¹⁶. These authors reported a trend not dissimilar to that of Khoury *et al.*⁶ where specimens heated at 0.2 °C/min⁻¹ initially showed greater values of LITS than specimens heated at 2 °C/min⁻¹. However, after 2-4 hours of constant temperature following the transient heating stage, LITS values were reported to be almost identical. Petkovski and Crouch suggested that the magnitude of LITS was in fact solely dependent on temperature. They concluded that only the rate of LITS development was affected by heating rate and that this depended on “moisture conditions within the specimen”.

Using specimens heated at both 2 °C/min⁻¹ and 0.033 °C/min⁻¹ Hansen and Eriksson⁷ reported that a permanent reduction in the modulus of elasticity occurred in material subjected to the higher heating rate. This corresponds with the results of Petkovski¹ who found that both the hot strength and loading stiffness decreased when concrete was heated at a faster rate of 2 °C/min⁻¹ over 0.2 °C/min⁻¹. Conversely, Khoury *et al.*¹⁷ found that the residual strength of specimens heated at the lower rate of 0.2 °C/min⁻¹ was marginally less than that of specimens heated at 1 °C/min⁻¹. This may again have been as a result of the differing boundary conditions employed in each test.

An understanding of the microstructural changes in specimens heated at differing rates would help to elucidate its impact on the magnitude of LITS and its rate of development. However, for *ex-situ* tests a slow heating rate and long equilibration time are crucial in order to maximise the development of LITS and ensure the microstructural observations are not associated with other processes.

2.4.4. Moisture Content

It had been suggested that LITS occurs as a result of the micro-diffusion of water within the cementitious microstructure^{7,14}. However, on heating, the redistribution of water in the porous structure of sealed cement paste was found to be complete within a few hours¹¹. Since research has shown that LITS may take up to 30 days to develop to its full extent in sealed specimens at temperatures below 100 °C^{10,7} it was suggested that the two processes were not connected. Additionally, Khoury *et al.*²² hypothesise that moisture migration between gel pores and capillary pores is likely to be reversed to some extent on cooling which is incompatible with LITS where no continuation or recovery takes place.

In unsealed tests, moisture may escape from the specimen on increase in temperature. and LITS has been found to occur “quasi-instantaneously”². Khoury *et al.*⁶ reported that an initial moisture content of between 65% Relative Humidity (RH) and 100% RH had no significant effect on LITS development. Specimens conditioned under oven dry conditions at a temperature of 105 °C did appear to experience a LITS development profile which was different to that of those at higher RH’s. However, as discussed earlier, specimens which have previously experienced elevated temperatures in an unloaded condition, will not develop LITS until the earlier temperature is surpassed in the presence of load. This means that no LITS would be experienced by oven dried specimens until 105 °C was exceeded. Despite this pre-heating, comparison of the results for the three RH’s considered shows that beyond 250 °C, LITS development is not affected by initial moisture content.

Whilst current experimental work indicates that initial moisture content does not affect LITS development, the boundary conditions of a test which will control moisture egress do appear to have clear implications. In fact, based on their observations of LITS development beyond the transient heating phase in partially sealed tests at 250 °C, Petkovski and Crouch¹⁶ suggested that if the temperature were increased at a sufficient rate with respect to “moisture transport conditions” in the specimen which included; boundary conditions, specimen permeability, and specimen size then LITS would continue to develop until “hygral equilibrium” is reached.

The effect of LITS on the mechanical strength also appears to be altered by experimental boundary conditions. Khoury *et al.*¹⁷ performed uniaxial compression tests on unsealed LITS affected specimens. They found that the residual cold strengths were significantly higher than those of a control sample that had experienced heating only. A review of previous research on unsealed uniaxial

and biaxial compression testing by Schneider¹⁹ reported similar findings. However, research by Petkovski¹ found that in partially sealed conditions, specimens which were loaded uniaxially before heating, did not experience any significant change in hot strength or stiffness with respect to a heat only control specimen when tested to peak stress in the same load orientation. Conversely, when tested to peak stress in the opposite direction these specimens experienced a decrease in hot strength and loading stiffness with respect to the heat only control.

Care is required to differentiate the effects on mechanical strength of processes connected with the development of LITS and other processes connected with moisture migration. Even without the presence of a confining mechanical stress, the boundary conditions during heating have been shown to play a role in degradation of mechanical strength. Testing by Lankard *et al.*²³ at temperatures up to 260 °C revealed that unsealed specimens experienced a negligible loss of uniaxial compressive strength and only a small reduction in the modulus of elasticity. However, sealed specimens lost approximately 50 % of compressive strength and up to 70 % of their elastic modulus.

This dramatic reduction in strength and stiffness for specimens heated in sealed conditions which correspond with saturated steam pressures is explained to be as a result of hydrothermal reactions in the cement paste which transform the original highly cementitious C-S-H phases to lime rich calcium silicate hydrates that have much reduced cementing properties²³. It is therefore possible that the microstructural effects of LITS which are beneficial to the strength of unsealed specimens are suppressed during heating in sealed conditions.

The aforementioned reduction in the diffusivity of LITS affected specimens when compared with those which experienced thermal treatment only described by Černý *et al.*²⁹ was thought to occur because of cracks induced in the material as a result of mechanical loading before an increase in temperature. These cracks are said to have reduced the build-up of vapour pressure in micropores during heating and thereby prevented explosive microcrack opening.

In contrast to this however, Thienel and Rostasy¹⁸ also attributed an expansion in the unloaded axis to an increase in moisture content which was restricted from escaping through the closure of shrinkage cracks by high hydrostatic loadings. The consequences of this being a higher moisture content during transient heating in stressed specimens over those which did not experience mechanical load.

Whilst, initial moisture content does not seem to affect LITS development or mechanical strength, the boundary conditions and subsequent moisture behaviour do appear to have some form of influence. A record of the difference in mass loss between LITS affected and heat only specimens would provide additional information on the role of moisture in LITS development. As described previously, the work of Černý *et al.*²⁹ indicates that greater material damage may be expected in heat only specimens

with respect to those which experience LITS. However the reverse is true if the hypothesis of Thienel and Rostasy¹⁸ is taken into account.

2.4.5. Maturity

Beyond 28 days, Schneider¹⁹ reported that the age of the material had no effect on the formation of LITS. Khoury *et al*⁶ corroborated this observation with specimens aged one and nine years. The effect of changes in the type of concrete, initial moisture content and stress level on LITS was not altered by maturity.

2.5. SUMMARY

A review of existing literature regarding the macroscopic effects of LITS on cement and concrete materials has informed key details of the experimental design:

- Microstructural observations shall be carried out on specimens which are subjected to temperatures of between 150 and 250 °C to maximise LITS development
- Observations on material microstructure are important in both *ex-situ* and *in-situ* conditions in order to understand the differences between residual and hot strengths recorded in the literature
- *Ex-situ* conditioned specimens shall be conditioned under hydrostatic compressive stress
- *Ex-situ* analysed specimens must be conditioned under a regime with a slow heating rate and extended steady state period so as to capture the full extent of changes within the material microstructure
- Whilst LITS appears to be unaffected by material age, mature specimens with an age greater than six months will be employed so as not to confuse key microstructural features of LITS with other processes occurring during hydration
- Microstructural analysis should take account of localised effects such as those around aggregate inclusions as well as bulk effects in the material

Macrostructural observations also provide some insight into the microstructural processes that occur in LITS affected specimens:

- Since changes are recorded in both strength and transport properties of LITS affected specimens, it is reasonable to expect that the porous phase within the material may see significant alterations. It is therefore prudent to focus on this phase during microstructural investigations.

3. Mechanisms for the development of LITS in mature concrete

3.1. INTRODUCTION

In this chapter an overview of the key literature concerning the characteristics of concrete microstructure will first be undertaken in order to highlight the primary features that control macroscopic material behaviour i.e. cement chemistry, solid structure and porosity. The mechanisms which have been proposed for both basic and drying creep will then be assessed before the existing hypotheses for LITS development are presented. This information will be used to inform the design of an experimental programme for microstructure investigation and provide key features of interest that may act as indicators of a LITS mechanism.

3.2. CONCRETE MICROSTRUCTURE

Concrete is a composite material consisting of coarse and fine aggregates bound together in a solid matrix. Modern concrete uses two main types of binding material to form the matrix phase. The most common material is ordinary Portland cement (OPC). This material in its raw form consists of a finely ground powder which undergoes a number of complex chemical and physical reactions when combined with water in a process known as hydration. Hydration products are distributed throughout the matrix phase leaving a solid porous structure with desirable strength and durability. Due to environmental concerns stemming primarily from the manufacture of OPC and the resulting production of CO₂, the use of supplementary cementitious materials such as Pozzolans is becoming increasingly common. Pozzolans which include industrial by-products such as pulverised fuel ash (PFA) and silica fume react with calcium hydroxide and water to form a binder. LITS is widely recorded to occur in cement paste containing only OPC as a binder⁹ and therefore supplementary cementitious materials are not thought to play a role in its development.

The solid microstructure of concrete can be decomposed into three distinct regions. These are; the microstructure of the aggregate, the microstructure of the bulk binding material and the microstructure of the binding material in the region surrounding the aggregate known as the interfacial transition zone (ITZ). In cement paste specimens where aggregate is omitted, LITS is reported to be increased by as much as 2 – 3 times over concrete specimens with the same geometry⁶. LITS has also been reported to be unaffected by the type of aggregate other than in situations where gravel is used with poor dimensional stability⁶. The focus of this investigation will therefore be placed on the

microstructure of the bulk binding material and ITZ regions both in this review and the following microstructural investigations.

During the hydration of concrete, many complex chemical and physical processes which take place in concrete may obscure microstructural development connected with LITS. Therefore, beyond the brief introduction to hydration chemistry in the following section which highlights the key constituents of the matrix phase, this thesis will focus only on the behaviour of mature cementitious materials beyond the age of six months.

3.2.1. Solid structure

The principal features within the microstructure of hardened Portland cement depend heavily on the cement hydration process. Cement powder (clinker) contains the following oxides in varying quantities; CaO, SiO₂, Al₂O₃ and Fe₂O₃. These are present in the form of tricalcium silicate 3CaO·SiO₂ (C₃S), dicalcium silicate (C₂S), tricalcium aluminate (C₃A) and calcium ferroaluminate (C₄AF) where nomenclature in parentheses represents the compound in cement chemistry notation. Additional admixtures such as gypsum may also be added to control the rate of reaction.

When mixed with water these compounds undergo a complex set of reactions which occur at both different rates and ages and may be considered independent from one another. In essence, the compounds undergo dissolution from the OPC grains into the pore water and eventually precipitate out as solid hydration products. A summary of the principal products and their features is presented in table 3.1 followed by a detailed explanation of each based upon Mindess and Young²⁴.

Table 3.1: Summary of properties of hydration products in Portland Cement paste (from Mindess and Young²⁴)

Compound	Crystallinity	Morphology in paste	Typical crystal dimensions in paste
C-S-H	Very poor	Spines: Unresolved morphology	1 x 0.1 μm (Less than 0.01 μm thick)
CH	Very good	Non porous striated material	0.01 - 0.1 mm
Ettringite	Good	Long slender prismatic needles	10 x 0.5 μm

C-S-H phase

According to Mindess and Young²⁴ calcium silicate hydrates (C-S-H) make up one-half to two-thirds of the total volume of the hydrated cement paste. They are therefore likely to dominate the behaviour of the bulk material. The C-S-H phase is formed through the reaction of tricalcium silicate (C₃S) and dicalcium silicate (C₂S) with water. This reaction also produces calcium hydroxide (CH) and heat²⁴:



C-S-H which can also be known as tobermorite gel²⁷ may exist with a number of different compositions. Both semi-crystalline and amorphous products may be observed.

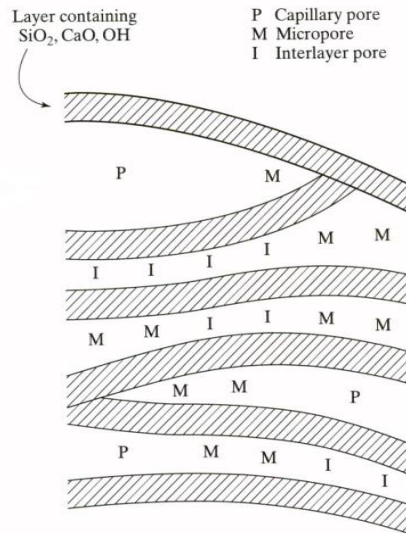


Figure 3.1: – Schematic model of C-S-H in cement paste after Mindess and Young²⁴

Due to the size of the features within the C-S-H phase it is not possible to observe their structure directly using any currently available experimental equipment. The exact structure is therefore the subject of a number of microstructural models. In essence each one considers C-S-H to be composed of sheets of calcium silicate in a similar microstructure to that of clay and separated by water which may be bound to the structure in varying states. However, unlike clay, the sheets exist in a disordered formation (Figure 3.1) because of the manner in which the material forms and the variation in composition of the solid structure. Direct interaction between sheets is thought to be controlled via van der Waals' type bonding in interlayer spaces (I).

Two types of pore space can also exist in the C-S-H models. These are the micropores (M) and capillary pores (P). The sheets which form the bounding surface of micropores lie close enough so that menisci cannot form during wetting and drying. In this case water may have acted structurally by exerting a “disjoining pressure”²⁴ to keep sheets apart. Conversely, the capillary pores are of a magnitude where water may behave as a bulk material. Further discussion on the role of water in mature cementitious materials will be undertaken in section 3.2.3.

Calcium hydroxide

Unlike the C-S-H structure, calcium hydroxide (CH) develops a crystalline structure which is easily observable using optical microscopy and X-ray diffraction. It occupies between 20-25 percent of the paste microstructure and forms within the capillary pore structure in the C-S-H²⁴. Crystals vary significantly in geometry which depends heavily on the location in which they are grown and differs significantly from crystals grown *ex-situ* in laboratory conditions. These crystals may act as a restraint to creep and shrinkage. Pure calcium hydroxide crystals do contain slip plains, but in cement, the crystals contain silica and C-S-H components which are believed to inhibit this²⁷.

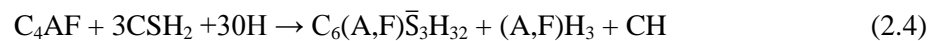
Ettringite

Calcium sulfoaluminate or Ettringite occupies only 10-15 percent of the volume of hydrated cement paste²⁴ and is a relatively minor constituent despite having the potential to significantly affect the durability of the microstructure via sulphate attack. Ettringite may be formed via two hydration mechanisms:

1. In the presence of water, tricalcium aluminate reacts with any gypsum present in the cement to form ettringite (Aft) and heat:



2. Calcium ferroaluminate may also react with free gypsum present to form ettringite, lime and alumina hydroxide:



Ettringite crystals take the form of hexagonal prisms with a “needle like” high aspect ratio. Due to the volume of this phase with respect to other components of well hydrated cement, it is not likely to be the direct cause of creep or shrinkage. However, some research has indicated that differing proportions of this phase may cause difference in shrinkage and creep behaviours²⁷.

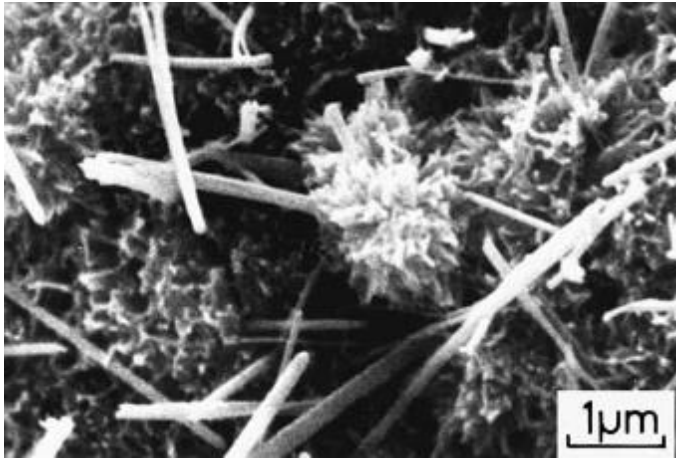


Figure 3.2: Micrograph of ettringite needles from Scrivener³⁰

Ettringite is an unstable hydration product particularly at elevated temperature and reacts with tricalcium aluminate once all gypsum has been consumed to form monosulfate aluminate hydrate via the following reaction:



Anhydrous cores

Anhydrous cores represent the remains of Portland cement grains in well hydrated cement. These are well crystallised structures and may act as restraints to paste deformation. This may be the reason why cements with a low w/c ratio exhibit little shrinkage²⁷.

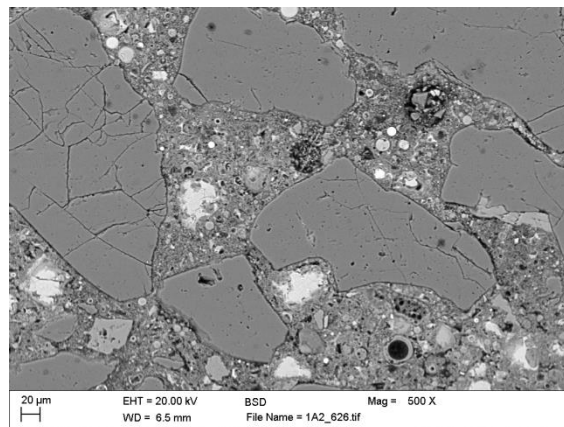


Figure 3.3: Micrograph of anhydrous cores

3.2.2. Pore structure

Porosity in concrete extends across a wide range of length scales from millimetres to nanometres in equivalent diameter. As highlighted in the earlier introduction to C-S-H, pores are classified with respect to their size and the behaviour of water within them. Common nomenclature and properties of

pore sizes are shown in Table 3.2. Whilst the porous phase in general has the most significant effect on the strength and permeability of concrete, pores of individual classes may have varying influence on these properties. In this work, pores will be referred to according to concrete science terminology.

Table 3.2: Size distribution of pores in cementitious materials and accepted nomenclature³¹

Size range (Diameter)	1 nm	10 nm	100 nm	1 μm	10 μm	100 μm	>1 mm
Name of pores according to IUPAC	←→ Micropores		←→ Mesopores		←→ Macropores		
Name of pores according to concrete science terminology	←→ Gel pores		←→ Capillary pores			←→ Air voids	

The pore structure of concrete is commonly characterised by pore volume fraction, pore size distribution and internal surface area. These properties give an insight into the effect of porosity on mechanical strength. Additionally, geometric properties such as connectivity and tortuosity can be used to characterise flow and transport properties.

Air voids

Air voids represent the largest features within the pore structure of concrete. They commonly exhibit a spherical geometry and are a direct result of the entrainment of air within the concrete during mixing. Often, air entraining agents are added to the concrete mix to increase the quantity of air voids in order to aid placement and frost resistance in the mature material. During placement, the concrete is vibrated in order to remove excess air voids which may agglomerate; particularly in mixes with large aggregate volumes. However, in general, air voids have only a limited effect on permeability and other transport properties as they are likely to be isolated from the capillary transport network. Air voids may however have a significant impact on strength and act as nucleation sites for crack growth²⁴.

Capillary pores

Capillary pores are characterised as pores with an equivalent diameter of approximately 10 nm to 10 μm. They are the remains of moisture filled spaces between hydration products and form the main transport network for aqueous species and gasses through the material²⁴. Development of the

capillary pore network is a function of both the maturity and the water/cement (w/c) ratio of the fresh concrete²⁴. This means that a concrete with greater maturity has a less well developed capillary structure and a concrete with a high w/c ratio is likely to be significantly more permeable than one with a low w/c ratio (Figure 3.4). Capillary pores play a significant role in material strength and are also known to influence material shrinkage at high humidities²⁴.

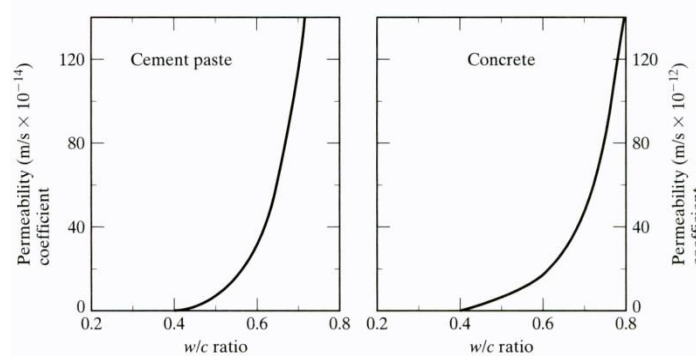


Figure 3.4: Relationship between w/c and permeability in cement paste and concrete (from Mindess and Young²⁴)

Gel pores

Conversely, the volume and geometry of micro-pores is often regarded to be independent of w/c ratio as long as enough water is present to allow hydration to proceed to its full extent²⁴. Gel pores are an intrinsic part of the C-S-H phase and their development is governed only by the maturity of the concrete. Gel pores exist on the nanometre length scale with typical sizes of between 0.5 to 10 nm (less than ten water molecules in width³²). Lachowski and Diamond³³ previously proposed that the size of gel pores depends on their location within the C-S-H phase with larger pores (~5 to 10 nm) existing in the outer product C-S-H and smaller pores (<5 nm) existing in the dense inner product C-S-H.

Due to their size, gel pores cannot be observed using scanning electron microscopy. Gel pores are therefore studied using techniques such as nitrogen adsorption that allow only indirect analysis of their properties including total porosity and pore size distribution. Despite this limitation, nitrogen adsorption testing has provided some support to the existence of high density and low density regions within the C-S-H. By studying the regions of cement paste which could be expected to contain low density C-S-H, Jennings³⁴ found that the surface of low density particles were accessible to nitrogen along with a small volume of interior pores. In high density areas, the surface of C-S-H particles was not accessible to nitrogen although a much large volume of interior pores could be accessed in these regions.

3.2.3. The role of water

The bulk hardened cement paste alone may have an internal surface area of 500 m² per cm³³⁵. Coupled with the hydrophilic nature of these surfaces, this means that internal forces due to the interaction of solid structure with water can be the dominating factor governing stress levels within concrete microstructure³². According to Powers³⁶ these so-called **capillary** and **adsorption forces** far exceed any stresses that are induced in the microstructure due to external applied forces. A summary of key moisture interactions with solid structure are summarised here.

Water within the air voids and the capillary pore system of a mature concrete will behave as a bulk material²⁴. This means that it is not heavily influenced by surface forces and menisci can form at the air/water interface on drying. The curved meniscus has an equilibrium vapour pressure lower than a plane surface as determined by the Kelvin equation. Water will not therefore be lost by evaporation from these capillaries until the surrounding vapour pressure, as determined by the relative humidity, reaches the value required by the Kelvin equation (Equation 2.6):

$$\ln \frac{P_0}{P} = K \cdot \frac{2\gamma}{r}; \quad (2.6)$$

where P_0 and P are the equilibrium vapour pressures for a plane surface and a curved surface respectively, γ is the surface tension of water, r is the radius of capillary (radius of meniscus curvature) and K is a constant²⁷. The presence of menisci induces hydrostatic tension which creates a corresponding compressive stress in the solid phase known as **capillary stress**²⁷.

According to Young²⁷, calculations based on the Kelvin equation shows that all pores above about 350 Angstroms (0.035 microns) are emptied in the r.h range 100-98 % with relatively little induced compressive stress. As the humidity decreases, smaller pores empty and the hydrostatic tension increases until at 50 % r.h pores of 15 Angstrom radius empty creating a stress of around 100 MPa²⁷. At lower r.h the tensile strength of the menisci is exceeded and they cannot form²⁷.



Dots—Water molecules, 1—Anhydrous cement, 2—Cement gel (inner products), 3—Cement gel (outer products), 4—Air with water vapor, 5—Capillary water, 6—Free adsorbed water, 7—Hindered adsorption

Figure 3.5: Schematic representation of cement microstructure as proposed by the microprestress-solidification model (from Bazant *et al.*³²)

At the solid – pore structure interface, a layer of water molecules remains even on the formation of menisci (Figure 3.5). The thickness of this adsorption layer is a function of the relative humidity³⁶. At a relative humidity of 12 % only a single layer of water molecules will remain³⁷. The maximum thickness of water molecules occurs on saturation with a relative humidity of 100 % where five layers of water molecules cover the solid surface³⁶. In regions where the diameter of the gel pores is less than that of ten layers of adsorbed water, the full thickness cannot develop. These areas within the microstructure of concrete are known as regions of hindered adsorption³⁶.

The tendency to push the two surfaces separated by a region of hindered adsorbed water apart to achieve thermodynamic equilibrium is resisted by the solid which thereby induces a transverse compressive stress in the water. This stress is known as the **disjoining pressure** and may be calculated thermodynamically^{27,36}. Bazant³⁵ showed through thermodynamic calculation that a disjoining pressure of 172 MPa may be present in pores with an equivalent diameter of two water molecules at 25 °C and 100 % relative humidity.

Both the capillary and disjoining pressures are therefore capable of exerting localised stresses on the concrete microstructure far in excess of the compressive strength of the material. Both have also been widely used to explain creep and drying shrinkage in concrete and may also play a role in LITS.

3.3. MECHANISMS FOR BASIC AND DRYING CREEP IN CONCRETE

It is commonly suggested that the irreversible components of both basic and drying creep may be considered as different manifestations of the same physical processes^{27,38,39}. A number of different hypotheses have been posed to explain these microstructural mechanisms⁴⁰. They include but are not limited to:

- Plastic flow theory³⁹
- Viscous flow theory⁴¹
- Seepage theory^{37,42,43}
- Microdiffusion theory^{35,44,45}
- Micro-prestress solidification theory^{32,46}

These mechanisms may be broadly separated into two categories dependent on their reliance on the presence of water. The presence of some evaporable water would seem essential to creep, but it is not clear if it is the water movement itself or a secondary function in moving the solid constituents of the cement paste that is responsible³⁹. Discussion will be limited here to seepage theory, microdiffusion theory for drying creep and microprestress-solidification theory due to their later advancement to explain the development of LITS.

3.3.1. Seepage theory/ Hindered adsorbed water theory

The first iteration of seepage theory was conceived by Lynam⁴³ in 1934. Lynam explained basic creep in similar terms to the consolidation of clay where pore water between particles is forced out of the material under load. However, this simple mechanism was disproved through the observations that the application of compressive stress does not cause an appreciable increase in water loss from concrete and also that creep in sealed concrete is not negligible⁴⁴. Seepage theory was developed further by Powers^{37,42} in the 1960's who explained creep in terms of both bulk movement and local movement from gel pores to capillary pores. Powers ascribed the development of basic creep to changes in the internal vapour pressure because of volumetric alterations under an external load. In this way the mechanism could also explain drying creep which directly results in a reduction of internal vapour pressure.

The effect of a change in internal vapour pressure was thought to be two-fold. In capillary pores which are isolated from the exterior of the concrete microstructure, water may only empty indirectly through adsorbed water layers in the gel pores via a time dependent diffusion process⁴². The surface tension of the adsorbed water film increases and this film tension is transferred to the capillary water as water moves to maintain equilibrium due to the reduction in relative humidity. Menisci will then

form in isolated capillary pores through the nucleation of air bubbles once the relative humidity in the pore drops below the saturation level⁴² (See (5) in Figure 3.5). The hydrostatic tensile stress which results in the liquid will induce an additional compressive stress in the solid structure of the concrete that is one source of the creep observed. Such hydrostatic tension will not develop in a capillary if free absorption can occur directly from the meniscus. However, in a well hydrated cement it can be expected that the majority of the capillary spaces will be isolated from the exterior of the material⁴².

Additionally, changes in the gel pore water content associated with the aforementioned time dependent diffusion process were thought to cause a reduction in the disjoining pressure in areas of hindered adsorption within the cement paste structure⁴². As disjoining pressures gradually decreased a concurrent reduction in the volume of the paste was expected as the spacing between particles in the gel reduced. Load removal was expected to result in a drop in the pressure of the load bearing water.

A number of problems still exist with the improved seepage hypothesis presented by Powers⁴². It is difficult to explain how any appreciable load could be transferred to water which is not adsorbed to the cement as its volume compressibility is more than twenty times that of concrete^{44,47}. The theory also could not explain the development of creep in sealed or immersed specimens where changes in moisture content were prevented. Further, even in conditions where moisture loss is possible, creep has been recorded to continue for periods well beyond 24 hours after loading when hygral equilibrium would be expected to have been achieved⁴⁸. Finally, the acceptance of such a mechanism would imply that creep would be negligible in specimens which were dried before loading. However testing by Wittman⁴⁹ indicated that creep does occur under such conditions.

3.3.2. Micro-diffusion theory for drying creep

The movement of moisture through regions of hindered absorption within the cementitious microstructure has also been used to describe drying creep via a subtle enhancement of seepage theory to microdiffusion theory. Bazant and Chern⁴⁴ explained water movement through concrete in terms of macro-diffusion (J) that occurs between capillary pores and micro-diffusion (j) which occurs between gel pores and capillary pores through hindered absorbed layers (Figure 3.6).

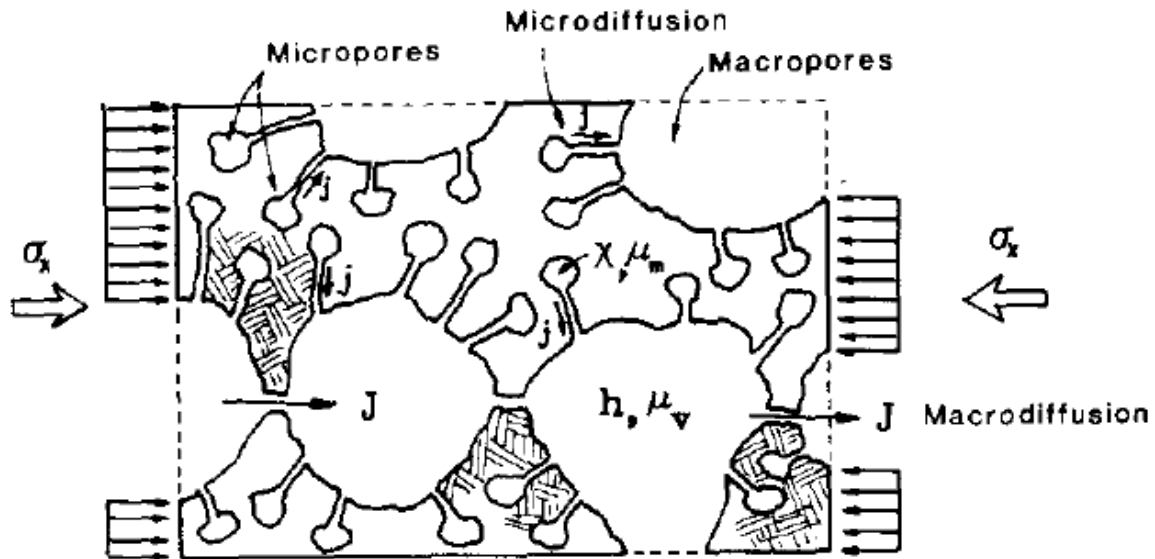


Figure 3.6: Macro and Microdiffusion (from Bazant and Chern⁴⁴)

In order to avoid difficulties associated with the lack of evidence showing bulk water transport simultaneous with creep, Bazant and Chern explained micro-diffusion as having an equal probability for vectors of displacement in all directions. Consequently, micro-diffusion was not connected with any macroscopic movement of water which contradicts the observed hygral equilibrium attained within 24 hours⁴⁸.

The local flux of water molecules associated with micro-diffusion was thought to occur because of a delay in the establishment of thermodynamic equilibrium between micropores and capillary pores following a change in relative humidity during drying under load. Macroscopic drying creep was expected to occur due to an increase in the rate of breakage of atomic bonds in the C-S-H structure because of the micro-diffusion process. The micro-diffusion theory provided a mechanism for Bazant³⁵ and Bazant and Moschovidis⁴⁵ who had previously posed that the bond breakage in the C-S-H structure was the root cause of creep.

However, the mechanism of micro-diffusion in disrupting C-S-H bonds lacks a precise explanation³². Bazant^{44,50} assumes that creep is likely to be a result of debonding and rebonding within the solid structure of the cement despite the lack of experimental evidence to this effect. The micro-diffusion theory also failed to provide a unified theory for both basic and drying creep as no accepted mechanism to induce a change in relative humidity under load at constant temperature is presented.

3.3.3. Microprestress-solidification – a unified theory of basic and drying creep

To explain this disruption of C-S-H bonds within the structure of the cement paste, Bazant *et al.*³² later presented a unified theory of basic creep and drying creep based on the relaxation of a transverse normal stress known as the microprestress (S , in Figure 3.7). Bridges across micropores containing hindered adsorbed water form localised sites where atomic bonds experience elevated tensile stress – this is the microprestress. The layers of hindered adsorbed water consequently form slip planes that are the principal cause of the flow component of basic creep. In accordance with this theory, the applied macrostress (P_d , Figure 3.7) causes shear-slippage even when applied uniaxially due to the random orientation of the micropores.

In terms of drying creep the microprestress depends linearly on the humidity (h). This is because the tensile microprestress acts in reaction to the disjoining pressure. Consequently as the disjoining pressure changes as a result of a change in relative humidity in an adjacent pore so does the tensile microprestress. This is believed to occur almost instantaneously³².

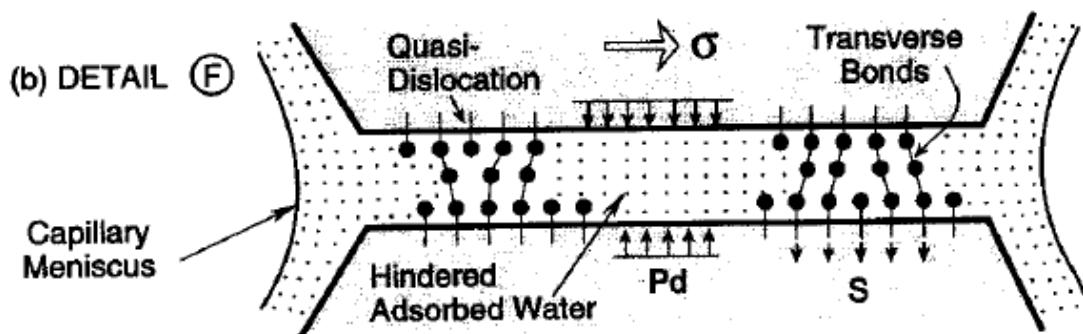


Figure 3.7: Microprestress-solidification model after Bazant *et al.*³²

In accordance with this model, long term creep therefore originates from viscous shearing and reformation of these bonds which carry the tensile microprestress under an applied pressure³². These bond breaks occur at different overstressed locations (creep sites) and at varying times. Bond breakage and stress relaxation at one site causes other creep sites to become overstressed. This continues until all creep sites are exhausted and creep rate slows³². Such shear slips do not only cause shear creep. Due to the heterogeneity of the microstructure of hardened cement paste, hydrostatic macrostresses within the solid structure cause both shear and normal stress resulting in volumetric creep³².

Bonds may also break and not reform. Bazant explains that this is also a component of creep and it causes tensile microcracking. This is the source of the non-linear creep component due to the resulting reduction in stiffness of the material. Bazant *et al.*⁴⁶ incorporate distributed smeared cracking into their microstress-solidification model to account for the drying environment.

With respect to the long term age effect on creep behaviour, Bazant *et al.*'s³² model explores the stiffening of existing hydration products without additional volume growth. This is a development of the earlier solidification theory^{47, 51} where the deposition of unstressed hydration products over time acts to stiffen the material and reduce viscosity. Solidification theory was disproved because basic creep has been recorded to continue for an extended period of time after volume growth associated with hydration has ceased. Viscosity in the provision for flow of Bazant's³² model is again controlled by microstress carried by bonds crossing gel pores

The microstress-solidification model agrees relatively well with test data⁵¹. However, from a physical view point it still faces a significant problem. This is that creep is heavily dependent on age at loading even after many years. No mechanism is provided in the literature for the stiffening of existing hydration products over extended time frames.

3.4. MECHANISMS FOR LITS IN CONCRETE

Hypothetical mechanisms for the development of basic and drying creep have seen two main advancements towards an explanation for LITS. First, microstress-solidification theory has been advanced by Bazant *et al.*⁵² to explain the principal features of TTC and second, micro-diffusion theory has been suggested by Petkovski¹ to be responsible for the combined components of LITS. Each will be reviewed in turn.

3.4.1. Microstress-solidification theory for TTC

As explained, the model of Bazant *et al.*³² accounted for drying creep through a change in the rate of bond breakage and reformation in the C-S-H microstructure due to an increase in the microstress which is linearly related to relative humidity. This model was extended in Bazant *et al.*⁵² to account for the combined effects of drying creep and transient thermal creep thereby encompassing LITS. In this work, Bazant *et al.*⁵² hypothesised that the magnitude of the microstress would be influenced in the same way by a change in temperature as by a change in relative humidity.

Consequently, if a specimen experiences an increase in temperature, the bond breakages and restorations accelerate, thereby increasing the creep rate⁵². This is however countered to a limited extent by an increase in cement hydration/solidification due to the increase in temperature which is not enhanced with a change in relative humidity that results in concrete aging and creep reduction⁵².

However in a mature concrete where aging is not significant the increase in bond breakages would be expected to dominate resulting in a total acceleration of creep rate.

The model of Bazant *et al.*⁵² was applied in the same work to investigate its similarity to published experimental results. It showed reasonable agreement with the work of Fahmi *et al.*⁵³ who recorded TTC in specimens at temperatures up to 60 °C. The model does however simulate an increase in TTC during the transient temperature period on cooling which is not recorded elsewhere in existing literature.

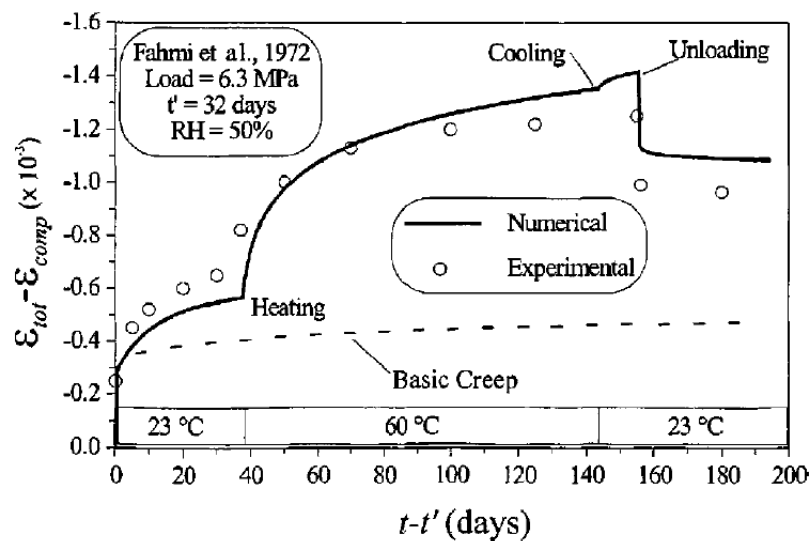


Figure 3.8: Transitional thermal creep at variable water content after Bazant *et al.*⁵²

With respect to the material microstructure this model would likely result in a significant change in porosity. The material microstructure would also be likely to show evidence of an increase in hydration over specimens which experience heat load only which is propagated by the presence of a confining mechanical load.

3.4.2. Load induced thermal damage

The second mechanism consists of increased material damage during LITS development due to increased pore pressures. The mechanism is based on a development of the micro-diffusion theory for the movement of water between gel pores and adjacent capillary pores forming the concrete capillary system. However, in this case, moisture movement causes additional specific damage to the material. This load induced thermal damage (LITD) was used by Petkovski¹ as a system to provide explanation for observations which show LITS dependency on moisture transport properties above the equilibrium heating rate¹⁶ without contradicting work which shows that LITS can occur in both dry and submerged conditions⁷.

It would be reasonable to expect that, with a rise in temperature, pressure in the gel pores would increase. This would have the effect of increasing micro-diffusion of water into concrete capillary pores and thereby accounting for the measured LITS through the Hansen and Eriksson's⁷ supposition that "the micro-diffusion of water disrupts the solid microstructure of cement gel by promoting the de-bonding and re-bonding process that is source of creep".

3.5. CONCLUSIONS

Both of the mechanisms described here to explain the development of LITS would result in changes to the microstructure of the concrete. Such mechanisms would aid in the explanation of certain macroscopic observations on material behaviour which were reviewed in Chapter 2. If the initial loading of a specimen was not sufficient to open all gel pores to capillary macro-pores through the pressurisation of water contained within them then it could be expected that an increase in pressure due to an increase of temperature may result in further damage to the micro-structure of the concrete. For specified stress, temperature and moisture transport conditions (if above the equilibrium heating rate) a finite amount of damage would therefore occur and thus a finite LITS. Consequently, a specimen that was cooled and reheated to the same temperature would not experience an increase in LITS. However, an increase in temperature beyond this level would lead to an increase in pressure in as yet undamaged micro-pores resulting in further LITS.

Research on the mechanical strength of LITS affected specimens also provides further evidence of an incremental damage mechanism. Using one of the aforementioned LITS evolution mechanisms, it could be expected that crack formation would progress randomly throughout a hydrostatically loaded specimen, accounting for a significant reduction in strength in any meridional loading plane. Similarly, if a specimen were to experience a uni-axial load during heating, cracks would be expected to form in the normal plane. Once again this is borne out in the results with strength in the loaded orientation unaffected but strength in the two unloaded axes experiencing a decrease. Petkovski¹ also reported that whilst under load, thermal cycling which did not exceed the maximum temperature achieved in previous cycles yielded no further decreases in strength or loading stiffness.

The irrecoverable nature of the LITS phenomenon is explained through the supposition that prior heating of cementitious materials will reduce the likely microstructural changes during an LH test. This mechanism may also have the effect of altering the pore size distribution through the coagulation of hydrate particles¹¹. In fact, it may be the case that both of these mechanisms may promote similar microstructural processes and a greater understanding of these may help explain some of the conflicting research above.

With respect to the concrete pore structure where the work of this thesis will be focussed, such a mechanism would be expected to result in the following:

- An increase in accessible porosity and a migration in the distribution of pore sizes present in the material.
- Both air void and capillary porosity would be expected to increase in frequency with the opening of gel pores through bursting and bond breakage.
- It may also be expected that because LITS is known to occur in the cement paste only, material behaviour in the interfacial transition zone may be modified in LITS affected specimens.

Here we will use some well-known techniques quantitatively and some new ones which will be reviewed in the next section

PART 2: *EX-SITU* ANALYSIS

4. *Ex-situ* specimen conditioning

4.1. INTRODUCTION

A better understanding of microstructural changes during the development of LITS is of great importance in concrete science, both in theoretical and experimental contexts. As outlined in Chapter 3, it is hypothesised that the principal components of LITS result from the development of solid phases and changes of the pore structure within the hardened cement paste. To obtain a quantitative understanding of the difference between the microstructure of LITS affected concrete and that which has experienced only heat loading would help to understand the LITS development mechanisms and hence to develop better models of cement based materials under coupled thermo-mechanical load.

The majority of experimental techniques for the investigation of concrete microstructure require significant specimen preparation and are thus only suitable for studying materials in a pre or post conditioned state where conditioning involves the application of a thermo-mechanical or thermal only loading regime. In this work these experiments will be called *ex-situ* investigations. Such experiments are the focus of the second part of this thesis which is presented in the following chapters. Novel experimental techniques for the study of material microstructure during conditioning do exist and one such technique; *in-situ* X-ray Computed Tomography (X-ray CT) will be investigated in part three.

With *ex-situ* experimental methods conditioning can be carried out using a variety of experimental apparatus. As summarised in Chapter 2, uniaxial testing, equal biaxial and true multiaxial experimental rigs have been developed to study the macroscopic effects of LITS in concrete.

In this experimental program the apparatus for testing concrete under multiaxial compression at elevated temperature (mac^{2T})³ based in the Department of Civil and Structural Engineering at the University of Sheffield was used for all conditioning regimes. This chapter describes the experimental setup used to condition specimens for *ex-situ* microstructural analysis and basic specimen preparation which was employed for all microstructural analyses. LITS development in test specimens is discussed with reference to the principal literature along with cold strength and specimen weight loss.

4.2. THE MAC^{2T} APPARATUS

The mac^{2T} apparatus is a test facility designed for the investigation of the material properties of structural concrete under combined thermal and mechanical loading. The facility is capable of testing 100 mm cubed specimens which represent the minimum representative elementary volume of a mix

design incorporating 20 mm aggregate³ to 400 MPa in true triaxial compression ($\sigma_1 \neq \sigma_2 \neq \sigma_3$) at temperatures of up to 300 °C³.

Load is applied to specimens by the mac^{2T} rig by three 4 MN hydraulic actuators installed in each of the three independent load frames which are interlaced within each other (Figure 4.1). The frames are designed to have a high degree of stiffness – both the tensile bars and their associated crossheads are kept short – in order to prevent any significant deformation in the rig which may result in brittle failure when the strength of the specimen is exceeded³. Load from the actuators to the specimen is transferred via rams which incorporate the heating and cooling equipment and loading platens. To reduce friction between the loading platens and the specimen, six 1 mm thick steel tiles are placed at the interface. These are in turn covered in 0.25 mm thick PTFE sheets which contact with the surface of the specimen. The steel plates and the PTFE sheet are replaced after each test to ensure good surface contact. The measurement of forces applied to the specimen is enabled via three 4MN load cells with a precision of ± 4 kN. These are installed on the reaction crosshead of each frame.

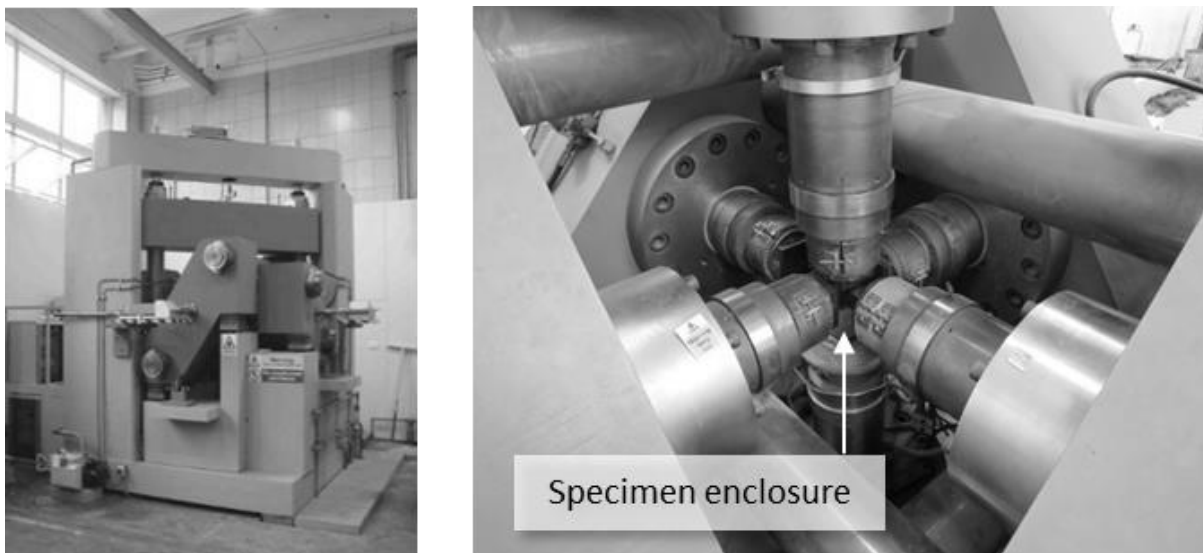


Figure 4.1: Mac2T experimental apparatus (Left) and load frames including specimen enclosure (Right)

Specimens are heated via conduction from six 240 W ceramic band heaters which encase the platens. The platens are fabricated from Durehete 1055 (20CrMoVTiB4-10) which has good long-term creep and relaxation resistance for experiments where extended high temperature operation is required³. A cold water labyrinth positioned behind each of the platens is used to prevent heat transfer to the actuator and load cell on each frame³. This is fed from a room-temperature reservoir.

Specimen deformation is recorded using a system of six laser interferometers. The system was designed to mitigate the effects of thermal expansion which would be difficult to remove during calibration from the alternative linear variable displacement transducer (LVDT) design. The system is composed of a laser head, a linear interferometer, a linear retro-reflector and a dedicated PC with a

calibrator board installed. Retro-reflectors are installed at the end of a stainless steel tube which penetrates the centre of each of the platens. The tube is evacuated to 10^{-5} bar to prevent the ingress of steam generated on heating that was found to interrupt the laser beam. The interferometer is connected to a pin at the end of the tube closest to the specimen. This pin penetrates the platen surface and the 1 mm steel tile and PTFE sheet to provide direct contact with the specimen surface. Consequently, only thermal expansion in the pin and the retro-reflector require correction – a distance of 47 mm³. The laser interferometer system has an accuracy of 10^{-6} m even over a displacement of 200 mm.

Data acquisition and experimental control is provided using National Instruments hardware along with a dedicated input-output control script written in LabVIEW³. Control variables are calculated from input values received from the laser interferometer strain measurement systems, the load cells, pressure transducers and LVDT back-up systems using PID (proportional-integral-derivative) control modules. These variables are the input signals for the actuators and temperature controllers³.

4.3. MATERIALS AND EXPERIMENTAL SET-UP

4.3.1. Materials

The specimens for this investigation were prepared in 2003 as part of an experimental program on the strength of Advanced Gas-cooled Reactor (AGR) pressure vessels¹⁶. One concrete type with a mix typical of that used to construct the Heysham 2 AGR pressure vessel was considered with the constituents and mass proportions shown in Table 4.1. Whilst it has been shown that LITS is unaffected by material maturity beyond 28 days, these specimens were chosen because all microstructural processes connected with hydration were likely to have been completed making it easier to determine microstructural features connected with LITS.

Table 4.1: Concrete mix proportions (OPC = Ordinary Portland cement; PFA = Pulverised fuel ash)

Constituent Name	OPC	PFA	Sand	Quartz-diorite 10 mm	Quartz-diorite 20 mm	Plasticiser SP4	Water
Cement Mass Ratio	1	0.33	2.45	1.39	2.78	0.0006	0.56
Constituent/binder mass ratio	0.75	0.25	1.84	1.05	2.16	0.0045	0.42

The concrete was cast in slabs with dimensions of 740 x 620 x 150 mm and immersed in temperature controlled water tank with a 10 day temperature matched curing cycle in which the temperature reached a maximum of 65 °C (Figure 4.2). This simulated the transient temperature increase observed on casting of AGR pressure vessels. Following the 10 day cycle, the slabs were de-moulded and returned to the water tank for a further 60 days at 20 °C¹⁶.

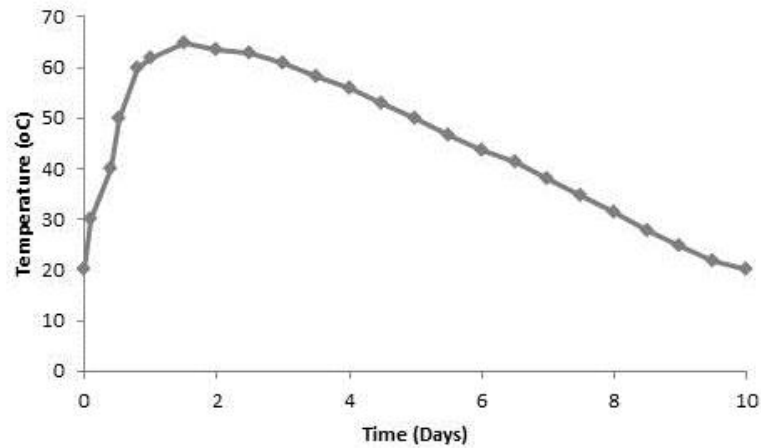


Figure 4.2: Temperature matched curing profile for concrete showing instrument controlled water bath temperature during first ten days following casting.

Each concrete slab was then cut and ground using water cooled equipment to form right regular 100 mm cubes. The machined cubes were stored at room temperature and humidity until conditioning. A mean uniaxial compressive strength 59 MPa was recorded for these specimens at 70 days beyond which no significant increase in strength were recorded¹⁶. Specimens were weighed and measured in all three axes using a calibrated digital micrometre before conditioning in order to enable accurate strain calculation.

4.3.2. Specimen Conditioning

The mac^{2T} experimental apparatus was used to condition the 100 mm cubed specimens under the load regimes shown in Table 4.2 and Figure 4.3. Three principal conditioning regimes were studied: thermal treatment only (H250), mechanical load followed by thermal treatment (LITS affected, L06H250) and unconditioned control specimens. Following the loading/heating the specimens were held under steady state conditions for a period of 24 hours. This enabled thermal gradients within the material to dissipate. Each conditioning regime was repeated twice to allow for statistical analysis.

Table 4.2: Conditioning regimes of the concrete cubes for microstructural analysis (f_{cu} = uniaxial compressive strength of concrete)

Conditioning Name	H250	L06H250	Control
Mechanical Loading	-	$0.6 f_{cu}$	-
Thermal Treatment	250 °C	250 °C	-

A heating/cooling rate of 0.2 °C/min was employed in all tests involving elevated temperature. This corresponds with the test conditions employed by Petkovski and Crouch¹⁶ and allows for the direct comparison of strain development in specimens and strength testing presented in a later paper by Petkovski¹. The maximum temperature obtained in elevated temperature testing was 250 °C. This corresponds with the design peak temperature experienced by the concrete pressure vessel of an AGR station during a LOCA.

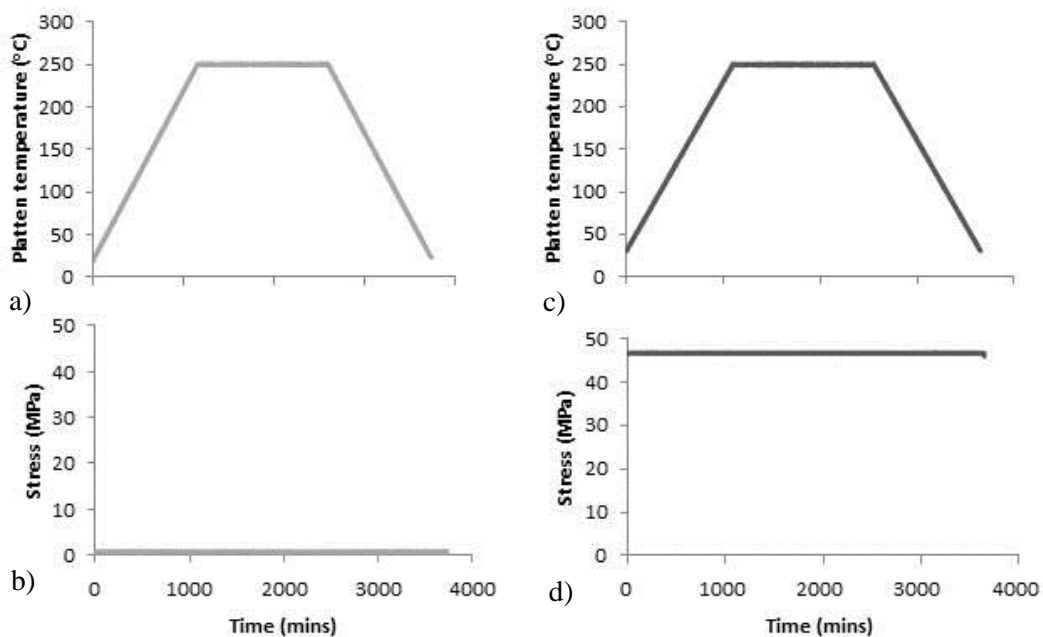


Figure 4.3: (a) Temperature profile in H250 tests (b) Stress profile in H250 tests, (c) Temperature profile in L06H250 tests, and (d) Stress profile in L06H250 tests.

To prevent microstructural damage to the material due to deviatoric loading which could mask key microstructural indicators for LITS, all mechanical load was hydrostatic in compression to a level of $0.6 f_{cu}$ (46 MPa). The strain measurements obtained from these tests were used to calculate LITS which is defined as the difference between the L06H250 and the H250 conditioning regimes. On

return to room temperature, the hydrostatic confinement stress was unloaded and the specimen removed from the mac^{2T} apparatus for further analysis.

4.3.3. Mass reduction testing

A key indicator of a reduction in the free and bound water content can be found in the measurement of mass loss during conditioning. Mass loss was measured by subtracting the weight of the specimen immediately after removal from the mac^{2T} apparatus from the mass of the specimen taken immediately before the start of conditioning. A calibrated balance with a precision of 0.001 g was employed for all tests.

4.3.4. Specimen preparation and residual strength testing

Since the specimens were conditioned for microstructural analysis, a conventional uniaxial residual strength test according to BS 1881 could not be carried out directly on each of the cubes due to its destructive effects. In order to overcome this issue, a 28 mm core was extracted from the centre of each cube as shown in Figure 4.4. The core diameter was chosen in order to capture the features of both the bulk cement paste and the interfacial transition zone surrounding the 20 mm diameter aggregate inclusions. The diameter of this core corresponded with the dimension required to achieve the lowest image resolution of 15 μm observed using X-ray computed tomography. Following the removal of the core an unconventional uniaxial strength test could be carried out on the remaining cube material. This was undertaken by placing the specimen with the cored faces in contact with the loading platens in a Controls Automax 5 uniaxial strength test apparatus. Thus, the residual strength of each specimen employed in microstructural analysis could be ascertained.

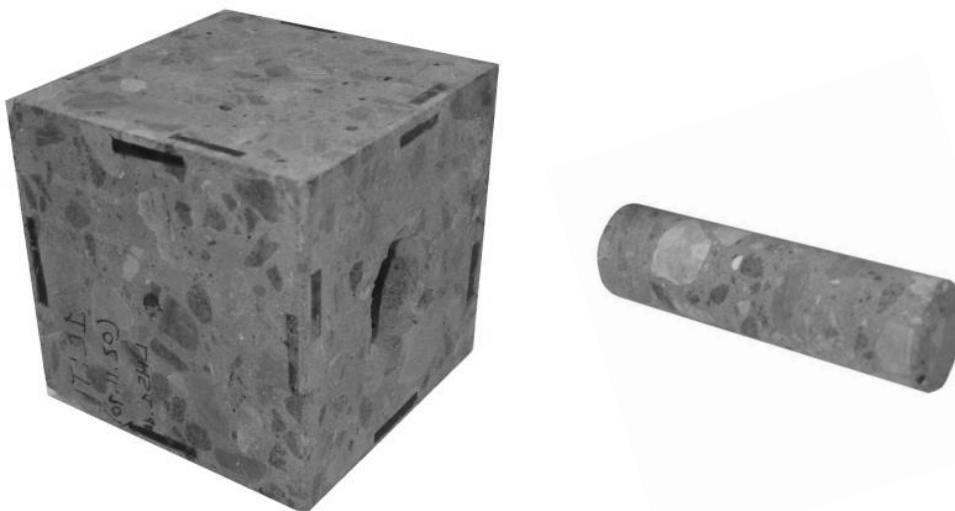


Figure 4.4: Cube with core extracted. Extraction carried out using a water cooled diamond tipped coring drill. Each core specimen was surface dried on extraction and stored at ambient temperature in the laboratory environment.

4.4. EXPERIMENTAL RESULTS

Results from the H250 and L06H250 (LITS affected) conditioning regimes are shown in Figure 4.5. The graphs show the volumetric strain measured by the mac^{2T} apparatus. Instantaneous elastic strain due to hydrostatic compression has been removed from the L06H250 results to provide for direct comparison between conditioning regimes. A high degree of repeatability can be seen for specimens in both of the conditioning regimes.

Within the first 500 minutes of the conditioning the strain profiles of all specimens are dominated by thermal expansion of the material. This time corresponds with the period required to reach 100 °C. Whilst thermal expansion dominates, the competing LITS component in L06H250 specimens is visible in that these specimens expand slightly less over this time period.

During heating beyond 500 minutes a significant change can be detected in the strain profile of L06H250 specimens with respect to H250 specimens. Thermal expansion in LITS affected specimens is completely suppressed up until 950 minutes corresponding with 220 °C. Beyond this time the specimens appear to experience a slight volume reduction (increase in compressive strain) up until the start of the steady state period after 1100 minutes. The volume reduction after 2600 minutes is due to cooling to ambient temperature.

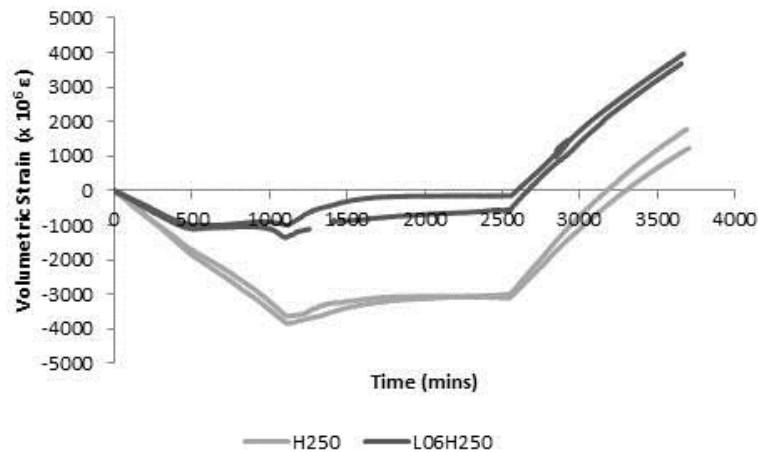


Figure 4.5: Volumetric strain in conditioned specimens. Elastic strains due to hydrostatic compression removed from L06H250 specimen traces for comparison. Compactive strains shown positive.

Figure 4.6a shows the results of data post processing to obtain the total strain minus thermal expansion. Due to the slow heating rate, thermal expansive strains in all specimens were assumed to be a linear function of temperature ($8.5 \mu\epsilon/^\circ\text{C}^{-1}$) in all three axes. Instantaneous strain due to the applied load in L06H250 conditioned specimens is once again removed. Strain histories for the two H250 specimens in this Figure represent the effects of drying shrinkage (ϵ_{sh}). This appears to be nil for the first 500 minutes of the test up to 125 °C. Between 125 and 220 °C an increase of 500 μS is

recorded. Beyond this temperature, drying shrinkage appears to stabilise. Strain histories for the L06H250 specimens shown here indicate the sum of LITS and drying shrinkage in these specimens. The temperature-strain graphs indicate once again that during heating, the tests show a high degree of repeatability.

Figure 4.6b indicates the evolution of LITS in each L06H250 specimen. LITS can be seen to develop from first heating under load. A significant increase in the rate of LITS development can be observed at temperatures above approximately 125 °C. At around 220 °C a slight reduction in the rate of LITS development is also observed. In total after heating to 250 °C the magnitude of the LITS component of strain in the specimen is approximately 2500 $\mu\epsilon$.

Figure 4.6c shows the strain development in all specimens during the steady state period following the cessation of heating. The values indicated in this figure are normalised to zero at the beginning of the steady state period in order to allow for direct comparison between L06H250 and H250 specimens. An average of 746 $\mu\epsilon$ is recorded in the specimens with a standard deviation of 170 $\mu\epsilon$. One specimen within the H250 conditioning regime appears to exhibit a slightly reduced strain development whilst all other specimens experience a very similar magnitude of strain at the end of this period. However, since the standard deviation is very low compared to the difference between the total strain of L06H250 and H250 specimens this variation was not considered to have a large influence on microstructural development. No evidence of LITS development into the steady state period can be observed.

In common with the steady state period, H250 and L06H250 specimens do not appear to differ significantly during cooling. The volumetric strain profiles shown in Figure 4.6d are corrected for thermal contraction using the same factor as for expansion ($8.5 \mu\epsilon/^\circ\text{C}^{-1}$). The results indicate that no LITS related development or recovery occurs during the transient temperature phase on cooling.

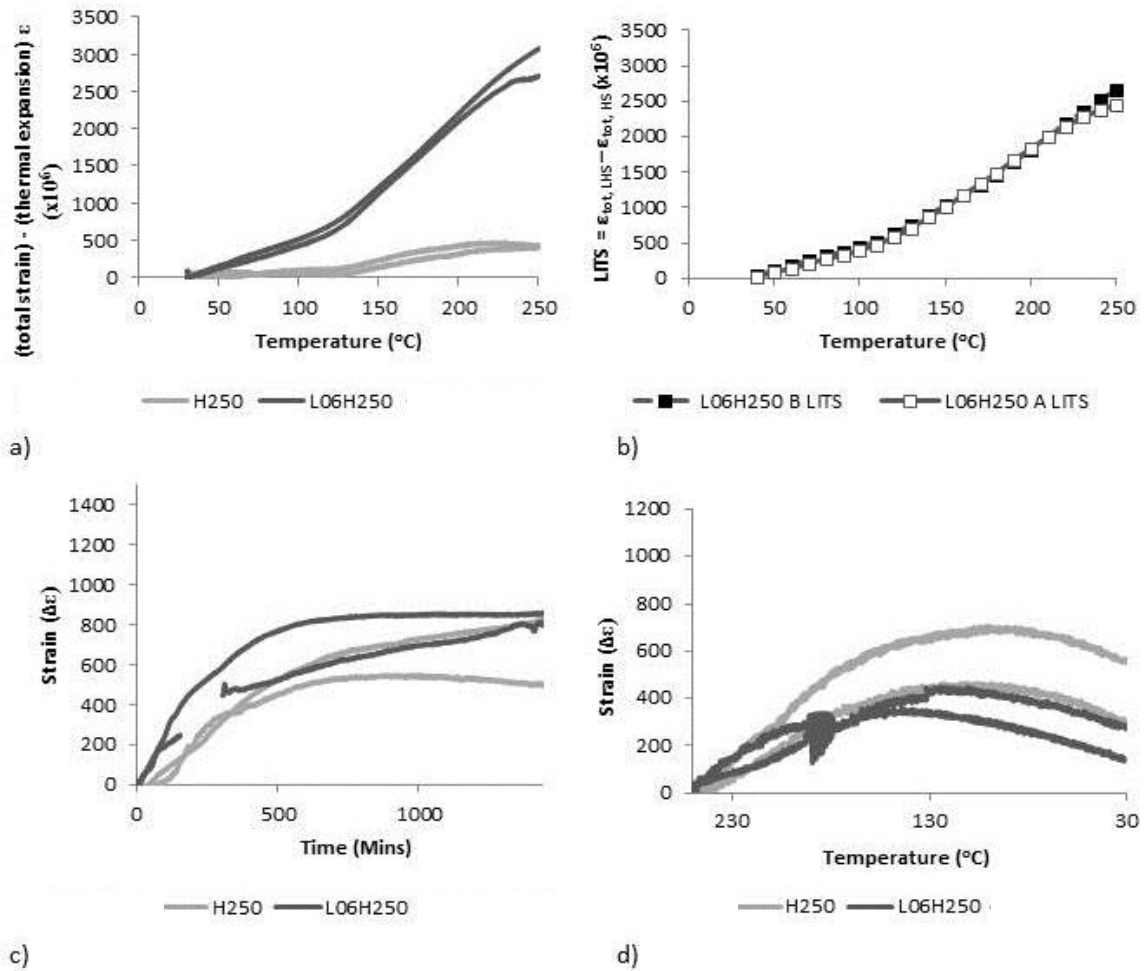


Figure 4.6: (a) shows the change in volumetric strain in conditioned specimens with temperature during heating. Here, the contribution of thermal expansive strains within the specimens has been removed.

(b) shows the evolution of LITS with increase in temperature calculated by subtracting the strain measured in L06H250 specimens from the mean average of the strain recorded in the H250 specimens.

(c) and (d) indicate the strain evolution in the specimen during steady state and cooling respectively. In both Figures, time and volumetric strain have been bench marked at zero for comparison across conditioning regimes. No significant difference can be observed between the H250 and L06H250 conditioning regimes during the steady state period. LITS development does not therefore show any sign of continuation on cessation of heating.

4.4.1. Mass reduction

Figure 4.7 (b) indicates the mass loss of specimens calculated following the removal of cubes from the mac^{2T} apparatus. An average of approximately 51 g is lost from each conditioned specimen. LITS affected specimens conditioned at 250 $^{\circ}\text{C}$ do not appear to show any difference in mass loss compared to H250 specimens.

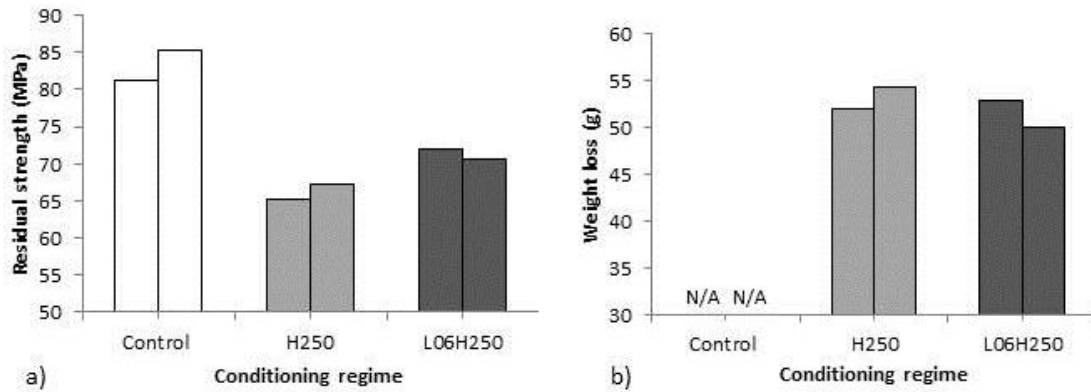


Figure 4.7: (a) Residual strength in concrete cubes following removal of 28 mm diameter core for microstructural analysis. (b) Mass loss in specimen following removal of cube from mac^{2T} apparatus

4.4.2. Residual compressive strength

The results of residual compressive strength tests on the cored cubes are shown in Figure 4.7 (a). These results indicate that both H250 and L06H250 (LITS affected) specimens exhibit a residual reduction in strength of approximately 21 % and 14 % respectively. A clear reduction in strength is evident in H250 specimens in comparison with the L06H250 (LITS affected) specimens. Despite the unconventional nature of these tests, the results for all conditioning regimes appear to have a high degree of repeatability.

4.5. DISCUSSION

The data obtained from the strain profile of specimens conditioned under the H250 and L06H250 (LITS affected) regimes indicates that LITS development commences immediately on first heating under load. LITS development in this temperature range has been reported by many authors^{16,7,6,26} in concrete heated under uniaxial stress. However, the results presented here are in direct contradiction to the research of Petkovski and Crouch¹⁶ who reported the suppression of LITS in specimens loaded in hydrostatic compression at 0.22 and 0.44 f_{cu} at temperatures up to 100 °C. The hypothesis presented by these authors that the absence of LITS under hydrostatic compression at temperatures of less than 100 °C may be explained by the closure of microcracks through volumetric compaction which reduces permeability and therefore restricts moisture movement would appear to be invalidated. An increase in hydrostatic compression above the levels attained in Petkovski and Crouch's study could be expected to enhance this effect. Instead material behaviour appears to be more similar to that described by Khoury *et al.*⁶ who found that at 0.5 f_{cu} LITS appeared to develop as an increasing function of stress.

Care should be exercised in making direct comparisons between the work presented in this thesis and that of Petkovski and Crouch¹⁶. Whilst specimens in both investigations were taken from the same batch, uniaxial compression testing of unconditioned specimens for this work indicated an increase in strength of approximately 20 MPa over the 70 day strength in the interim period of approximately five years between experiments. Whilst unusual, this may be as a result of an increase in the strength of the material beyond the 70 day period.

In light of this, another explanation for the difference in behaviour in the results presented here to those in the work of Petkovski and Crouch¹⁶ may be maturity. Maturity has been discounted as a factor in LITS development by a number of authors including Khoury *et al.*⁶ and Schneider¹⁹. However, in explaining the difference in material behaviour observed, other than applied load, an enhanced maturity of approximately five years represents the only variable.

Despite the differences highlighted between the LITS data from this investigation and the Petkovski and Crouch research, H250 specimens in both experiments exhibit a good correlation in both strain profile and final recorded values. This correlation continues above 100 °C to the maximum temperature attained in both experiments of 250 °C.

Both the results of this study and those of Petkovski and Crouch¹⁶ indicate an increase in the rate of LITS development at approximately 120 °C. This change is more marked in the work of Petkovski and Crouch and this is possibly due to the complete suppression of LITS below this value. The final value for LITS in this study is approximately 250% greater than that for specimens conditioned at 0.44 f_{cu} in the work of Petkovski and Crouch. Once again this finding provides support for the hypothesis of Khoury *et al.*⁶ where LITS develops as an increasing function of applied load above 0.5 f_{cu} . These observations coupled with the behaviour of the material below 100 °C are in direct contrast to the work of Anderberg and Thelandersson² who found a mostly linear relationship between LITS and applied load in uniaxially loaded specimens.

During the steady state phase, no additional development of LITS is recorded in this experiment. In this respect, the results are in line with the work of Petkovski and Crouch¹⁶ for specimens conditioned at a similar rate of heating. Hence, the results do not dispute the equilibrium heating rate theory proposed by these authors.

The steady-state results of all the conditioned specimens are not dissimilar with those presented by Khoury²⁶ for a Basalt type concrete under a uniaxial compressive load of 0.2 f_{cu} at 300 °C in the first day following the cessation of heating at a rate of 1 °C/min. However, for specimens that are only heated the results presented here show a significantly higher magnitude of strain development during this period compared with equivalent specimens heated at 1 °C/min.

A difference in magnitude between the results of the Khoury²⁶ experiments and those presented here can be explained by a difference in the composition of the materials under test. However a difference between the conditioning regimes must have some other explanation. Khoury²⁶ explains the difference between the strains measured in each test immediately following the cessation of heating to be as a result of the different starting points in terms of creep action. Due to the high heating rate, the author explains that LITS may continue beyond the cessation of heating. In the tests presented here, the slow heating rate employed is shown to prevent LITS development beyond the transient temperature stage. Also, in the tests presented here, the contribution of basic creep during the steady state temperature stage is likely to be reduced because the load was in place for around 20 hours before these data were recorded. The strain measured during the steady-state period is therefore likely to have been dominated by drying shrinkage. When the steady state results for the tests carried out by Khoury²⁶ are considered between one day following the cessation of heating and five days following the cessation of heating the differences observed between specimens heated with and without load become almost negligible.

In line with previous research^{8,10,11}, no evidence is detected here to suggest that any of the LITS components experience recovery on cooling. Towards the end of the cooling phase all specimens appear to exhibit expansive strains. This effect was also observed by Khoury⁵⁴ in cylindrical specimens heated to temperatures above 400 °C. This author attributed the effect in part to the rehydration of lime (CaO) which is formed from the dissociation of Ca(OH)₂ beyond 400 °C. This hypothesis, whilst not discredited, is not likely to be the principal contributor in the experimental results presented here. In addition, Khoury proposed that moisture absorption from the surrounding atmosphere may also contribute. Partially sealed boundary conditions may restrict such mechanisms here.

With respect to the residual strength of specimens a similar effect to that reported by Khoury *et al.*¹⁷ is found here. The aforementioned author reported that for specimens heated to 600 °C, residual strength was increased by as much as 15 % in LITS affected specimens over those which experienced only heat. Schneider¹⁹ also found that “stressed strength was higher than unstressed strength” in specimens tested at ambient temperature. Further support for the supposition that LITS is beneficial to the residual strength of cementitious materials can be obtained by considering the results of Černý *et al.*²⁹. These authors reported that the moisture diffusivity of specimens heated without mechanical load was found to be twice as great as that of specimens heated under load. An increase in diffusivity is likely to be concurrent with enhanced cracking which would weaken the material structure.

In comparison, under exactly the same conditions, Petkovski¹ found that hydrostatically loaded specimens experienced a decrease in the hot strength of the material of around 10 % in uniaxial compression over specimens heated without load. This degradation of mechanical strength was

explained as a detrimental effect of a LITS specific damage mechanism¹. Whilst this may appear unusual, the difference in these two results may not be mutually exclusive. The presence of a confining load during cooling may have some effect which whilst not visible in the strain profile reduces the damage associated with the differential thermal properties of the concrete constituents.

4.6. CONCLUSIONS

Specimens conditioned under the L06H250 and H250 conditioning regimes showed a high degree of repeatability which will lend support to any findings on microstructural behaviour presented in Chapters 5, 6 and 7. LITS development is shown to occur from first heating under the conditions analysed here. This differs from the results presented by other authors on the same specimens under lower levels of mechanical loading. No LITS development or recovery is shown to occur on cooling.

5. Multi-scale X-ray Computed Tomography

5.1. INTRODUCTION

In Part 1 of this thesis it has been identified that LITS has a significant effect on macroscopic properties such as loading stiffness, strength and durability of cementitious materials. A detailed review of the microstructural characteristics of these materials has also shown that the same macrostructural properties are likely to be heavily influenced by the makeup of the material pore structure. Further, one mechanism that has been advanced to explain the origins of LITS depend directly on damage caused by microdiffusion between the gel pore and macropore structure. In light of this, the microstructural investigation into LITS development mechanisms presented in this thesis will focus on elucidating changes in features pertaining to material pore structure. In this Chapter, a brief review of the foremost techniques used to study concrete pore structure is undertaken and conclusions are drawn on an appropriate research methodology. The results of an investigation into the pore structure of LITS affected materials using X-ray computed tomography is then presented.

5.2. EVALUATION OF EXPERIMENTAL TECHNIQUES FOR PORE STRUCTURE ANALYSIS

A broad range of experimental investigations may be employed to study the pore structure of cementitious materials. Unfortunately, no single technique can give a complete suite of information on concrete pore structure. Due to the type and quality of information provided by each technique a balance must be sought between competing factors such as: observed feature size vs specimen size, the quality of information vs degree of specimen preparation and destructive vs non-destructive testing. To overcome these difficulties this research seeks to utilise a number of different techniques which may be used to corroborate data and substantiate experimental findings. A brief review of the principal techniques for pore structure analysis of cement based materials is now presented.

5.2.1. X-ray computed tomography

Micro-focus X-ray computed tomography (CT) is a 3D microstructural imaging technique which was developed from 2D radiography. X-ray CT analysis yields a 3D image composed of voxels (3D pixels). Via the exponential attenuation law, the intensity of each voxel is determined from the composition of the material which it represents. Using a variety of image segmentation algorithms the

grey-scale images can therefore be binarised to highlight the material phase of interest. Quantification algorithms can then be used to calculate the 3D geometric properties of the selected material.

X-ray CT is a powerful technique for microstructural analysis which can yield a far greater range of information than that from a 2D microscopy technique. Its application in the field of concrete technology, whilst not yet having reached the mainstream due to the limited availability of suitable analytical equipment, is no longer novel. Studies incorporating X-ray CT analysis have been performed to determine the porosity and pore network properties of hydrated OPC mortars^{55,56,57,58,59} and alkali activated binders^{55, 60}. X-ray CT has also been used to characterise cement hydration⁶¹ and microstructural degradation in cementitious materials due to mechanisms including freeze thaw action⁶², leaching⁶³, sulphate attack⁶⁴ and mechanical load^{65,66,67,68,69,70}.

The latter studies which investigate the development of cementitious microstructure over time highlight a particular strength of X-ray CT; which is to obtain data in 4D. Since the technique is non-destructive, multiple scans can be taken of the same specimen before and after or even during conditioning – this opportunity is explored in Part III of this thesis. In this section, all microstructural investigations will be carried out using specimens which have been conditioned *ex-situ* as detailed in Chapter 4.

Despite the promising nature of this technique there are however some limitations which must be considered:

1. Phase quantification is sensitive to the segmentation technique chosen to binarise the 3D grey-scale image. The segmentation technique is equally dependent on the quality of the raw data obtained in the experiment. Care must be taken to rigorously employ repeatable procedures in data acquisition, segmentation and quantification in order to obtain quantitative results.
2. Whilst extremely high image resolutions can be obtained with voxel sizes of approximately 30 nm⁷¹, the field of view in such experiments is extremely limited. When studying microstructural processes that are likely to have diffuse effect, a representative elementary volume must be considered to ensure the statistical validity of observations. A trade-off is therefore sought between microstructural detail and data quantity.
3. Whilst X-ray CT is a non-destructive technique, in practice the size of the specimen must fit within the field of view of the experimental equipment in order to obtain the optimum image properties for segmentation. Region of interest scans can be obtained where the specimen exceeds the field of view but these are challenging to undertake and often suffer from artefacts introduced by irregular X-ray transmission. In consequence for high resolution scans, physical specimen segmentation must be carried out which is likely to lead to microstructural damage.

5.2.2. Scanning electron microscopy

In conjunction with a backscattered electron detector, scanning electron microscopy (SEM) can provide 2D greyscale images of the material phase composition at the specimen surface. Whilst at a high magnification, the field of view for each image is well below that which would represent a representative elementary area and multiple images have to be obtained at different locations across the specimen in order to construct a statistically significant data field. Unlike optical microscopy, pore segmentation of backscattered electron SEM images is aided by the high contrast which can be obtained between pores and solid material microstructure. This technique does however have some limitations in the study of cementitious materials:

1. Significant specimen preparation is required for backscattered electron imaging which is known to have a detrimental effect on the material microstructure.
2. The images obtained from SEM analysis only allow the observation of a 2D plane through a 3D material microstructure. In accordance with Scrivener³⁰, information pertaining to the 3D properties of the material must be interpreted carefully and data relating to pore connectivity cannot be determined.

5.2.3. Mercury intrusion porosimetry

Mercury intrusion porosimetry (MIP) is an experimental technique which can be used to determine the properties of pores across a wide range of length scales from an equivalent diameter of > 1 mm to $0.001 \mu\text{m}$ depending upon the maximum pressure that can be applied with the chosen equipment. This ability has led to wide usage of MIP for the microstructural analysis of cement based materials. MIP has previously been used to study changes in cementitious microstructures due to hydration^{72,73,74,75,76}, compressive loading^{29,77,78,79} and thermal cycling^{80,81,82,83,84,29,85}.

However, due to the method of pore size measurement where intrusion pressure is related to intruded pore diameter, criticism has been raised over the interpretation of MIP results and their validity in porous solids such as cement and concrete. Diamond⁸⁶ reported that due to the specific features of the pore structure in cement and concrete, mercury intrusion may be restricted until a certain pressure corresponding with a threshold pore diameter is reached. Following the achievement of this pressure, other pores in the bulk structure of the material are filled indiscriminately without size differentiation.

5.2.4. Other techniques

Small angle X-ray and neutron scattering (SAXS and SANS) have seen limited use to study C-S-H gel structure^{87,88}. These techniques involve the study of the width and intensity of individual scatter paths and the scattered profile as a whole to determine the geometrical form and volume fraction of features of the specimen within an incident X-ray/neutron beam. SAXS and SANS are used for the

quantification of microstructural features in the 1 nm to 100 nm range. However, access to suitable experimental equipment is often limited to synchrotron type facilities.

Nitrogen adsorption is a more widely adopted technique which is often used alongside MIP to characterise pore structure in cement and other porous materials within the 0.3 nm to 300 nm range⁸⁹. The technique involves filling the pores of the specimen with nitrogen in a series of controlled inputs. Specimens must be dried in a similar manner to that during MIP testing as the presence of free water within the pore structure will impede measurements. Weak molecular attractive forces will cause a certain quantity of the gas to adsorb onto the surfaces of the pores. By measuring changes in the pressure of the nitrogen due to this adsorption, the volume of adsorbed gas can be found. By considering the cross section of one adsorbed gas molecule, the surface area of the pore structure and its volume can be calculated. According to Garci Juenger and Jennings⁹⁰, with the application of a rigorous experimental procedure, the technique can provide reliable information on pore structure in cementitious materials.

5.2.5. Conclusions


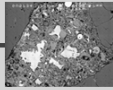
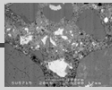
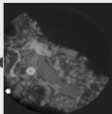
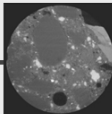
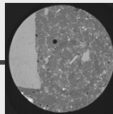
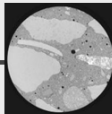
Size range (Diameter)	1 nm	10 nm	100 nm	1 μm	10 μm	100 μm	>1 mm
Name of pores according to concrete science Terminology*	Gel pores		Capillary pores			Air voids	
MIP	←						
SEM			←				
X-ray CT							

Figure 5.1: Pore sizes and techniques for microstructural analysis

As figure 5.1 shows, the aforementioned techniques allow the study of pore structure across the complete range of length-scales encountered in an OPC based cementitious material. MIP is the only technique which can provide a full analysis of open porosity in a specimen from one experiment. The time duration for each test and the requisite analysis is also relatively short compared to other techniques. The drawback to this technique is that the pore size distribution data may misrepresent certain pore size classes meaning results must be interpreted carefully. X-ray CT and SEM offer the opportunity to study additional properties of the pore structure beyond volume fraction and pore size

distribution. Information on the connectivity of pores and the relationship between porosity and other structures in the cement paste may be analysed using these techniques. Here the drawbacks are of statistical validation and feature resolution. A combination of the three techniques will allow for adequate comparison and validation of experimental data. At this stage, the limited access to SAXS and SANS equipment and the extended time period for data analysis has discounted this technique from employment in this thesis. Nitrogen adsorption would offer the possibility of the validation of MIP results at the nanometre length-scale and will be put forward as an area for future study the LITS microstructure investigation.

5.3. X-RAY CT IMAGING PRINCIPALS

In this Chapter the four experiments which are presented were carried out on laboratory based X-ray CT equipment. Consequently this introduction covers only the details of polychromatic cone beam instruments. X-ray CT allows the internal structure of an object to be imaged in three-dimensions through the computerised reconstruction of a set of 2D radiographs taken at different viewing angles on a single axis of rotation. The radiograph image is detected on a Charge Coupled Device (CCD) positioned in a plane normal to the x-ray beam (Figure 5.2a). Each pixel of the radiograph shows the total attenuation of x-rays by features within the corresponding area of the specimen.

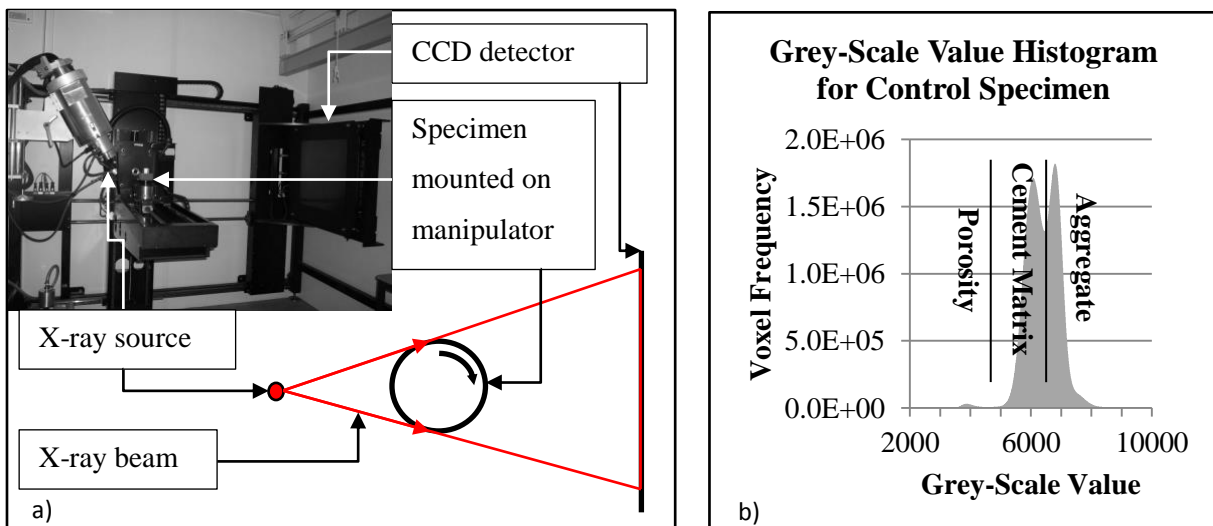


Figure 5.2: a) Nikon Custom Bay at the HMXIF with a schematic plan of the XCT equipment Grey-scale value histogram showing tri-modal distribution of 16-bit XCT data and approximate phase distribution for a control specimen

The length-scale over which pore characterisation may be carried out using X-ray CT is ultimately limited by image resolution. The image resolution is often recorded in terms of the dimensions of a single voxel making up the 3D image. In practice however, the minimum size of a feature detectable in a 3D dataset is equal to two or more voxels because of the necessity to differentiate true features

from artifacts/image noise. This correction is known as the feature resolution and represents the smallest feature/pore detectable in any particular dataset.

Artifacts and noise in X-ray CT images arise from a number of different sources. In some cases these sources can be controlled and designed out of the experiment via careful planning but in others they are inherent to the equipment or type of experiment. A short synopsis of some sources of artifacts/noise which can be controlled is now presented. A detailed description of mitigating measures is also presented later in the results/discussion:

- **Beam hardening:** Due to the variation in thickness of a specimen, X-ray absorption will vary across each 2D radiograph in both monochromatic and polychromatic beams. In laboratory based CT equipment where the X-ray beam originates from a point source and no monochromator is employed to filter the beam this effect is particularly apparent. X-rays are generated with a range of energies up to a limit determined by the accelerating voltage applied across the electron gun. On interaction with a specimen the softer X-rays (those with lower energies) will be attenuated to a greater extent than those with a higher energy. The variation results in a dishing effect in reconstructed images where material at the extremities of a specimen appears brighter than that at the centre of a specimen which can prove problematic when segmenting the image.
- **Spot size and penumbral blurring:** With respect to laboratory based cone beam X-ray CT equipment the spot size refers to the size of the x-ray source. It is recorded as the diameter of the interaction area between accelerated electrons and the source target material. The size of the spot is governed by the design of the experimental equipment and by the accelerating voltage applied on the electron gun where a higher voltage leads to a larger spot. A larger spot size will lead to an increase in penumbral blurring where X-rays counted on the CCD detector may have originated from more than one location⁹¹. This effect is particularly important at high magnifications.
- **Reconstruction:** In order to reconstruct the 2D images into a 3D dataset it is first necessary to find the centre of rotation of the object within the field of view. This centre of rotation provides a datum upon which all images can be benchmarked. Depending on the quality of the dataset, the centre of rotation (COR) may be found either computationally using an automated algorithm or manually using visual referencing. The accuracy of COR determination will have a significant effect on the quality of reconstructed data.

5.4. X-RAY CT METHODOLOGY

In this investigation, X-ray CT imaging was carried out at the Manchester X-ray Imaging Facility (MXIF), University of Manchester. This facility is home to a range of laboratory based X-ray CT

equipment which can provide imaging across a broad spatial scale from 50 nm. To capture the features of the concrete pore structure over the complete range of length-scales it was decided that a multi-resolution investigation would be undertaken. This approach employs three individual X-ray CT devices; Nikon 225 kV Custom Bay, Xradia microXCT and Xradia nanoXCT each with increasing capabilities with respect to feature resolution achievable. The principal limitation to this technique is that for each increase in feature resolution, the field of view of the X-ray detector decreases meaning that the volume of material observed is reduced. Additionally, in order to achieve an optimum frequency of X-rays incident on the detector, the thickness of the specimen must be reduced to suit the X-ray power levels achievable with each apparatus.

It is possible to carry out scanning using a methodology known as region of interest scanning. In this technique the specimen size may be larger than the detector size and thus the centre of rotation must be adjusted based upon observable features within the material. However, such scans are challenging to reconstruct because the interior of the material often lacks distinct features because of the poor X-ray penetration of thick specimens.

To overcome this challenge, region of interest scans were not employed here. All specimens were physically segmented before being analysed at higher resolution. The precise methodology is as follows:

5.4.1. 15 micron imaging

Experimental Setup

Specimens were analysed using the Nikon 225/320 kV Custom Bay at the MXIF, University of Manchester (Figure 5.2a). The 225 kV static source with a tungsten target was used in conjunction with a 1.5 mm thick copper filter in order to optimise the emitted x-ray beam energy spectrum. A power level of 160 kV and 200 μ A was selected to achieve good radiograph contrast. Cylindrical specimens with 28 mm diameter and 100 mm length, taken from the cored conditioned cubes (Chapter 4) were mounted on the precision 5-axis manipulator arm and positioned within the CCD detector field of view. Two scans were then taken, one above and one below the specimen centre line. Once a scan had been commenced, the manipulator arm allowed radiographs to be taken at accurate angular steps of 0.115 degrees which equated to 3142 radiographs over a 360° rotation. The source to specimen distance was 73.5 mm, the source to detector distance was 1007 mm and the acquisition time per radiograph was 1000 ms.

After data acquisition, all 3142 projections were reconstructed using Metris CT pro software with corrections for the centre of rotation, beam hardening and noise reduction. The reconstructed data in the form of 3D pixels or “voxels” was then down sampled from 32 bit to 16 bit grey-scale in order to reduce file sizes for image analysis.

Image Analysis

Image analysis of the 15 μm data was performed using the Aviso Fire software package. A region of interest (ROI) was selected from each scan with dimensions 1700 x 1200 x 1200 voxels. This corresponds to a volume of 25.2 mm x 18 mm x 18 mm. The ROI was chosen from the centre of the cylindrical specimen in order to exclude voxels in the background regions and minimise effects from the cone shaped x-ray beam.

Pore segmentation was carried out using the classic minima thresholding technique. Segmented voxels were then analysed using the Aviso XQuant Quantification features in Aviso Fire to determine their connectivity. In this procedure, the six faces of each voxel in the image are evaluated to ascertain whether a voxel of the same segmented phase is connected¹⁰. Voxels of the same phase which are connected using this criterion are then grouped into clusters or pores in our study. Data is presented with respect to the equivalent pore diameter which is calculated by assuming that all pores are spherical in shape.

Finally, the Nyquist-Shannon sampling theorem¹¹ was used to determine the minimum size of features that could be resolved based on the image resolution of 14.6 μm . This theorem proves that a digital image must have more than two pixels per resolvable element in order to ensure that all features are sampled sufficiently to detect their presence. In this case, three voxels was chosen as the feature resolution limit meaning the smallest detectable porosity in this study has a diameter of 31.5 μm .

Statistical Qualification

Various methods are proposed in the literature to facilitate the segmentation of data into distinct phases^{8,9}. Here, as a result of the distinct tri-modal grey-scale distribution shown in Figure 5.2b, it was possible to use classic minima thresholding to differentiate porosity from cementitious and aggregate phases within the concrete. A sensitivity analysis of the grey-scale value (GSV) distribution was carried out at three increments of 10, 25 and 100 both above and below the GSV corresponding with the minima of one ROI. An error of less than two percent could be achieved by selecting a GSV within ± 25 points of the actual minima. This accuracy was easily obtainable through sorting of the GSV data.

5.4.2. 5 micron imaging

Experimental Setup

Following the completion of the 15 micron imaging, specimens were physically segmented using a circular masonry saw fitted with a diamond blade into ten disks of approximately 8 mm in thickness. In order to reduce dust and prevent the blade from binding in the material water was used during cutting – specimens were surface dried using paper towels following the completion of the procedure.

For the 5 micron imaging and below, due to restrictions on equipment access, only one specimen per conditioning regime could be analysed using X-ray CT. Using the 15 micron datasets, one disk was selected from each of the specimen cores. A volume from within this disk was identified based upon the presence of bulk cement paste and a further 5 mm diameter core was taken using a core drill with a diamond tip. Water was once again employed as a coolant/lubricant and to prevent dust. The size of the core was chosen in order to achieve the maximum resolution available on the Nikon 225 kV Custom Bay.

In this case no filter was employed on the 225 kV static source during imaging. A power level of 90 kV and 150 μ A was selected to achieve good radiograph contrast. The cylindrical specimens were mounted on the precision 5-axis manipulator arm and positioned within the CCD detector field of view. A single scan of each specimen was then taken. Once a scan had been commenced, the manipulator arm allowed radiographs to be taken at accurate angular steps of 0.129 degrees which equated to 2801 radiographs over a 360° rotation. The source to specimen distance was 25.45 mm, the source to detector distance was 1007 mm and the acquisition time per radiograph was 1000 ms.

After data acquisition, all 2801 projections were reconstructed using Metris CT pro software with corrections for the centre of rotation, beam hardening and noise reduction. The reconstructed data was then down sampled from 32 bit to 16 bit grey-scale in order to reduce file sizes for image analysis.

Image Analysis

Image analysis was performed using the same method as that for the 15 μ m X-ray CT data using the Aviso Fire software package. An ROI was selected from each scan with dimensions 400 x 400 x 800 voxels. This corresponds to a volume of 2 mm x 2 mm x 4 mm. The ROI was chosen from the centre of the cylindrical specimen in order to exclude voxels in the background regions and minimise effects from the cone shaped x-ray beam. Minima segmentation was used to differentiate phases for quantification.

5.4.3. 0.6 micron imaging

Experimental Setup

Further physical segmentation was carried out on the concrete specimens to enable 0.6 μ m imaging to be carried out. Using the results of the 5 μ m analysis, a suitable region of interest was identified in the cement paste phase from each of the three specimens. A scalpel blade was used to separate the required material from the existing core. The chosen fragment was then mounted on a thin wooden stick using epoxy resin. The scalpel blade was again used along with a magnifying glass to shape the fragment into a conical form with a broadly equal dimensional aspect ratio in the x-y rotational plane.

Finally, a single gold sphere with a diameter of 10 μm was then mounted on the tip of the finished fragment in order to facilitate the search for the centre of rotation during imaging setup.

The Xradia MicroXCT 400 system based at the MXIF, University of Manchester was employed to obtain 0.6 μm images. A power level of 50 kV and 200 μA was selected to achieve good radiograph contrast. A low energy X-ray filter (grade 1) was also employed in order to achieve an average transmission of 30 % through the thickest part of the specimen. Radiographs were captured using the 20 x objective lens giving a field of view of 2048 x 2048 pixels and an image resolution of 0.6 μm . For each specimen, 2201 images were obtained at equal increments through a rotation of 180°. Each image represented the X-ray accumulation over a 30 second exposure time. The source to specimen distance was 45 mm and the source to detector distance was 51 mm.

After data acquisition, the 2201 projections were reconstructed using Xradia XMReconstructor software with corrections for the centre of rotation, beam hardening and noise reduction. The reconstructed data in the form of 3D pixels or “voxels” was then down sampled from 32 bit to 16 bit grey-scale in order to reduce file sizes for image analysis.

5.4.4. 0.15 micron imaging

Experimental Setup

The Xradia NanoXCT system based at the MXIF, University of Manchester was employed to obtain 0.15 μm images from a specimen of no more than 65 μm in thickness. An accelerating voltage of 8 kV was selected to achieve good radiograph contrast. Radiographs were captured with a field of view of 65 x 65 microns and an image resolution of 0.15 μm . For each specimen, 1001 images were obtained at equal increments through a rotation of 180°. Each image represented the X-ray accumulation over a 180 second exposure time.

5.5. RESULTS

5.5.1. 15 micron imaging

A typical reconstructed data set from the ROI of a control specimen is visualised using 3 orthoslices in Figure 5.3a along with the segmented pore structure in Figure 5.3b. The orthoslices show the clear presence of large aggregate particles, cementitious matrix and porosity. Both igneous and sedimentary rock forms are present which is indicative of the Whinstone aggregate source used for material in this experiment.

When viewed at this resolution (14.6 μm), the resolved pores do not form a long range network and can be classified as air voids. No interaction of the porous structure with aggregate phases was

observed. Again, this was also expected as any increase in porosity within the Interfacial Transition Zone (ITZ) between the cement paste and aggregate particles is known to occur within 50 μm of the aggregate surface¹² which is only just above the feature resolution of data presented here.

It is also clear from Figure 5.3b that a small number of very large pores exist in the control specimen considered, with typical diameters in excess of 2000 μm . Pores of this magnitude are observed to a varying degree in all specimens and their presence is thought to be a result of inherent variability in the material rather than a result of the conditioning regimes. Their size with respect to the ROI is sufficient so as to raise doubts over whether they may be considered quantitatively and therefore equivalent pore diameter data is only presented for pores below 500 μm .

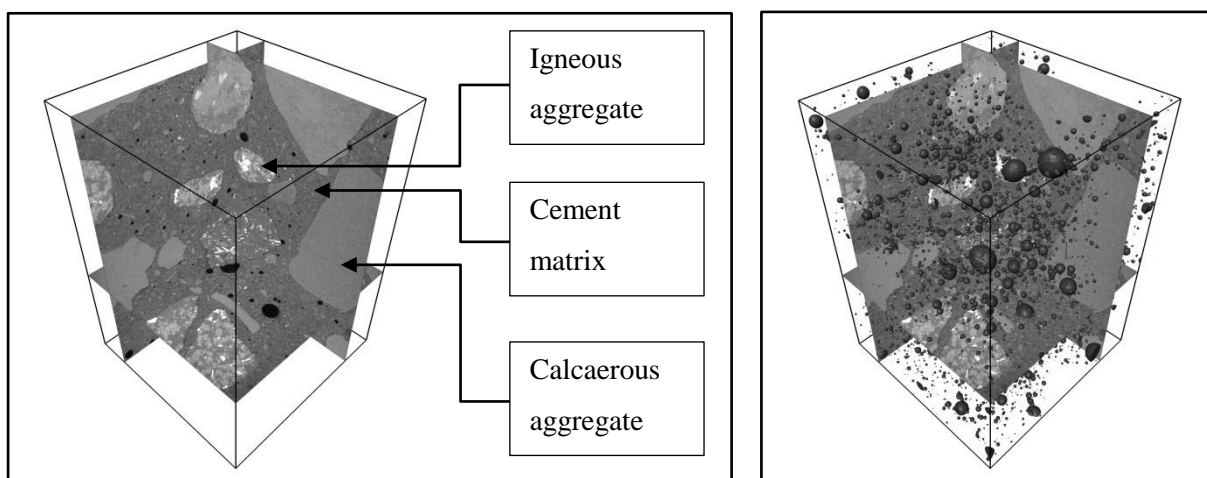


Figure 5.3: a) ROI showing orthoslices of the reconstructed data from a control specimen and b) Segmented porosity within the same volume

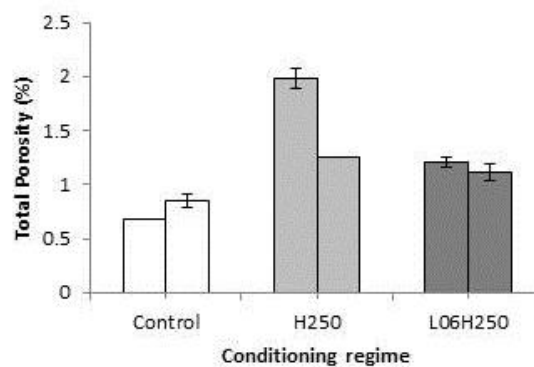


Figure 5.4: Porous volume results for the three conditioning regimes.

Figure 5.4 shows the total air void porosity for each conditioning regime of voids larger than 31.5 μm . The results from the two conditioned specimens in each conditioning regime are presented with standard error bars indicating statistical variation for the two scans of each specimen. A significant

increase in volume is visible for specimens both specimens conditioned at 250 °C and those in the L06H250 (LITS affected) regime over unconditioned specimens.

A wide variation in porosity is observed between the two specimens in the H250 regime. Unfortunately due to specimen damage on coring the second specimen in this regime could only be scanned once. It is therefore not possible to determine with a high degree of confidence if there is a significant difference between the H250 and L06H250 conditioning regimes in terms of total porosity.

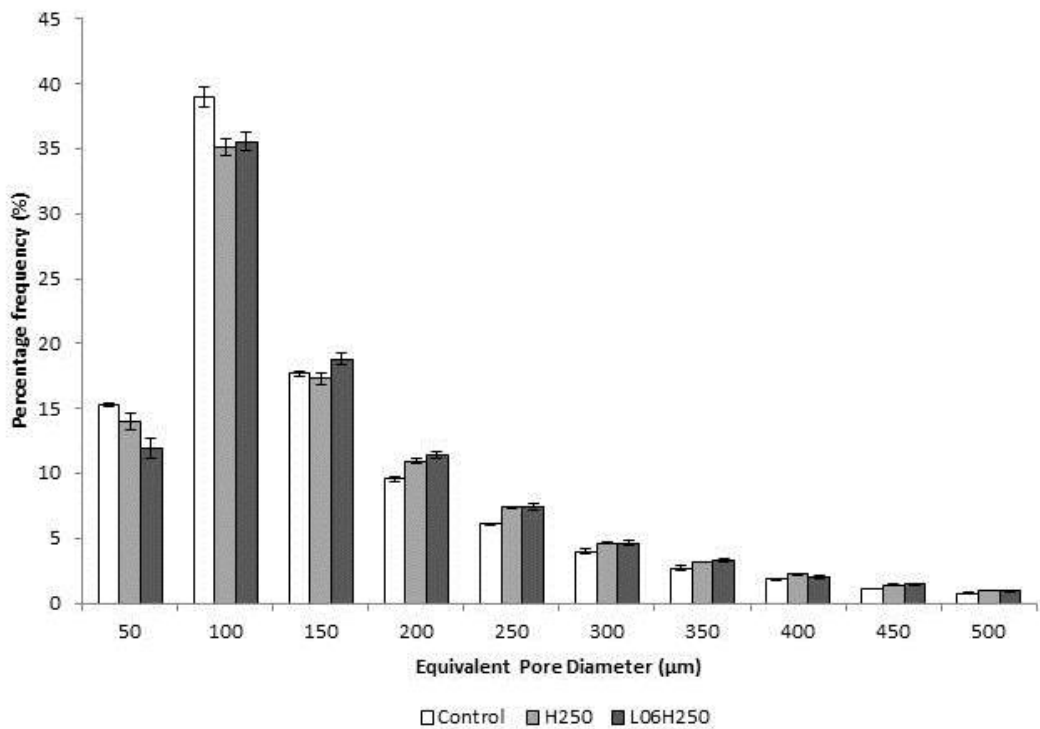


Figure 5.5: Equivalent pore diameter distribution results for three conditioning regimes; H250, L06H250 and the unconditioned control. Error bars show standard error calculated for 4 X-ray CT scans from 2 cubes repeated using the same conditions.

Figure 5.5 shows the equivalent diameter distribution of pores for each of the conditioning regimes. It can clearly be identified from Figure 5.5 that thermal treatment (sample H250 and L06H250) results in a decrease in the measured frequency of pores below the 100 µm diameter threshold and in parallel an increase in pores with a diameter greater than 200 µm compared to the control specimens. The presence of mechanical load for specimens which also experience thermal treatment produces a further decrease in pores below 50 µm over those which have experienced thermal treatment only.

5.5.2. 5 micron imaging

The reconstructed unconditioned control dataset is illustrated in Figure 5.6. The three orthogonal orthoslices shown in this dataset indicate that porosity in the form of air voids and the largest capillary pores are present despite the continued absence of a long range connected pore network at a feature resolution of 7.82 μm . Also present are fine siliceous aggregate particles which display similar X-ray absorption properties to the hydrated cement. This property makes the aggregate challenging to segment and consequently no attempt was made to do this. Finally, the brightest features observable in these images are the largest anhydrous cement grains and iron particles from the PFA SCM. Figure 5.6 also shows the 3D segmented porosity which was characterised in this work. As for the 15 μm image resolution data, pores which lie on the boundary of the chosen ROI are included in the total volume results but not in the pore size distribution data.

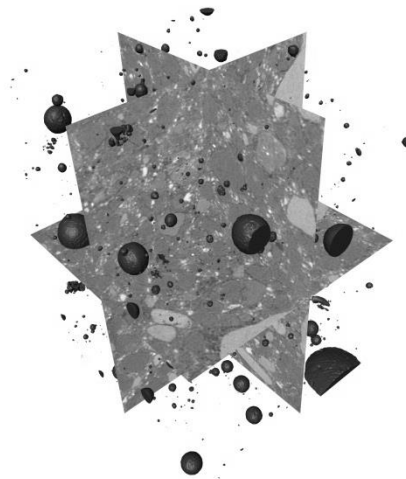


Figure 5.6: ROI showing orthoslices of the reconstructed data from an unconditioned control specimen and segmented porosity within the same volume

The result of an analysis of the total volume of porosity within one specimen from each of the three conditioning regimes is shown in Figure 5.7. In a similar manner to the 15 μm image resolution data both the H250 and L06H250 specimens experience an increase in porosity with respect to the control specimen. In this case however, the increase in pores for the L06H250 conditioning regime is approximately fifty percent greater than that observed in the H250 specimen within this pore size range. Due to limited beam access, only one specimen from each conditioning regime could be analysed and therefore no statistical verification of these results can be undertaken.

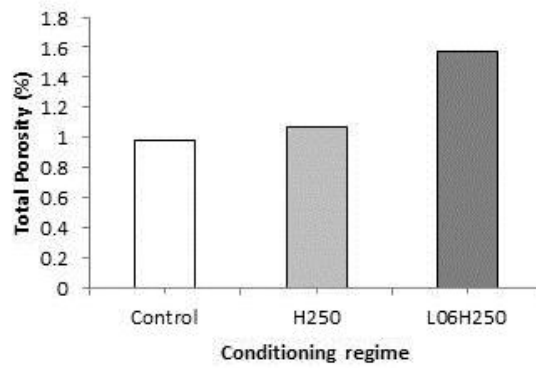


Figure 5.7: Porous volume results from 5 μm image resolution data for the three conditioning regimes.

The distribution of pore size equivalent diameters for the 5 μm image resolution data is shown in Figure 5.8. These results indicate that above 40 μm in equivalent diameter, the frequency of pores in both the H250 and L06H250 regimes is similarly increased. In the 30 μm range, the frequency of pores from the H250 conditioning regime is higher than those of both the control and L06H250 specimens. The observed increase in total porosity would appear to stem from an increase in the frequency of pores with the 20 μm equivalent size distribution category. Pores within the H250 specimen at this size distribution are suppressed to a small extent with respect to the unconditioned control.

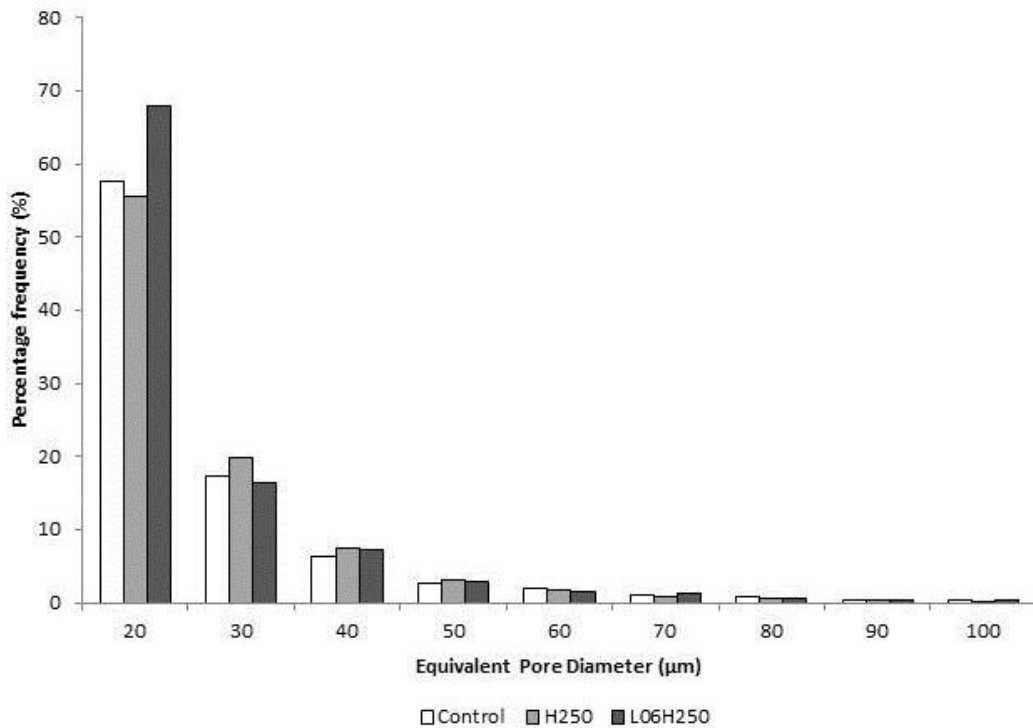


Figure 5.8: Pore size distribution results from the 5 μm image resolution data.

5.5.3. 0.6 micron imaging

A single 2D orthoslice image from the unconditioned control dataset is shown in Figure 5.9. In a similar manner to the 5 μm image resolution data the image contains fine siliceous aggregate particles which are computationally indistinguishable from hydrated cementitious material due to the similar absorption coefficient of each material and because the absorption contrast of the dataset could not be optimised due to specimen geometry and beamline conditions. Porosity is again present in the form of air voids and larger capillary pores. Once again no connected pore network could be observed at this resolution. Anhydrous cement grains and PFA particles can also be observed.

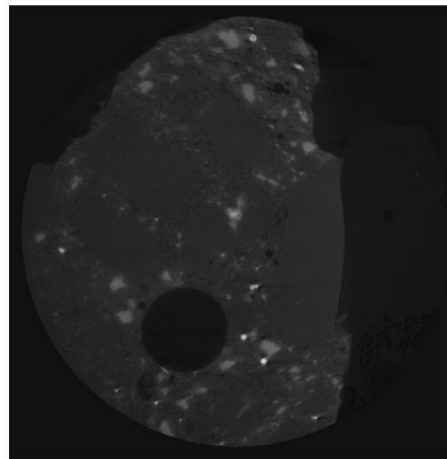


Figure 5.9: Median filtered orthoslice from an unconditioned control specimen imaged at a resolution of 0.6 μm

The total porosity of the individual conditioning regimes as obtained from the 0.6 μm imaging is shown in Figure 5.10. The porous volume fraction of the 0.6 μm images is the lowest of all datasets and in all cases is below 0.5 %. The control and L06H250 specimens exhibit no significant difference from one another with a porosity of $\sim 0.35\%$. The H250 specimen appears to indicate an increase in porosity of approximately 40 % with respect to the other conditioning regimes.

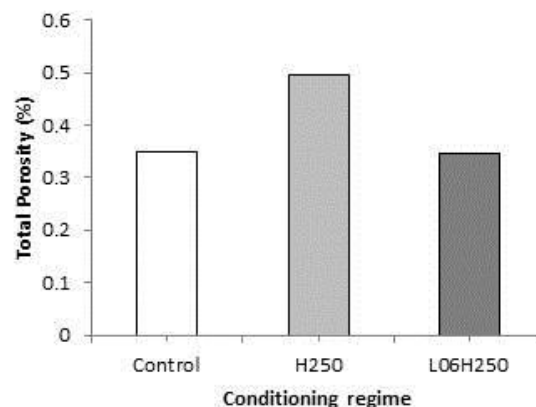


Figure 5.10: Total porosity from 0.6 μm datasets

Figure 5.11 shows the pore size distribution results from the 0.6 μm image resolution results. Once again these results neglect to include pores which are connected to the boundary voxels of the ROI. No significant trends can be observed in each dataset with respect to the others. However, in general, the L06H250 conditioning regime exhibits an increase in pore frequency at the 1 μm interval and above 9 μm .

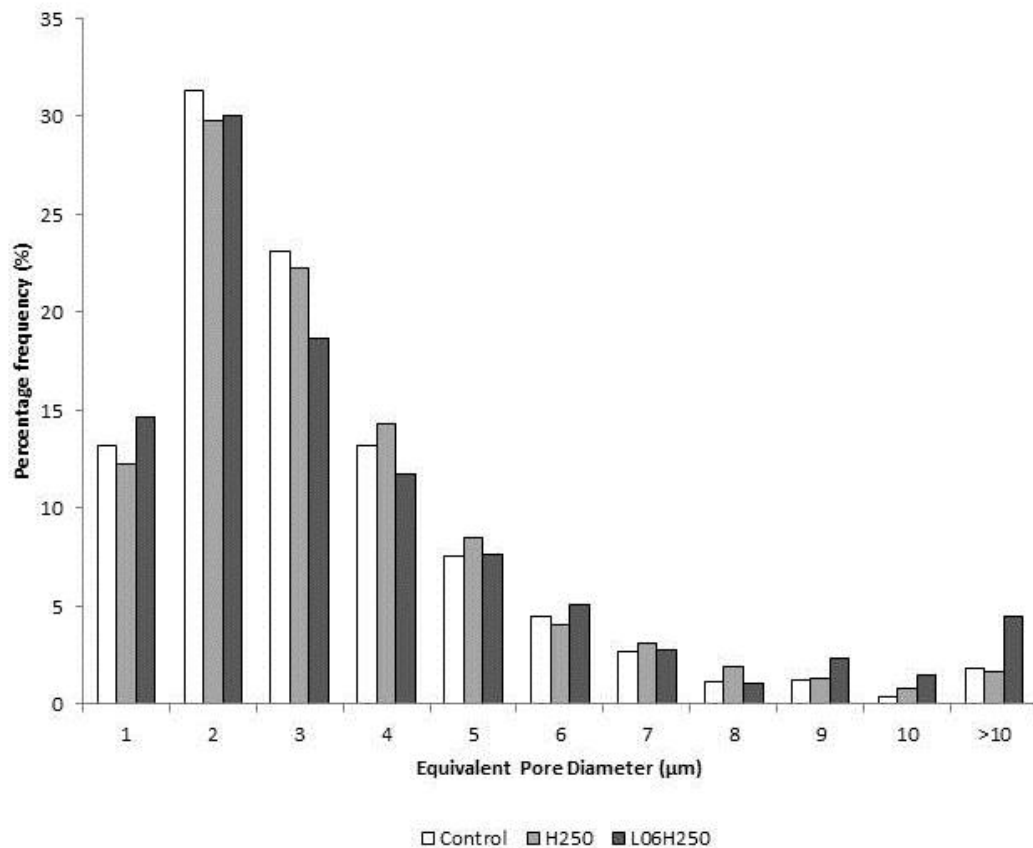


Figure 5.11: Pore size distribution results from the 0.6 μm image resolution data.

5.5.4. 0.15 micron imaging

A single experiment was carried out to characterise the pore structure of an unconditioned control specimen at 0.15 μm . An orthoslice of the associated dataset is presented in Figure 5.11. This image shows a heterogeneous mixture of hydration products with varying density, a bright PFA particle similar to those observed in investigations at lower resolution and areas which may represent connected capillary porosity.

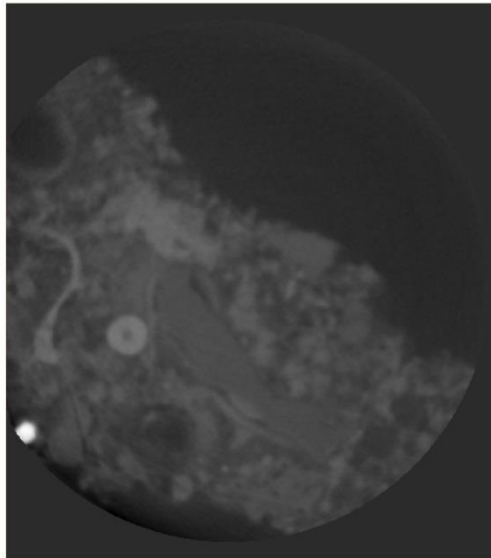


Figure 5.12: Median filtered orthoslice from an unconditioned control specimen imaged at a resolution of 0.15 μm

Attempts were made to segment the dataset using a curve fitting algorithm and visual thresholding which yielded porosities of 46.4 % and 30.8 % respectively. The significant variation in results stems from the low feature contrast which yielded a histogram with few distinguishable features. Whilst the results provide further insight into the structure of the cement paste phase, they would offer no quantitative indication of the behaviour of cement microstructure due to LITS. For this reason, no further experiments were carried out at this resolution.

5.6. DISCUSSION

This chapter has dealt with the analysis of thermo-mechanically loaded concrete using multi length-scale (15, 5 and 0.6 microns) X-ray CT. 15 micron resolution analysis was first carried out on 28 mm diameter cores extracted from pre-conditioned cubes. Two scans were obtained from each of two cores in each conditioning regime allowing a statistical representation of these results. 5 micron X-ray CT analysis was then carried out on a 5 mm diameter core extracted from one of the cores in each conditioning regime. Only one scan could be carried out on each conditioning regime at this and higher resolutions due to access restrictions on X-ray CT equipment. Finally, the 5 mm core was physically segmented using a scalpel to obtain a fragment of material for 0.6 micron resolution analysis. The control specimen was also subjected to 0.15 micron analysis but the data quality was insufficient to justify further scans at this resolution.

Results from the 15 micron analysis indicate that conditioning under both H250 and L06H250 regimes causes permanent changes in both the volume and composition of the air void pore structure in concrete. 5 micron data shows a similar trend in terms of total porosity with both H250 and L06H250 specimens indicating elevated levels of porosity with respect to the control specimen.

However the pore size distribution results from the 5 micron analysis show a different behaviour to those at 15 microns, which does not lend support to the validity of the 5 micron results since no repeat specimens were analysed for any of the conditioning regimes.

For the 5 micron data in the equivalent size distribution categories from 30 to 50 microns the L06H250 specimen experiences an increase in the frequency of pores recorded whereas in the 15 micron data, the frequency of pores in this size range is reduced significantly. This is likely to be as a result of the volume analysed from the 5 micron dataset lying below that required to count as a representative elementary volume. This would also discount the results of the single specimen analysis carried out at the 0.6 micron resolution. Support for the findings of the 15 micron datasets can be found in the favourable comparison of repeat specimens.

Whilst this finding represents a setback for the use of the X-ray CT technique for use in the analysis of capillary porosity in concrete, reliable information on the behaviour of air void porosity is challenging to obtain from other techniques. MIP is likely to underestimate the frequency of air void pores due to the ink bottle effect and SEM analysis only offers information in 2D as discussed in section 5.2.2.

The levels of air void porosity displayed in the control specimens at the 15 micron resolution compare well with the results of Promentilla and Sugiyama⁶² who showed that for a non-air entrained concrete with a mix incorporating 30% binder mass ratio of PFA the void fraction was approximately 1.3 % in 12 micron resolution datasets before the onset of freeze-thaw action.

One feature which is evident in all images but which does not pertain to a LITS mechanism is that the material studied here is exceptionally well hydrated and has a capillary pore structure that does not form a long range connected network until below 0.6 microns. This provides evidence of the good mix design employed in the AGR reactor fleet pressure vessels which display good durability and strength properties.

Pore size distribution changes due to thermal treatment in the 15 micron resolution scans may be a consequence of the internal deposition of calcium hydroxide and/or ettringite¹⁴. Whilst the results for pores below 100 μm in diameter support this, there is an increase in the frequency of thermally loaded pores above 200 μm . However, these results present data as a frequency percentage and thus a decrease in pores in the measured region below 100 μm would be compensated by an increase in pores which are larger in diameter. This is because pores below 100 μm may have been reduced sufficiently in diameter to drop below the feature resolution of these X-ray CT images. Also, for any uniform increase in cement hydration and therefore uniform deposition of hydration products, smaller pores would experience a greater change in diameter with respect to larger pores.

It also appears that the presence of load during heating increases the change in pore size distribution at diameters below 100 μm . It has been observed that the presence of load below a uniaxial stress of $0.6 f_{cu}$ results in a decrease in the gas permeability of concrete¹⁵. This would be even more pronounced under hydrostatic loading, which suggests that the escape of water present in capillary pores as a result of heating above 100 °C was possibly restricted. One potential effect of this is that further hydration of the cement conditioned with load and heat over that of concrete which experiences thermal treatment only may be enhanced. However, further chemical testing would be required in order to ascertain with a greater certainty the likelihood of this hypothesis.

To obtain the highest quality of results from X-ray CT analysis which is necessary for quantitative data evaluation this research has indicated that the specimen must be of a cylindrical geometry. Non-uniform geometries do not facilitate accurate phase quantification across the material. This factor makes a multi-scale analysis exceptionally challenging, particularly at higher resolutions where physical segmentation is required. Consequently, X-ray CT lends itself to *in-situ* analysis where the process under observation can be observed to develop in the same specimen rather than the situation which has arisen here in *ex-situ* analysis where reliance is placed upon the statistical probability of detecting similar features in multiple specimens. In the case of *in-situ* analysis, the challenge would rest upon developing equipment that can condition specimens within the relevant high resolution X-ray CT equipment. This problem is addressed in part 3 of this thesis (Chapters 8 and 9).

5.7. CONCLUSIONS

The X-ray CT analysis of concrete specimens from a research program into the behaviour of AGR pressure vessel concrete conditioned under mechanical load and heat treatment has revealed the following:

- Laboratory based X-ray CT is a useful technique for determining quantitative changes in the characteristics of the 3D air void structure in concrete which cannot be discerned using other techniques such as MIP. Experimental testing shows a good degree of repeatability between similarly conditioned specimens of batch cast concrete.
- A reduction in pores with an equivalent diameter of between 30 and 100 μm and an increase in pore diameters above 200 μm occur as a result of thermal treatment at 250 °C with respect to an unconditioned control specimen. The presence of hydrostatic mechanical load at $0.6 f_{cu}$ during thermal treatment appears to increase the presence of equivalent pore diameter frequency below 100 μm .
- X-ray CT does not however appear to be a useful technique for the *ex-situ* study of sub-micron porosity. The specimen preparation required and the extended scanning times resulting in elevated costs means that the analysis of a suitable population of specimens is

unreasonable. Despite this, X-ray CT may have useful applications as an *in-situ* scanning technique and this will be discussed in Chapters 8 and 9.

6. Scanning Electron Microscopy

6.1. INTRODUCTION

Microstructural information regarding the solid phase distribution and pore structure of concrete can be imaged using a number of two-dimensional microscopy techniques including optical and scanning electron microscopy (SEM). SEM in particular is a versatile technique that can be used to obtain high quality images of concrete microstructure down to a feature resolution of 100 nm³⁰. A number of different detectors can be used to capture images on an SEM. The most common detectors are those which analyse secondary electron (SE) and backscattered electron (BSE) emission from the specimen. The SE detector can be used to image the morphology of hydration products and fracture surfaces whilst the BSE mode can be used to capture the composition and distribution of phases. In addition, it is also possible to use energy dispersive X-ray microanalysis (EDX) which will yield information on the chemical composition of the material.

Due to the heterogeneity of cement based materials only qualitative information can be obtained from the study of a single SEM image because of the limited field of view. To obtain quantitative data, a statistically significant sample of images must be analysed. The sample size is influenced by the size of features under investigation and the spatial resolution of the captured images. Numerical data is obtained through phase segmentation in the same manner as that employed in X-ray CT. BSE images in particular lend themselves to segmentation and image analysis (IA) since the peaks in image greyscale histograms represent individual phases within the concrete (See 6.2.). Another issue which must be considered is the difficulty in the calculation of 3D properties using 2D images. Information on material properties such as pore size distribution and pore connectivity are limited due to the nature of interpreting the 2D images.

In common with X-ray CT, a rigorous methodology is required to obtain quantitative information both during image acquisition and image processing. In addition to X-ray CT, specimen preparation which is necessary to yield a flat-polished section for image analysis must also be considered. In a conventional evacuated SEM without any environmental provision, cementitious specimens must be dried, impregnated with an epoxy resin and surface coated with an electrically conducting film before image acquisition to prevent specimen volatilisation and to dissipate the potential generated by the electron beam. This technique is therefore destructive and damage induced during drying, polishing and resin impregnation can significantly affect measured pore characteristics and properties⁹².

Despite these issues, BSE – IA has been used extensively to quantify the volume fraction and morphology of porosity and solid material phases. This has allowed a greater understanding of many microstructural processes which are important in concrete technology such as; the hydration of OPC materials⁹³; the hydration of cement replacement materials⁹⁴; the transport properties of mortars⁹⁵ and crack propagation in mechanically loaded concrete^{30,96,97}.

In this chapter, BSE-IA will be used to quantify the porous volume fraction along with data relating to the gradient in porosity both within and beyond the ITZ in the H250, L06H250 (LITS affected) and control conditioning regimes. Two specimens from each conditioning regime will be studied in order to assess the significance of the experimental results.

6.2. SEM IMAGING PRINCIPALS

Images were obtained using a Zeiss Evo 50 tungsten filament scanning electron microscope fitted with a quadrant semi-conductor diode backscattered BSE detector. Figure 6.1 shows a schematic representation of this equipment. Electrons are emitted from the tungsten filament with a range of energies from 0.2 to 30 kV depending upon the electrical potential applied across the electron gun. Using electro-magnetic lenses, the electrons are manipulated into a focussed beam at the surface of the specimen. The spot size indicates the area of interaction between the electron beam and the specimen. This is dependent upon the acceleration voltage and working distance. In the case of the equipment employed in this experiment the manufacturers data indicates a spot size of between 2 and 4.5 nm. Deflecting coils are used to raster scan the beam spot across the specimen in order to create the image.

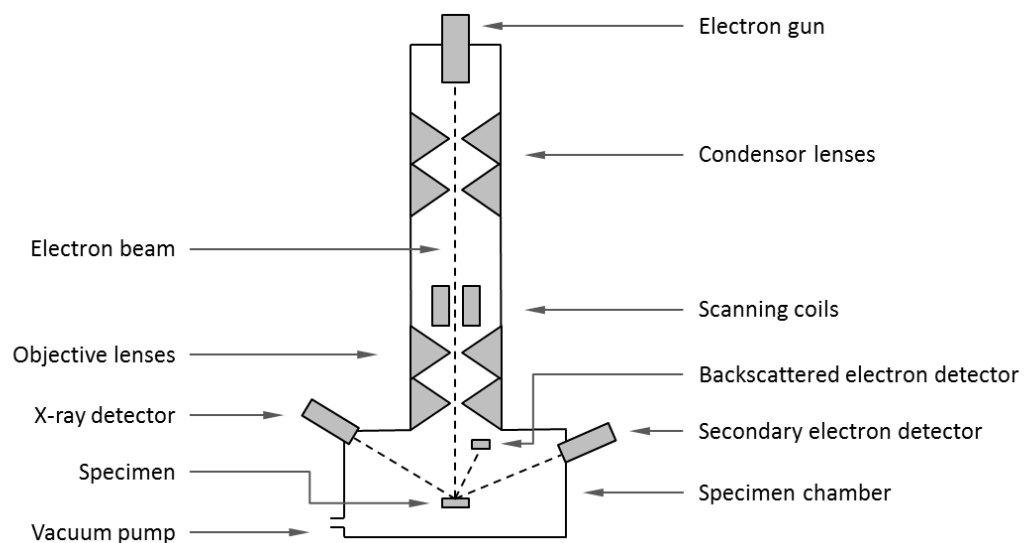


Figure 6.1: Schematic of SEM.

Backscattered electrons are high energy electrons which have been reflected or backscattered during the interaction of an SEM electron beam with atoms in an interaction volume at the surface of a specimen (Figure 6.2). Atoms with a high atomic number backscatter a larger number of electrons than those with a low atomic number and therefore areas with heavier atoms appear brighter in the resulting image. BSE images are therefore used to detect differences in the chemical phase composition of material at the surface of a specimen.

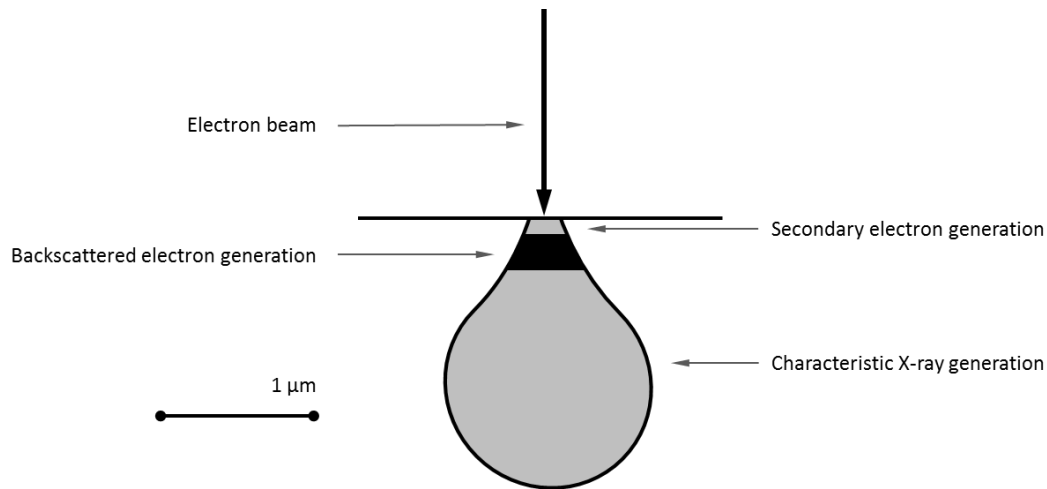


Figure 6.2: Signal generation in the Scanning Electron Microscope (SEM) from Scrivener³⁰

In the case of BSE imaging of OPC based concrete specimens, it was identified by Scrivener³⁰ that the brightest material was that of the anhydrous cement grains. In the images presented here, the addition of PFA leads to the detection of particles containing iron which appear similar or brighter than the cement grains (Figure 6.3). Aggregate particles along with hydrated phases including C-S-H and calcium hydroxide lie in the central region of the greyscale histogram and appear as various shades of light and dark grey. Finally, the epoxy resin filling the pore space within the material appears black due to the low atomic number of this material with respect to the solid structure of the cement paste.

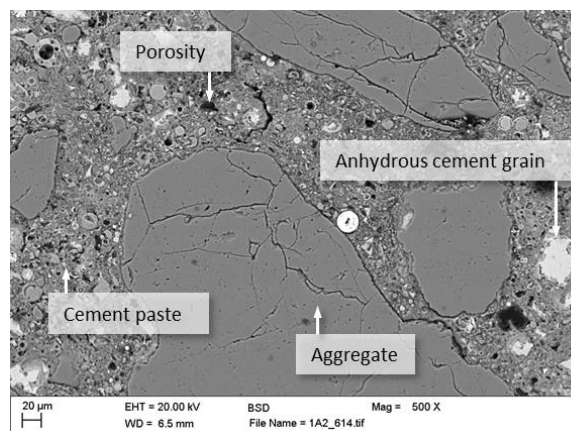


Figure 6.3: Phase identification in BSE-SEM image

6.3. SPECIMEN PREPARATION

The chosen method of specimen preparation can have an important effect on the quality of data provided through SEM analysis. This is particularly true for BSE images where a highly polished surface is required. Unprepared surfaces and those that are poorly prepared are likely to show no resemblance to the bulk microstructure of cementitious material and therefore may yield images that are unrepresentative⁹⁸. In order to mitigate this problem, the method of *Wong et al.*⁹⁹ was followed. The process of specimen preparation can be divided into three stages: cutting and drying, epoxy impregnation and grinding/polishing.

6.3.1. Specimen cutting and drying

Disk 6 was removed from each of the H250, L06H250 and control specimens in the same manner as that described in Chapter 5 for the 5 micron resolution X-ray CT analysis. These specimens were immersed in acetone for three days before being evacuated to 30 mbar in a vacuum chamber for 24 hours to remove free water within the microstructure.

6.3.2. Epoxy impregnation

A low viscosity epoxy resin was chosen to impregnate the specimen. Impregnation was carried out by placing the specimen with the face chosen for analysis at the bottom of a two part circular plastic mould into a shallow layer of freshly mixed epoxy resin. Additional epoxy resin was then added into the mould to a level which covered the whole specimen. The specimen was then evacuated to 30 mbar pressure by placing inside a vacuum chamber for 15 minutes to remove entrained air. Following removal from the vacuum chamber, the specimen was cured at atmospheric temperature and pressure for at least 48 hours before further preparation took place.

6.3.3. Grinding/polishing

After curing of the epoxy resin, the chosen surface was then ground by hand using silicon carbide paper with successively finer grit sizes of 220, 500, 1000 and 1200 (68, 30, 18 and 14 μm). The specimens were then washed in acetone and polished on individual cloth wheels with abrasive diamond paste at 6, 3, 1, and $\frac{1}{4}$ μm fineness. Polishing was carried out using a polishing wheel at 60 rpm with a 10 N contact force. Specimens were polished at each stage for 5 minutes in order to minimise preferential wearing of the softer cement matrix with respect to aggregate. The specimens were cleaned in acetone after each stage and following polishing were coated with a conductive layer of carbon using an evaporative coater. Silver Dag paint was also applied to allow charge conduction to the equipment stage.

6.4. BSE IMAGE ACQUISITION

An accelerating voltage of 20 kV and a working distance of 7 mm were found to yield optimum image contrast. To prevent the loss of valuable grey-scale information from images, the brightness and contrast was adjusted during acquisition to ensure a buffer zone of grey-scale bins between the dataset and the 0/265 extremities in the image histogram. This corresponds with the work of Wong *et al.*⁹⁹ who avoided pixel registration in the 0-10 and 245-255 grey values of the captured image. Due to limitations of the SEM used here, such specifications could not be met exactly but only small variations have been found in the results which are deemed not to have an influence on the image analysis process.

Thirty images were collected from each disk with a magnification of 500x. This magnification represents a trade-off between the analysis of a larger area (low magnification) and an increase in resolution (high magnification)³⁰. The images were stored with a resolution of 1024 x 768 pixels, giving a field of view of 512 μm x 384 μm and a pixel size of 0.5 μm^2 . In accordance with Wong *et al.*⁹⁹ images were obtained in an equally spaced grid pattern in order to capture features such as the bulk cement paste and interfacial transition zone (ITZ) with a frequency representative of their contribution to volume fraction and aggregate distribution in an unbiased manner.

6.5. BSE IMAGE ANALYSIS

To quantify pore and solid phase properties from the BSE images, it is necessary to segment the greyscale images into binary images representing only the phase chosen for analysis. This involves assigning a 1 or 0 to each pixel within the images based upon its location or value with respect to a global threshold, H .

$$f_H(x, y) = \begin{cases} 1, & \text{if } f(x, y) \geq H \\ 0, & \text{if } f(x, y) < H \end{cases}$$

The methodology employed for the segmentation of each phase is described below.

6.5.1. Aggregate segmentation

The grey-scale value of the bulk aggregate is similar to that of the cementitious matrix as a result of their similar chemical composition. This means that aggregate cannot be removed from BSE images by global thresholding like the porosity and anhydrous cement cores. To overcome this issue, a methodology similar to that of Yang and Buenfeld¹⁰⁰ was adopted. This allowed the segmentation of image features based on their morphology.

First, a low pass filter was employed to smooth image features. A Canny edge detection algorithm was then applied to detect regions where only a small change in greyscale was present. The Canny

edge detection algorithm was chosen as it appeared to give a better representation of aggregate edges than the gradient based edge detection algorithm employed by Yang and Buenfeld¹⁰⁰. Following edge detection a number of morphological operators were applied using the same routine as the aforementioned authors. Porosity and cracking within the aggregate was also removed after aggregate segmentation using a hole filling operation for consistency. The complete aggregate segmentation script as composed in MATLAB is presented in Appendix A. The efficacy of the aggregate segmentation routine was assessed visually for each image. Good segmentation was recorded in all cases. The results of one such segmentation are shown in Figure 6.4.

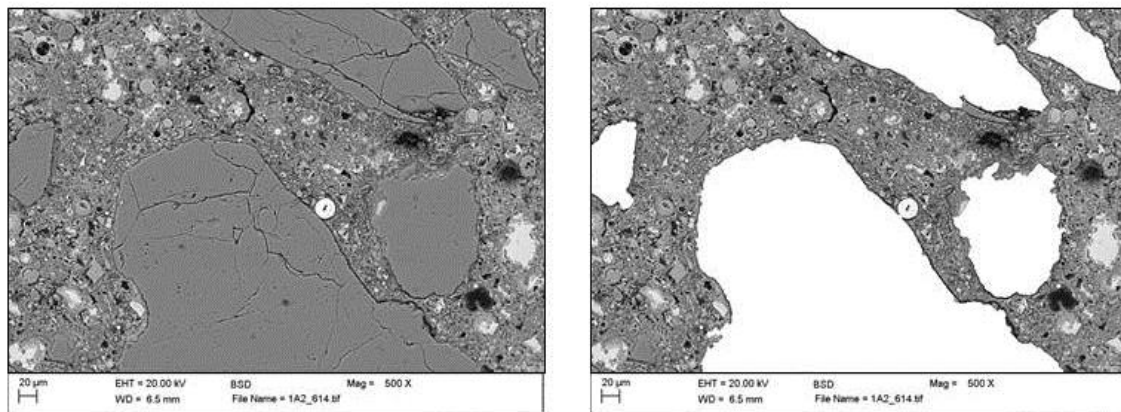


Figure 6.4: Aggregate segmentation

6.5.2. Pore segmentation

The challenges associated with the selection of a global threshold value, H for the segmentation of features within grey-scale images were reviewed in Chapter 5. For the BSE images captured in this study simple minima thresholding was used to determine the area fraction of anhydrous cement grains. Conversely, the method of Wong *et al.*⁹⁹ was used for the segmentation of porosity and cracking because of its reliability in processing images where no specific peak exists in the greyscale histogram for the phase under examination (Figure 6.5).

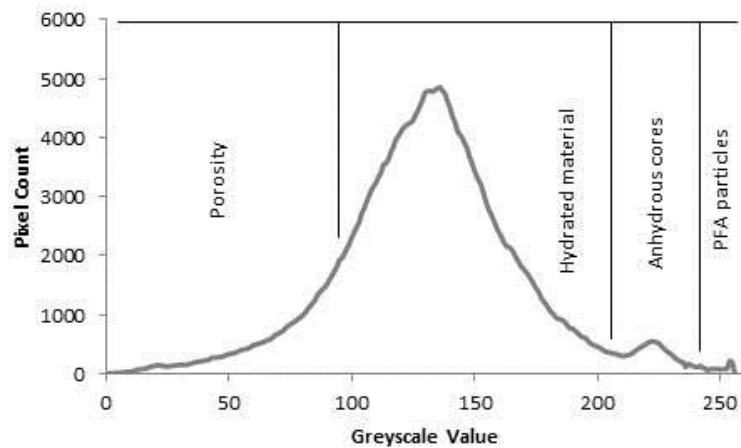


Figure 6.5: Greyscale histogram for a typical BSE image used in this study. The phases of interest and their greyscale ranges are approximately identified. The challenges associated with a lack of phase peak for porosity can be observed.

Accordingly, the global threshold for porosity/cracking was determined from the point of inflection of the cumulative greyscale intensity plot (Figure 6.6). Termed the point of “overflow”⁹⁹, this represents the value where a small increase in the global threshold will yield a sudden increase in image area. The point of “overflow” is clearly observed between 90 % and 100 % of the threshold level. In line with Wong *et al.*⁹⁹, the pore area fraction was therefore chosen at 90 % of the value determined from the inflection point calculation.

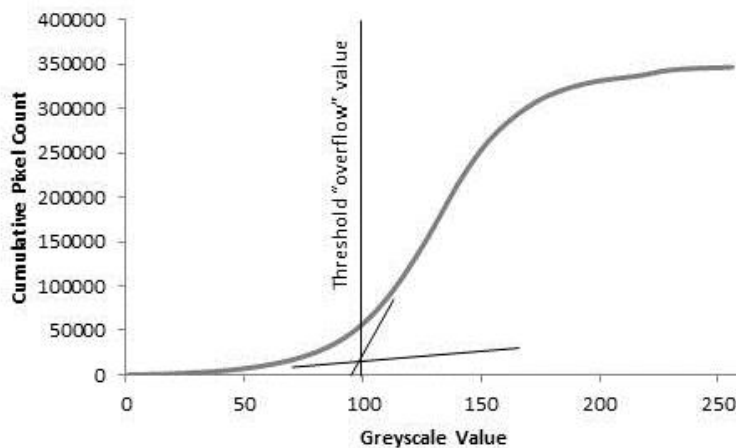


Figure 6.6: Cumulative greyscale intensity plot for a typical BSE image.

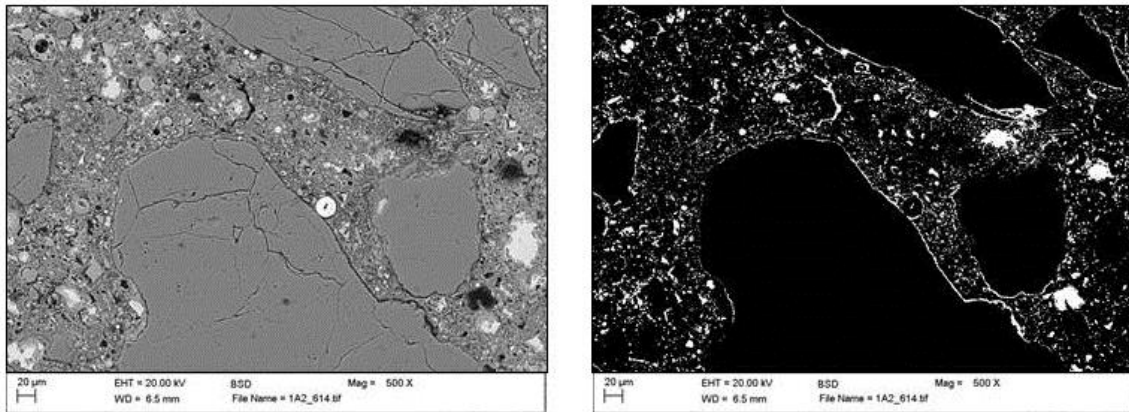


Figure 6.7: Porous segmentation

It is assumed that based upon the principals of stereology¹⁰¹ and that a representative elementary area of material is analysed, the area fraction of phases within the cement matrix is equivalent to the volume fraction of phases within the bulk material. The volume fractions of porosity and anhydrous cement content were thus calculated as a percentage of their segmented area to the total area of the image. To account for noise in the BSE images, all features with a total area smaller than five pixels were removed⁹⁹. This resulted in features with an equivalent diameter of less than 0.63 µm being excluded from the analysis.

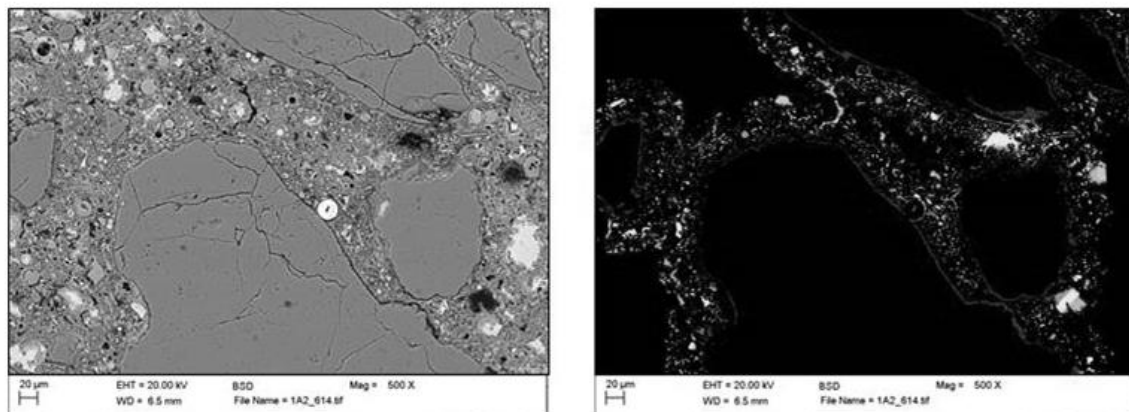


Figure 6.8: Typical SEM image and segmented porosity within the ITZ

Porous volume information within the ITZ was calculated by performing a distance mapping operation on the segmented aggregate image. The aggregate distance map and the segmented porosity were compared and a value representing the distance in pixels from the surface of an aggregate particle was assigned to each pixel representing a pore. A simple filtering operation could then be used to determine those pores within bands 10, 20, 30, 40 and 50 µm from the surface of the aggregate.

6.6. RESULTS

A typical BSE image from each of the three conditioning regimes is shown in Figure 6.9. A qualitative review of the images shows an appreciable difference in the homogeneity of the bulk cement paste between the H250 conditioning regime and both the L06H250 (LITS affected) and control regimes. A densification of the cement paste surrounding anhydrous cement particles in the H250 specimen microstructure appears to be present, indicated by lower porosity in these areas. A qualitative reduction in the size of anhydrous cement grains is also visible in the H250 specimens. However, in locations away from anhydrous cement grains, no apparent differences to similar areas in the L06H250 and control regimes could be observed.

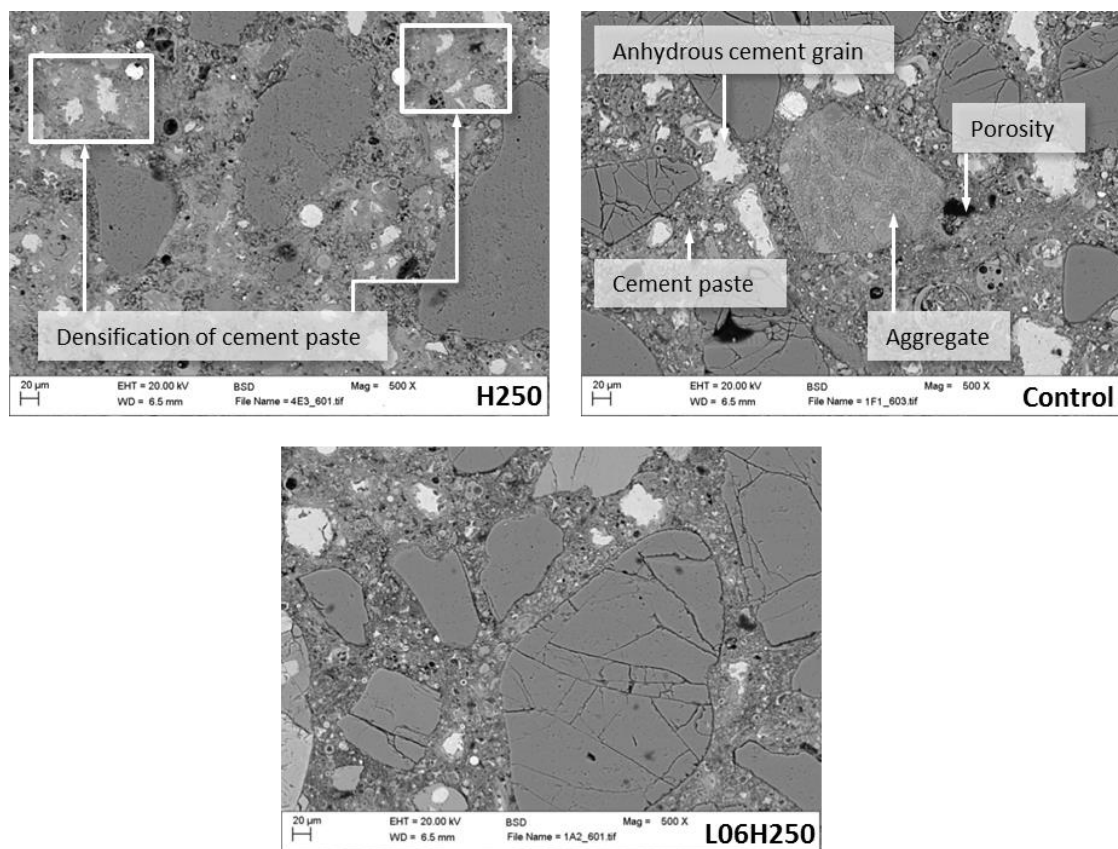


Figure 6.9: Typical BSE images from each of the conditioning regimes indicating features of interest.

6.6.1. Scatter of experimental results

Figure 6.10 shows the change in average capillary porosity within the concrete with respect to the number of images analysed. A relatively stable value for total porosity is observed to occur after analysing approximately twenty-five images. These results indicate that even if further images of each specimen with the same magnification and resolution were added to the analysis, the accuracy of the data would not be significantly affected. A similar trend can be observed in the data for ITZ porosity (not shown here).

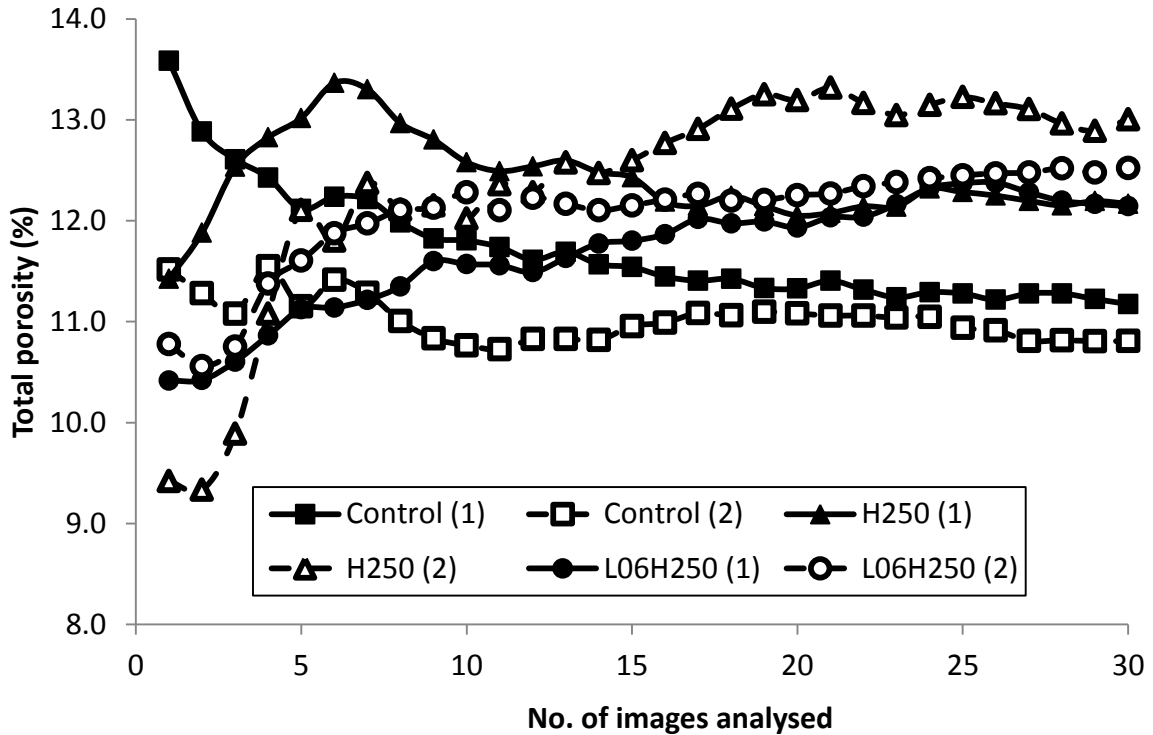


Figure 6.10: Variation of average total porosity with number of frames analysed. After twenty-five frames a relatively stable value of porosity was obtained. (Do average here.)

Tables 6.1, 6.2, and 6.3 show the results of a statistical analysis using the Analysis of Variance (ANOVA) method and pairwise comparisons of key results. The tests are used here to understand if treatment regime affects total porosity, as well as porosity within the ITZ. Values of F represent the test statistic and values of p represent the significance of the test. Significant values are indicated by a * character. For each set of analyses (ANOVAs, pairwise comparisons) Holm's sequential Bonferonni correction was applied to mitigate the increased risk of obtaining false significant results when conducting multiple tests. The correction works as follows. For the ANOVAs analysing the effects of treatment, and samples (within treatment) there were a total of 18 tests. The p values resulting from the analyses are ranked from most significant to least significant. The most significant p value needs to be less than $0.05/18$ to count as a significant result. The next most significant p value needs to be less than $0.05/17$ to count as a significant result. The next most significant p value needs to be less than $0.05/16$ to count as a significant result, etc. Values which lost significance after the Bonferonni correction was applied are indicated in bold.

The ANOVAs results in Table 6.1 indicate that for total porosity and ITZ porosity at 10, 20, 30, 40 and 50 μm from the surface of the aggregate, the treatment regime indicated by the Treatment term was significant. With respect to sample variance within the treatment, sample was nested within treatment. The Sample [Treatment] term indicates that only in the case of ITZ porosity within the 50

μm region was a variation between samples of the same treatment significant. These results lend support to the significance of the findings presented in the following text.

Table 6.1: Treatment effects. (F is the test statistic. P is the significance value)

	Total		10 μm		20 μm	
	F	p	F	p	F	p
Sample [Treatment]	1.87	0.14	0.17	0.92	3.68	0.01
Treatment	16.87	<.0001*	51.11	<.0001*	37.33	<.0001*

	30 μm		40 μm		50 μm	
	F	p	F	p	F	p
Sample [Treatment]	0.08	0.97	0.36	0.78	5.87	0.0008*
Treatment	11.89	<.0001*	15.02	<.0001*	27.88	<.0001*

The IA results from BSE images obtained for each specimen are shown in Figure 6.11. Within this Figure, both the average results and the standard error are shown for the capillary porosity and pore distribution inside the ITZ at 10 μm increments from the surface of the aggregate up to a maximum of 50 μm .

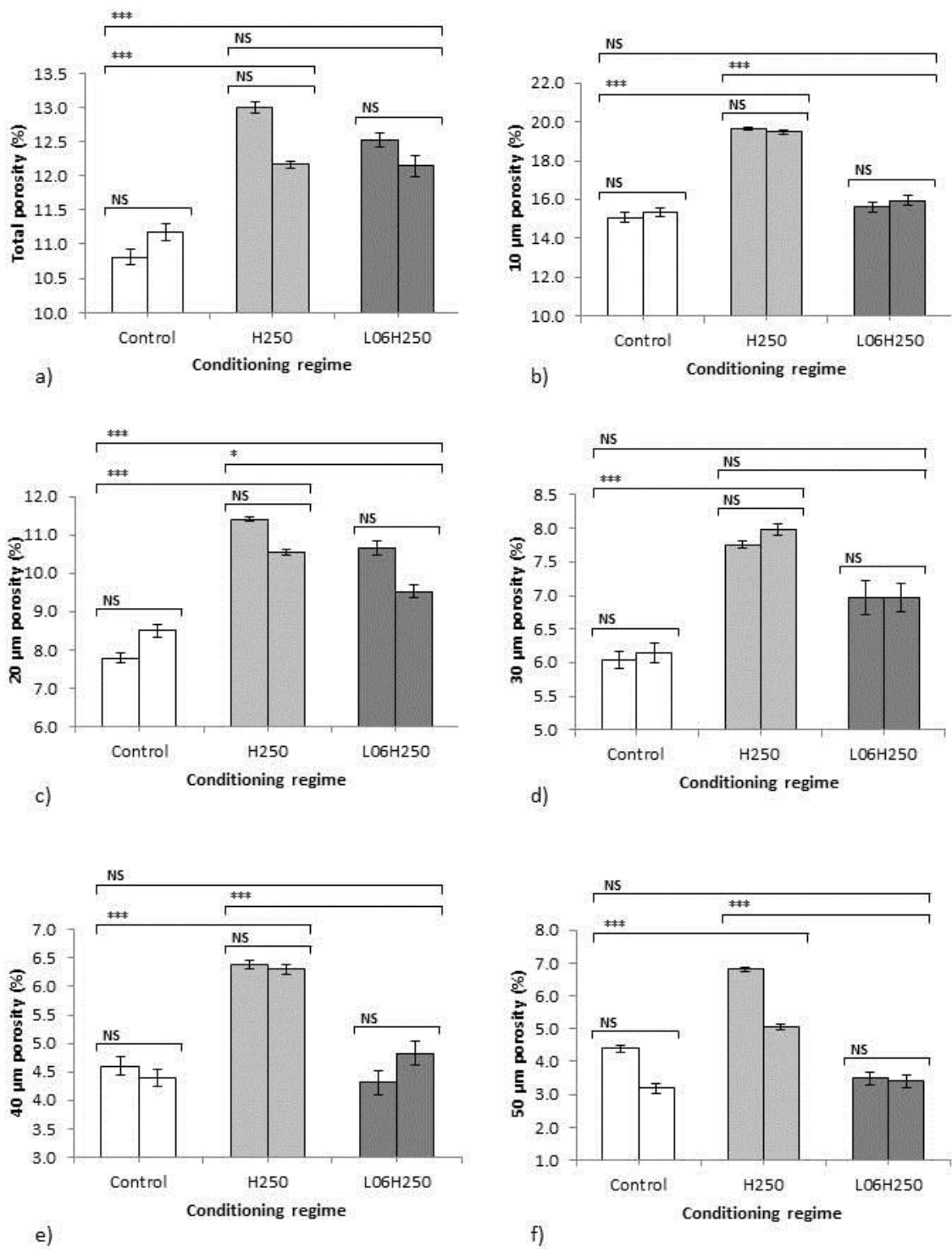


Figure 6.11: Statistical analysis of results for total porosity and porosity within the ITZ region at increments of 10, 20, 30, 40 and 50 μm away from the surface of the aggregate. Significance is indicated by *.

Table 6.2: Pairwise comparisons.

	Total		10 μm		20 μm	
	F	p	F	p	F	p
Control, H250	29.20	<.0001*	86.62	<.0001*	71.33	<.0001*
Control, L06H250	20.69	<.0001*	1.52	0.22	33.65	<.0001*
H250, L06H250	0.73	0.39	65.18	<.0001*	7.00	0.0089*

	30 μm		40 μm		50 μm	
	F	p	F	p	F	p
Control, H250	23.79	<.0001*	23.37	<.0001*	35.21	<.0001*
Control, L06H250	5.76	0.02	0.03	0.86	0.92	0.34
H250, L06H250	6.13	0.01	21.66	<.0001*	47.51	<.0001*

Table 6.3: With-in treatment effects.

	Total		10 μm		20 μm	
	F	p	F	p	F	p
Control	0.77	0.38	0.20	0.66	2.22	0.14
H250	4.03	0.05	0.04	0.84	3.21	0.08
L06H250	0.82	0.37	0.26	0.61	5.62	0.02

	30 μm		40 μm		50 μm	
	F	p	F	p	F	p
Control	0.04	0.84	0.15	0.70	5.63	0.02
H250	0.21	0.65	0.02	0.88	11.95	0.0007*
L06H250	0	0.99	0.91	0.34	0.03	0.87

6.6.2. Total pore volume

Figure 6.11a indicates that both the H250 and L06H250 (LITS affected) specimens experience an increase in porosity of approximately 1.5 % with respect to the control specimens with a > 95 % confidence level (Table 6.2). Table 6.2 also indicates that pairwise comparisons between the H250 and L06H250 conditioning regimes show no significance for values of total porosity. No significance is detected between repeat specimens within any of the conditioning regimes (Table 6.3).

6.6.3. ITZ porosity

Figure 6.11b-f shows the porous volume in regions 10, 20, 30, 40 and 50 μm away from the surface of aggregate particles segmented from the BSE images in the manner visualised in Figure 6.4. It is important to note that the incremental values used here to differentiate regions within the ITZ are based upon equatorial measurements from the assumed centre of aggregate particles. To convert measurements from plane values to true perpendicular values a correction factor of 0.81 was employed according to Scrivener and Nemat⁹⁶. In this case, a length of 12.4 μm in the 2D plane of the BSE images is equivalent to 10 μm on average in the plane perpendicular to the surface of the aggregate).

Pairwise comparisons show that control and H250 treatments differ significantly in porosity at 10, 20, 30, 40 and 50 μm increments. Values for the ITZ porosity of H250 specimens are greater than that of control specimens by a difference of at least two percent with a certainty exceeding 99.9999% in all cases.

No significance is detected between the control and L06H250 treatments at 10, 30, 40 and 50 μm increments but a difference is apparent between these two conditioning regimes at the 20 μm interval. At this interval the porosity of the L06H250 specimens is increased by approximately two percent.

In contrast to the experimental data for total pore volume, values for the porosity within the ITZ in H250 and L06H250 conditioned specimens differ for all increments apart from within the 20 μm region. From pairwise comparison of the results in this region a reduced confidence interval of 99.99 % is evident in the difference in values between the two conditioning regimes. Confidence interval values exceed 99.9999 % in all other cases (Table 6.2).

Whilst values for the porosity in the first 10 μm of the ITZ are increased over those recorded for total porosity, in all other increments values are reduced in comparison. This effect is enhanced with distance with cement paste in the 50 μm band being lower by approximately 7.5 % for control specimens. This effect appears to be enhanced for the H250 and L06H250 specimens with values differing by approximately 9 %.

6.6.4. Anhydrous cores

Efforts to segment the anhydrous cores from the BSE images were unsuccessful due to the similarity of this material to PFA particles. The combination of similar grey-scale values and particle geometries lead to significant variation in results that even advanced segmentation techniques such as the watershed thresholding algorithm could not overcome.

6.7. DISCUSSION

The investigation of H250, L06H250 (LITS affected) and control specimens using BSE-IA indicates that in terms of total porosity within the length-scales considered, both the H250 and the L06H250 specimens experience an increase in porosity above that of control specimens. No appreciable difference can be detected between the H250 and L06H250 specimens. With respect to porosity in the ITZ region, H250 specimens experience a significant increase in porosity across that area over that of both the control specimens and the L06H250 specimens. In the case of the 20 μm band surrounding aggregate particles, the L06H250 specimens show a slight increase in porosity. However, in all other regions reported here, no difference between these specimens and the control specimens can be detected.

Statistical analysis of the results using ANOVAs and pairwise comparison indicates that these findings are significant. In comparison to other BSE-IA investigations though, the required number of images to produce a stable result is slightly increased. As Figure 6.10 indicates, the analysis of around twenty-five images was necessary in order to produce stable values of total and ITZ porosity and in each case thirty images were obtained. This compares unfavourably with the work of Wong *et al.*⁹⁹ who found that twenty images were sufficient to produce a reliable value for porosity. The principal reason for this difference is likely to be the study material. In the case of Wong *et al.*⁹⁹ the study data pertains to a mortar whilst the results presented in this work are for concrete. Consequently the material considered here is likely to be more heterogeneous and thus require a greater frequency of images to obtain a stable result.

Whilst the results presented here do not appear to give any indication of the validity of the either microprestressing-solidification theory or micro-diffusion theory for LITS, they do indicate a difference in microstructural characteristics in LITS affected specimens. The increase in ITZ porosity which is evident in H250 specimens is expected due to differential thermal expansion between aggregate particles and the cement paste. As highlighted in Chapter 2, the thermal expansion coefficients of the major concrete constituents; cement paste and aggregate differ significantly. This will be manifested in microstructural damage within but not limited to the ITZ after a thermal cycle at 250 °C.

In contrast however, L06H250 (LITS affected) specimens do not appear to sustain any significant damage in the ITZ as a result of thermal incompatibility. In fact, results indicate only a slight difference to the control specimens. This finding may be at least partly responsible for observations regarding material strength presented in Chapter 4 and other literature, along with conclusions provided by other authors on the effect of LITS on diffusivity and other transport properties in LITS affected materials.

With respect to mechanical strength, in Chapter 4 it was found that whilst the residual strength of both H250 and L06H250 specimens was reduced over that of control specimens. L06H250 specimens experienced a lower reduction in strength. Similar observations have been reported by Khoury *et al.*¹⁷ who reported that strength loss varied depending upon the aggregate used in each test, Schneider¹⁹ who concluded that “stressed strength was higher than unstressed strength” and Abrams²⁰ and Malhotra²¹ who recorded an increase in hot strength of between 5-25 % for all specimens heated under the presence of mechanical load.

The ITZ is likely play a significant role in the strength and loading stiffness of concrete since the porosity is greater and hydration is lower in this region. An increase in porosity within this region such as that recorded in this study for H250 specimens could be expected to weaken the material by providing a location from which cracking may propagate. In comparison, a lower porosity such as that recorded for the L06H250 (LITS affected) specimens would provide a greater resistance to crack propagation and lead to material behaviour more similar to that of the control specimen.

With further research on specimens conditioned under uniaxial and biaxial mechanical load this new hypothesis may be developed to bound observations by other researchers on the anisotropic behaviour of LITS affected specimens. It is conceivable that the suppression of ITZ damage observed here in LITS affected specimens may be influenced by the orientation of the confined load. Thus, damage within ITZ regions in specimens conditioned under uniaxial and biaxial stress may be orientated only in unrestrained axes.

In terms of diffusivity and transport properties, the observations on ITZ properties made here could also explain the research of Černý *et al.*²⁹ who reported that the moisture diffusivity of specimens heated without mechanical load was found to be twice as great as that of specimens heated under load. Interconnectivity between individual ITZ regions where porosity is increased has previously been reported to play a significant role in the bulk transport properties of cementitious materials⁹⁶. Based upon the results presented here, the findings of Černý *et al.* may therefore be explained by an increase in ITZ porosity in H250 specimens which is not observed in L06H250 (LITS affected) specimens.

6.8. CONCLUSIONS

The results of a BSE-IA investigation into the material behaviour of concrete conditioned under load and heat indicates that L06H250 (LITS affected) specimens show a similar increase in total porosity to that of H250 specimens over that of unconditioned control specimens. Microstructural changes within the ITZ however appear to show that at least in a residual condition, porosity in H250 specimens is increased over that of L06H250 (LITS affected) and control specimens. A statistical analysis of the results indicates a good degree of confidence in the results.

7. Mercury Intrusion Porosimetry

7.1. INTRODUCTION

Mercury intrusion porosimetry (MIP) is a versatile technique which can be used to characterise a number of properties describing the pore structure of cementitious materials. MIP is unique in that it provides a straightforward method of obtaining data regarding the distribution of pore sizes from 0.001 μm to 1000 μm according to the applied mercury pressure. However, for the reasons briefly addressed in Chapter 5, care must be taken in the interpretation of MIP measurements.

Here, the MIP technique will be described in detail along with a review of limitations of application. Results from the MIP pore structure analysis of *ex-situ* conditioned H250, L06H250 and control specimens is presented along with a statistical analysis of key data sets. Finally a discussion is outlined detailing the key findings.

7.2. MERCURY INTRUSION PRINCIPALS

MIP analysis is carried out by intruding mercury into an evacuated porous specimen over an increasing pressure range. Initially, a suitably sized specimen is placed within the thimble of a penetrometer tube (Figure 7.1a). This penetrometer is inserted into the low pressure port of the experimental apparatus (Figure 7.1b). Here, air is removed from the penetrometer and specimen to yield a high vacuum environment. Mercury is then introduced into the penetrometer first at low pressure and then following the transfer of the penetrometer to the high pressure port up to 200 MPa.

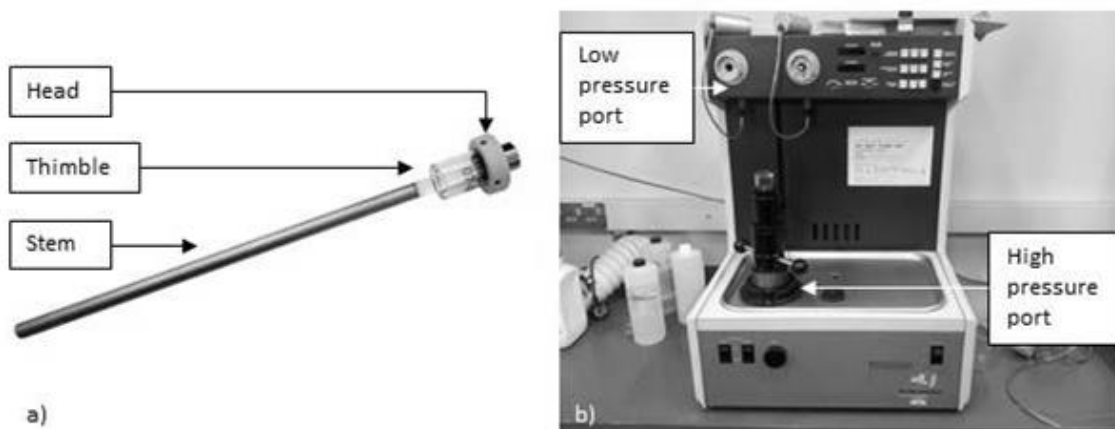


Figure 7.1: a) Mercury Penetrometer, b) Micromeritics PoreSizer 9320 mercury intrusion porosimeter

The volume of mercury intruded into the specimen is measured through the change in mercury volume in the stem of the penetrometer which functions as an electrical capacitance dilatometer. A decrease in the volume of mercury in the stem which corresponds with an increase in intrusion pressure consequently leads to a proportional reduction in capacitance. According to the equipment manufacturer this change in volume can be measured with an accuracy of $< 0.1 \mu\text{m}^3$ ¹⁰².

Mercury is chosen as the liquid for intrusion because of its high contact angle with solid surfaces which mean that it is non-wetting and will not be drawn into the material pore structure by capillary suction. At the interface between the mercury and an un-intruded pore there is a surface tension in the liquid which acts tangentially to the opening. This surface tension will remain until the forces maintaining it are in equilibrium with the external pressure applied to the mercury by the experimental equipment. At this point the pore will start to be intruded.

In general, the pressure required to overcome the surface tension is inversely proportional to the size of the pores where a low pressure is required to intrude large pores and very high pressures are necessary to intrude pores in the nanometre range. By making certain assumptions about the pore geometry, intrusion pressure is directly related to pore diameter using the Washburn equation.

7.2.1. The Washburn equation

The Washburn equation has been adopted extensively in existing literature to characterise the pore size distribution of cementitious specimens using mercury intrusion data. In order to calculate the diameter of pores intruded at a particular pressure, the Washburn equation makes a key assumption that pores in the material under investigation are cylindrical¹⁰³. The pressure (P) required to intrude pores with a diameter greater than d is as follows:

$$P = -4\gamma\cos\theta/d ;$$

Where γ is the surface tension of the mercury and θ is the contact angle between the solid and the mercury (Figure 7.2). Thus by measuring the volume of mercury intruded into the specimen as the pressure increases, the volume of pores at each corresponding diameter can be calculated.

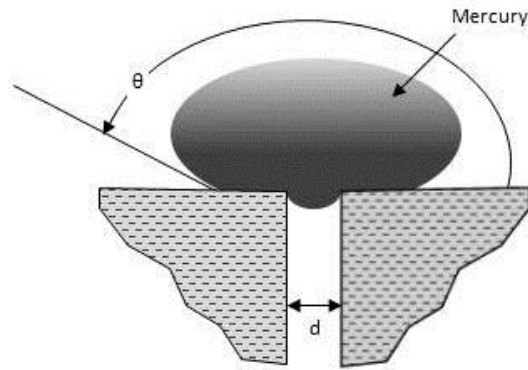


Figure 7.2: Contact between liquid mercury and a porous solid recreated from Guang¹⁰⁴

7.2.2. Material properties

From the analysis of intrusion data and the application of the Washburn equation the following material properties can be calculated:

- The total porosity as a percentage of the specimen volume may be calculated without the Washburn equation by dividing the total volume of mercury intruded into the specimen up to the maximum pressure by the envelope volume of the specimen. The envelope volume itself is calculated by subtracting the total volume of mercury in the full penetrometer with no specimen present from the volume of mercury in the penetrometer before pressurisation with a specimen present¹⁰².
- The bulk density of the specimen is also calculated without the Washburn equation by dividing the mass of the specimen measured before MIP analysis by the envelope volume measured as above. The bulk density represents the density of the solid material, open pores within the material which may be intruded by mercury and closed pores within the material which are isolated or are connected to the pore network with access pore diameters smaller than the minimum diameter intruded at maximum pressure.
- The skeletal density of the specimen is calculated by dividing the mass of the specimen before MIP analysis by the skeletal volume of the specimen. The skeletal volume in turn derived by subtracting the volume of mercury intruded into the specimen at maximum pressure from the envelope volume¹⁰². The skeletal density therefore represents the density of only the solid material and closed pores. The Washburn equation is not required for this measurement.
- Total pore surface area is calculated from incremental pore volume¹⁰² using the data derived from the Washburn equation:

$$A = \int_{i=D_{min}}^{i=D_{max}} \frac{D_i}{V_i}$$

Where D_i and V_i are the representative diameter and mercury intrusion volume for the pore size class in question.

- Average pore diameter (D_{mean}) is calculated using the assumption of cylindrical pores employed in the Washburn equation:

$$D_{mean} = 4 \frac{V}{A} ;$$

Where V is the volume of intruded mercury and A is the total surface area of the pores.

- The pore size distribution dV/d is calculated using the method of Ritter and Drake by taking the pore volume V_{pore} per unit interval of the pore diameter (d):

$$dV(d) = - \frac{V_{pore}}{d} \cdot \frac{dV}{dp}$$

- The pore size distribution differential curve is calculated by plotting the slope of the pore size distribution curve $dV/d \log d$ against $\log d$ (Figure 7.3)

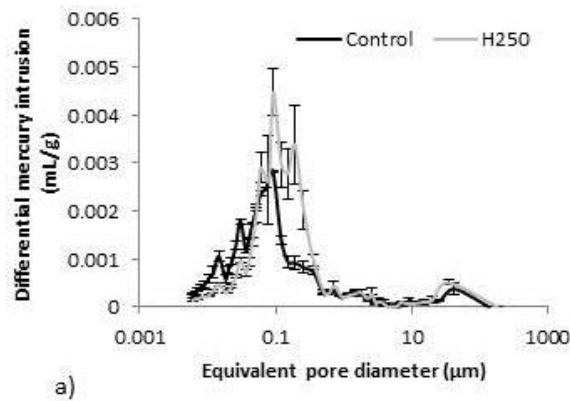


Figure 7.3: Pore size distribution

7.3. MIP LIMITATIONS

When interpreting the results of MIP experiments, care must be taken in two principal areas of analysis: the interpretation of results derived using the Washburn equation which makes specific assumptions about pore geometry and the fundamental nature of the testing which requires specific specimen drying and high pressure intrusion. These points will be addressed in respective order.

7.3.1. Pore geometry

With respect to the experimental procedure, a large proportion of pores within cementitious specimens may only be accessed through a network of smaller pores⁸⁶. Once the intrusion pressure

required to intrude the narrow pores has been exceeded, both the narrow pores and the larger interior pores will be intruded at the same time. This phenomenon is known as the “ink bottle” effect and is likely to result in the overestimation of frequency of small pores and suppression of data regarding larger pores. Isolated pores where no connectivity is present will also be excluded from the results.

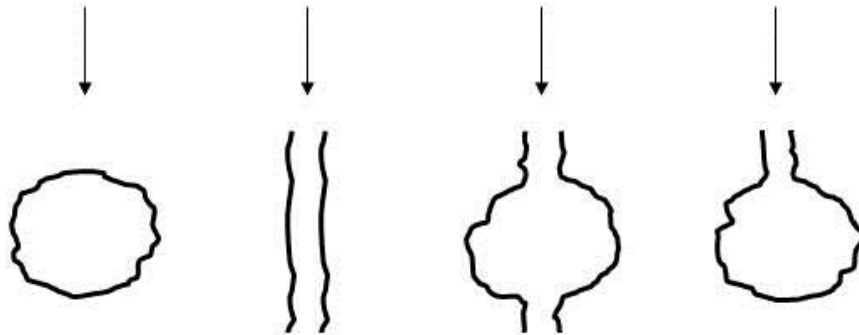


Figure 7.4: Classification of pore geometry: a) closed pore, b) connected pore, c) connected pore with “ink bottle” and d) cul-de-sac pore with “ink bottle”.

With respect to data analysis, the Washburn equation¹⁰³ makes the assumption that pores are both cylindrical and open ended in order to allow the calculation of pore size distribution, total pore area and average pore diameter data. The BSE imaging results presented in Chapter 6 along with the work of other authors^{86,30} indicates that this assumption is not valid. In fact, pores appear to have highly non-uniform geometries.

7.3.2. Damage on drying and intrusion

In order to allow the mercury to intrude the complete range of porosity present in the concrete, MIP specimens must be dried to remove all water which would inhibit mercury intrusion before analysis. In the same manner as SEM specimen preparation, the method of drying is known to have an influence on the experimental values recorded. Damage may also be caused to the pore structure by the high pressure mercury intrusion necessary to study pores on the nanometre length-scale¹⁰⁵. This is likely to increase the recorded volume fraction of pores and alter the size distribution characteristics of the material. The effects are likely to be common throughout all specimens however.

The limitations of MIP outlined above provide a framework for consideration when interpreting MIP results with respect to other methods of microstructural analysis. With careful experiment design they do not however detract from the relative comparison which can be obtained between different conditioning regimes using this technique.

7.4. METHODOLOGY

7.4.1. Specimen preparation

Mercury intrusion porosimetry was carried out on disks 3, 7 and 8 from the two cores in each of the three conditioning regimes; Control, H250 and L06H250 (LITS affected). These disks were weighed and then heated at 105 °C until a constant weight was achieved in order to remove any free water remaining in the concrete pore structure following conditioning. For this investigation, oven-drying (105 °C) was employed in a variation to that used by Kaufmann¹⁰⁶ (50 °C). Oven drying is known to cause additional damage to that of vacuum or freeze drying. However since two out of the three conditioning regimes had experienced temperatures in excess of 105 °C this was thought to be of negligible influence. In all cases drying took no longer than three days. Following heating the specimens were cooled and stored in a vacuum desiccator until testing.

7.4.2. Experimental procedure

Intrusion experiments were carried out using a Micromeritics Instrument Corporation Poresizer 9320. Before the experiment commenced, the bulk weight of the specimen was measured along with the weight of the empty penetrometer using an analogue balance with a precision of ± 0.001 g. All specimens were composed of a single disk of concrete with a weight of between 6 and 8 g. The atmospheric pressure and temperature were also measured at this stage in order to calculate the instantaneous mercury density.

Two identical penetrometers were used in this experiment with a total volume of 16 mL and a stem volume of 1.13 mL. The penetrometers were chosen based upon a supplementary investigation to ensure that in compliance with equipment parameters; the porosity of the specimen was greater than 20 % of the stem volume.

The equipment incorporates both a low pressure port and a high pressure port. Once the specimen was sealed within the penetrometer head, the stem was inserted into the low pressure port where it was evacuated to a pressure of 80 μmHg in three incremental steps. On obtaining the required vacuum, mercury was introduced into the penetrometer at a pressure of 0.012 MPa. This corresponded with the pressure required to force mercury along the stem and into the head without intruding the porous network within the specimen. The pressure was then returned to 0.186 MPa through approximately ten incremental steps using a manual application process. Evacuation and mercury filling in the low pressure port lasted approximately one hour.

Following the end of low pressure testing, the penetrometer was removed and weighed in order to determine the weight of mercury present in the penetrometer in comparison with earlier weight measurements. The penetrometer was then inserted into the high pressure port where pressure was

applied automatically at predefined steps from 0.186 to 200 MPa. An equilibration time of 10 seconds was used at each step and the total time to run a high pressure test was approximately two hours. A surface tension of 0.48 N/m² (Pa) and a contact angle between mercury and solid material structure of 130° were used in all calculations.

7.5. RESULTS

The results of MIP analysis of control specimens and those conditioned under the H250 and L06H250 (LITS affected) regimes are presented in Figures 7.5 and 7.6. All error bars are indicated with respect to standard error and statistical analysis of the data presented in Figure 7.5 was undertaken using the ANOVAs and pairwise comparison methods detailed in Chapter 6.

The ANOVAs results in table 7.1 indicate that for total porosity, bulk density, skeletal density and average pore size, the treatment regime indicated by the Treatment term was significant. In the case of total pore surface area, no significant difference between any of the conditioning regimes could be detected. In a similar manner to Chapter 6, the Sample[Treatment] term indicates that sample was nested within treatment to test the significance of individual samples within the same conditioning regime. In all cases, no significance was detected between samples within the same treatment. These results provide an indication that the findings presented here are robust.

Table 7.1: Treatment effects.

	Total porosity		Bulk density		Skeletal density		Total pore area		Average pore diameter	
	F	p	F	p	F	p	F	p	F	P
Sample[Treatment]	1.7811	0.2042	1.0635	0.4009	5.3845	0.0140	0.1098	0.9527	5.1379	0.0163
Treatment	13.4100	0.0009	7.5290	0.0076	26.4885	<.0001	0.8018	0.4712	36.3721	<.0001

Figure 7.5a shows the total porosity and standard deviation for each of the three conditioning regimes. It is observed that both the H250 and the L06H250 (LITS affected) specimens experience a statistically significant increase in porosity of approximately 2.5 % with respect to the control specimens. According to the pairwise comparison results presented in Table 7.2, the presence of load during heating does not appear to yield any significant alteration in total porosity.

Table 7.2: Pairwise comparisons.

	Total porosity		Bulk density		Skeletal density		Average pore diameter	
	F	p	F	p	F	p	F	p
Control, H250	16.9666	0.0014	9.0781	0.0108	3.8852	0.0722	72.4987	<.0001
Control, L06H250	22.8293	0.0005	13.1354	0.0035	49.7504	<.0001	21.9627	0.0005
H250, L06H250	0.4342	0.5224	0.3737	0.5524	25.8298	0.0003	14.6550	0.0024

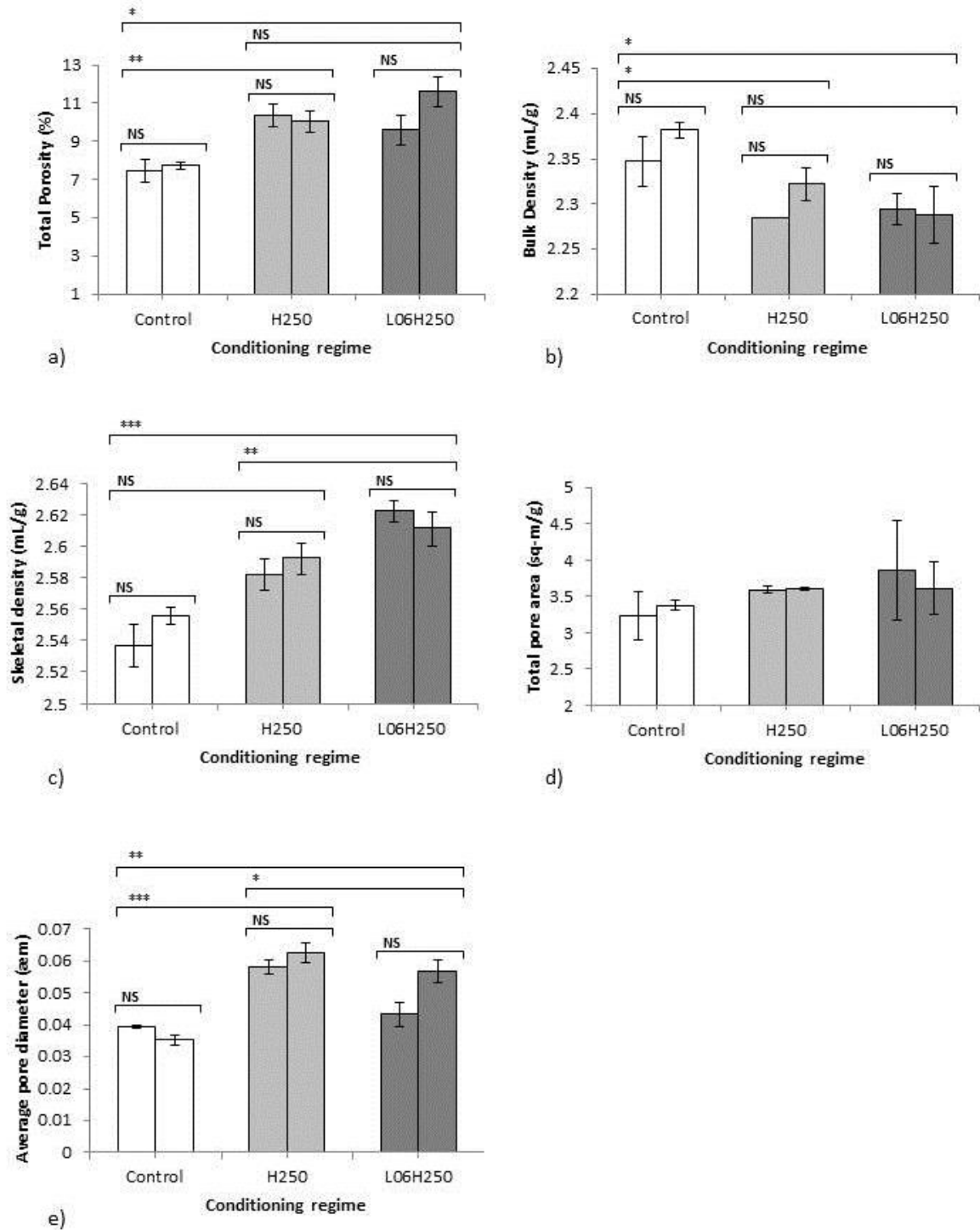


Figure 7.5: Other metrics results

Figure 7.5b indicates a reduction in the bulk density of both H250 and L06H250 conditioned specimens with respect to the control. This is in line with the increase in porosity of these specimens recorded in Figure 7.5a. In both cases, significance is reduced but still lies within the 95% confidence interval. No significance can be detected between the results from the H250 and L06H250 regimes.

Conversely, if the results of the skeletal density measurements are considered (Figure 7.5c), the values for L06H250 conditioned specimens are significantly elevated over those of both the control and the H250 regimes. No significance is detected between the control and H250 regimes. These results indicate a reduction in the frequency of closed pores within LITS affected specimens, which does not occur in specimens which experience only heating.

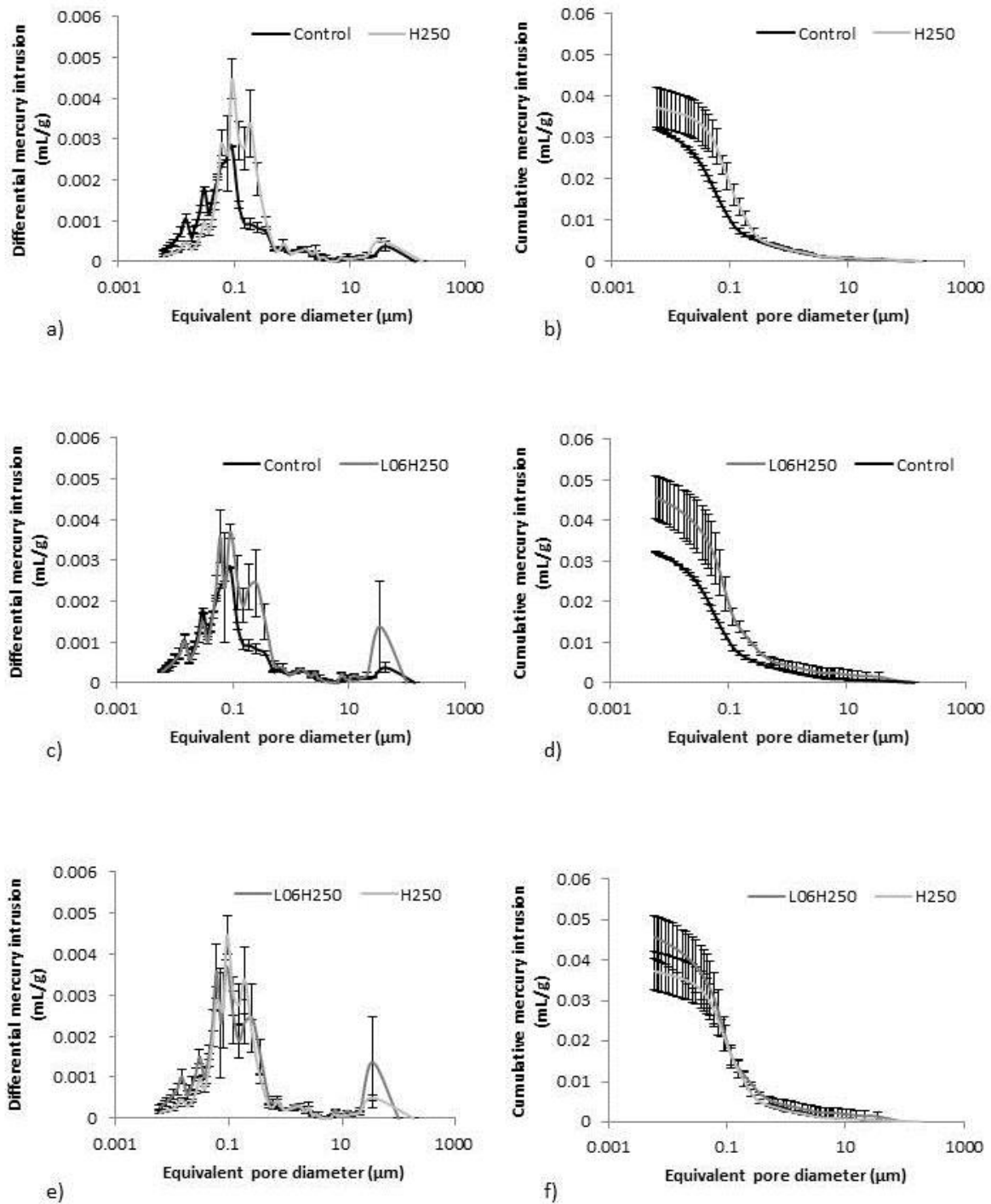


Figure 7.6: Pore size distribution

Results for the total pore area of specimens (Figure 7.5d) indicate that in line with the ANOVAs presented in Table 7.1, no difference is recorded between conditioning regimes. Figure 7.5e shows the variation in mean average pore diameter. In this case, each of the conditioning regimes is determined to be significant from one another. Both the H250 and L06H250 specimens experience elevated average pore diameters over those of control specimens. However, H250 specimens are shown to experience the greater increase and this correlates with the pore size distribution results presented in the following text where the frequency of the smallest pores in the H250 conditioning regime appear to be suppressed.

The pore size distribution of each of the three conditioning regimes as measured by MIP is shown in Figure 7.6 both with respect to cumulative and differential measurements. For clarity, the results are presented in three sections; Control – H250 (Figure 7.6 a,b), Control – L06H250 (Figure 7.6 c,d) and H250 – L06H250 (Figure 7.6 e,f). First considering the differential mercury intrusion plots, several peaks can be observed in all datasets. These correspond with a greater frequency of pores for the associated equivalent diameter.

Peaks corresponding with equivalent pore diameters of greater than 1 μm are not discussed here since by considering the limitations of MIP analysis presented earlier it is unlikely that pores in this size range will be recorded accurately. Therefore, beginning with the largest pores, the first significant peak is seen to occur between 0.05 and 0.5 μm . It is clear from Figure 7.6a and 7.6c that the H250 and L06H250 specimens show a significant increase in measured pore volume over Control specimens that show a less pronounced peak. In this range, experimental error is also seen to increase for the H250 and LITS affected specimens.

Two additional peaks are detected below 0.01 μm . In this region the variance in results appears to be consistent across all conditioning regimes. Pores from the L06H250 and Control regimes appear to occur with a similar frequency in this region. Specimens from the H250 conditioning regime do however show significant differences with the frequency of pores broadly suppressed with respect to the other conditioning regimes. Despite this, the same pattern of peak occurrence is visible.

7.6. DISCUSSION

The investigation of H250, L06H250 (LITS affected) and control specimens using MIP indicates that the total porosity within the pore sizes accessible using this technique is increased for both the H250 and the L06H250 specimens by approximately 2.5% with respect to that of unconditioned control specimens. A statistical analysis of the results has indicated that no significant difference in total porosity exists between that of H250 and L06H250 specimens. Conversely, Bulk density of both the H250 and L06H250 specimens is suppressed when compared to that of the control. However, this

may be expected to coincide with the aforementioned changes in total porosity. An increase in the porous content of specimens will reduce the quantity of solid material per unit volume.

The combination of an increase in total porosity and reduction in bulk density for H250 and L06H250 specimens with respect to an unconditioned control provides some explanation for the significant reduction in both hot and residual material strengths which are variously reported in existing literature. A lack of any distinct variation in values between the two conditioning regimes indicates that any LITS specific damage mechanism exists as a variation of an existing damage mechanism that is inherent in heated specimens, or that the LITS damage mechanism is masked by other changes in the material.

In comparison, the skeletal density of L06H250 specimens as reported through the ANOVA studies of the MIP data is significantly increased over that of both the control and H250 specimens. H250 specimens show no significant difference to control specimens. Skeletal density provides an indication of the density of the material and any closed porosity which is inaccessible to mercury. Two explanations exist to explain this result. The first is that closed porosity within the L06H250 specimens has been opened by some LITS specific damage mechanism. The second is that components of the solid material microstructure have undergone some process of chemical consolidation.

With respect to the first explanation, closed porosity is that which exists below minimum pore diameter accessible to the mercury or that which is isolated within the C-S-H gel structure. In either case the pores are sufficiently small that changes in their size are masked by changes in the larger porous structures in the material recorded in the measurements on total porosity and bulk density. Changes in the skeletal density of the material which were ascribed to an opening of inaccessible porosity within the material microstructure would provide direct support for the microdiffusion and LITD theories on LITS evolution.

Considering the second explanation, the research of Parrott⁹ found that transitional thermal creep – a major LITS component coincided with the formation of increased quantities of poly-silicates within the C-S-H. These chemical alterations are likely to cause changes in the density of the solid structure of the material which would be manifested in skeletal density measurements.

Measurements taken using MIP pertaining to the average pore diameter of specimens indicates that H250 specimens experience a significant increase in average pore diameter in specimens of approximately 60% with a 99.9% confidence interval. L06H250 specimens also experience an increase in average pore diameter with respect to control specimens. However the increase is much reduced of around 30 % with a confidence interval of 95%. The average pore diameter is one of a number of factors which will influence transport properties within cementitious materials. When

comparing two specimens which have the same porosity, the specimen with the larger average pore diameter is likely to have a greater permeability.

The increase in average pore diameter is again visible when the results of the pore size distribution analysis are considered. The peaks that exist between 0.05 and 0.5 μm are known as capillary porosity. These peaks correspond with the “threshold” pore width⁷⁵ where the highest rate of mercury intrusion is observed for any increase in pressure. They are significantly augmented in H250 specimens even with respect to L06H250 specimens. Conversely, in the lower range below 0.01 μm in equivalent diameter, pore frequency is suppressed in H250 specimens whereas L06H250 specimens exhibit a similar behaviour to those of the control regime. These pores which are known as gel pores by Cook *et al.*⁷⁵ but are classified as capillary pores using concrete science notation are likely to be less influential on material transport properties.

These observations may provide an explanation to the increase in moisture diffusivity of heat only specimens with respect to LITS affected specimens reported by Černý *et al.*²⁹. These authors suggested that the presence of load before heating could have caused cracking which reduced the build-up of vapour pressure in gel pores during heating and thereby prevented explosive microcrack opening. This hypothesis appears plausible when the results of this study are considered. The smallest pores appear undamaged in L06H250 specimens whereas larger capillary pores experience a greater increase in frequency in H250 specimens.

The results also provide support for the hypothesis presented by Khoury *et al.*¹⁷, who proposed that the increase in residual strength which these authors observed in LITS affected concrete specimens was due to a suppression mechanism that reduced the damage associated with specimens heated without a confining load.

The results presented here do not however support the microdiffusion theory or LITD to any great extent since the hypothesis of Bažant and Chern⁴⁴ and Petkovski¹ who proposed that the mechanism causing LITS involved the microdiffusion of moisture between gel pores and capillary pores which would result in increased damage particularly located at this interface.

7.7. CONCLUSIONS

No evidence has been found to suggest that LITS results in an increase in the porous volume fraction with respect to specimens that have experienced heat only. Quantitative differences in the microstructural characteristics of LITS affected specimens have been observed both in the size distribution of pores and in the density of the material. These changes indicate the presence of a microstructural mechanism which causes LITS as a result of changes to the pore structure.

PART 3: *IN-SITU* ANALYSIS

8. *In-situ* specimen conditioning and experimental methodology

8.1. INTRODUCTION

The experimental investigation of microstructure evolution *in-situ* using X-ray CT represents a new research front in the study of fracture mechanics in engineering materials. These experiments allow for the quantification of material properties during incremental loading and for the validation of 3D FE models meshed from unloaded datasets.

8.2. EXISTING LITERATURE

The research presented in Part 2 of this thesis involved observation of material microstructure *ex-situ*. Here, specimen preparation precluded the analysis of individual specimens in both the *pre* and *post* conditioned state meaning the chronology of LITS development could not be studied. The nature of the conditioning and particularly the cooling of specimens has also meant that it cannot be discounted that the microstructural changes which were observed may have been due to processes other than LITS. Additionally, it was necessary to frame the observations in the context of a statistical analysis of a number of datasets which limited the applicability of X-ray CT results in particular.

To overcome these challenges, *in-situ* X-ray CT experiments have been employed in existing literature to study the evolution of material properties during conditioning. X-ray CT is a particularly amenable technique for *in-situ* characterisation since it is non-destructive. The X-ray CT equipment can often also accommodate significant supplementary experimental apparatus which may be required to condition specimens.

To conduct an *in-situ* X-ray CT investigation, a specimen is placed within the experimental equipment and scanned under ambient conditions. The microstructural process which is the subject of the study is then allowed to progress. This may be a chemical process such as that which occurs during cement hydration or a physical process such as the application of a confining pressure. Further scans of the specimen are obtained at subsequent incremental stages in the conditioning process. Provided that identical beam conditions are employed throughout the experiment and that post processing steps are comparable in each case, a direct comparison of datasets obtained during the experiment can then be undertaken. In addition to the quantitative review of material phase evolution, a technique known as

digital volume correlation (DVC) can also be carried out on the 3D dataset to map the strain development profile across the microstructure.

In-situ X-ray CT has been used to study microstructural evolution in a variety of materials. What was likely to be the first application of the technique was carried out by Guvenilir *et al*¹⁰⁷ in 1997. These authors studied the developing crack morphology of a notched tensile sample of an aluminium alloy at a number of stress intensity increments using a bespoke manufactured load frame. A recent review of the field by Stock¹⁰⁸ indicates that the technique has been used to study the behaviour of animal bone structures under load¹⁰⁹, aluminium foam deformation¹¹⁰, three point bending in laminated composite materials¹¹¹ and solidification^{112,113} among other processes.

With respect to the study of cementitious materials, *in-situ* characterisation has been applied to investigate the development of hydration products and porosity of OPC paste specimens^{114,115,116,61}, crack propagation in mortar^{65,66,117,69,118} and paste¹¹⁹ specimens under uniaxial loading and splitting in cylindrical mortar specimens^{120,121}. In each of the investigations, the content and morphology of the pore structure and solid structure of the material could be characterised with respect to time and applied load. In the case of uniaxial tests and split cylinder tests, these quantitative measurements could then be related to fracture energy and bulk splitting strength in order to investigate the relationship between macroscopic material properties and microstructural evolution.

To obtain high quality data during *in-situ* analysis of microstructural processes using X-ray CT a number of challenges must be overcome which are not present during *ex-situ* X-ray CT. In order to obtain an accurate representation of material behaviour due to the process under investigation, both the process and any experimental apparatus must be unaffected by the prolonged exposure to the X-ray source. For biological materials this requirement is particularly challenging. Whilst, cementitious materials are not affected to any great extent, this requirement extends to experimental apparatus where certain precautions may need to be taken to ensure adequate protection is provided to electronic equipment.

Another of the principal challenges encountered is that of minimising acquisition times to prevent image blur due to continued evolution of material microstructure during scanning. This challenge requires detailed knowledge of the process occurring within the material, appropriate specimen and rig design and an understanding of the capabilities of the X-ray CT equipment.

Finally, *in-situ* specimen conditioning equipment must be designed to minimise or negate X-ray attenuation by component parts which would result in a reduction in contrast within the material under test. Any absorption must be uniform across the specimen in order to facilitate image segmentation and feature quantification.

The *in-situ* study of cementitious microstructure under coupled thermal and mechanical loading using X-ray CT has not at this stage been the subject of any previous investigation. However, a number of recent studies have attempted to characterise the microstructure of aluminium alloys in both compression and tension at elevated temperature. Phillion *et al*¹²², investigated an Al-Mg alloy subjected to tensile load at 528 °C over a range of strains up to material failure. These authors were able to characterise the development of porosity formed during casting at an image resolution of 9 µm. An Instron load frame with a 4.5 kN load cell was employed for the test with heating provided by electrical resistance heaters situated both above and below the specimen.

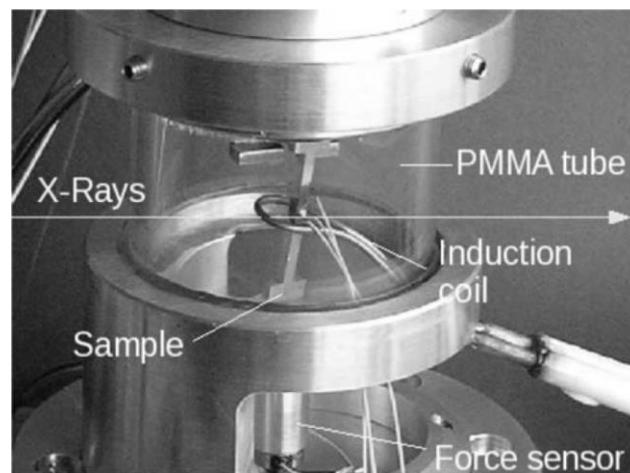


Figure 8.1: High temperature tensile rig employed by Terzi *et al*¹²³

Other authors have utilised induction coils to heat the specimen locally^{123, 124}, however this technique would not be feasible with the material under investigation here. Alternatively, furnace equipment has been designed to enclose the specimen to provide uniform heating throughout the chamber¹²⁵. This equipment consumes a large volume and is limited to use on parallel beam synchrotron X-ray sources.

Here, an *in-situ* X-ray rig will be designed and built in order to condition mortar and paste specimens under combined thermal and mechanical loading allowing LITS to be induced in specimens. The key challenges as described in this literature review will be addressed and the methodology for preparation of appropriate specimens is presented. An extensive commissioning test programme will also be presented to verify material behaviour before the results of a full X-ray CT analysis are presented in Chapter 9.

8.3. EXPERIMENTAL DESIGN AND METHODOLOGY

8.3.1. Existing rig

An *in-situ* tension rig was already part of the existing capability at the HMXIF, University of Manchester before the start of this investigation. This equipment was designed at the Institut national

des sciences appliquées (INSA), Lyon and built by the Science and Technology Facilities Council (STFC), Daresbury. The rig shown in Figure 8.2 was equipped with twist lock grips designed to restrain T-shaped specimens. The rig was specified with a screw type motor unit rated at 10 kN, a calibrated 5 kN load cell and a linear variable displacement transducer (LVDT) for displacement measurement. Measurements from the load cell showed an accuracy of ± 2 N and the LVDT ± 2 μ m. The specimen chamber had an inner diameter of 60 mm with specimen sizes governed by the capability of the load cell in particular. Whilst no facility for compressive loading was originally provided the rig offered a number of advantages as a base unit for conversion to a coupled thermo-mechanical load rig.



Figure 8.2: 5 kN uniaxial compression rig at the HMXIF

Firstly, because the control systems for the mechanical loading system were already in place and required only minor software modifications to convert the load cell to register compressive loading, significant savings in terms of both cost and time could be achieved over designing an entirely new rig. Secondly, as a result of its design which incorporates a wide compression ring, the rig is capable of being used on a variety of different X-ray CT equipment including both cone beam laboratory based sources and parallel beam synchrotron sources. This allows significant flexibility which does not limit experiments to a particular equipment location. Such capability is especially useful when beam time is infrequent and expensive.

These benefits were sufficient in persuading the author to adopt the existing tension rig as a base unit for modification in this experimental programme. However, the design of the rig also enforced certain restrictions on the modified components. These restrictions fell principally in the area of the Poly(methyl methacrylate) (PMMA) compression ring redesign which will be discussed in section 8.3.2 and on the heating/cooling system design which will be addressed in section 8.3.3.

8.3.2. Replacement window

The PMMA ring supporting the motor unit above the specimen shown in Figure 8.2 fulfils two roles. The first is to support the motor unit and transfer the reactionary force generated through applied loading to the base unit. The second is to provide a window which is transparent to X-rays and does not significantly absorb X-rays. These two roles apply competing restrictions on its design and a trade-off must be sought to obtain the optimum design. If a new rig were to be designed, this problem could be overcome by using non-rotational tension/compression bars. This design removes the requirement for a window by mounting the load frame on the X-ray CT equipment outside the rotational stage and by using bearings to transfer load from the load frame to the specimen stage.

In our case, the existing window was designed to allow specimens to be loaded in tension and thus a compressive force was induced in the PMMA. However, for the rig to be operated in compression the window would be required to resist tensile forces. Whilst the existing material could withstand compressive forces up to 5 kN it could not withstand compressive forces of this magnitude – particularly at the connections.

An optioneering study was carried out to determine the best solution to this problem. An increase in thickness in the PMMA material was considered along with a change in material to high grade aluminium. First, the required thickness of material was calculated based upon the tensile, compressive and shear strength properties of each. Mechanical failure was assessed both in the ring and at the connections to the base unit and motor body – the latter placing the greatest restrictions on material thickness. Both the loading and the material were factored to account for user error and material defects respectively. The mass attenuation law (Equation 1) was then used to calculate X-ray transmission (I/I_0) across the range of likely applied energies. The mass attenuation coefficients for each material were obtained from the National Institute of Science and Technology material database¹²⁶. The results of the study can be observed in Figure 8.3.

$$I/I_0 = \exp[-(\mu/\rho)x]$$

0-1: Exponential attenuation law where a narrow beam of monoenergetic photons with an incident intensity I_0 , penetrating a layer of material with mass thickness x and density ρ , emerges with an intensity I .

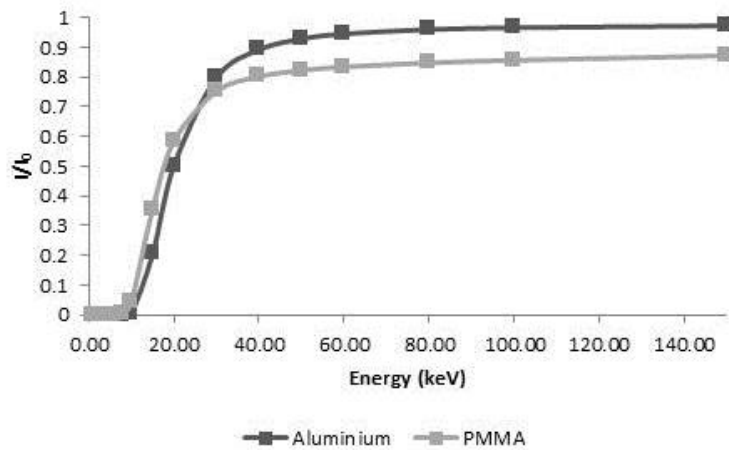


Figure 8.3: Optioneering study

The data shown in Figure 8.3 represents X-ray transmission through a 2 mm thick sheet of aluminium versus that through an 8 mm thick sheet of PMMA. Below 20 keV the materials show similar behaviour. However, above this level and particularly in the region between 60 and 100 keV where laboratory based X-ray CT experiments studying cementitious materials are often carried out, the aluminium is significantly less attenuating on the order of approximately 10 %. Aluminium also offers benefits in terms of durability and heat resistance. The argument against this material is that it is not possible to see the specimen to gain visual confirmation that it is seated correctly. In mitigation, this is possible once the equipment is installed in the X-ray CT device. On balance it was decided that aluminium would be chosen as the material for the manufacture of the new window. Fabrication drawings are presented in Appendix B.

8.3.3. Heating/Cooling system

Due to the prolonged exposure of specimens to high temperature conditions it was necessary to design a cooling system which insulated the mechanical control systems from the heating elements to prevent damage to the electrical control components. Due to the application of compressive loading to the specimen the material which was chosen to thermally isolate the heaters and specimen needed to be capable of withstanding both thermal and mechanical loads. A ceramic material known as Macor which is a machineable glass ceramic offered the desired properties. Macor has a compressive strength of 345 MPa and is thermally stable up to temperatures in excess of 800 °C in compression¹²⁷.

A finite element analysis of the proposed system incorporating the Macor insulation was carried out using the Abaqus software package. This analysis indicated that a mechanism to permit the removal of heat would be required in order to facilitate extended operating at temperatures of approximately 200 °C. The methodology employed on the mac^{2T} apparatus³ to achieve this function consists of a water cooled labyrinth system within a Durehete steel casing. Other options such as liquid nitrogen

and air cooled systems were evaluated. However, due to the availability of a water chiller and pumping system from an existing furnace rig at the MXIF it was decided that a water cooled system similar to the mac^{2T} would be the most effective option.

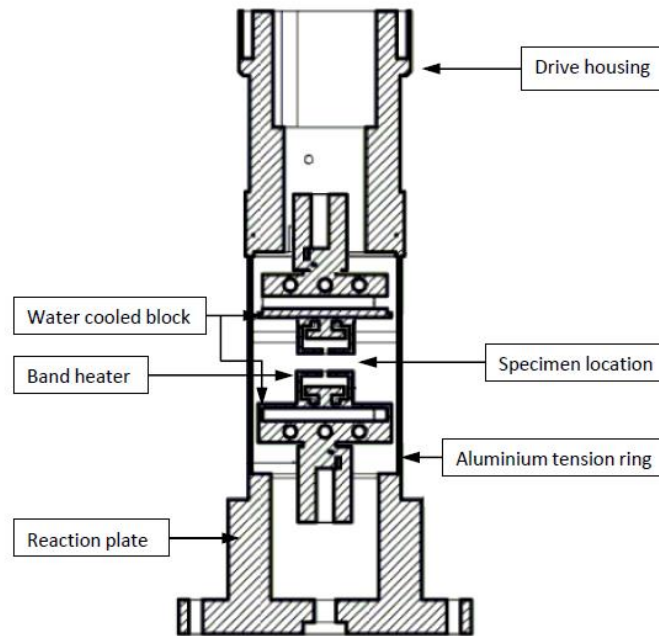


Figure 8.4: Schematic drawing of key rig components

Further Abaqus modelling indicated that with the design illustrated in Figure 8.4, a water cooled block system positioned both above and below the specimen with a heat sink to return water at 20 °C would be capable of maintaining the desired temperature within the specimen. Durehete 950 steel was once again chosen as the material for the fabrication of both the water cooled blocks and the loading plattens due to its low creep and thermal relaxation properties¹²⁸. Two types of loading platen were designed to accommodate both compressive loading on a flat platen and tensile loading using a twist grip platen for T-shaped specimens similar to those on the original equipment. Heating was provided using two SQ5 240 Volt band heaters provided by Elmatic.

8.3.4. Heating Control System

Thermal control is provided by a national instruments control system and a labview based code. The code performs three distinct functions. The first is to generate setpoint values over time from a user initialised point activated through the proportional-integral-derivative (PID) on/off switch based upon the target temperatures at times specified in the user interface. The setpoint values represent the target temperature at each time increment following initialisation and these are passed into system through a selection function which allows for a zero temperature value to be sent to the system once the final user specified time target has been reached to prevent further uncontrolled heating.

The second function provides temperature input from a series of five thermocouples located on the rig. These input values provide both for monitoring and for continuous feedback provided through the PID controller discussed below. Due to issues encountered with electronic noise in the data which was determined to be as a result of the magnetic field induced around the power supply cabling for the heaters which was in close proximity to the thermocouple cabling a modal filter was applied to the raw data averaged over ten iterations which was sufficient to remove these erroneous values and prevent heater firing and thermal runaway. This function also incorporates a data logger which outputs the filtered temperatures from the five thermocouples to a .CSV file along with the current time and the setpoint temperature from function one.

The third and final function incorporates the PID controller which determines the output voltage to be applied to the heaters based upon the setpoint temperatures from function one and the current temperatures from function two. A PID controller is a control loop feedback mechanism which calculates an error value from the difference between the temperatures measured on the rig in function two and the setpoint specified in function one. By adjusting the process control output which in this case is the voltage supplied to power the heater, the PID controller attempts to minimise this error.

The process, integral and derivative terms are used to denote the three separate constant parameters that are used to weight the effect of the present error (P), the accumulation of past errors (I) and the prediction of future errors (D) based on the current rate of change. Here, values of 1, 0.1, and 0 were used for the P,I and D parameters respectively as this was found to give the most accurate response.

Downstream from the PID controller, two additional controls were implemented to allow a greater control of the input temperature to setpoint temperature tolerance. Firstly, a control parameter was introduced to the voltage output signal from the PID controller which prevented the heaters from being energised whilst input temperatures were of a greater magnitude than the setpoint values. Secondly, a pulse wave modulation function applying square waves with a frequency of 1 Hz to the PID output was incorporated. These two controls enabled a tolerance of ± 2 °C to be achieved in temperature control.

8.3.5. Thermo-mechanical load rig

An image of the completed system is given in Figure 8.5 indicating key components and the complexity of the wiring system. For simplicity, the control systems for the thermal and mechanical loading were operated as separate systems with datalogging aligned by starting experimental time simultaneously. The mechanical control unit is connected to the rig via five independent data streams. These are; the motor input stream, the LVDT output stream, the load cell output stream and two limit switches. The thermal control unit is connected to the rig via six independent data streams. These are; five thermocouple output streams and one voltage control input stream for the two band heaters which

are control as one unit. Four water lines are also required to run between the chiller cabinet and the water cooled load blocks. Extensive cable runs are required in order to allow the operating systems and chiller cabinet to be located outside of the X-ray CT device.

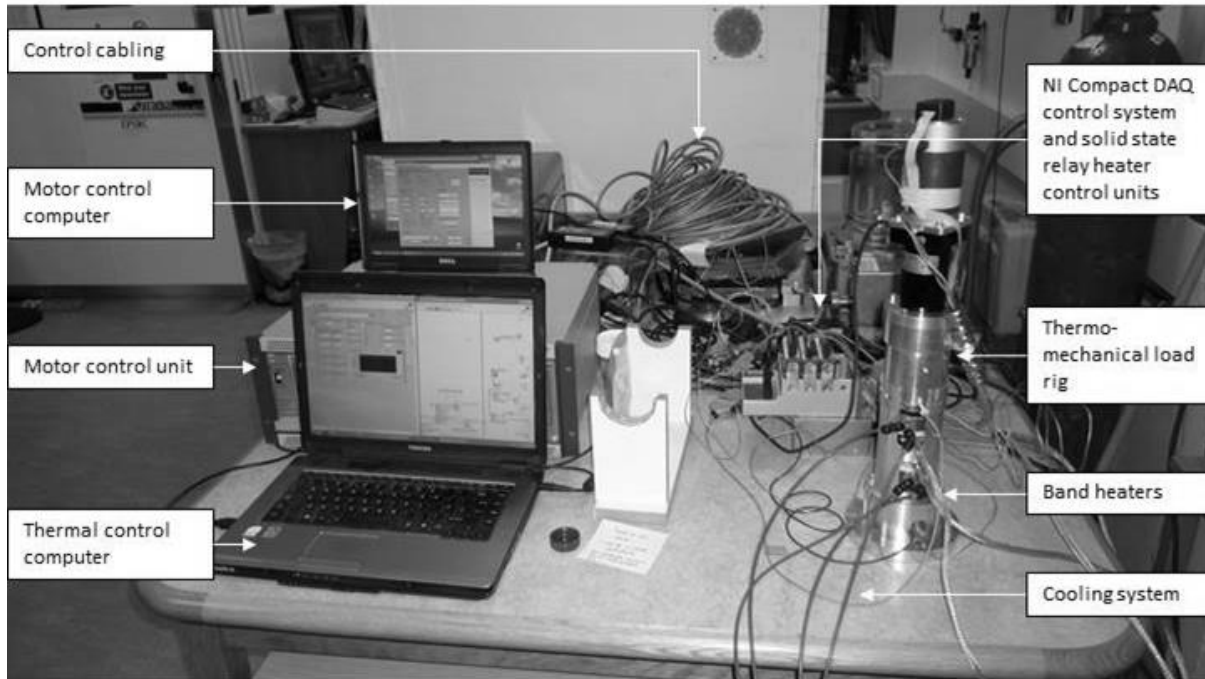


Figure 8.5: Thermo-mechanical load rig

8.4. MATERIALS

Three mix specifications were prepared for the *in-situ* investigation. First, as a result of the limitations encountered when using microstructural analysis techniques to study cementitious materials with large aggregates which have distinct crystalline phases, cement paste specimens were prepared with a mix design according to table 8.1.

Table 8.1: Cement paste mix proportions (OPC = Ordinary Portland cement; PFA = Pulverised fuel ash)

Constituent Name	OPC	PFA	Plasticiser SP4	Water
Cement Mass Ratio	1	0.33	0.0006	0.56
Constituent/binder mass ratio	0.75	0.25	0.0045	0.42

Trial mixes were been produced and uni-axial compressive strength testing on 100 millimetre cubes is presented in table 8.2.

Table 8.2: Cement paste trial compressive strength test results

	3 days	7 days	28 days
Compressive strength (MPa)	30.35	36.64	44.05

Secondly, mortar specimens with a mix design specified in table 8.3 were produced. The choice of mortar specimens was made in order to provide a comparison between cement paste and structural concrete. Data on the macroscopic stress-strain response will not be valid when compared with the behaviour of typical structural concrete. However, according to Landis et al.⁶⁵ if such concrete is considered as a two phase material, with mortar as one phase and large aggregate as another, then the results of this study will have relevance to the first.

To provide a comparison with the tests on concrete carried out in part 2 of this thesis, the mix designs were proportioned to match the mortar phase of the earlier specimens. However, due to the required specimen dimensions, which will be discussed later, a maximum aggregate size of 0.5 mm was attained through sieving.

Table 8.3: Mortar mix proportions (OPC = Ordinary Portland cement; PFA = Pulverised fuel ash)

Constituent Name	OPC	PFA	Sand	Plasticiser SP4	Water
Cement Mass Ratio	1	0.33	2.45	0.0006	0.56
Constituent/binder mass ratio	0.75	0.25	1.84	0.0045	0.42

8.4.1. Specimen casting and storage

The three mixes were cast in slabs with dimensions of 740 x 620 x 150 mm and immersed in temperature controlled water tank with a 10 day temperature matched curing cycle in which the temperature reached a maximum of 65 °C (Figure 8.6). This simulated the transient temperature increase observed on casting of AGR pressure vessels. Following the 10 day cycle, the slabs were de-moulded and returned to the water tank for a further 60 days at 20 °C¹⁶. Each slab was then cut and ground using water cooled equipment to form right regular 100 mm cubes. The machined cubes were stored at room temperature and humidity until conditioning before further specimen preparation was carried out.

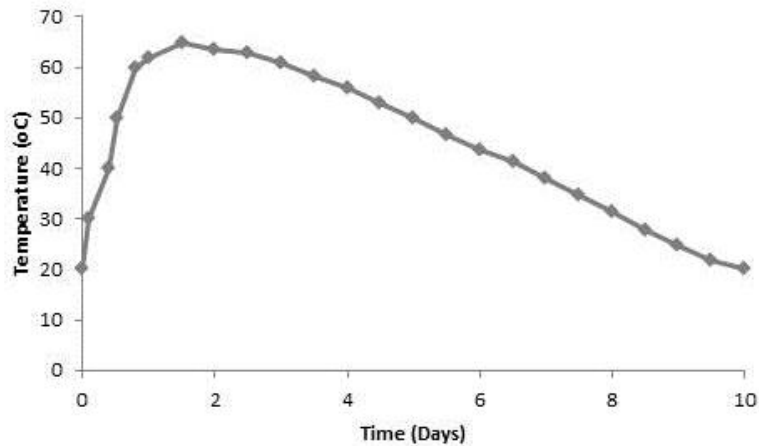


Figure 8.6: Temperature matched curing profile for concrete showing instrument controlled water bath temperature during first ten days following casting.

8.4.2. Specimen preparation

A number of methods were explored to prepare specimens for microstructural analysis using X-ray CT. The ideal specimen geometry consists of a cylinder of material for optimum X-ray adsorption conditions across the height of the material. This specification left a number of options for specimen preparation including; casting specimens directly into moulds, coring specimens and polishing the top and bottom faces right regular and cutting right regular slices of the material followed by coring directly from the slices.

With respect to casting cylindrical specimens directly, since it was necessary to carry out the experiments on mature material and the exact dimensions of the specimen were dependent on the Beamline configuration which could not be known until the construction of the rig was complete, It was deemed too high a risk to cast specimens of a particular diameter and height well in advance. In this case, previous experiences indicated a difficulty in obtaining representative samples due to the orientation of sand particles in mortar specimens which appear to agglomerate to a greater extent in smaller specimens. For these reasons this method was discounted.

A method of coring and polishing the top and bottom faces of specimens was also considered. However, previous experience showed this to be a challenging process where quality was difficult to control, particularly with a large batch of material. Therefore the method of choice used to prepare specimens was to use a diamond tipped saw blade to cut the cubed specimens into disks of varying thickness. A diamond tipped coring drill of an appropriate internal diameter was then used to cut cores from these disks. A high rotational speed and slow vertical acceleration during drilling was found to yield specimens with no obvious signs of damage. In all cases and for each operation, water was used

to cool the cutting faces. Following cutting the specimens were surface-dried and stored at room temperature/relative humidity.

8.5. RIG COMMISSIONING

To convert the existing rig to operate as a load frame in compression as well as tension required the reassignment of channels on the load cell data logging card. The data logging card was equipped with 5000 channels which resulted in a reduction in the precision of logged data by a theoretical amount of approximately twice the original value of ± 1 N. To determine the practical effect this recalibration would have on the accuracy of data readout from the load cell a specimen was held under a nominal compressive force of 50 N in Force control during a thermal cycle between 25 and 200 °C. The results presented in Figure 8.7 indicate that the precision of the load cell is reduced further than theoretical predictions to ± 5 N.

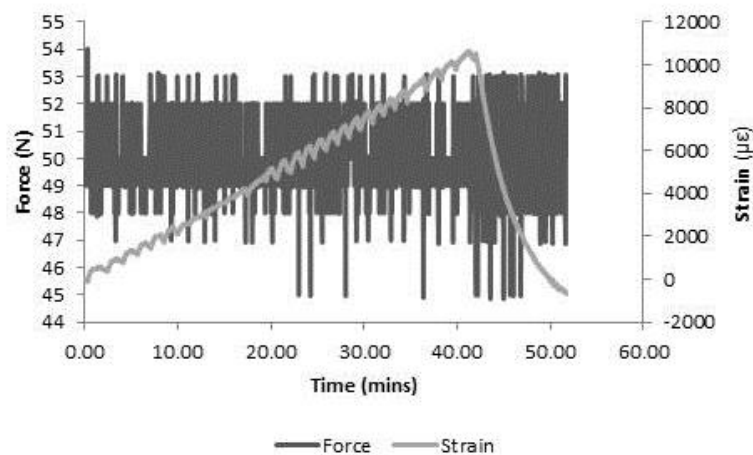


Figure 8.7: Force data logging readout in force control during one thermal cycle of heating between ambient temperature and 200 °C

Verification of the functionality and precision of temperature control systems is provided by the results in Figure 8.8. A mortar specimen was heated from ambient temperature to 200 °C at 5 °C/min which represents the fastest heating rate required of the apparatus. The results indicate that a precision of ± 4 °C is achieved with the selected hardware and software setup.

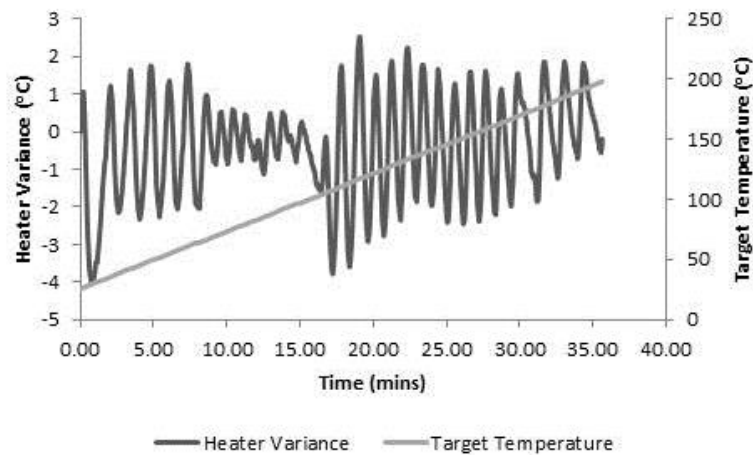


Figure 8.8: Variance in heater temperature with respect to the target temperature during one heating cycle from ambient temperature to 200 °C

Under test conditions the temperature of the specimen could only be ascertained from the temperature recorded in the thermocouples mounted on the heaters. To verify that the specimen temperature followed that of the heaters within an acceptable tolerance a K-type thermocouple was mounted in the centre of a specimen using thermally stable glue. The specimen was then mounted in the rig and subject to one thermal heat cycle from ambient temperature to 200 °C. The results shown in Figure 8.9a indicate that the temperature within the specimen lies within ± 2 °C of the target temperature during heating within the aforementioned temperature range.

In addition to temperature measurement within the specimen, a thermocouple was mounted both in the body and in the base of the rig behind the cooling platens to ensure that no heat flux was transferred to the motor unit of X-ray CT manipulator arm respectively. Figure 8.9b illustrates the temperatures measured by these thermocouples during one heating cycle from ambient temperature to 200 °C. No increase in temperature outside of the cooling platens is detected.

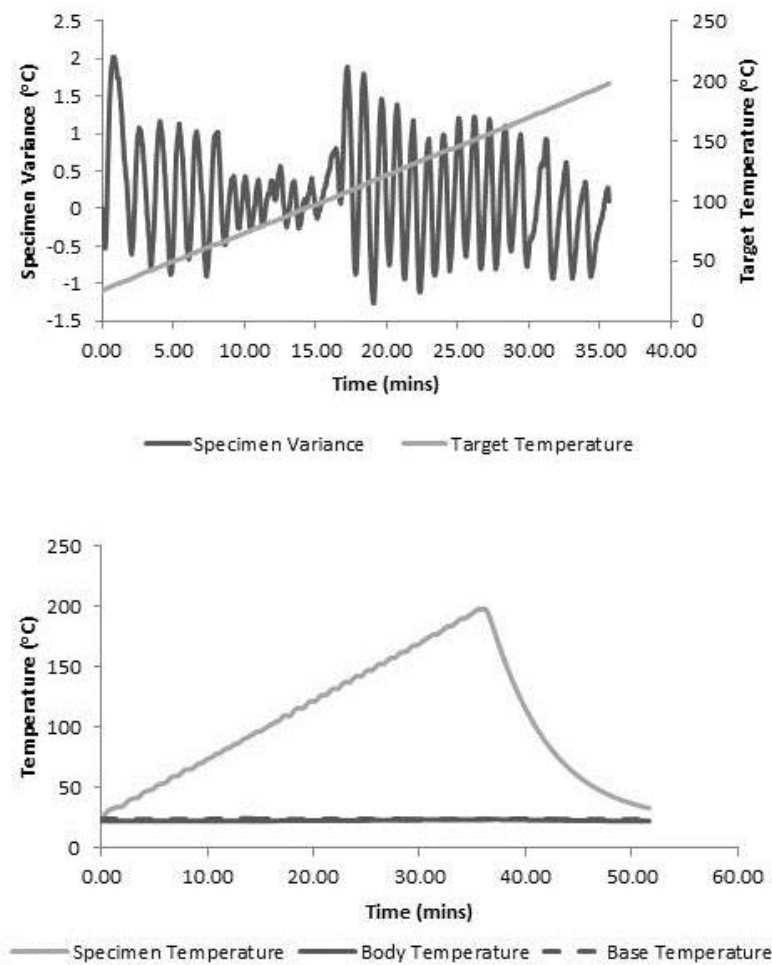


Figure 8.9: a) Specimen temperature variance with respect to target temperature during one thermal heat cycle from ambient temperature to 200 °C, b) Temperature recorded in thermocouples mounted within the body and base of the rig during one thermal heat cycle from ambient to 200 °C

The LVDT for the measurement of strain within the specimen is located outside of the heating zone. This setup was chosen to avoid damage to the LVDT caused by a thermal gradient within its housing. However, it does mean that the additional strain measured from the thermal expansion of the cooling platens, heaters and loading platens must be accounted for when calibrating measurements taken from this equipment. In this case, calibration was carried out by manufacturing three specimens composed of three different metallic materials with differing thermal expansion coefficients. Aluminium, copper and mild steel disks with a diameter of 10 mm and heights of 10 mm were fabricated from material with supplier datasheets indicating the thermal expansion coefficients shown in Table 8.7. Figure 8.11 along with Table 8.7 also indicates the difference in thermal expansion between the three reference materials during one thermal cycle from ambient temperature to 180 °C. To obtain a unitary value of thermal expansion in the non-specimen rig components the actual value of thermal expansion calculated using the datasheet was subtracted from the measured expansion using the LVDT. When

comparing the values obtained from this calculation for the three materials a good agreement for component expansion of $117.34 \mu\text{m} \pm 1.5 \mu\text{m}$ was observed. By dividing this by the increase in temperature, a value of $0.757 \mu\text{m}/^\circ\text{C}$ was calculated for the rig.

Table 8.4: Thermal expansion coefficients, measured and actual expansion in three reference materials

	Aluminium	Copper	Steel
Thermal expansion coefficient (m/m/ $^\circ\text{K}$)	2.20E-05	1.66E-05	1.40E-05
Measured expansion(μm)	152	144	136
Actual expansion(μm)	34.10	25.73	21.70

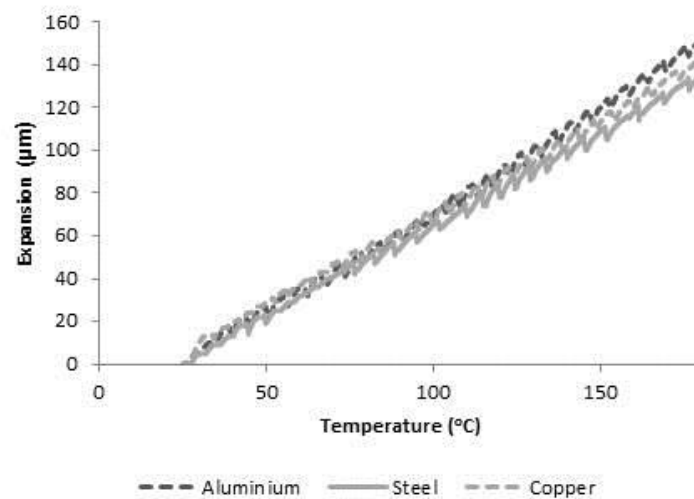


Figure 8.10: Thermal expansion of aluminium, copper and mild steel during one thermal cycle between ambient and 180 °C

In order to verify the behaviour of the specimens as a representative elementary volume of material, the stress-strain behaviour and ultimate strength data for three specimens tested under uniaxial compression to failure following four incremental load increases through $0.25 f_{cu}$, $0.5 f_{cu}$ and $0.75 f_{cu}$ were compared. The results of these tests are shown in Figure 8.11 and Table 8.8. A good correlation between the behaviour of specimens is observed in all cases.

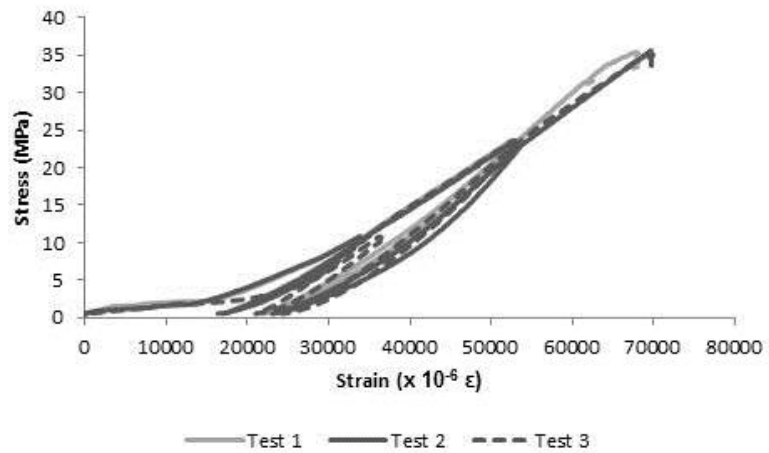


Figure 8.11: Stress - strain data for three 11 mm diameter, 10 mm high specimens loaded in a cyclic profile at 0.25, 0.5 and 0.75 f_{cu} before testing to failure

Table 8.5: Mechanical strength of three specimens tested under uniaxial compression at elevated temperature

	Test 1	Test 2	Test 3	Average
Ultimate compressive strength (MPa)	45.18	43.40	44.76	44.44

8.6. DISCUSSION

The precision of the load cell data logging shows a reduction in precision with respect to the calculated theoretical values. The reason for this reduction is unclear but may be a result of electrical noise in the system. To improve the accuracy of the data logging, new hardware with an increase in channels could be installed. However, since the current precision is represents a value of approximately 0.1 % of the force applied to specimens at failure the effort required to increase the accuracy of force data logging was not thought to be worth the budget and schedule costs.

The new systems designed to control heating on the rig show a reasonable ability to apply thermal load to specimens. A precision of ± 4 °C is higher than that specified in our prerequisites before construction. However, this is a significant improvement over the precision provided by the burst fire relay control system which was originally implemented to apply voltage to the heaters. The solid state relay applied in the final hardware configuration has proved significantly more successful and further adjustment of the control software could have yielded a greater level of precision albeit with an increase in schedule costs. On viewing the results of temperature data from the thermocouple embedded in a test specimen, it was decided that the extra effort required to improve the precision of the heater control was unnecessary since the lag caused by heat transfer meant that the cyclic variance in temperature within the specimen was within the specified tolerance of ± 2 °C.

The results from temperature measurements taken both above and below the cooling platens indicate that these systems are successful in removing heat and preventing damage to rig and X-ray CT equipment. However, their size coupled with that of the heaters and loading platens has meant that a large correction must be applied to displacement data in order to calculate thermal strain within the specimen itself. The magnitude of this correction means that it is difficult to isolate the LITS component in strain measurements.

A similar challenge prompted the development of the complex laser interferometry displacement measurement system on the mac^{2T} apparatus³. Unfortunately in this case such a system would not be possible without a significant redesign of the rig due to the limited space available. This would have significant budget and schedule implications that would have moved the project beyond a realistic proposition for the time available in this project.

The calibration of displacement measurements during heating could have been improved by adopting a method used for the calibration of displacement measurements on the mac^{2T} apparatus. This method involved the use of a water cooled tube inserted between the pins connected to the reflector prisms on each axis. In this way the platens could be heated up to the maximum experimental temperature without any specimen displacement thereby giving readings of the exact platen displacement only. However, this method was deemed to be too complex for the limited space available between the platens on our thermo-mechanical load rig.

Finally, results pertaining to the behaviour of mortar specimens under compressive loading to failure show good agreement with one another. This indicates that specimens are large enough to capture a representative elementary volume of material. This vindicates the decision to restrict the size of aggregate in mortar specimen and gives confidence that the results of the X-ray CT analysis will be representative of bulk material behaviour. Such behaviour has not been presented in other instances of the use of *in-situ* X-ray CT analysis in cement based materials.

8.7. CONCLUSIONS

A new capability has been developed to allow the *in-situ* characterisation of cement based materials under thermo-mechanical load. Significant hardware and software modifications were made to an existing tension rig to enable this new range of experiments to be carried out. The results of a number of tests carried out to commission the new thermo-mechanical load rig and calibrate data have been presented here. These indicate that the rig offers a reliable capability with the best possible configuration achievable within budget and schedule constraints. Chapter 9 will next present the results of an experimental programme to investigate the microstructural origins of LITS using *in-situ* X-ray CT analysis.

9. *In-situ* thermo-mechanical loading

9.1. INTRODUCTION

The experimental investigation of microstructure evolution *in-situ* using X-ray CT represents a new research front in the study of fracture mechanics in engineering materials. These experiments allow for the quantification of material properties during incremental loading and for the validation of 3D FE models meshed from unloaded datasets. Here the *in-situ* experimental thermo-mechanical load rig presented in Chapter 8 will be used to investigate the development of LITS and the effect of LITS on the fracture process in an OPC-PFA mortar. The results of this analysis will provide for comparison between *in-situ* and *ex-situ* testing and particularly to elucidate the discrepancy between the hot strength and residual strength of concretes recorded in the literature.

9.2. EXPERIMENTAL SET-UP

9.2.1. Beamline Configuration

Specimens were analysed using the Nikon 225/320 kV Custom Bay at the HMXIF, University of Manchester. The new *in-situ* thermo-mechanical load rig was installed on the manipulator arm within the X-ray CT equipment. However, the rig control equipment including the thermal and mechanical load control systems and the chiller cabinet could not be placed within the X-ray CT bay in order to avoid the potential for damage to the sensitive electronic equipment for the X-ray source and electrical fields associated with the electron gun.

To overcome this problem, this equipment was installed on laboratory benches on the exterior of the X-ray CT equipment and cables/pipework was fed through a labyrinth system situated in the wall of the bay to prevent direct line of sight between users external to the bay and the X-ray source. To reach the rig, the cables and pipework were suspended for the overhead lifting beam above the manipulator arm. This prevented the cables from becoming tangled and interrupting the X-ray acquisition process. Cables and pipework were secured to the rig using tape close to their connection points in order to avoid loosening during rotation. The manipulator arm positioning detailed in section 8.2.3 was chosen in order to obtain the maximum geometric magnification whilst preventing interaction between the *in-situ* rig and the X-ray source.

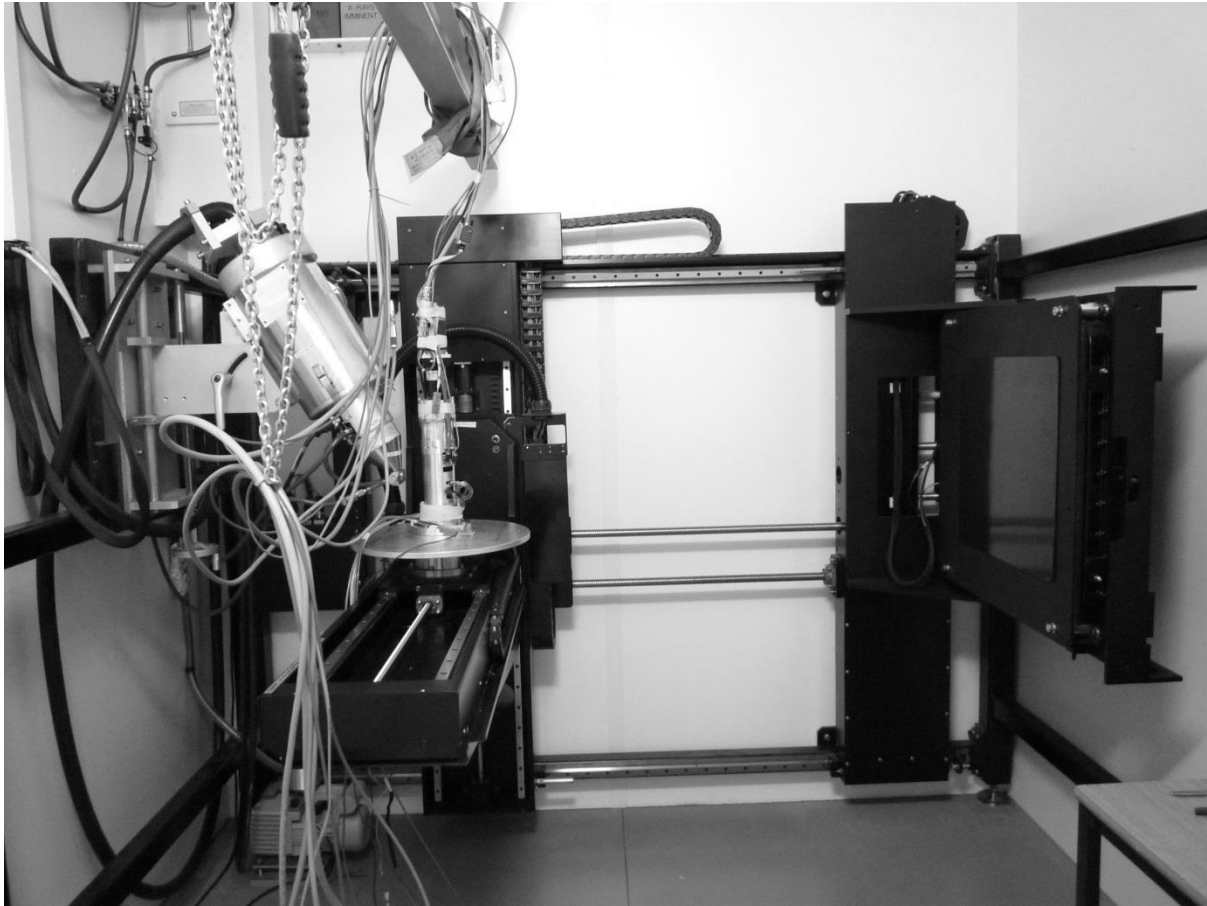


Figure 9.1: *In-situ* rig installed within Nikon Custom bay at the HMXIF

9.2.2. Experimental Methodology

The experimental methodology for the work presented in this chapter can be divided into two sections. These are the conditioning phase of testing and the deviatoric loading phase of testing. First, the *in-situ* loading rig was used to condition the specimens with a diameter of 11 mm and a height of 10 mm. Three principal conditioning regimes were studied (Table 9.1): thermal treatment only (H200L), mechanical load followed by thermal treatment (LITS affected, LH200) and unconditioned control specimens. Following all heating the specimens were held under steady state conditions for a period of 40 minutes before scanning to enable thermal gradients within the material to dissipate.

Table 9.1: Conditioning regimes of the concrete specimens for microstructural analysis (f_{cu} = ultimate compressive strength of concrete)

Conditioning Name	H200L	LH200	Control
Mechanical Loading	-	$0.25 f_{cu}$	-
Thermal Treatment	200 °C	200 °C	-

A heating/cooling rate of 0.5 °C/min was employed in all tests involving elevated temperature. This is higher than that employed in the *ex-situ* tests. The acceleration of heating was necessitated by the limited Beamline access. The maximum temperature obtained in elevated temperature testing was 200 °C. This is again different to that employed in the *ex-situ* tests and represents the limit of the *in-situ* experimental apparatus which could be achieved over an extended period of time without promoting elevated temperatures in the motor body.

Following conditioning, the deviatoric loading stage was commenced. Deviatoric loading was undertaken at 0.25 f_{cu} intervals up to material failure at 1 f_{cu} . In the final interval between 0.75 f_{cu} and 1 f_{cu} , load increase was undertaken in displacement mode rather than force mode to prevent catastrophic material failure. The strain measurements obtained from these tests were used to calculate LITS which is defined as the difference between the LH200 and the H200L conditioning regimes.

9.2.3. Image Acquisition

The 225 kV static source on the Nikon Custom bay was used along with a tungsten target. No X-ray filters were employed since the aluminium tension ring on the *in-situ* rig provided adequate filtering. A power level of 85 kV and 120 μ A was selected to achieve good radiograph contrast. The *in-situ* rig was mounted on the precision 5-axis manipulator arm and the specimen was positioned within the CCD detector field of view. X-ray CT scans were then obtained in line with the appropriate conditioning regimes specified in section 8.2.2. Once a scan had been commenced, the manipulator arm allowed radiographs to be taken at accurate angular steps of 0.199 degrees which equated to 1801 radiographs over a 360° rotation. The source to specimen distance was 88.88 mm, the source to detector distance was 1407 mm and the acquisition time per radiograph was 750 ms.

After data acquisition, all 1801 projections were reconstructed using Metris CT pro software with corrections for the centre of rotation applied. No beam hardening or noise reduction filters were deemed to be necessary at this stage. The reconstructed data in the form of 3D pixels or “voxels” was then down sampled from 32 bit to 16 bit grey-scale in order to reduce file sizes for image analysis.

9.3. IMAGE ANALYSIS

9.3.1. Segmentation

Image analysis of the *in-situ* data was performed using a bespoke 3D image analysis code written specifically for the task in Matlab (Appendix C). A region of interest (ROI) was selected from each scan with dimensions 1000 x 1000 x 500 voxels. This corresponds to a volume of 12 mm x 12 mm x 6

mm. The ROI was chosen to exclude data from the top and bottom of the scan where the presence of the loading platens caused increased noise and blurring in component images.

A 3D median noise reduction filter was applied to the data with a kernel of 3x3x3 voxels in order to improve image quality. This was followed by a 3D shrink-wrapping algorithm which was used to convert voxels outside of the specimen to a null value. Pore segmentation was carried out using the classic minima thresholding technique. Segmented voxels were then analysed using the image processing toolbox algorithms in Matlab to determine their connectivity. In this procedure, the six faces of each voxel in the image are evaluated to ascertain whether a voxel of the same segmented phase is connected¹⁰. Voxels of the same phase which are connected using this criterion are then grouped into clusters or pores in our study. Data is presented with respect to the equivalent pore diameter which is calculated by assuming that all pores are spherical in shape.

Finally, the Nyquist-Shannon sampling theorem¹¹ was used to determine the minimum size of features that could be resolved based on the image resolution of 14.6 μm . This theorem proves that a digital image must have more than two pixels per resolvable element in order to ensure that all features are sampled sufficiently to detect their presence. In this case, three voxels was chosen as the feature resolution limit meaning the smallest detectable porosity in this study has a diameter of 31.5 μm .

9.3.2. Statistical Verification

Statistical verification of the *in-situ* results was undertaken using two methodologies. The first followed the rationale of that applied in Chapter 5 where a sensitivity analysis of the grey-scale value (GSV) distribution was carried out at three increments of 10, 25 and 100 both above and below the GSV corresponding with the minima of one ROI. An error of less than two percent with respect to the total porosity of the material was achieved by selecting a GSV within ± 25 points of the actual minima. This accuracy was easily obtainable through sorting of the GSV data.

The second methodology involved the scanning of a specimen in the unloaded condition on two occasions. In this manner the effects of image blurring/noise, detector sensitivity and image segmentation could be evaluated. Both datasets were subjected to the same process of reconstruction, segmentation and evaluation and the results indicated that variation in total porosity between specimens was once again less than two percent of the value for total porosity.

9.4. RESULTS

The stress-strain response of the three analysed specimens is presented in Figure 9.2a up to 75 % of the ultimate compressive strength of the material. The ultimate compressive strengths of these specimens and one replicate for each conditioning regime is also provided. A significant reduction in strength is observed in both H200L and LH200 specimens over those which were loaded to failure at

ambient temperature of 19.6 % and 16.9 % respectively. H200L conditioned specimens show a small but significant increase in strength loss over LH200 specimens of approximately 2.7 %. The stiffness of H200L and load only specimens appears to be similar throughout the loading range. This behaviour contrasts with that of LH200 specimens which exhibit an increase in stiffness over the other conditioning regimes following the LITS development period at 25 % f_{cu} .

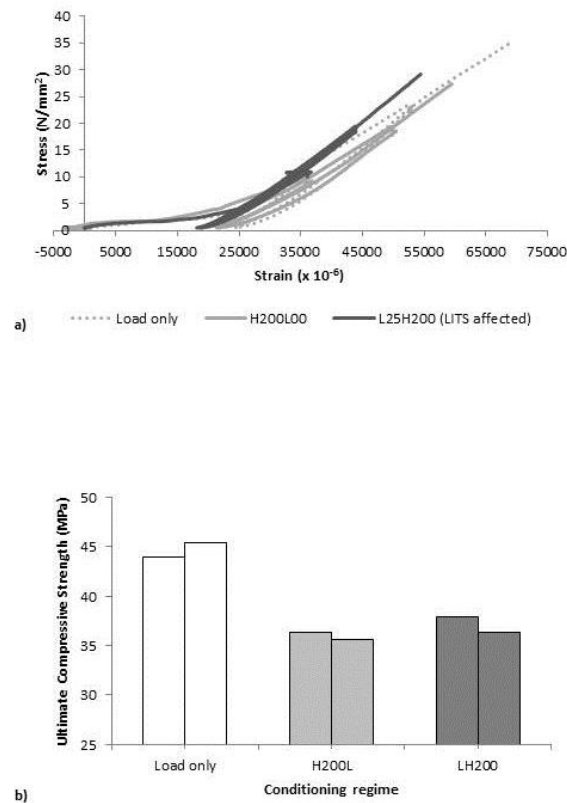


Figure 9.2: a) Stress-strain profiles for Load only, H200L and LH200 (LITS affected) *in-situ* conditioning regimes, b) Ultimate compressive failure strengths for two specimens tested under each regime.

Figure 9.3a summarises the development of shrinkage strains and LITS in the H200L and LH200 specimens which were characterised *in-situ* using X-ray CT. Figure 9.3a shows the strain profile from each specimen following the subtraction of thermal expansive strains that were assumed to apply linearly across the tested temperature range. As discussed in Chapter 8, due to the precision of the LVDT, significant error has been introduced into strain measurements. In order to calculate the magnitude of LITS development in the LH200 specimens a line of best fit was plotted for each dataset. By subtracting the line profile of the H200L specimen from the LH200 specimen LITS evolution between 40 °C and 150 °C could then be calculated. The LH200 specimen exhibited a non-linear strain development above 150 °C.

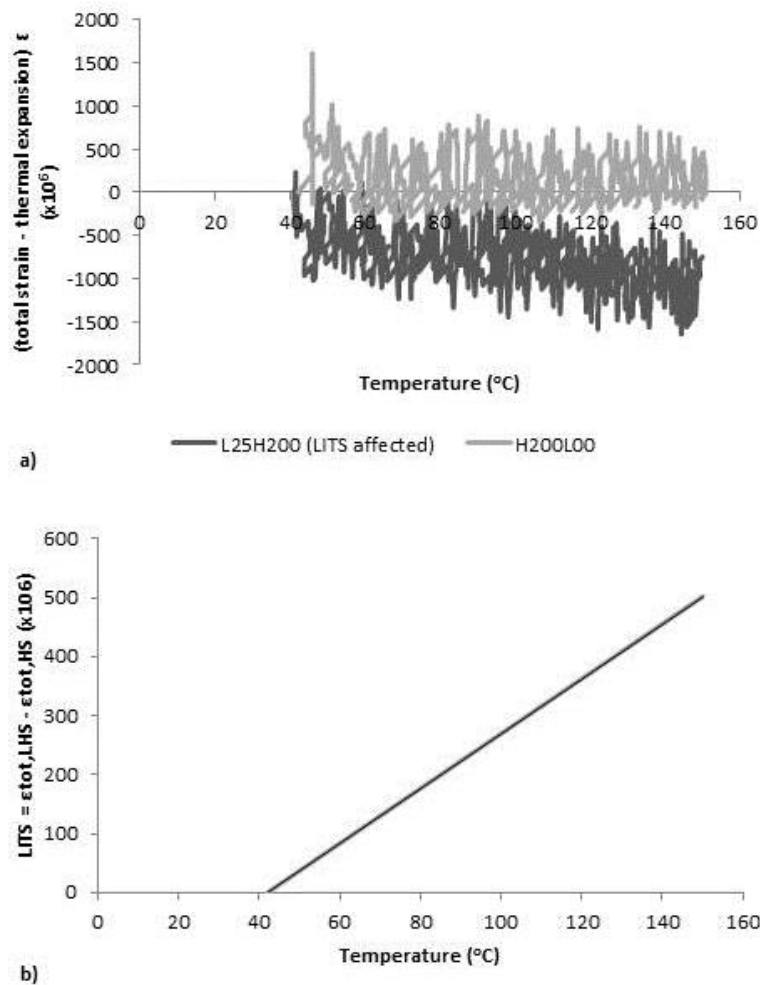


Figure 9.3: a) Average temperature-strain relationships from H200L and LH200 tests: a) LITS and shrinkage, b) LITS. Compactive strains are shown as positive. Instantaneous strain has been removed from LH200 test results.

Figures 9.4, 9.5 and 9.6 show the results of image analysis applied to each of the datasets in the three conditioning regimes analysed in this study. The load only specimen analysis is shown in Figure 9.3. Five scans were performed on the specimen at 0, 25, 50, 75 and 100 % of the compressive strength of the material at ambient temperature (Figure 9.4a). Figure 9.4b indicates the change in total porosity and number of pores across the five scans. Between 0 and 25 % of the material compressive strength, the total porosity experiences a slight reduction of approximately 0.8 %. However, the number of pores decreases sharply in this period. Figure 9.3c indicates that this reduction in pores originates in the smallest equivalent pore size diameter category of $< 30 \mu\text{m}$. A further reduction in porosity is recorded between 25 and 50 % f_{cu} but the change in number of pores is reversed with a partial recovery particularly focussed in the < 30 and $< 40 \mu\text{m}$ pore size categories (Figure 9.4c).

At 75 % f_{cu} a significant increase in total porosity and number of pores over that at 0 % f_{cu} is recorded. This is mirrored in Figure 9.3c by a significant increase in pores within the $> 100 \mu\text{m}$ category. This

change corresponds with the development of large cracks within the specimen. Total porosity continues to increase between 75 and 100 % f_{cu} to a lesser extent along with the number of pores. However, this is significantly less than that in the earlier load increment. The increase in pores is distributed equally across the equivalent diameter range.

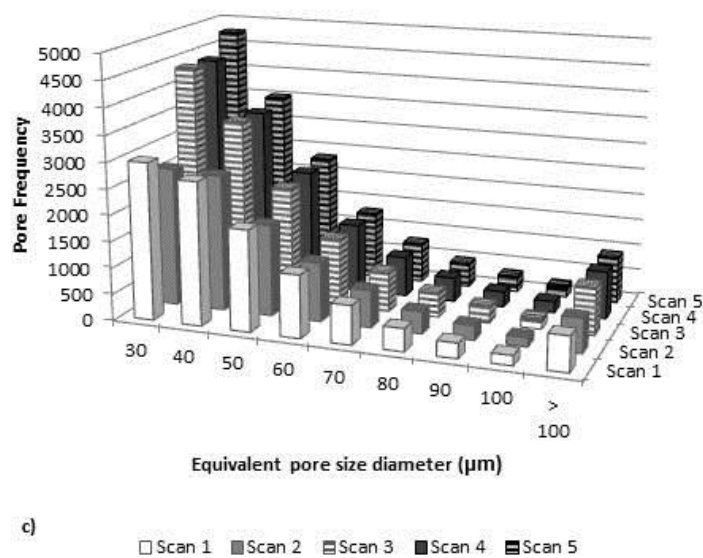
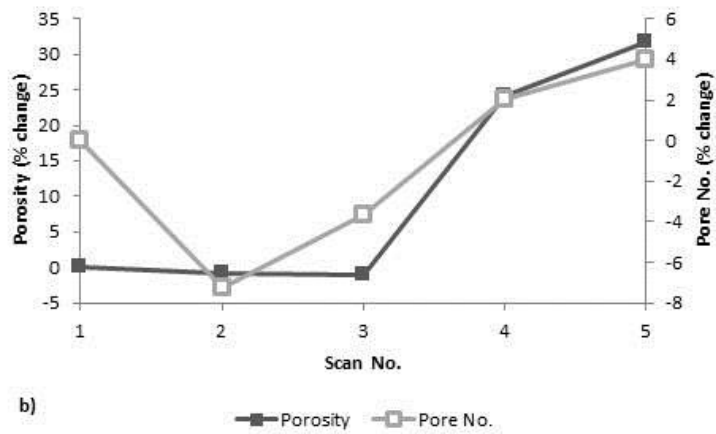
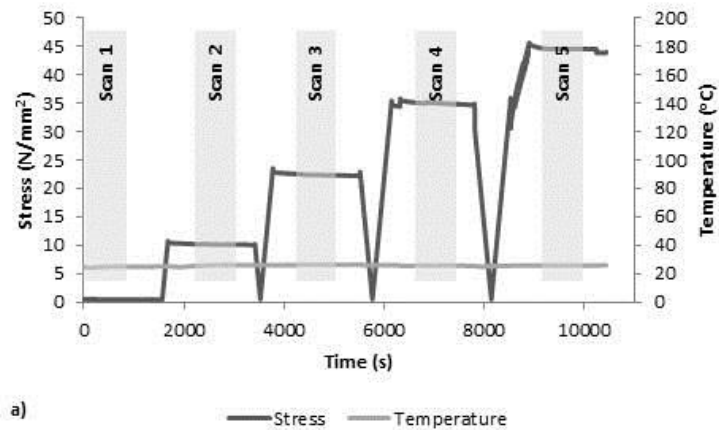


Figure 9.4: Image analysis results from *in-situ* X-ray CT study of porosity in one specimen tested to failure under load: a) Conditioning regime and approximate scan times, b) percentage change in total porosity and No. of pores during conditioning, c) Equivalent pore size diameter distribution during conditioning.

The H200L specimen analysis is shown in Figure 9.5. Six scans were performed on the specimen; in the unloaded ambient temperature state, following heating to 200 °C, and following loading at 25, 50, 75 and 100 % f_{cu} at 200 °C (Figure 9.5a). Figure 9.5b indicates the change in total porosity and number of pores across the six scans. Between ambient temperature and 200 °C, an increase in both total porosity and number of pores is observed. This trend is continued across all scans up to the failure strength of the material. In terms of total porosity a significant increase in the gradient of pore development is observed between 25 % and 50 % f_{cu} which corresponds with a marked increase in pore frequencies in the < 30 and < 40 μm pore size intervals (Figure 9.5c).

The rate at which total porosity increases does not change significantly beyond 50 % f_{cu} . A further increase in pore frequency in the < 30 μm pore size interval is however observed between 75 and 100 % f_{cu} and this corresponds with an increase in the rate of total pore number development. No significant cracking is detected at high loading levels as for the load only specimens and this can be observed both in the pore size distribution data where pore frequencies greater than 100 μm in size remain constant throughout all tests and in the image data where no visible signs of cracking at this image resolution are observed.

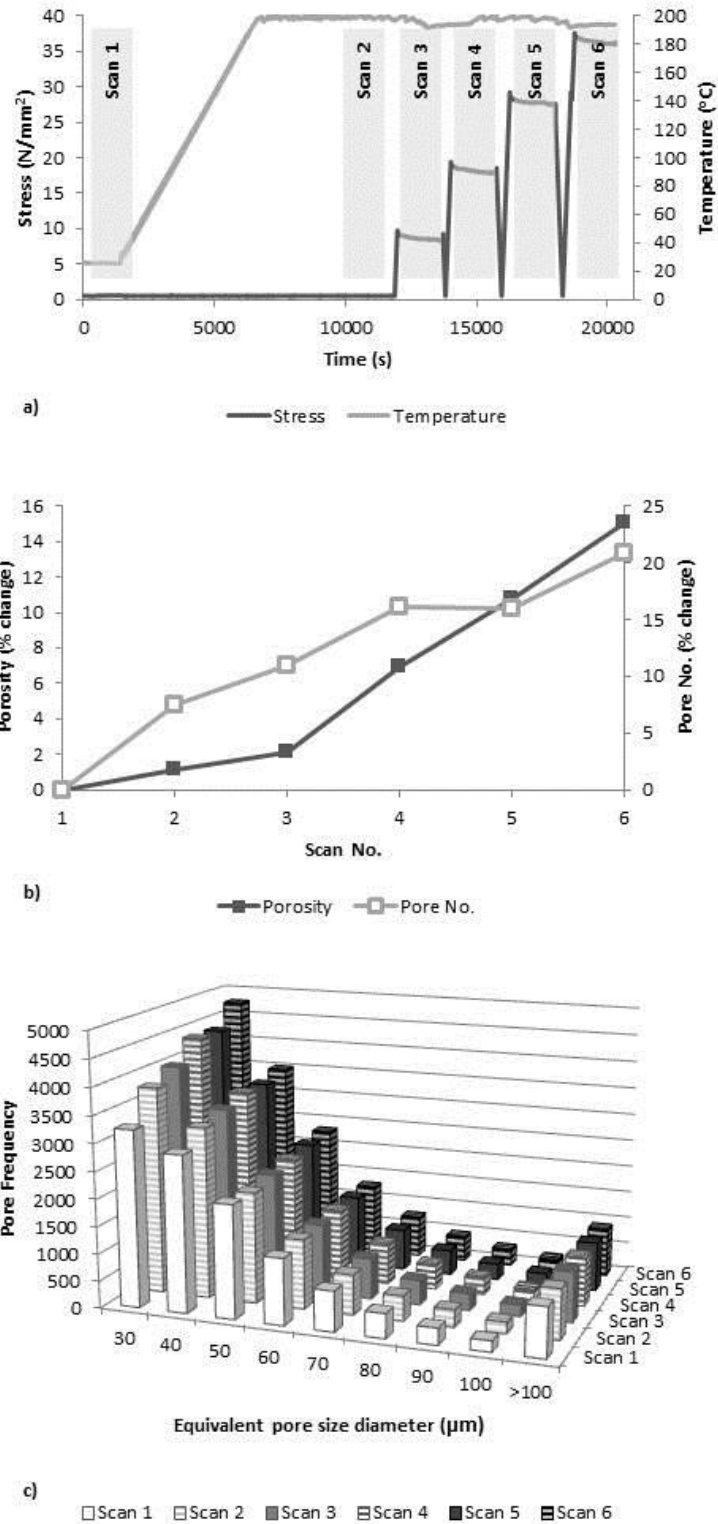


Figure 9.5: Image analysis results from *in-situ* X-ray CT study of porosity in one specimen tested to failure under load following heating (H200L): a) Conditioning regime and approximate scan times, b) percentage change in total porosity and No. of pores during conditioning, c) Equivalent pore size diameter distribution during conditioning.

The LH200 specimen analysis is shown in Figure 9.5. Six scans were performed on the specimen; in the unloaded ambient temperature state, following loading to 25 % f_{cu} , heating to 200 °C whilst holding load and subsequently at 50, 75 and 100 % f_{cu} at 200 °C (Figure 9.6a). Figure 9.6b indicates the change in total porosity and number of pores across the six scans. Between 0 and 25 % f_{cu} a reduction in porosity of approximately 0.8 % is recorded which is similar to that recorded during the load only testing. During heating, the total porosity of the specimen increases above that of the initial value by a magnitude 0.2 % higher than that recorded in the H200L tests during heating.

Following heating the LH200 specimen exhibits significantly different behaviour to that of the other two conditioning regimes. Total porosity is decreased significantly across the loading range along with the number of pores between 75 and 100 % f_{cu} . With respect to pore size distribution, Figure 9.6c indicates little change in the size distribution category greater than 100 μm and no evidence of cracking similar to that in the load only test is observed. At lower length scales a significant increase in pore frequency is observed in the < 30 μm size interval due to heating but this is also accompanied by a reduction in pore frequency in the < 40 μm size interval. Following heating the frequency of pores in these two categories reduces to a level approximately of that before the start of the thermo-mechanical loading.

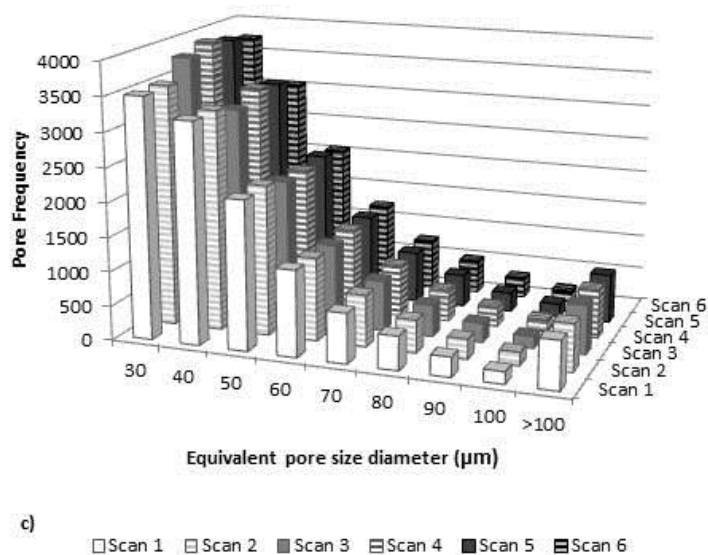
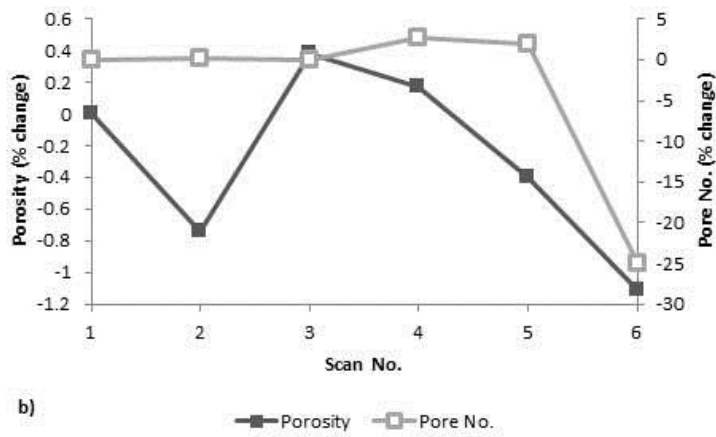
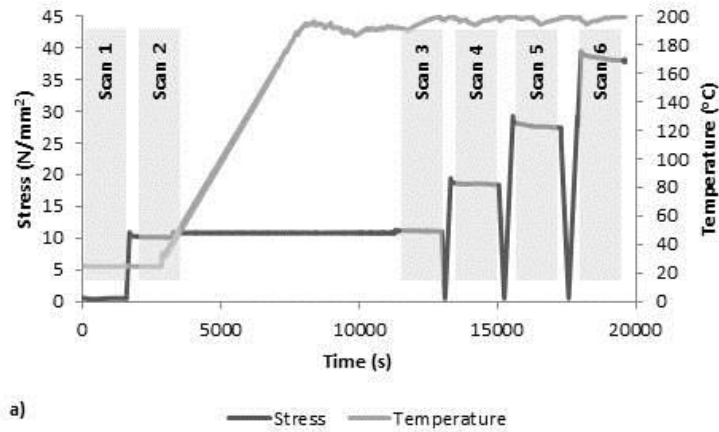


Figure 9.6: Image analysis results from *in-situ* X-ray CT study of porosity in one specimen tested to failure under load following LITS development (LH200): a) Conditioning regime and approximate scan times, b) percentage change in total porosity and No. of pores during conditioning, c) Equivalent pore size diameter distribution during conditioning.

9.5. DISCUSSION

The results of an *in-situ* X-ray CT investigation into the behaviour of concrete under combined thermo-mechanical loading indicates that with respect to air void porosity, a specimen which is subjected to mechanical loading in uniaxial compression to failure experiences an increase in porosity of around 30 %. Secondly, a specimen that is heated to 200 °C before testing to failure in uniaxial compression experiences an increase in porosity of approximately 15 %. Finally, a specimen which is heated to 200 °C under a uniaxial compressive force of 25 % f_{cu} and then loaded to failure in uniaxial compression experiences a reduction in porosity of 1 %.

Additionally, with respect to the total number of pores present in each specimen; over the complete range of scanning we see 9 % increase in load only scans, a 37 % increase in heat load scans and a 5.4 % increase in LITS affected scans. Load only scans see a wide increase in frequency of pores across all size ranges following the start of cracking between 50 and 75 % f_{cu} . Changes in pore frequency for both the H200L and LH200 tests are mainly centred around the lower < 30 and < 40 μm pore size categories.

These results appear to indicate that pores of different length scales are instrumental in the failure of each of the three specimens conditioned under different thermo-mechanical loading regimes. Air voids are known to have a significant impact on strength and to act as nucleation sites for crack growth²⁴. This appears to be true for Load only specimens and to some extent for H200L specimens. In the case of LITS affected specimens however, air voids appear to have little influence on the failure mechanics of the material. The 1 % reduction in porosity observed in this conditioning regime at failure may simply be a result of an elastic response to the applied compressive force. The nucleation and development of cracking leading to specimen failure must occur in this specimen within the gel and capillary porosity which cannot be resolved in these scans.

With respect to pore development during heating in the case of H200L and LH200 specimens both appear to exhibit a similar pattern in terms of total porosity, number of pores and pore size distribution. This behaviour indicates that any LITS mechanism operates in either the capillary or gel pore network which cannot be resolved here. The application of heating in both cases has the same effect on the air void porosity.

The results presented here regarding the ultimate compressive strength of specimens conditioned under the three regimes shows a similar trend to those presented by Abrams²⁰, Malhotra²¹ and Khoury *et al.*¹⁷. However, a reduction in the difference between H200L and LH200 specimens compared with this author is present. Khoury *et al.*¹⁷ proposed that the beneficial increase in strength for LH200 specimens occurred as a result of suppression mechanisms which reduced the damage associated with specimens heated without a confining load where the residual strength was found to be less than 50%

of the unheated value. With reference to features in the air void porosity this hypothesis is not disputed.

In terms of loading stiffness, the modulus of elasticity for LITS affected specimens does appear to be increased above H200L specimens in line with Schneider¹⁹. However, the results also show the modulus of elasticity of LITS affected specimens increase over those which were tested to failure in uniaxial compression at ambient temperature. The elevated temperatures applied to LITS affected specimens is unlikely to be beneficial to loading stiffness and consequently the validity of stress-strain data may be called in to question. The use of LVDT and load cell equipment with a greater accuracy would help to improve stress strain measurement and digital volume correlation of displacement fields would also aid verifying the results recorded here. The same conclusion must be drawn from the calculations presented in Figure 9.3 to calculate the LITS component from H200L and LH200 tests where experimental error has made data interpretation difficult.

The results regarding the moisture diffusivity of specimens heated with and without mechanical load presented by Černý *et al.*²⁹ may also be interpreted further in light of the data presented here. These authors reported that the moisture diffusivity of specimens heated without mechanical load was found to be twice as great as that of specimens heated under load. These tests were carried out in unsealed conditions at 800 °C, under a uniaxial stress of 0.9 f_{cu} and a relatively high heating rate of 6.7 °C/min⁻¹. The large disparity between moisture diffusivity values was presented with the assumption that the load applied before heating caused cracks which allowed pore pressures to dissipate.

Within the pore range observed in these tests however, the opposite appears to occur where the presence of load before heating consolidates and reduces the porous volume fraction of the material. The effects of heating then appear to be relatively uniform between the two specimens but the sum of the loading and heating steps for the LITS affected specimen yields a material with lower porosity overall. During compression close to the failure strength of the material though the results are clear; for air void pores, greater material damage is recorded in heat only specimens with respect to those which experience LITS.

During the X-ray CT scanning under compressive loading and at elevated temperature, some load relaxation is observed. The scanning time was optimised in order to minimise the effect of this but as expected, relaxation values increase with the applied load. In all cases however, load relaxation is within 5 % of the applied load and consequently the influence of this process on X-ray CT reconstruction was expected to be small. An automatic algorithm was used to find the centre of rotation in specimens and no problems were encountered during image processing.

The final element of uncertainty surrounds both our small specimen size and our small sample set size. There is most certainly a significant statistical variance surrounding both. The small specimen size is likely to lead to an increase in experimental scatter due to the fact that a characteristic defect will have much larger influence. Unfortunately at this point in time there is no solution to the small sample set size. Limited access to the X-ray CT facility has prevented a larger frequency of specimens from being analysed.

9.6. CONCLUSIONS

With respect to the microstructural mechanisms which have been proposed to cause the development of LITS, these results do not provide definitive information to elucidate the exact process and further scanning at feature resolutions below 1 μm would be required to better understand LITS development using this microstructural analysis technique. Despite this, these results do indicate that LITS does not result in an increase in accessible air void porosity or a migration in the distribution of pore sizes present in the material which is significantly different to that of H200L specimens during the conditioning phase of the tests. Thus it seems unlikely that bursting and bond breakage is occurring in gel and capillary pores as this would be likely to be manifested in a general increase in air void porosity through coagulation.

PART 4: SUMMARY OF RESULTS

10. General Discussion

This investigation aimed to use a range of microstructural analysis techniques:

- To verify the quality and validity of the selected techniques used to characterise concrete microstructure
- To quantify the development of microstructure and porosity in mature mortar and concrete subjected to LITS
- To test the hypothesis that LITS occurs as a result of load induced thermal damage

Three different experimental analysis techniques were employed; MIP, BSE-IA and X-ray CT. Each technique has offered useful insight into aspects of concrete microstructure development. However, individually these techniques have been shown to lack the ability to fully describe microstructural behaviour across the range of length-scales present in cement based materials.

MIP has provided quantitative information on the porous volume fraction, bulk density, skeletal density, total pore area, average pore size and pore size distribution of the material in *ex-situ* conditions on pore sizes from 0.005 μm in equivalent diameter to $>1000 \mu\text{m}$ in equivalent diameter (Chapter 7). However, the technique is destructive allowing no further characterisation to be carried out on the specimen. Additionally, due to the “ink bottle” effect, data pertaining to pore size distribution and individual pore properties may not be representative.

The key findings from the *ex-situ* MIP analysis were as follows:

- No evidence was found to suggest that LITS results in an increase in the porous volume fraction with respect to specimens that have experienced heat only.
- Quantitative differences in the microstructural characteristics of LITS affected specimens were observed both in the size distribution of pores and in the density of the material. These changes indicate the presence of a microstructural mechanism which causes changes to pore structure concurrently with LITS development.

BSE-IA has provided quantitative information in *ex-situ* conditions on porous volume fraction and ITZ porosity on pores in the size range 0.5 μm in equivalent diameter to $>1000 \mu\text{m}$ in equivalent diameter (Chapter 6). Once again, this technique employs a destructive specimen preparation methodology and cannot reliably provide any data on the 3D properties of individual pores or the pore network.

The key findings from the *ex-situ* BSE-IA analysis were as follows:

- Both H250 and L06H250 (LITS affected) specimens show a similar increase in total porosity over that of unconditioned control specimens.
- Microstructural changes within the ITZ however appear to show that porosity in H250 specimens is increased over that of L06H250 (LITS affected) and control specimens.

X-ray CT has been used to provide quantitative information on the air void porosity of LITS affected specimens both in *ex-situ* conditions (Chapter 5) and *in-situ* (Chapter 9) using a purpose built thermo-mechanical loading rig. In each case, information pertaining to porous volume fraction and pore size distribution was available on pore sizes from 20 μm in equivalent diameter to >1000 μm in equivalent diameter. Attempts to characterise the pore structure of concrete at higher resolutions using *ex-situ* X-ray CT ultimately proved unsuccessful because the frequency of scanned specimens did not sum to a representative elementary volume.

The key findings from the *ex-situ* X-ray CT analysis were as follows:

- Both H250 and L06H250 (LITS affected) specimens show a similar increase in air void porosity over that of unconditioned control specimens.
- A reduction in pores with an equivalent diameter of between 30 and 100 μm and an increase in pore diameters above 200 μm occur as a result of thermal treatment at 250 °C with respect to an unconditioned control specimen. The presence of hydrostatic mechanical load at $0.6 f_{cu}$ during thermal treatment appears to increase the presence of equivalent pore diameter frequency below 100 μm .

Finally, the key findings of the *in-situ* X-ray CT analysis were as follows:

- The results do indicate that LITS does not result in an increase in accessible air void porosity or a migration in the distribution of pore sizes present in the material which is significantly different to that of H200L specimens during the conditioning phase of the tests.

This discussion will first focus on porous volume fraction information obtained from the three techniques. All *ex-situ* techniques indicate that both LITS and Heat only specimens experience an equal increase in porosity over specimens which have not experienced any thermal treatment. The 15 micron X-ray CT shows an increase in air void porosity for both heated and LITS affected specimens over unconditioned specimens of approximately 0.45 % with values of 1.2 % and 0.75% respectively. These values are much lower than those presented for the porous volume fraction using other

techniques, evidently because these scans only show a small section of the total porosity in the specimen.

MIP and BSE-IA show much higher values of porosity for all specimens. This is to be expected since they cover a much larger range of pore sizes. MIP analysis indicates that total porosity is increased for both H250 and L06H250 specimens to around 10 % with control specimens exhibiting a porosity of approximately 2.5% less. BSE-IA indicates that total porosity for H250 and L06H250 is similar and increased over that of the control by approximately 1.5 % with values of 12.5 % and 11% respectively.

It may be expected that the MIP technique would indicate the total porous volume of specimens to be the highest of each of the three techniques. In particular, since the BSE-IA technique only allows for the analysis of pores with an equivalent diameter of 0.5 μm or greater. The image analysis technique does however yield values for porosity slightly higher than those reported using the MIP technique. This is in contrast to the results of Wong *et al.*⁹⁵ who compared their image analysis results of cement mortars to those on cement paste using MIP by Cook & Hover⁷⁵. Wong *et al.* found that the image analysis technique gave significantly lower values, since it allowed only for the analysis of pores with a size greater than the image resolution. This limitation on image analysis is also valid in the present case.

A number of reasons exist for this apparent discrepancy. Both the BSE-IA technique and X-ray CT are able to detect closed pores in the material which cannot be accessed through mercury ingress. Over the same length scales, it may therefore be expected that BSE-IA would detect a greater level of porosity than MIP. Additionally, MIP specimens were dried at elevated temperature whereas BSE-IA specimens were dried in a vacuum with acetone. The additional drying at elevated temperature with the presence of water may have caused enhanced hydration in the MIP specimens thereby reducing their porous volume. Finally, BSE-IA specimen preparation may induce additional damage beyond the specimen drying which is a common preparation step across the two techniques through the resin impregnation and polishing process. MIP specimens have been dried further which may cause additional hydration. Since the trend in data appears similar for both techniques: both LITS affected and heat only specimens experience similar levels of elevated porosity with respect to control specimens, it is likely that the discrepancy in values between MIP and BSE-IA analysis is due to specimen preparation.

Taking into account the differences in loading orientation and test temperature, a comparison can also be made between the *ex-situ* and *in-situ* experimental results. For comparison with *ex-situ* results, the most relevant *in-situ* results for comparison are scan 2 from the H200L regime where the specimen has simply been heated to 200 °C and scan 3 from the LH200 regime where the specimen has been loaded to 25 % f_{cu} and heated to 200 °C.

In both cases the *in-situ* data indicates that air void porosity is elevated above the control scans in each test in a similar manner to that of the X-ray CT *ex-situ* tests. However the effect of heating is much reduced in *in-situ* tests. Values for LH200 and H200L specimens are elevated by approximately 0.015 % whereas *ex-situ* 15 μm X-ray CT results indicated that porosity is elevated by approximately 0.45 % when heated to 250 °C in both the LITS and no-LITS regimes.

This discrepancy may have arisen from two areas. First, the unconditioned porosity of the specimens employed in the *in-situ* tests is significantly higher (~3%) than that in *ex-situ* tests (~1%). Despite the effort taken to create a mortar with similar properties to that of the bulk concrete specimens used in the *ex-situ* tests, the omission of an igneous aggregate may have altered the thermal stability of the material meaning that the effect of heating was lessened in *in-situ* testing.

Secondly, the *in-situ* values are recorded at elevated temperature before cooling. Differential thermal strains are known to cause significant changes to cementitious materials during cooling⁵⁴ which are likely to be manifested in alterations in the pore structure. This may have caused the additional increase in air void porosity recorded in specimens which were subject to *ex-situ* microstructural investigation.

The observations surrounding the development of porosity up to specimen failure in *ex-situ* tests are also worthy of discussion. Porosity of unheated specimens was shown to be +25% of that before mechanical loading whilst that of H200L and LH200 specimens was shown to be 15% and -1% respectively.

Due to the increase in sub-micron sized pores in specimens which have experienced elevated temperatures as shown in the *ex-situ* MIP tests one explanation may be that crack development occurs at a level below the feature resolution of the *in-situ* X-ray CT and therefore does not manifest itself at the same levels in visible pores in H200L and LH200 specimens. In line with this argument the suppression of pores below 0.01 microns in size in heat only specimens with respect to LITS affected specimens recorded in the MIP testing may further suppress cracking in the LITS affected specimens.

Due to the limitations of the X-ray CT technique regarding the quantification of pores at a resolution higher than 15 μm as highlighted in Chapter 5, the results regarding pore size distribution from *ex-situ* X-ray CT and MIP are complementary rather than comparable in that the 15 μm X-ray CT data covers an area which may not be reliably represented by the MIP results due to the “ink bottle” effect. From the 15 micron data, both H250 and L06H250 specimens show a pore frequency which is suppressed in the 50 μm category with L06H250 specimens experiencing a greater reduction in this category. Both H250 and L06H250 specimens show pore suppression in the 100 μm category to the same extent. Above 200 μm in equivalent diameter, both H250 and L06H250 are increased over control specimens to a similar extent.

MIP data indicates that within the same range, L06H250 specimens experience a significant increase in pores over that of the control and H250 specimens. No difference can be detected between H250 specimens and control specimens. Despite the acknowledged impact of the “ink bottle” effect, MIP data therefore shows a similar trend to that of X-ray CT data in that L06H250 and H250 pores in this region generally occur with a higher frequency than those in control specimens.

At lower length scales, MIP data indicates that a significant peak in pore size distribution frequency occurs between 0.05 and 0.5 μm . Both H250 and L06H250 specimens show elevated levels of pore in this domain with respect to control specimens. Whilst an increase in experimental error within the data at this point in the pore size distribution curve has been acknowledged, a trend where H250 specimens show higher levels of pores in this region may be observed. When the results of the ITZ porosity analysis are considered from the BSE-IA technique it is suggested that the increase in pore size frequencies for H250 specimens may correlate with an increase in damage within the ITZ region.

With respect to the efficacy of this investigation, there are a number of areas which would benefit from further investigation in order to provide a better understanding of the effect of LITS on cementitious microstructures. First, the decision to focus solely on pore structure whilst driven by the capabilities of the techniques employed here and by difficulties posed in the segmentation of individual PFA and anhydrous cement grains could yield more information on LITS microstructure development.

The microstructural analysis of solid phases including anhydrous cement grains was attempted with BSE-IA and X-ray CT. However, the addition of PFA in the mix design employed in this work led to insurmountable difficulties in the segmentation of these bright inclusions meaning no quantifiable data could be obtained. Since LITS is known to occur in OPC pastes, a future investigation may benefit from a simplified mix design. The limitation of such an approach would be that the mix design would be less relevant to real world applications such as that of understanding the behaviour of the AGR pressure vessel. Aggregate inclusion in both the BSE-IA and X-ray CT data could be successfully segmented. In the former case this process was instrumental in the quantification of ITZ porosity. With respect to the 15 micron X-ray CT data, the accuracy of aggregate segmentation could have been improved through the use of large aggregate solely from a calcareous source since the crystals in the igneous basalt reduced the efficacy of the segmentation algorithm employed.

Nitrogen sorption and neutron tomography were both suggested in the experimental appraisal presented in Chapter 5 as alternative techniques for the analysis of pore structure in cementitious materials. With hindsight, the addition of an additional technique with the capability of analysing pore structure on the nanometre length-scale would have provided a useful counterpoint for comparison

with MIP data. In fact, with the adoption of a more rigorous method of physical segmentation of specimens, X-ray CT may also have been more effective at higher resolutions.

However, with the limited time and resources available in this project it would not have been possible to perform the specimen preparation and experimental work necessary. Again with respect to X-ray CT, easy access to experimental equipment also proved a barrier and prevented the application of learning from experience in higher resolution scans. The improvement of high resolution scans would have allowed the quantification of the 3D pore network which may have given useful insight into its development under LITS conditioning.

Neutron tomography offers a new and developing area for the exploration of concrete pore structure. However the technique remains in its infancy and its use would have represented an even more novel approach than that using X-ray CT and it is likely that the collection of useful data would have taken more time than could be allowed here. Additionally, gaining access to the appropriate experimental equipment is not a straight forward process.

Beyond the scope of the initial experimental appraisal, X-ray diffraction (XRD) could have provided valuable information on changes in the crystal structure of LITS affected materials. In fact, a preliminary study was carried out into the use of XRD where it was identified that quantitative data could be obtained using the Rietveld refinement technique¹²⁹. However, time pressures once again led to the exclusion of further investigations in this area. Since the primary aim of the thesis was to investigate the existence of physical damage to the material microstructure, XRD was thought to be less appropriate than the three techniques already selected.

The results presented in this investigation may with further underpinning research and development influence both the construction and nuclear industries. Microstructural information detailing the evolution of the material under combined thermo-mechanical loading such as that provided by the *in-situ* X-ray CT analysis can be used to validate a finite element model. The initial dataset can be discretised into elements and its evolution under load can be compared with that of later CT datasets. The validation of such a model under LITS affected and no-LITS conditions would provide assurance for the development of the model to support reactor construction and fire modelling.

11. Conclusions

In this thesis, the development of concrete and mortar pore structure in LITS affected specimens was investigated using a multi-technique based experimental program. Specimens were characterised first *ex-situ* and ultimately *in-situ* using a new in-situ thermo-mechanical load rig which was designed and commissioned for laboratory and synchrotron based X-ray CT. The correlation between LITS development and pore structure evolution was investigated in order to determine the validity of the load induced thermal damage hypothesis as the principal mechanism driving the phenomenon. The practicality and precision of each of the experimental techniques employed was also assessed.

11.1. KEY FINDINGS

The key findings from the *ex-situ* and *in-situ* microstructural investigations are as follows:

- *Ex-situ* MIP measurements indicate that LITS does not lead to an increase in the porous volume fraction of specimens over those which are heated without load. However, evidence of quantitative differences in size distribution of pores and the density of the material has been shown between LITS specimens and those heated without mechanical loading.
- *Ex-situ* BSE-IA analysis again does not appear to indicate that H250 and L06H250 (LITS affected) specimens experience a differing increase in total porous volume. An analysis of the ITZ in specimens conditioning under each regime does however appear to indicate an increase in porosity within this region in specimens heated without load. LITS affected specimens appear to display similar ITZ properties to control specimens.
- *Ex-situ* X-ray CT analysis indicates that air void porosities in H250 and L06H250 (LITS affected) specimens are elevated by a similar amount in each regime with respect to unconditioned control specimens. Differences in the pore size distribution between H250 and L06H250 (LITS affected) specimens is however evident where the later specimens show an increase in pore frequency below 100 μm in equivalent diameter.
- *In-situ* X-ray CT analysis once again does not show any significant differences in the porosity of LH200 (LITS affected) and H200L specimens. Both are elevated with respect to their unconditioned state.

11.2. GENERAL CONCLUSIONS

Through consideration of the key findings and with respect to the main objectives of this research, the general conclusions are given below:

- Evidence of load induced thermal damage as the primary mechanism for the development of LITS cannot be clearly identified from the results presented here. The total porosity of LITS affected specimens appears to be similar to that of specimens which have experienced only heating.
- LITS specific changes in the microstructure of concrete have been identified from *ex-situ* analysis and changes in the fracture mechanics of the material are evident in *in-situ* tests. Microstructural changes within the ITZ identified in the *ex-situ* BSE-IA analysis appear to show that at least in a residual condition, an increase in porosity is suppressed in LITS affected specimens. Whilst likely to be a side effect of any potential LITS mechanism since LITS is known to occur in cement paste, this alteration in behaviour could explain the change in the observed change in fracture mechanics and the reduction in permeability with respect to heat only specimens observed by other authors²⁹.
- Laboratory based X-ray CT applied on both *ex-situ* and *in-situ* conditioned specimens is a useful technique for determining quantitative changes in the characteristics of the 3D air void structure in concrete. For the study of capillary and gel pores a synchrotron source is preferable and the experimental procedure must be well developed in order to ensure high quality results.

11.3. FURTHER RESEARCH

The key findings of this research presented in section 11.1 offer an indication of areas where further research may benefit the understanding of the subject. These areas can be summarised as follows:

- BSE-IA has proved a useful tool for the analysis of concrete microstructure however the specimen preparation required in order to realise high quality images is likely to damage the material microstructure. The application of an environmental SEM may help to overcome these issues.
- Further research is required using a refined methodology based upon the findings of this thesis. The study of a simplified cementitious microstructure would be desirable – ideally an OPC paste. The experimental program employed here would also benefit from the supplementation of sub-micron *in-situ* X-ray CT analysis in order to identify changes to the connected pore network within the material. Tomography scans should be obtained not only

of the material at elevated temperature but also following cooling in order to identify the microstructural features of the material in the residual state for comparison with existing literature. The experimental program should also be broadened to include the analysis of crystalline structures within LITS affected material. This could be undertaken *in-situ* using synchrotron based XRD.

- With respect to realising industry benefits from this research, the *in-situ* X-ray CT datasets could be used to validate finite element models of the material under the conditions employed in the tests presented here.

REFERENCES

1. Petkovski, M. Effects of stress during heating on strength and stiffness of concrete at elevated temperature. *Cem. Concr. Res.* **40**, 1744–1755 (2010).
2. Anderberg, Y. & Thelandersson, S. Stress and deformation characteristics of concrete: experimental investigation and material behaviour model. *Univ. Lund, Sweden Bulletin* **5**, (1976).
3. Petkovski, M., Crouch, R. S. & Waldron, P. Apparatus for Testing Concrete under Multiaxial Compression at Elevated Temperature (mac2T). *Exp. Mech.* **46**, 387–398 (2006).
4. Bary, B., Ranc, G., Durand, S. & Carpentier, O. A coupled thermo-hydro-mechanical-damage model for concrete subjected to moderate temperatures. *Int. J. Heat Mass Transf.* **51**, 2847–2862 (2008).
5. Glasser, F. P. & Hong, S. Thermal treatment of C – S – H gel at 1 bar H₂O pressure up to 200 °C. *Cem. Concr. Res.* **33**, 271–279 (2003).
6. Khoury, G. A., Grainger, B. N. & Sullivan, P. J. E. Strain of concrete during first heating to 600°C under load. *Mag. Concr. Res.* **37**, 195–215 (1985).
7. Hansen, T. C. & Eriksson, L. Temperature change effect on the behaviour of cement paste, mortar and concrete under load. *J. Am. Concr. Inst.* **63**, 489–504 (1966).
8. Illston, J. M. & Sanders, P. D. Characteristics and prediction of creep of a saturated mortar under variable temperature. *Mag. Concr. Res.* **26**, 169–179 (1973).
9. Parrott, L. J. A study of transitional thermal creep in hardened cement paste. *Mag. Concr. Res.* **31**, 99–103 (1979).
10. Illston, J. M. & Sanders, P. D. The effect of temperature change upon the creep of mortar under torsional loading. *Mag. Concr. Res.* **25**, 136–144 (1973).
11. Parrott, L. J. The influence of thermal treatment on the creep of cement systems. *7th Int. Congr. Chem. Cem. Paris* **4**, 817–820 (1980).
12. Colina, H. & Sercombe, J. Transient thermal creep of concrete in service conditions at temperatures up to 300 °C. *Mag. Concr. Res.* **56**, 559–574 (2004).
13. Hassen, S. & Colina, H. Transient thermal creep of concrete in accidental conditions at temperatures up to 400 C. *Mag. Concr. Res.* **58**, 201–208 (2006).
14. Rainford, E. & Timusk, J. Creep of Hardened Portland Cement Paste Under Cyclic Temperature. *J. Am. Ceram. Soc.* **61**, 380–385 (1978).
15. Thelandersson, S. On the multiaxial behaviour of concrete exposed to high temperature. *Nucl. Eng. Des.* **75**, 271–282 (1983).
16. Petkovski, M. & Crouch, R. Strains under transient hygro-thermal states in concrete loaded in multiaxial compression and heated to 250 °C. *Cem. Concr. Res.* **38**, 586–596 (2008).

17. Khoury, G. A., Grainger, B. N. & Sullivan, P. J. E. Strain of concrete during first cooling from 600°C under load. *Mag. Concr. Res.* **38**, 3–12 (1986).
18. Thienel, K. C. & Rostasy, F. Transient creep of concrete under biaxial stress and high temperature. *Cem. Concr. Res.* **26**, 1409–1422 (1996).
19. Schneider, U. Concrete at high temperatures--A general review. *Fire Saf. J.* **13**, 55 – 68 (1988).
20. Abrams, M. S. Compressive strength of concrete at temperatures to 1600 °F. *ACI Spec. Publ. SP25* 33–58 (1971).
21. Malhotra, H. L. The effect of temperature on the compressive strength of concrete. *Mag. Concr. Res.* **8**, 85–94 (1956).
22. Khoury, G. A., Grainger, B. N. & Sullivan, P. J. E. Transient thermal strain of concrete: literature review, conditions within specimen and behaviour of individual constituents. *Mag. Concr. Res.* **37**, 131–144 (1985).
23. Lankard, D. R., Birkimer, D. L., Fondriest, M. J. & Snyder, M. J. Effects of moisture content on the structural properties of portland cement exposed to temperatures up to 500 deg F. *ACI Spec. Publ. SP25 Detroit*, 59–101 (1971).
24. Mindess, S. & Young, J. *Concrete*. 671 (Prentice Hall, Inc., 1981).
25. Parrott, L. J. Structure and thermal creep of cement paste. *7th Int. Congr. Chem. Cem. Paris* **3**, (VI–131)–(VI–134) (1980).
26. Khoury, G. a. Strain of heated concrete during two thermal cycles. Part 1: strain over two cycles, during first heating and at subsequent constant temperature. *Mag. Concr. Res.* **58**, 367–385 (2006).
27. Young, J. An assessment of the influence of microstructure on time-dependent deformations of hardened cement paste. in *First Aust. Conf. Eng. Mater.* 3–28 (1974).
28. Khoury, G. a. Strain of heated concrete during two thermal cycles. Part 3: isolation of strain components and strain model development. *Mag. Concr. Res.* **58**, 421–435 (2006).
29. Černý, R. *et al.* Thermal and hygric properties of Portland cement mortar after high-temperature exposure combined with compressive stress. *Cem. Concr. Res.* **33**, 1347–1355 (2003).
30. Scrivener, K. Backscattered electron imaging of cementitious microstructures: understanding and quantification. *Cem. Concr. Compos.* **26**, 935–945 (2004).
31. Aligizaki, K. K. *Pore structure of cement based materials: testing, interpretation and requirements*. 293 (Taylor and Francis, 2006).
32. Bazant, Z., Hauggaard, A., Baweja, S. & Ulm, F. Microprestress-solidification theory for concrete creep. I: Aging and drying effects. *J. Eng. Mech.* 1188–1194 (1997). at <[http://ascelibrary.org/doi/abs/10.1061/\(ASCE\)0733-9399\(1997\)123:11\(1188\)>](http://ascelibrary.org/doi/abs/10.1061/(ASCE)0733-9399(1997)123:11(1188)>)

33. Lachowski, E. & Diamond, S. Investigation of the composition and morphology of individual particles of portland cement paste: 1. C-S-H gel and calcium hydroxide particles. *Cem. Concr. Res.* **13**, 177–185 (1983).
34. Jennings, H. A model for the microstructure of calcium silicate hydrate in cement paste. *Cem. Concr. Res.* **30**, 101–116 (2000).
35. Bažant, Z. Thermodynamics of interacting continua with surfaces and creep analysis of concrete structures. *Nucl. Eng. Des.* **20**, 477–505 (1972).
36. Powers, T. C. The thermodynamics of volume change and creep. *Mater. Struct.* **1**, 487–507 (1968).
37. Powers, T. C. Mechanisms of shrinkage and reversible creep of hardened cement paste. in *"The Struct. Concr. Proc. Intern. Conf.* (Brooks, A. E. & Newman, K.) 319 (1965).
38. Yun-Ping, X. & Jennings, H. M. Relationships between microstructure and creep and shrinkage of cement paste. *Mater. Sci. Concr.* **III**, 37–63 (1992).
39. Neville, A., Dilger, W. & Brooks, J. *Creep of plain and structural concrete.* 361 (1983).
40. Bažant, Z. P. Prediction of concrete creep and shrinkage: past, present and future. *Nucl. Eng. Des.* **203**, 27–38 (2001).
41. Reiner, M. On volume or isotropic flow as exemplified in the creep of concrete. *Appl. Sci. Reseach* **A1**, 475–488 (1949).
42. Powers, T. C. Physical properties of cement paste. in *Proc. Fourth Int. Symp. Chem. Cem.* 577–609 (1960).
43. Lynam, C. G. *Growth and movement in Portland cement concrete.* 139 (Oxford University Press, 1934).
44. Bazant, Z. & Chern, J. Concrete creep at variable humidity: constitutive law and mechanism. *Mater. Struct.* **18**, 1–20 (1985).
45. Bazant, Z. & Moschovidis, Z. Surface-diffusion theory for drying creep effect in portland cement paste and concrete. *J. Amer. Ceram. Soc.* **56**, 235–241 (1973).
46. Bazant, Z., Hauggaard, A. & Baweja, S. Microprestress-solidification theory for concrete creep. II: Algorithm and verification. *J. Eng. Mech.* 1195–1201 (1997).
47. Bazant, Z. & Prasannan, S. Solidification theory for concrete creep. I: Formulation. *J. Eng. Mech.* **115**, (1989).
48. Mindess, S., Young, J. & Lawrence, F. Creep and drying shrinkage of calcium silicate pastes I: Specimen preparation and mechanical properties. *Cem. Concr. Res.* **8**, 591–600 (1978).
49. Wittman, F. Einfluss des Feuchtigkeitsgehaltes auf das Kriechen des Zementsteines (Influence of moisture content on the creep of hardened cement). *Rheol. Acta.* **9**, 282–287 (1970).
50. Bazant, Z. & L'Hermite, R. *Mathematical modeling of creep and shrinkage of concrete.* (1988). at <<http://www.civil.northwestern.edu/people/bazant/PDFs/Backup of Papers/S21.pdf>>

51. Bazant, Z. & Prasannan, S. Solidification theory for concrete creep. II: Verification and application. *J. Eng. Mech.* **115**, 1704–1725 (1989).
52. Bazant, Z., Cusatis, G. & Cedolin, L. Temperature effect on concrete creep modeled by microprestress-solidification theory. *J. Eng. Mech.* 691–699 (2004). at <[http://ascelibrary.org/doi/pdf/10.1061/\(ASCE\)0733-9399\(2004\)130:6\(691\)>](http://ascelibrary.org/doi/pdf/10.1061/(ASCE)0733-9399(2004)130:6(691)>)
53. Fahmi, H. M., Polivka, M. & Bresler, B. Effect of sustained and cyclic elevated temperature on creep of concrete. *Cem. Concr. Res.* **2**, 591–606 (1972).
54. Khoury, G. a. Strain of heated concrete during two thermal cycles. Part 2: strain during first cooling and subsequent thermal cycle. *Mag. Concr. Res.* **58**, 387–400 (2006).
55. Lu, S., Landis, E. N. & Keane, D. T. X-ray microtomographic studies of pore structure and permeability in Portland cement concrete. *Mater. Struct.* **39**, 611–620 (2006).
56. Bentz, D. P. *et al.* Microstructure and transport properties of porous building materials . II : Three-dimensional X-ray tomographic studies. *Mater. Struct.* **33**, 147–153 (2000).
57. Promentilla, M. A. B., Sugiyama, T., Hitomi, T. & Takeda, N. Characterizing the 3D Pore Structure of Hardened Cement Paste with Synchrotron Microtomography. *J. Adv. Concr. Technol.* **6**, 273–286 (2008).
58. Diamond, S. & Landis, E. Microstructural features of a mortar as seen by computed microtomography. *Mater. Struct.* **40**, 989–993 (2006).
59. Promentilla, M. A. B., Sugiyama, T., Hitomi, T. & Takeda, N. Quantification of tortuosity in hardened cement pastes using synchrotron-based X-ray computed microtomography. *Cem. Concr. Res.* **39**, 548–557 (2009).
60. Provis, J. L., Myers, R. J., White, C. E., Rose, V. & van Deventer, J. S. J. X-ray microtomography shows pore structure and tortuosity in alkali-activated binders. *Cem. Concr. Res.* **42**, 855–864 (2012).
61. Bentz, D. P. *et al.* Four-dimensional X-ray microtomography study of water movement during internal curing. in *Int. RILEM Conf. Vol. Chang. Hardening Concr. Test. Mitig.* **C**, 11–20 (RILEM Publications SARL, 2006).
62. Promentilla, M. A. B. & Sugiyama, T. X-Ray Microtomography of Mortars Exposed to Freezing-Thawing Action. *J. Adv. Concr. Technol.* **8**, 97–111 (2010).
63. Sugiyama, T., Promentilla, M. a. B., Hitomi, T. & Takeda, N. Application of synchrotron microtomography for pore structure characterization of deteriorated cementitious materials due to leaching. *Cem. Concr. Res.* **40**, 1265–1270 (2010).
64. Stock, S., Naik, N., Wilkinson, A. & Kurtis, K. X-ray microtomography (microCT) of the progression of sulfate attack of cement paste. *Cem. Concr. Res.* **32**, 1673–1675 (2002).
65. Landis, E. N., Nagy, E. N., Keane, D. T. & Nagy, G. Technique to measure 3d work-of-fracture of concrete in compression. *J. Eng. Mech.* **125**, 599 (1999).
66. Landis, E. & Nagy, E. Three-dimensional work of fracture for mortar in compression. *Eng. Fract. Mech.* **65**, 223–234 (2000).

67. Landis, E. N., Nagy, E. N. & Keane, D. T. Microstructure and fracture in three dimensions. *Eng. Fract. Mech.* **70**, 911–925 (2003).
68. Ferrié, E., Buffière, J.-Y., Ludwig, W., Gravouil, A. & Edwards, L. Fatigue crack propagation: In situ visualization using X-ray microtomography and 3D simulation using the extended finite element method. *Acta Mater.* **54**, 1111–1122 (2006).
69. Landis, E. N., Zhang, T., Nagy, E. N., Nagy, G. & Franklin, W. R. Cracking, damage and fracture in four dimensions. *Mater. Struct.* **40**, 357–364 (2006).
70. Asahina, D., Landis, E. N. & Bolander, J. E. Modeling of phase interfaces during pre-critical crack growth in concrete. *Cem. Concr. Compos.* **33**, 966–977 (2011).
71. Provis, J. L., Rose, V., Winarski, R. P. & van Deventer, J. S. J. Hard X-ray nanotomography of amorphous aluminosilicate cements. *Scr. Mater.* **65**, 316–319 (2011).
72. Baroghel-Bouny, V., Mounanga, P., Khelidj, A., Loukili, A. & Rafaï, N. Autogenous deformations of cement pastes Part II. W/C effects, micro-macro correlations and threshold values. *Cem. Concr. Res.* **36**, 123–136 (2006).
73. Mounanga, P., Baroghel-Bouny, V., Loukili, A. & Khelidj, A. Autogenous deformations of cement pastes: Part I. Temperature effects at early age and micro–macro correlations. *Cem. Concr. Res.* **36**, 110–122 (2006).
74. Cebeci, Ö. Pore structure of air-entrained hardened cement paste. *Cem. Concr. Res.* **1**, 257–265 (1981).
75. Cook, R. A. & Hover, K. C. Mercury porosimetry of hardened cement pastes. *Cem. Concr. Res.* **29**, 933–943 (1999).
76. Lura, P., Jensen, O. M. & van Breugel, K. Autogenous shrinkage in high-performance cement paste: An evaluation of basic mechanisms. *Cem. Concr. Res.* **33**, 223–232 (2003).
77. Kumar, R. & Bhattacharjee, B. Porosity, pore size distribution and in situ strength of concrete. *Cem. Concr. Res.* **33**, 155–164 (2003).
78. Cerny, R., Poděbradská, J., Toman, J., Drchalová, J. & Rovnaníková, P. The effect of compressive stress on thermal and hygric properties of Portland cement mortar in wide temperature and moisture ranges. *Cem. Concr. Res.* **30**, 1267–1276 (2000).
79. Elaqla, H., Godin, N., Peix, G., Rmili, M. & Fantozzi, G. Damage evolution analysis in mortar, during compressive loading using acoustic emission and X-ray tomography: Effects of the sand/cement ratio. *Cem. Concr. Res.* **37**, 703–713 (2007).
80. Chan, S., Luo, X. & Sun, W. Effect of high temperature and cooling regimes on the compressive strength and pore properties of high performance concrete. *Constr. Build. Mater.* **14**, 261–266 (2000).
81. Luo, X. & Sun, W. Residual compressive strength and microstructure of high performance concrete after exposure to high temperature. *Mater. Struct.* **33**, 294–298 (2000).
82. Piasta, J., Sawicz, Z. & Rudzinski, L. Changes in the structure of hardened cement paste due to high temperature. *Matériaux Constr.* **17**, 291–296 (1984).

83. Xu, Y., Wong, Y. L., Poon, C. S. & Anson, M. Impact of high temperature on PFA concrete. *Cem. Concr. Res.* **31**, 1065–1073 (2001).
84. Chan, Y. N., Peng, G. F. & Anson, M. Residual strength and pore structure of high-strength concrete and normal strength concrete after exposure to high temperatures. *Cem. Concr. Compos.* **21**, 23–27 (1999).
85. Galle, C. Effect of drying on cement-based materials pore structure as identified by mercury intrusion porosimetry A comparative study between oven-, vacuum-, and freeze-drying. *Cem. Concr. Res.* **31**, 1467–1477 (2001).
86. Diamond, S. Mercury porosimetry:: An inappropriate method for the measurement of pore size distributions in cement-based materials. *Cem. Concr. Res.* **30**, 1517–1525 (2000).
87. Allen, A. J. & Thomas, J. J. Analysis of C–S–H gel and cement paste by small-angle neutron scattering. *Cem. Concr. Res.* **37**, 319–324 (2007).
88. Jennings, H. M., Thomas, J. J., Gevrenov, J. S., Constantinides, G. & Ulm, F.-J. A multi-technique investigation of the nanoporosity of cement paste. *Cem. Concr. Res.* **37**, 329–336 (2007).
89. Gerhardt, R. A review of conventional and non-conventional pore characterisation techniques. *MRS Proc.* **137**, 75 (1988).
90. Garci Juenger, M. C. & Jennings, H. M. The use of nitrogen adsorption to assess the microstructure of cement paste. *Cem. Concr. Res.* **31**, 883–892 (2001).
91. Kruth, J. P. *et al.* Computed tomography for dimensional metrology. *CIRP Ann. - Manuf. Technol.* **60**, 821–842 (2011).
92. Marusin, S. Sample preparation--the key to SEM studies of failed concrete. *Cem. Concr. Compos.* **9465**, 311–318 (1995).
93. Scrivener, K., Fullmann, T., Gallucci, E., Walenta, G. & Bermejo, E. Quantitative study of Portland cement hydration by X-ray diffraction/Rietveld analysis and independent methods. *Cem. Concr. Res.* **34**, 1541–1547 (2004).
94. Haha, M. Ben, De Weerd, K. & Lothenbach, B. Quantification of the degree of reaction of fly ash. *Cem. Concr. Res.* **40**, 1620–1629 (2010).
95. Wong, H. S., Buenfeld, N. R. & Head, M. K. Estimating transport properties of mortars using image analysis on backscattered electron images. *Cem. Concr. Res.* **36**, 1556–1566 (2006).
96. Scrivener, K. L. & Nemat, K. M. The percolation of pore space in the cement paste/aggregate interfacial zone of concrete. *Cem. Concr. Res.* **26**, 35–40 (1996).
97. Nemat, K. M., Monteiro, P. J. M. & Cook, N. G. W. A new method for studying stress-induced microcracks in concrete. *J. Mater. Civ. Eng.* **10**, 128–134 (1998).
98. Stutzman, P. E. & Clifton, J. R. Specimen preparation for scanning electron microscopy. in *Proc. twenty-first Int. Conf. Cem. Microsc.* 10–22 (NIST, 1999).

99. Wong, H. S., Head, M. K. & Buenfeld, N. R. Pore segmentation of cement-based materials from backscattered electron images. *Cem. Concr. Res.* **36**, 1083–1090 (2006).
100. Yang, R. & Buenfeld, N. R. Binary segmentation of aggregate in SEM image analysis of concrete. *Cem. Concr. Res.* **31**, 437–441 (2001).
101. Underwood, E. E. *Quantitative Stereology*. (Addison-Wesley, 1970).
102. Webb, P. A. An Introduction To The Physical Characterization of Materials by Mercury Intrusion Porosimetry with Emphasis On Reduction And Presentation of Experimental Data. *Micromeritics Instrum. Corp. Tech. Pap.* 1 (2001). at <http://www.micromeritics.com/pdf/app_articles/mercury_paper.pdf>
103. Washburn, E. The dynamics of capillary flow. *Phys. Rev.* **17**, 273–284 (1921).
104. Guang, Y. Experimental study and numerical simulation of the development of the microstructure and permeability of cementitious materials. 189 (2003).
105. Feldman, R. Pore structure damage in blended cements caused by mercury intrusion. *J. Am. Ceram. Soc.* **67**, 30–33 (1984).
106. Kaufmann, J. Characterization of Pore Space of Cement-Based Materials by Combined Mercury and Wood's Metal Intrusion. *J. Am. Ceram. Soc.* **92**, 209–216 (2009).
107. Guvenilir, A., Breunig, T., Kinney, J. & Stock, S. Direct observation of crack opening as a function of applied load in the interior of a notched tensile sample of Al–Li 2090. *Acta Mater.* **45**, 1977–1987 (1997).
108. Stock, S. R. Recent advances in X-ray microtomography applied to materials. *Int. Mater. Rev.* **53**, 129–181 (2008).
109. Bay, B. K., Smith, T. S., Fyhrie, D. P. & Saad, M. Digital volume correlation: Three-dimensional strain mapping using X-ray tomography. *Exp. Mech.* **39**, 217–226 (1999).
110. Toda, H. *et al.* 3-D Image-Based Mechanical Simulation of Aluminium Foams: Effects of Internal Microstructure. *Adv. Eng. Mater.* **8**, 459–467 (2006).
111. Brault, R. *et al.* In-situ Analysis of Laminated Composite Materials by X-ray Micro-Computed Tomography and Digital Volume Correlation. *Exp. Mech.* **53**, 1143–1151 (2013).
112. Limodin, N., Salvo, L., Suéry, M. & DiMichiel, M. In situ investigation by X-ray tomography of the overall and local microstructural changes occurring during partial remelting of an Al–15.8wt.% Cu alloy. *Acta Mater.* **55**, 3177–3191 (2007).
113. Limodin, N. *et al.* In situ and real-time 3-D microtomography investigation of dendritic solidification in an Al–10wt.% Cu alloy. *Acta Mater.* **57**, 2300–2310 (2009).
114. Artioli, G. *et al.* X-ray diffraction microtomography (XRD-CT), a novel tool for non-invasive mapping of phase development in cement materials. *Anal. Bioanal. Chem.* **397**, 2131–6 (2010).

115. Gallucci, E., Scrivener, K., Groso, a., Stampanoni, M. & Margaritondo, G. 3D experimental investigation of the microstructure of cement pastes using synchrotron X-ray microtomography (μ CT). *Cem. Concr. Res.* **37**, 360–368 (2007).
116. Gastaldi, D. *et al.* In situ tomographic investigation on the early hydration behaviors of cementing systems. *Constr. Build. Mater.* **29**, 284–290 (2012).
117. Shah, S. & Choi, S. Nondestructive techniques for studying fracture processes in concrete. *Int. J. Fract.* **98**, 351–359 (1999).
118. Landis, E. N. & Bolander, J. E. Explicit representation of physical processes in concrete fracture. *J. Phys. D. Appl. Phys.* **42**, 214002 (2009).
119. Wan, K. & Xue, X. In situ compressive damage of cement paste characterized by lab source X-ray computer tomography. *Mater. Charact.* **82**, 32–40 (2013).
120. Landis, E., Bridges, M. & Bolander, J. E. 3D tomographic imaging applied to split cylinder fracture. in *Fract. Mech. Concr. Concr. Struct. Korea Concr. Inst.* 100 (2010).
121. De Wolski, S. C., Bolander, J. E. & Landis, E. N. An In-Situ X-Ray Microtomography Study of Split Cylinder Fracture in Cement-Based Materials. *Exp. Mech.* (2014). doi:10.1007/s11340-014-9875-1
122. Phillion, a. B., Cockcroft, S. L. & Lee, P. D. X-ray micro-tomographic observations of hot tear damage in an Al–Mg commercial alloy. *Scr. Mater.* **55**, 489–492 (2006).
123. Terzi, S. *et al.* In situ X-ray tomography observation of inhomogeneous deformation in semi-solid aluminium alloys. *Scr. Mater.* **61**, 449–452 (2009).
124. Subroto, T. *et al.* Formation of Hot Tear Under Controlled Solidification Conditions. *Metall. Mater. Trans. A* **45**, 2855–2862 (2014).
125. Puncreobutr, C., Lee, P. D., Hamilton, R. W., Cai, B. & Connolley, T. Synchrotron Tomographic Characterization of Damage Evolution During Aluminum Alloy Solidification. *Metall. Mater. Trans. A* **44**, 5389–5395 (2012).
126. Hubbell, J. H. & Seltzer, S. M. Tables of X-ray Mass Attenuation Coefficients and Mass Energy-Absorption Coefficients from 1 keV to 20 MeV for Elements $Z = 1$ to 92 and 48 Additional Sunstances of Dosimetric Interest. *NIST* (1996). at <<http://www.nist.gov/pml/data/xraycoef/index.cfm>>
127. Ceramics, P. Macor Material Datasheet. at <<http://www.precision-ceramics.co.uk/macor-machinable-glass-ceramic-a-unique-material.htm>>
128. Steels, C. E. Durehete 950 Material Datasheet. *Tata Steel Eur.* (2000). at <[http://www.tatasteeleurope.com/file_source/StaticFiles/Business Units/Engineering steels/D950.PDF](http://www.tatasteeleurope.com/file_source/StaticFiles/Business%20Units/Engineering%20steels/D950.PDF)>
129. Rietveld, H. M. A profile refinement method for nuclear and magnetic structures. *J. Appl. Crystallogr.* **2**, 65–71 (1969).

Appendix A: BSE-IA Matlab Analysis Script

```

function ROBSEM(K)

% Analyses the porosity of SEM images with respect to aggregate.

%----- Routine written by Robert Stein on 09.06.2012 -----%
K = imread('C:/Users/Rob Stein/Documents/PhD/Mini Project
2/SEM/C1/2_200_1.jpg');

Large = rgb2gray(K);

[Rows,Columns] = size(Large);

m=1;
for m = 1 : 900
    n=1;
    for n = 1 : Columns
        Gray(m,n) = Large(m,n);

    end

end

%%%%%%%%%% start SEM image porosity threshold %%%%%%%%%%%

%Gray = zeros([900 1344]);

%for m = 1:900 % invert logical matrix
% n = 1;
% for n = 1:1344

% Gray(m,n) = Baddata(m,n);
% end
%end

[Rows,Columns] = size(Gray);

FF = Gray;

[countsA,xA] = imhist(Gray);

dA = size(xA);

dB = 32;

countsB = zeros(dB);
countscumB = zeros(dB);
GradientB = zeros(dB);
GradientBB = zeros(dB);
Gradientsign = zeros(dB);
xB = zeros(dB);

p = 0;
m = 1;
q = 1;
r = 1;
s = 0;
AA = 0;
BB = 0;
i = 1;

```

```

j = 1;
x = 0;
y = 0;

%%%%%%%%%%%%%%%%%%%%%%%%%%%%%%%%%%%%%%%%%%%%%%%%%%%%%%%%%%%%%%%%%%%%%%%% convert to 32 colours
for m = 1 : dB
    n=1;
    xB(m) = m;
    for n = 1 : 8

        countsB(m) = countsB(m) + countsA((p+n)); % downsize to 32
greyscale colours due to poor images
    end

    if (m <= 1)
        countscumB(m) = countsB(m);
    else
        countscumB(m) = countscumB(m-1) + countsB(m);
    end

    p = p + 8;
end
%%%%%%%%%%%%%%%%%%%%%%%%%%%%%%%%%%%%%%%%%%%%%%%%%%%%%%%%%%%%%%%%%%%%%%%% convert to 32 colours

%%%%%%%%%%%%%%%%%%%%%%%%%%%%%%%%%%%%%%%%%%%%%%%%%%%%%%%%%%%%%%%%%%%%%%%% anhydrous segmentation
m = 22;
n = 0;
Anhydthres = 0;
for m = 22 : dB
    n = countsB(m);

    if (n <= countsB(m-1))

        Anhydthres = m;
    end
end

Anhydthres = (1/256)*(Anhydthres*8);

Anhyd = im2bw(Gray, Anhydthres);

ae = strel('disk',5);

Anhydclose = imclose(Anhyd,ae);

Anhydfill = imfill(Anhydclose,'holes');

%%%%%%%%%%%%%%%%%%%%%%%%%%%%%%%%%%%%%%%%%%%%%%%%%%%%%%%%%%%%%%%%%%%%%%%% anhydrous segmentation

s = (100/(countscumB(dB)));

m = 1;

```

```

p = zeros(dB);

for m = 1 : dB

    p(m) = s*countscumB(m);
    q = m - 1;

    if (q <= 0) % calculates 1st and 2nd differential of
histogram
        GradientB(m) = p(m) - 0;
        GradientBB(m) = GradientB(m) - 0;
    else
        GradientB(m) = p(m) - p(m-1);
        GradientBB(m) = GradientB(m) - GradientB(m-1);
    end

    if (GradientBB(m) >= 0)
        Gradientsign(m) = 1;
    else
        Gradientsign(m) = 0;
    end

    if (GradientBB(m) >= 0.2)
        Gradientsign(m) = 2;
    end

    if (GradientBB(m) >= 1.5)
        Gradientsign(m) = 3;
    end
end

m = 1;

for m = 1 : 20
    if (Gradientsign(m) == 3)
        BB = BB + 1;
    end
    if (Gradientsign(m) == 1)
        AA = AA + 1;
    end
end

lineAx = zeros([AA 1]);
lineBx = zeros([BB 1]);
lineAy = zeros([AA 1]);
lineBy = zeros([BB 1]);

for m = 1 : 20
    if (Gradientsign(m) == 1)
        lineAx(i) = m;
        lineAy(i) = p(m);
        i = i + 1;
    end
    if (Gradientsign(m) == 3)
        lineBx(j) = m;
        lineBy(j) = p(m);
        j = j+1;
    end
end
end

```

```

lineA = polyfit(lineAx,lineAy,1);
lineB = polyfit(lineBx,lineBy,1);

x = (((lineB(2)-lineA(2))/(lineA(1)-lineB(1)))*8)*0.9);

%%%%%%%%%%%%%%%%%%%%%%%%%%%%%%%%%%%%%%%%%%%%%%%%%%%%%%%%%%%%%%%%%%%%%%%% end SEM image porosity threshold %%%%%%%%%%

SmallGray = imresize(Gray, [(Rows/4) (Columns/4)], 'lanczos3');

SmallGrayCanny = edge(SmallGray, 'canny');

GrayCanny = zeros(Rows, Columns);
GrayCannyLog = zeros(Rows, Columns);

%%%%%%%%%%%%% if the Small gray image is quarter size
m = 1;
for m = 1:(Rows/4)
    n = 1;

    for n = 1:(Columns/4)
        GrayCanny(((4*m)),((4*n))) = SmallGrayCanny(m,n);
        GrayCanny(((4*m)),((4*n)-3)) = SmallGrayCanny(m,n);
        GrayCanny(((4*m)),((4*n)-2)) = SmallGrayCanny(m,n);
        GrayCanny(((4*m)),((4*n)-1)) = SmallGrayCanny(m,n);

        GrayCanny(((4*m)-3),((4*n))) = SmallGrayCanny(m,n);
        GrayCanny(((4*m)-3),((4*n)-3)) = SmallGrayCanny(m,n);
        GrayCanny(((4*m)-3),((4*n)-2)) = SmallGrayCanny(m,n);
        GrayCanny(((4*m)-3),((4*n)-1)) = SmallGrayCanny(m,n);

        GrayCanny(((4*m)-2),((4*n))) = SmallGrayCanny(m,n);
        GrayCanny(((4*m)-2),((4*n)-3)) = SmallGrayCanny(m,n);
        GrayCanny(((4*m)-2),((4*n)-2)) = SmallGrayCanny(m,n);
        GrayCanny(((4*m)-2),((4*n)-1)) = SmallGrayCanny(m,n);

        GrayCanny(((4*m)-1),((4*n))) = SmallGrayCanny(m,n);
        GrayCanny(((4*m)-1),((4*n)-3)) = SmallGrayCanny(m,n);
        GrayCanny(((4*m)-1),((4*n)-2)) = SmallGrayCanny(m,n);
        GrayCanny(((4*m)-1),((4*n)-1)) = SmallGrayCanny(m,n);
    end

end

%%%%%%%%%%%%% End small gray image quarter size

m=1;
for m = 1:Rows %add porosity to on phase
    n = 1;
    for n = 1:Columns

%         if (Gray(m,n) <= x)
%             GrayCanny(m,n) = 1;
%         else
%             GrayCanny(m,n) = GrayCanny(m,n);
%         end
    end

end

```

```

end

m=1;
for m = 1:Rows % invert logical matrix
    n = 1;
    for n = 1:Columns

        if (GrayCanny(m,n) == 1)
            GrayCanny(m,n) = 0;
        else
            GrayCanny(m,n) = 1;
        end
    end
end

GrayCannyLog = im2bw(GrayCanny,0.5); % convert to binary image

se = strel('disk',10); % disk for open and eroding operations

GrayCannyOpen = imopen(GrayCannyLog,se); % canny image opening operation

[GCOLabels,ncont] = bwlabeln(GrayCannyOpen); % labels for image
reconstruction

%imshow(GrayCannyOpen);

GrayCannyErodedA = imerode(GrayCannyOpen,se);

GrayCannyErodedB = imerode(GrayCannyErodedA,se);

GrayCannyErodedC = imerode(GrayCannyErodedB,se); % eroded three times, this
works for 1_200_1.jpg but maybe not for others - depends on aggregate size
- is this appropriate?

%%%%%%%%%%%%%% start reconstruction routine %%%%%%%%%%%%%%%

[OELabels,OEncont] = bwlabeln(GrayCannyErodedC); % labels of what is left
after opening and erosion - this is messy and need to be repalced for XCT

a = zeros(OEncont); %array showing labels which are present both before and
after opening and erosion

m=1;
d=1; % counter for a
for m = 1:Rows % finds labels which are present both before and after
opening and erosion
    n = 1;
    for n = 1:Columns

        if (GrayCannyErodedC(m,n) == 1)

            b = 1;
            c = 1;
            for b = 1: OEncont
                if (a(b) == GCOLabels(m,n))
                    c = 0
                end
            end
        end
    end
end

```



```

        if (c == 1)
            a(d) = GCOLabels(m,n);
            d= d+1;
        end

    end

end

end

end

LabelsRecon = zeros(Rows,Columns);

m = 1;
for m = 1:Rows % invert logical matrix
    n = 1;
    for n = 1:Columns

        e = 0;
        e = GCOLabels(m,n);

        f = 1;

        for f = 1:OEncont
            if (a(f) == e) && (a(f) ~= 0)
                LabelsRecon(m,n) = 1;
            end
        end

    end

end

end

end

LRClose = imclose(LabelsRecon,se);
LRCFill = imfill(LRClose,'holes'); %%%%%%%%%%% might not be working
%properly (11/09/2012)

%%%%%%%%%%%%%% start place segmented aggregate in Greyscale image
m=1;
for m = 1:Rows
    n = 1;
    for n = 1:Columns

        if (LRCFill(m,n) == 0)%% LRCFill before 11/09/2012)
            FF(m,n) = FF(m,n);
        else
            FF(m,n) = 256;
        end

    end

end

end

%%%%%%%%%%%%%% start place segmented aggregate in Greyscale image

%%%%%%%%%%%%%% start remove anhydfill from agg
[AggAnhydLabels,AAncount] = bwlabeln(LRCFill);%% LRCFill before 11/09/2012)

AAccount = zeros(AAncount,1);
AggAnhydnpix = zeros(AAncount,1);
AggAnhydvalpix = zeros(AAncount,1);

```

```

AggAnhydavgray = zeros(AAncont,1);
KK = 0;

m=1;
for m = 1:Rows
    n = 1;
    for n = 1:Columns
        KK = Gray(m,n);
        KK = double(KK);
        if (AggAnhydLabels(m,n) >= 1)
            AggAnhydnpix(AggAnhydLabels(m,n)) =
AggAnhydnpix(AggAnhydLabels(m,n)) + 1;
            AggAnhydvalpix(AggAnhydLabels(m,n)) =
AggAnhydvalpix(AggAnhydLabels(m,n)) + KK;
        end
    end
end

Anhydthres = 220; % this is a fudge factor and needs changing

m=1;
for m = 1:AAncont
    AggAnhydavgray(m) = AggAnhydvalpix(m) / AggAnhydnpix(m);

    if (AggAnhydavgray(m) > Anhydthres)
        AggAnhydavgray(m) = 1;
    else
        AggAnhydavgray(m) = 0;
    end
end

m=1;
for m = 1:Rows
    n = 1;
    for n = 1:Columns
        if (AggAnhydLabels(m,n) >=1)
            if (AggAnhydavgray(AggAnhydLabels(m,n)) == 1)
                LRCHandle(m,n) = 0;%% LRCHandle before 11/09/2012)
            end
        end
    end
end

%%%%%%%%%%%%%%%%%%%%%%%%%%%%%%%%%%%%%%%%%%%%%%%%%%%%%%%%%%%%%%%%%%%%%%%% end remove anhydfill from agg

%%%%%%%%%%%%%%%%%%%%%%%%%%%%%%%%%%%%%%%%%%%%%%%%%%%%%%%%%%%%%%%%%%%%%%%% remove aggregate from anhydfill

for m = 1:Rows
    n = 1;
    for n = 1:Columns

        if (LRCHandle(m,n) == 1) && (Anhydfill(m,n) == 1)%% LRCHandle before
11/09/2012)
            Anhydfill(m,n) = 0;
        end
    end
end

%%%%%%%%%%%%%%%%%%%%%%%%%%%%%%%%%%%%%%%%%%%%%%%%%%%%%%%%%%%%%%%%%%%%%%%% remove aggregate from anhydfill

```

```

%use se with rad 10 pix

%%%%%%%%%%%%%% pore location analysis from both agg and anhyd %%%%%%%%%%%%%%%
LRCFill = logical(LRCFill); %% LRCFill before 11/09/2012)
ke = strel('disk',20); % disk for dilation

AGGten = imdilate(LRCFill, ke);%% LRCFill before 11/09/2012)
AGGtwenty = imdilate(AGGten, ke);
AGGthirty = imdilate(AGGtwenty, ke);
AGGforty = imdilate(AGGthirty, ke);
AGGfifty = imdilate(AGGforty, ke); % Aggregate
ANHten = imdilate(Anhydfill, ke);
ANHtwenty = imdilate(ANHten, ke);
ANHthirty = imdilate(ANHtwenty, ke);
ANHforty = imdilate(ANHthirty, ke);
ANHfifty = imdilate(ANHforty, ke); % Anhydrous

AGGtenSeule = zeros(Rows,Columns);
AGGtwentySeule = zeros(Rows,Columns);
AGGthirtySeule = zeros(Rows,Columns);
AGGfortySeule = zeros(Rows,Columns);
AGGfiftySeule = zeros(Rows,Columns);
ANHtenSeule = zeros(Rows,Columns);
ANHtwentySeule = zeros(Rows,Columns);
ANHthirtySeule = zeros(Rows,Columns);
ANHfortySeule = zeros(Rows,Columns);
ANHfiftySeule = zeros(Rows,Columns);

for m = 1:Rows
    n = 1;
    for n = 1:Columns
        %Aggregate
        if (LRCFill(m,n) == 1) && (AGGten(m,n) == 1) %% LRCFill before
11/09/2012)
            AGGtenSeule(m,n) = 0;
        else if (LRCFill(m,n) == 0) && (AGGten(m,n) == 1)%% LRCFill before
11/09/2012)
            AGGtenSeule(m,n) = 1;
        end
    end

    if (AGGten(m,n) == 1) && (AGGtwenty(m,n) == 1)
        AGGtwentySeule(m,n) = 0;
    else if (AGGten(m,n) == 0) && (AGGtwenty(m,n) == 1)
        AGGtwentySeule(m,n) = 1;
    end
end

    if (AGGtwenty(m,n) == 1) && (AGGthirty(m,n) == 1)
        AGGthirtySeule(m,n) = 0;
    else if (AGGtwenty(m,n) == 0) && (AGGthirty(m,n) == 1)
        AGGthirtySeule(m,n) = 1;
    end
end

    if (AGGthirty(m,n) == 1) && (AGGforty(m,n) == 1)
        AGGfortySeule(m,n) = 0;
    else if (AGGthirty(m,n) == 0) && (AGGforty(m,n) == 1)
        AGGfortySeule(m,n) = 1;
    end
end

```



```

        if (LRCFill(m,n) == 0) && (Anhydfill(m,n) == 0) && (Gray(m,n) <=
x)%% LRCFill before 11/09/2012)
            BinPores(m,n) = 1;
        end
    end
end
%%%%%%%%%%%%%%%%%%%%%%%%%%%%%%%%%%%%%%%%%%%%%%%%%%%%%%%%%%%%%%%%%%%%%%%% end assign pores to binary %%%%%%%%%

%%%%%%%%%%%%%%%%%%%%%%%%%%%%%%%%%%%%%%%%%%%%%%%%%%%%%%%%%%%%%%%%%%%%%%%% start colour image and analyse pores %%%%%%%%%

AGGColour = zeros(Rows,Columns,3);
ANHColour = zeros(Rows,Columns,3);
AGGColour = uint8(AGGColour);
ANHColour = uint8(ANHColour);

AGGPoreten = 0;
AGGPoretwenty = 0;
AGGPorethirty = 0;
AGGPoreforty = 0;
AGGPorefifty = 0;

AGGten = 0;
AGGtwenty = 0;
AGGthirty = 0;
AGGforty = 0;
AGGfifty = 0;

ANHPoreten = 0;
ANHPoretwenty = 0;
ANHPorethirty = 0;
ANHPoreforty = 0;
ANHPorefifty = 0;

ANHten = 0;
ANHtwenty = 0;
ANHthirty = 0;
ANHforty = 0;
ANHfifty = 0;
mmm = 0;
nnn = 0;

for m = 1:Rows %add porosity to on phase
    n = 1;
    for n = 1:Columns
        if (LRCFill(m,n) == 0)
            mmm = mmm + 1;
        end

        if (BinPores(m,n) == 1)
            nnn = nnn + 1;
        end

        % Aggregate image
        if ((AGGtenSeule(m,n) == 1))
            AGGten = AGGten + 1;
        end
    end
end

```

```

if ((AGGtenSeule(m,n) == 1))
    AGGtwenty = AGGtwenty + 1;
end

if ((AGGtenSeule(m,n) == 1))
    AGGthirty = AGGthirty + 1;
end

if ((AGGtenSeule(m,n) == 1))
    AGGforty = AGGforty + 1;
end

if ((AGGtenSeule(m,n) == 1))
    AGGfifty = AGGfifty + 1;
end

if (AGGtenSeule(m,n) == 1) && (BinPores(m,n) == 1)
    AGGColour(m,n,1) = 47;
    AGGColour(m,n,2) = 79;
    AGGColour(m,n,3) = 79;
    AGGPoreten = AGGPoreten + 1;
end

if (AGGtwentySeule(m,n) == 1) && (BinPores(m,n) == 1)
    AGGColour(m,n,1) = 102;
    AGGColour(m,n,2) = 139;
    AGGColour(m,n,3) = 139;
    AGGPoretwenty = AGGPoretwenty + 1;
end

if (AGGthirtySeule(m,n) == 1) && (BinPores(m,n) == 1)
    AGGColour(m,n,1) = 150;
    AGGColour(m,n,2) = 205;
    AGGColour(m,n,3) = 205;
    AGGPorethirty = AGGPorethirty + 1;
end

if (AGGfortySeule(m,n) == 1) && (BinPores(m,n) == 1)
    AGGColour(m,n,1) = 174;
    AGGColour(m,n,2) = 238;
    AGGColour(m,n,3) = 238;
    AGGPoreforty = AGGPoreforty + 1;
end

if (AGGfiftySeule(m,n) == 1) && (BinPores(m,n) == 1)
    AGGColour(m,n,1) = 187;
    AGGColour(m,n,2) = 255;
    AGGColour(m,n,3) = 255;
    AGGPorefifty = AGGPorefifty + 1;
end

%Anhydrous image

if ((ANHtenSeule(m,n) == 1))
    ANHten = ANHten + 1;
end

if ((ANHtenSeule(m,n) == 1))

```

```

        ANHtwenty = ANHtwenty + 1;
    end

    if ((ANHtenSeule(m,n) == 1))
        ANHthirty = ANHthirty + 1;
    end

    if ((ANHtenSeule(m,n) == 1))
        ANHforty = ANHforty + 1;
    end

    if ((ANHtenSeule(m,n) == 1))
        ANHfifty = ANHfifty + 1;
    end

    if (ANHtenSeule(m,n) == 1) && (BinPores(m,n) == 1)
        ANHColour(m,n,1) = 47;
        ANHColour(m,n,2) = 79;
        ANHColour(m,n,3) = 79;
        ANHPoreten = ANHPoreten + 1;
    end

    if (ANHtwentySeule(m,n) == 1) && (BinPores(m,n) == 1)
        ANHColour(m,n,1) = 102;
        ANHColour(m,n,2) = 139;
        ANHColour(m,n,3) = 139;
        ANHPorettwenty = ANHPorettwenty + 1;
    end

    if (ANHthirtySeule(m,n) == 1) && (BinPores(m,n) == 1)
        ANHColour(m,n,1) = 150;
        ANHColour(m,n,2) = 205;
        ANHColour(m,n,3) = 205;
        ANHPorethirty = ANHPorethirty + 1;
    end

    if (ANHfortySeule(m,n) == 1) && (BinPores(m,n) == 1)
        ANHColour(m,n,1) = 174;
        ANHColour(m,n,2) = 238;
        ANHColour(m,n,3) = 238;
        ANHPoreforty = ANHPoreforty + 1;
    end

    if (ANHfiftySeule(m,n) == 1) && (BinPores(m,n) == 1)
        ANHColour(m,n,1) = 187;
        ANHColour(m,n,2) = 255;
        ANHColour(m,n,3) = 255;
        ANHPorefifty = ANHPorefifty + 1;
    end
end
end

TotalVoxels = Rows*Columns;
Porosity = ((100/mmm)*nnn);

AGGten = (100/AGGten)*AGGPoreten;
AGGtwenty = (100/AGGtwenty)*AGGPorettwenty;
AGGthirty = (100/AGGthirty)*AGGPorethirty;
AGGforty = (100/AGGforty)*AGGPoreforty;

```

```
AGGfifty = (100/AGGfifty)*AGGPorefifty;

ANHten = (100/ANHten)*ANHPoretten;
ANHtwenty = (100/ANHtwenty)*ANHPorettwenty;
ANHthirty = (100/ANHthirty)*ANHPorethirty;
ANHforty = (100/ANHforty)*ANHPorefifty;
ANHfifty = (100/ANHfifty)*ANHPorefifty;

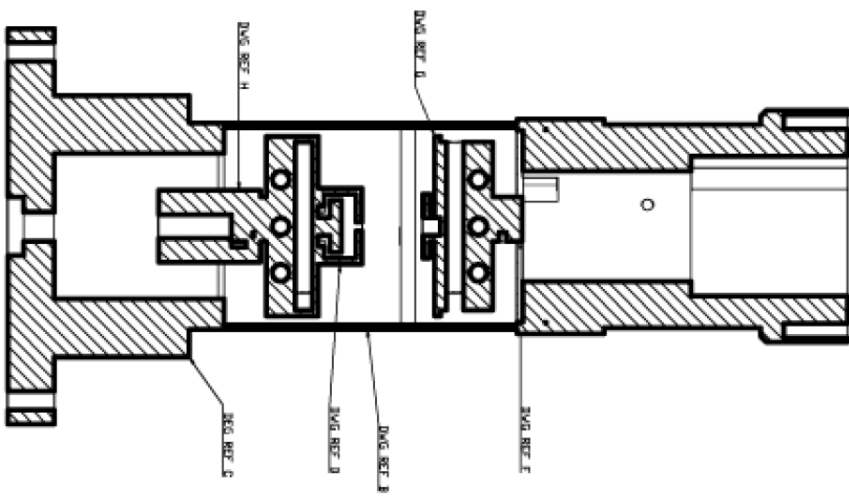
%%%%%%%%%%          end colour image and analyse pores          %%%%%%%%%%%

%%%%%%%%%%          end Script          %%%%%%%%%%%
```


Appendix B: Thermo-mechanical Load Rig Fabrication Drawings

General Notes

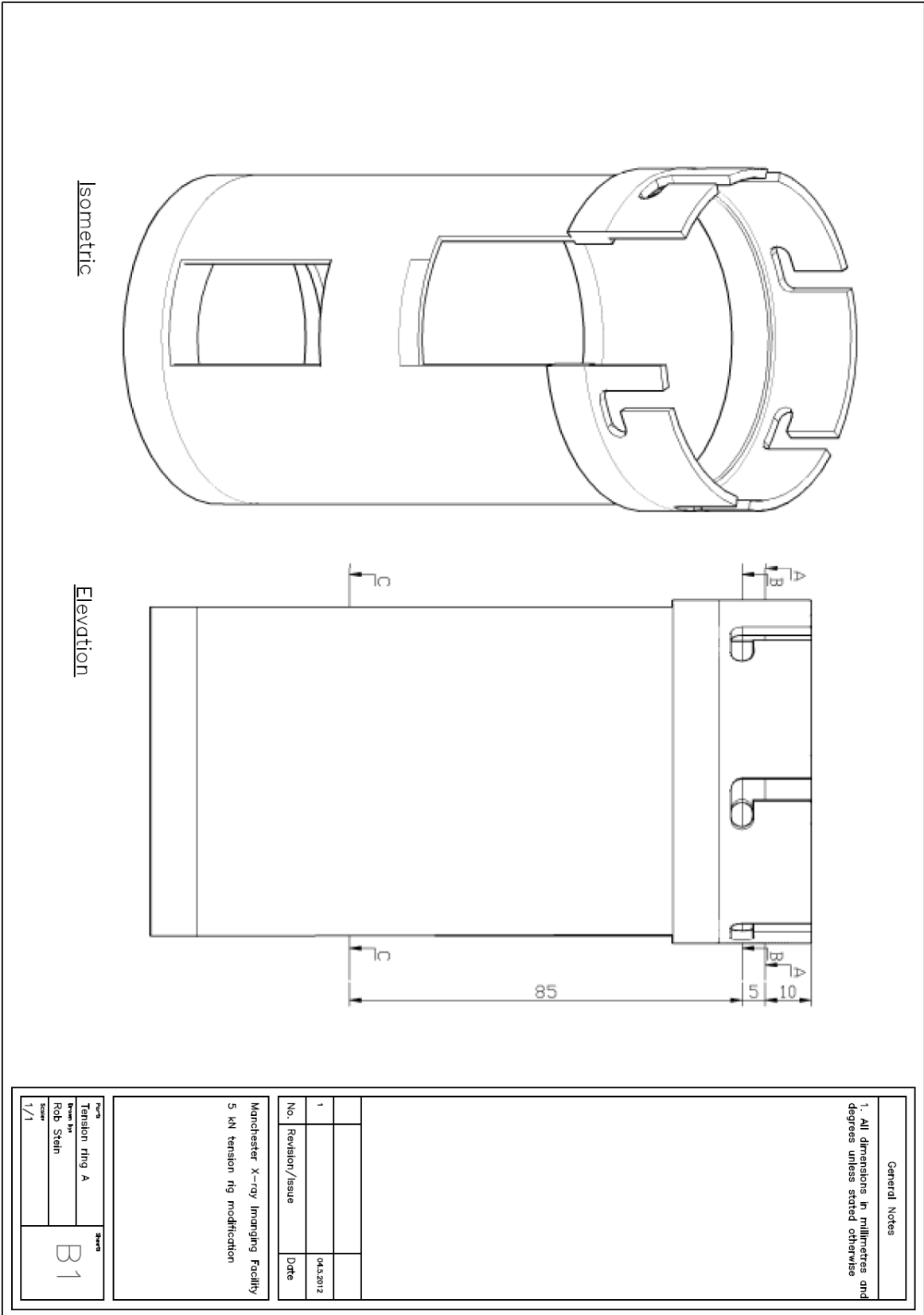
1. All dimensions in millimetres and degrees unless stated otherwise



No.	Revision/Issue	Date
1		04.8.2012

Manchester X-ray Imaging Facility
5 kN tension rig modification

Drawn by Rob Stein	Scale 1/1	Sheet A2
-----------------------	--------------	-------------



Isometric

Elevation

General Notes

1. All dimensions in millimetres and degrees unless stated otherwise

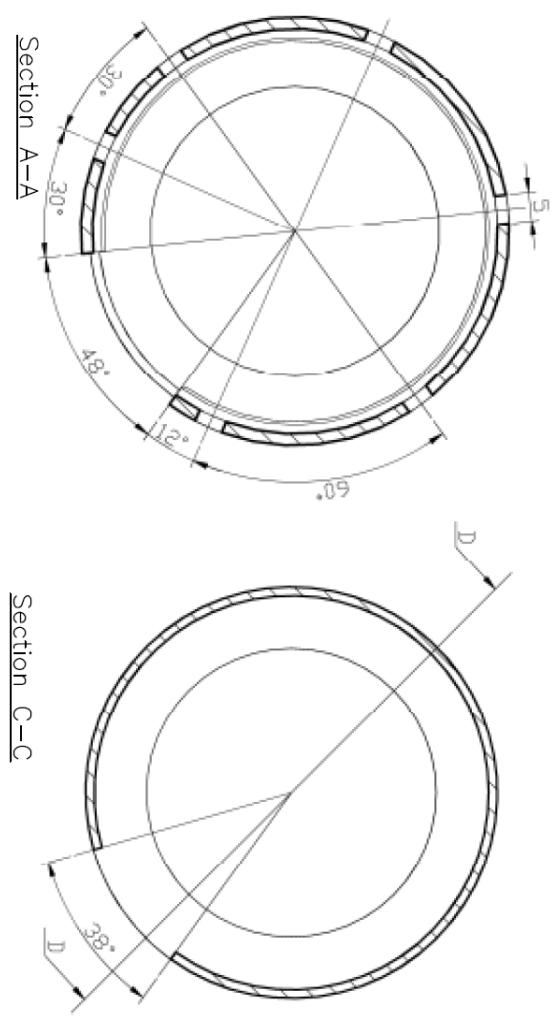
No.	Revision/Issue	Date
1		04.5.2012

Manchester X-ray Imaging Facility
5 kN tension rig modification

Part No	Tension ring A	Sheet	B1
Drawn by	Rob Stein		
Scale	1/1		

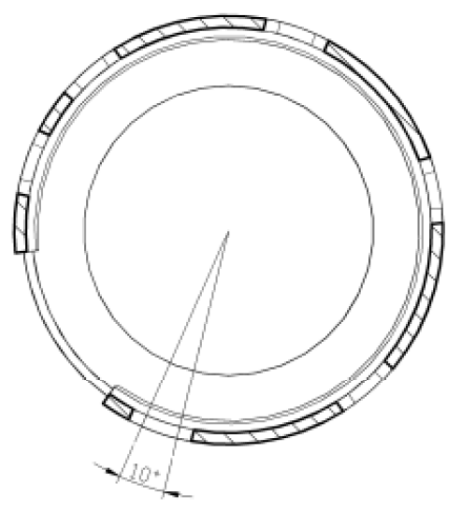
General Notes

1. All dimensions in millimetres and degrees unless stated otherwise



Section A-A

Section C-C

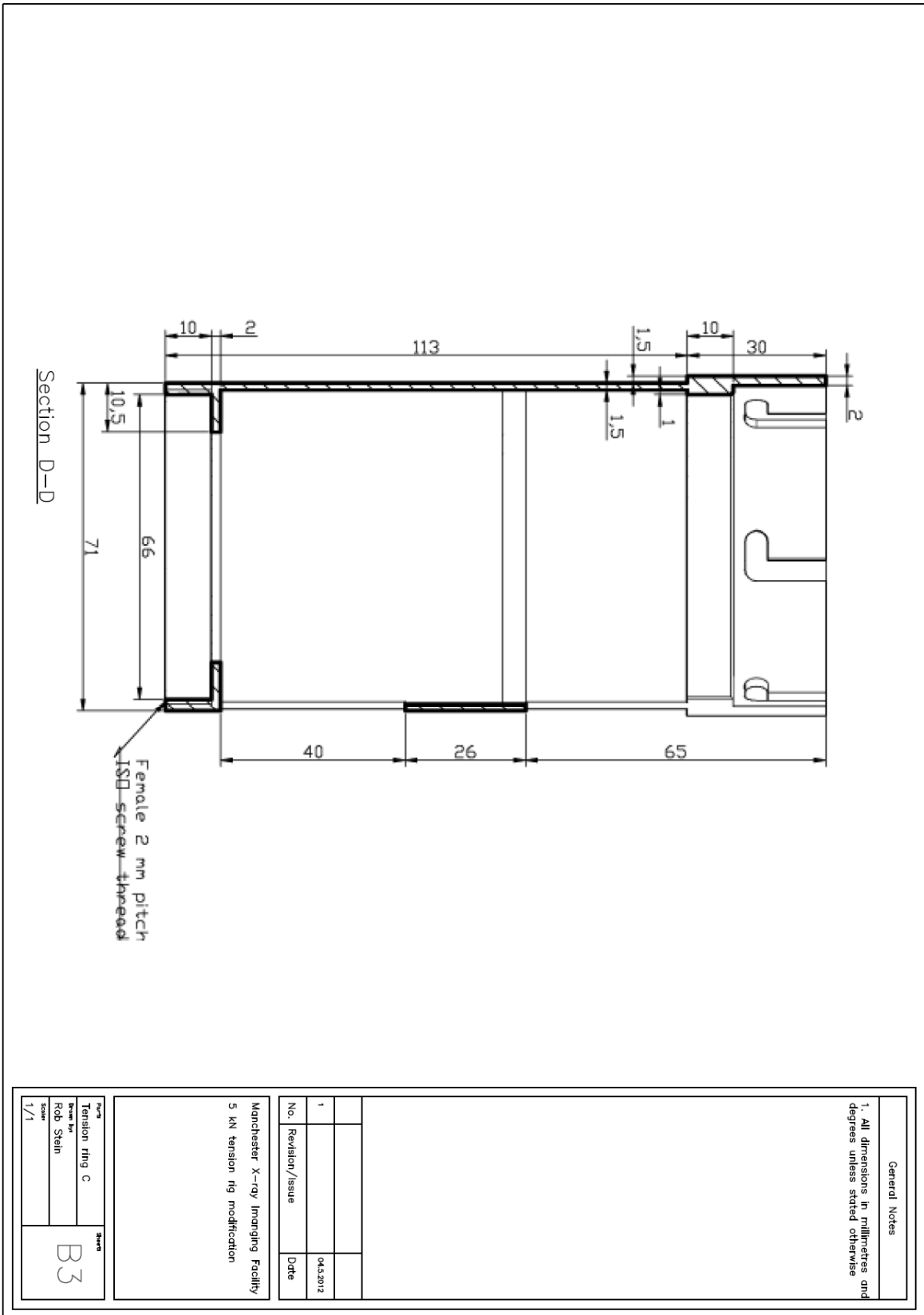


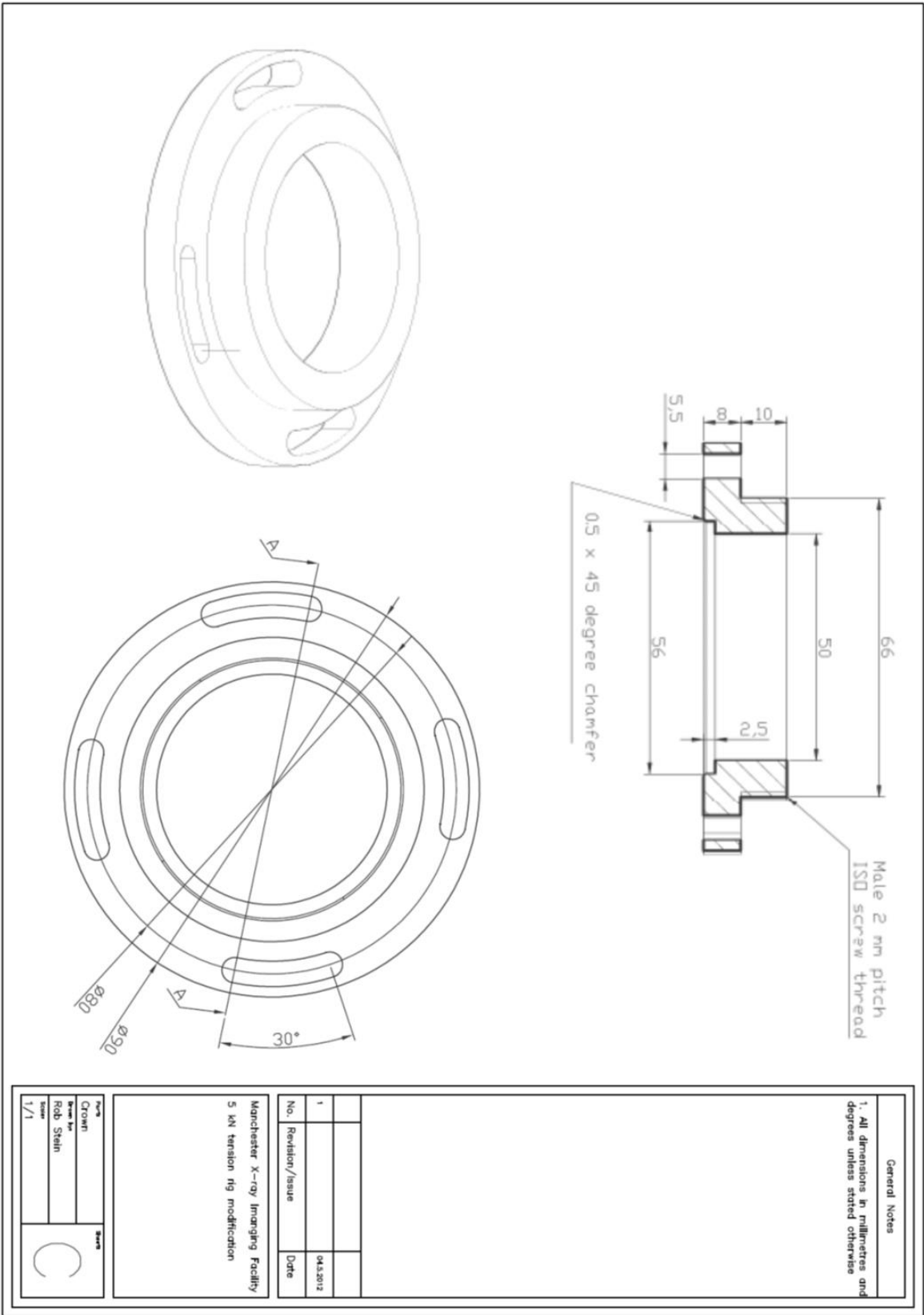
Section B-B

No.	Revision/Issue	Date
1		04.3.2012

Manchester X-ray Imaging Facility
5 kN tension rig modification

Rev	Drawn	Scale
	Tension ring B	B2
	Drawn by	
	Rob Stein	
	Scale	
	1/1	





General Notes

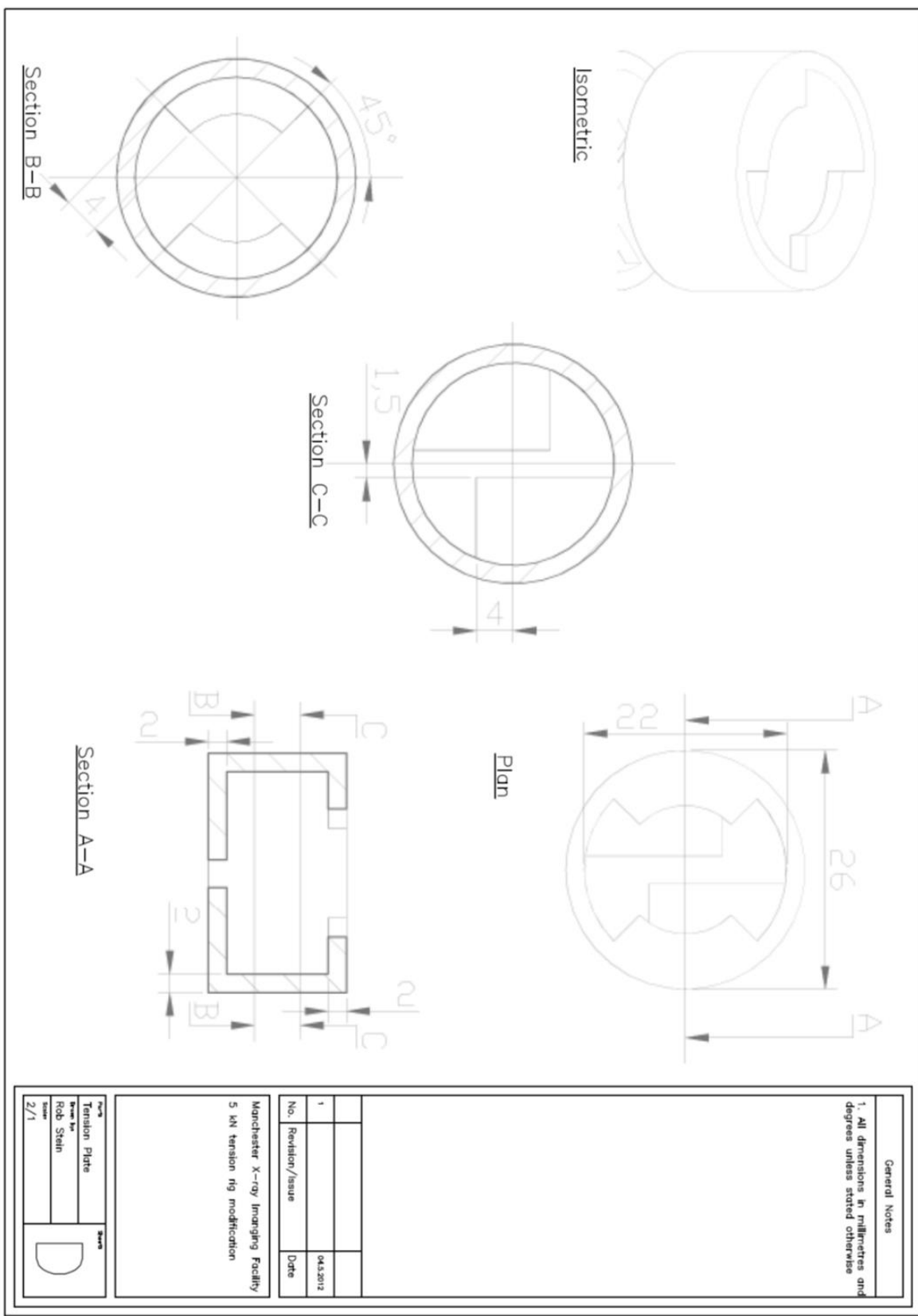
1. All dimensions in millimetres and degrees unless stated otherwise

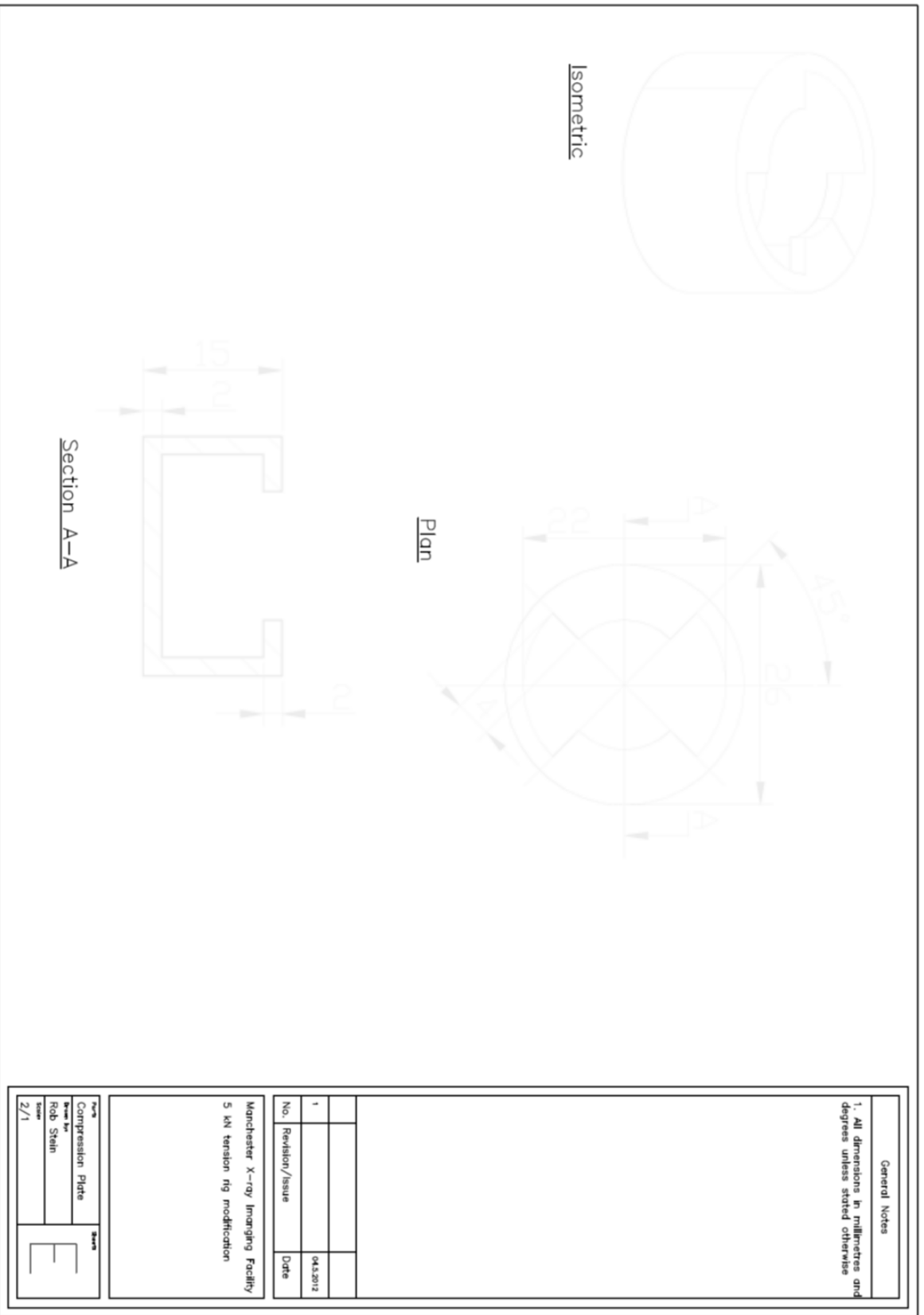
No.	Revision/Issue	Date
1		04.12.12

Manchester X-ray Imaging Facility
5 kN tension rig modification

Part	Drawn	Checked
CROWN	Rob Steinh	
Scale	1/1	







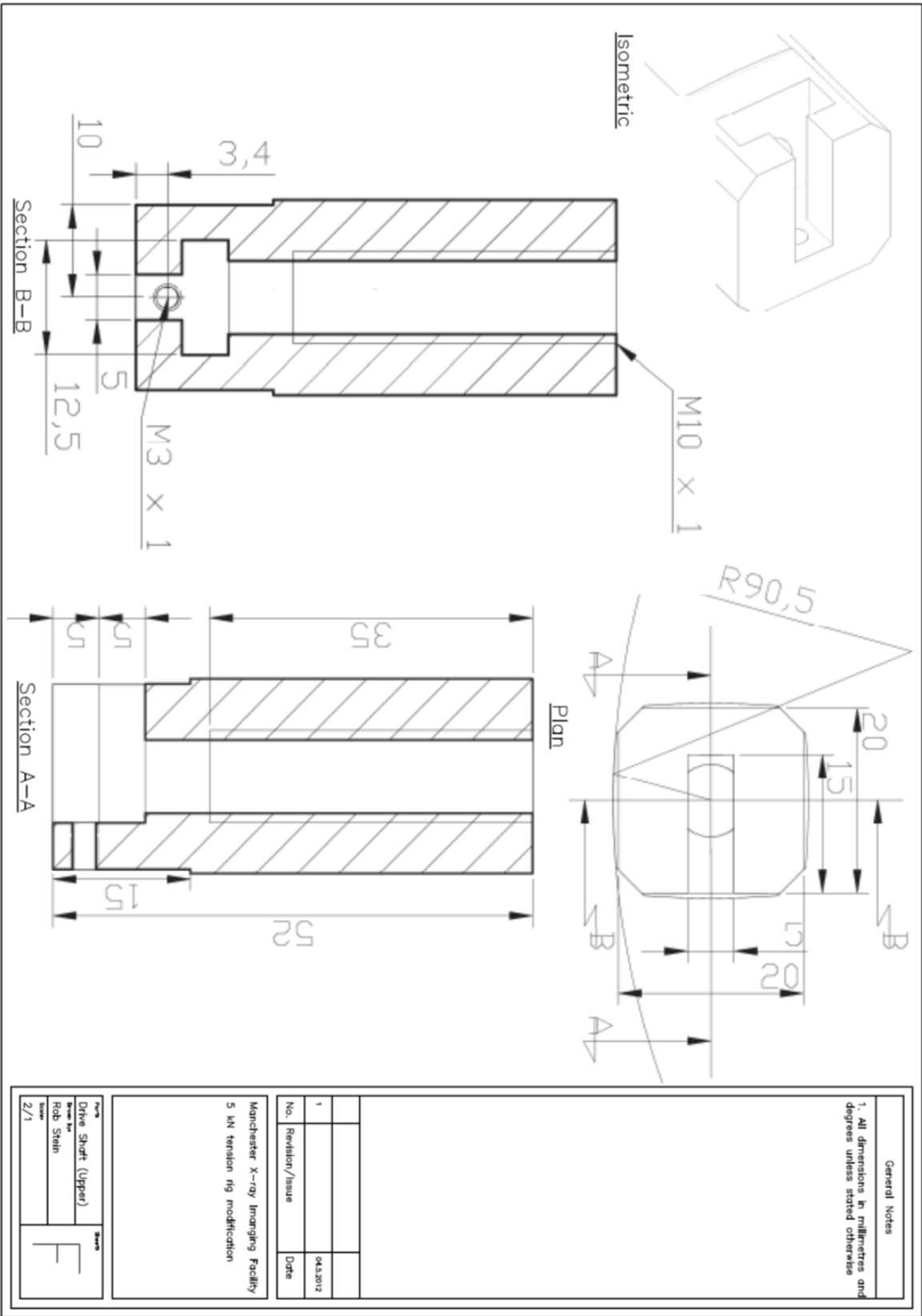
Isometric



Plan



Section A-A



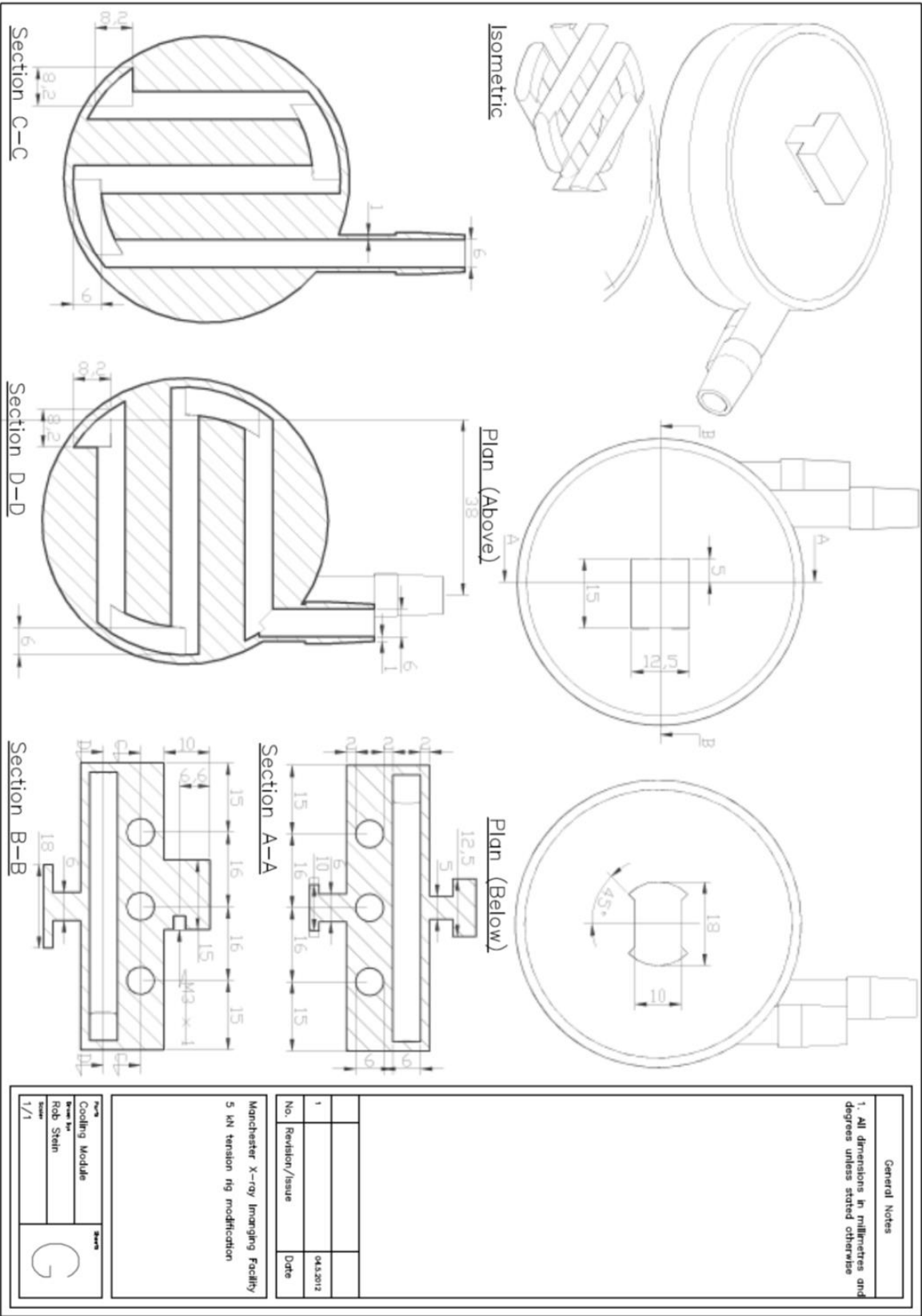
General Notes

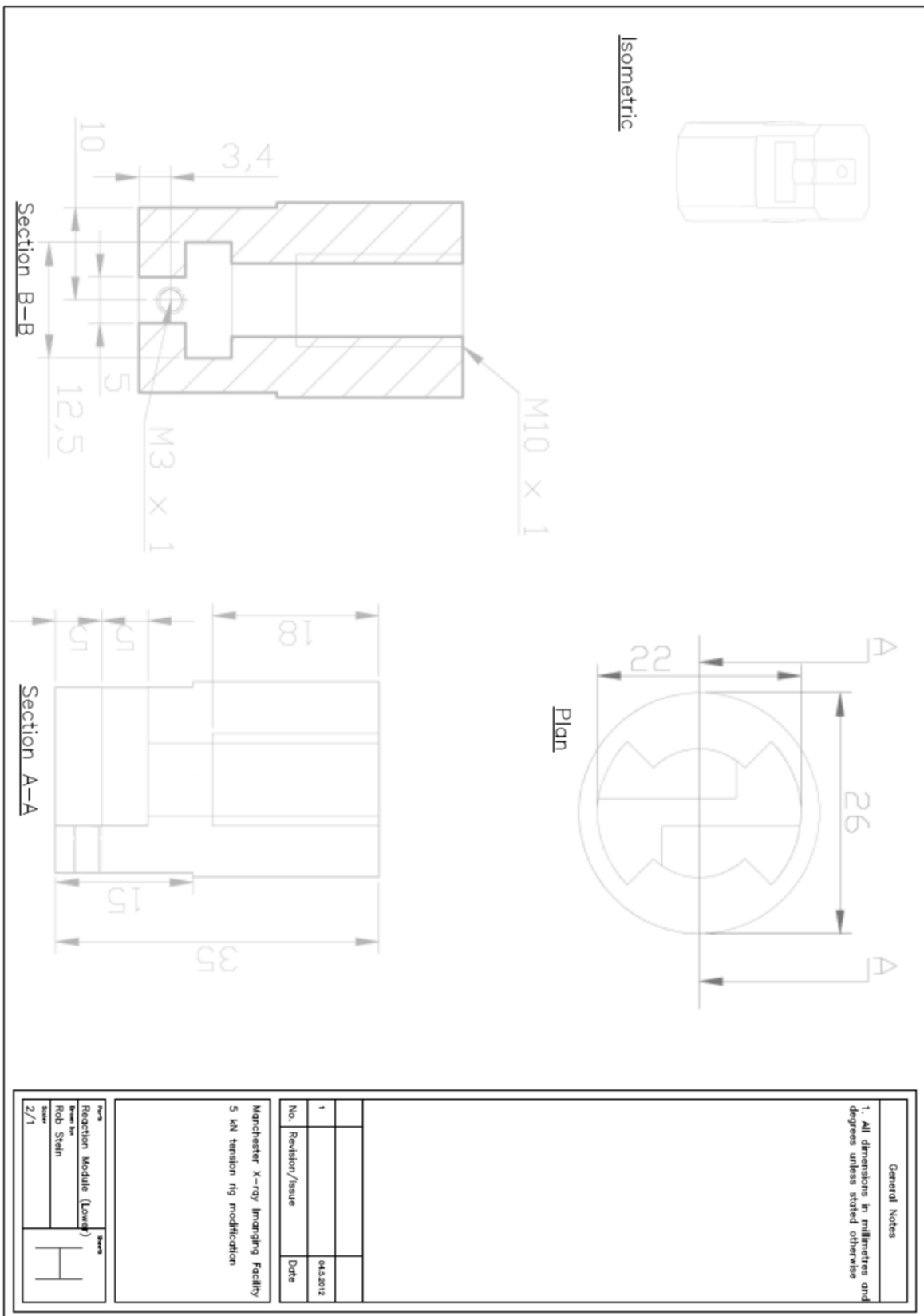
1. All dimensions in millimetres and degrees unless stated otherwise

No.	Revision/Issue	Date
1		04.3.2012

Manchester X-ray Imaging Facility
5 kN tension rig modification

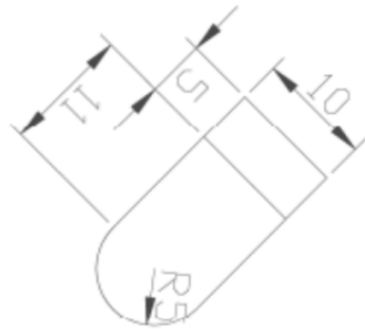
Part Name	Scale
Drive Shaft (Upper)	F
Drawn by Rob Steinhilber	
Issue 2/1	







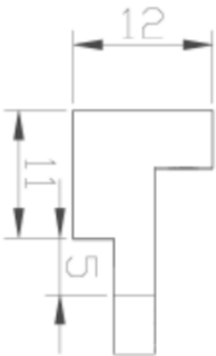
Isometric



Plan



Elevation B



Elevation A

General Notes

1. All dimensions in millimetres and degrees unless stated otherwise

No.	Revision/Issue	Date
1		04.2012

Manchester X-ray Imaging Facility
5 kN tension rig modification

Part	Drawn
Reaction Module (Lower)	
Drawn by	Robb Stein
Scale	2/1

Appendix C: *In-situ* X-ray CT Matlab Analysis Script

```

% Analyses the porosity of X-ray CT images

%----- Routine written by Robert Stein -----
-%

function RSprocessing

nslice = 1;
imname = 'S:\MetrisCB\Rob Stein\insitu\test01_16052013_scan6\slice_0';
imfile = '.tif';
i=1;
cutslice = 799;
h=0;

for i = 1:nslice
    ii = i + cutslice;
    temp = strcat(imname, num2str(ii),imfile);

    I = imread(temp);%load image slice
    disp(['Filtering and shrinkwrapping slice ' num2str(ii) '...']);

    Ifilt = medfilt2(I, [3 3]);%median filter image
    Ifilt3D(:,:,i) = Ifilt(:,:,:);%combine filtered image into 3D image
    %Isw = shrinkWrap(I,'ObjThresh',850000); %create shrinkwrapped image
    %Isw3D(:,:,i) = Isw(:,:,:);%combine shrinkwrapped image into 3D image
    h_tmp = histc(Ifilt(:), 0:65535);%calculate image histogram
    h = h+h_tmp;%calculate cumulative histogram
end

%segmentation start
im_hist_filt = medfilt1(h, 5);%filter histogram to remove erroneous peaks
[pk_intensity,pk_location] = findpeaks(im_hist_filt,'SORTSTR', 'descend',
'MINPEAKDISTANCE', 10000, 'NPEAKS', 2); %Calculate peak location
thres = (1/65535)*((pk_location(2)-
pk_location(1))/2)+(pk_location(1));%calculate threshold for binarisation

j = 1;
for j = 1:nslice
    Ibw3D(:,:,j) = im2bw(Ifilt3D(:,:,j), thres); %threshold filtered images
    Ibwinv3D(:,:,j) = 1 - (Ibw3D(:,:,j));%invert thresholded binary image
end
%segmentation end

[n,r,c] = size(Ibwinv3D);

%segment solid structure and pores together for closing to include cracks
[porelabelsA,porenumA] = bwlabeln(Ibwinv3D,26);
porestatsA = regionprops(porelabelsA, 'basic');
poreareasA = [porestatsA.Area];
% Get a list of the pores that meet our criteria and we need to keep.
i=1;
for i = 1:porenumA
    if poreareasA(i) <50000
        allowableAreaIndexesA(i) = i;
    else
        allowableAreaIndexesA(i) = 0;
    end
end

```

```

end% Take the large background object
keeperporesimageA = ismember(porelabelsA, allowableAreaIndexesA);
%end segment solid structure and pores together for closing to include
cracks

%close individual slices in new image
se = strel('disk',5);
for j = 1:nslice
    closedCracksA(:,:,j) = imclose(keeperporesimageA(:,:,j), se); %close
segmented images
    filledClosedCracksA (:,:,j) = imfill(closedCracksA(:,:,j), 'holes');
%fill any remaining holes
    erodeFilledClosedCracksA (:,:,j) = imerode(filledClosedCracksA(:,:,j),
se); %erode once
end
%end close individual slices in new image

segmentedImage = erodeFilledClosedCracksA .* Ibwinv3D;
%invFilledClosedCracksA = 1 - filledClosedCracksA;
%combinedSegmentedImage = segmentedImage + invFilledClosedCracksA;
%combinedSegmentedImage(:,:,1) = zeros(n,r);
%combinedSegmentedImage(:,:,c) = zeros(n,r);
%combinedSegmentedImageClear = imclearborder(combinedSegmentedImage)

%quantification for volume and images
[structlabels,structnum] = bwlabeln(erodeFilledClosedCracksA,26); %solid
structure
structstats = regionprops(structlabels, 'basic');
[Iseg3D,Iseg3Dnum] = bwlabeln(segmentedImage, 26); % Porosity
porestatsvol = regionprops(Iseg3D, 'basic');
Vol = 0;
k = 1;
for k = 1:Iseg3Dnum %Calculate porosity
    if (porestatsvol(k).Area) > 3
        Vol = Vol + (porestatsvol(k).Area);
        %porenumber = porenumber+1;
    end
    disp(['porevol ' num2str(k) '...']);
end
porosity = (100/(((structstats(1).Area))))*Vol; %porosity quatification
%end quantification for volume and images

%quantification for pore size distribution
segmentedImagePDIST = imclearborder(segmentedImage);%Ibw is just from
greyscale segmentation
[Iseg3DPDIST,Iseg3DPDISTnum] = bwlabeln(segmentedImagePDIST,26);
%quantification for pore size distribution
porestats = regionprops(Iseg3DPDIST, 'basic');
%end quantification for pore size distribution

fid=fopen('S:\MetrisCB\Rob
Stein\insitu\test01_16052013_scan1\binarypores.raw','w+');
fwte=fwrite(fid,Iseg3D,'uint16');
fclose(fid);

```



```
save('S:\MetrisCB\Rob Stein\insitu\test01_16052013_scan1\results.mat',  
'porosity', 'porestats', 'Iseg3Dnum', 'Iseg3DPDISTnum');  
end
```

```
%%%%%%%%%
```

```
end Script
```

```
%%%%%%%%%
```